Shining Light on Iridium: Merging Photocatalysis with Transition Metal Hydride Chemistry

Inauguraldissertation

Zur Erlangung der Würde eines Doktors der Philosophie

vorgelegt der Philosophisch-Naturwissenschaftlichen Fakultät
der Universität Basel

von

Mirjam Rebekka Schreier

aus Deitingen, SO

Basel, 2022

Genehmigt von der Philosophisch-Naturwissenschaftlichen Fakultät auf Antrag von

Fakultätsverantwortlicher / Dissertationsleiter: Prof. Dr. Oliver S. Wenger
Korreferentin: Prof. Dr. Catherine E. Housecroft

Basel, 23. Juni 2020

Prof. Dr. Martin Spiess, Dekan

“Education is the most powerful method which you can use to change the world.”
Nelson Mandela

für Mami, Papi, Lea & Simon

Acknowledgement

During the last decade at the University of Basel I have had the great luck to be surrounded by extremely talented, enthusiastic, and kind-hearted people, who all contributed to this thesis, be it in a scientific, administrative or social way.

First and foremost, I would like to thank my supervisor **Prof. Dr. Oliver Wenger** for giving me the opportunity to do a PhD in his group. Oliver, I highly appreciate the working atmosphere you are creating, which is based on mutual respect and scientific freedom. You always have an open ear for all of us and provide guidance, whenever it is needed. As a mentor, you motivate us to take over responsibility, but always with the awareness that you have our backs whenever it is needed. As such, you influenced not only who I became as a scientist, but you also helped my development as a person. I will always be grateful for everything you did and still do for me personally as well as for our entire group. Thank you!

I want to thank **Prof. Dr. Catherine Housecroft** for agreeing to be the co-examiner of my thesis. I am also thankful that I could profit from your passion for teaching; both as a student and when supervising practical courses under your supervision.

Furthermore, I would like to thank **Prof. Dr. Christof Sparr** for being the chair of my defense.

I am especially grateful to **Xingwei** for providing me guidance throughout the first years of my PhD. You have made an enormous contribution to all of my projects and I really appreciate your valuable inputs and our rewarding collaboration with developing both the iridium hydride project and the water-soluble iridium sensitizers.

I want to thank **Christoph**, **Björn** and **Debi** for the fruitful collaboration we had with the iridium sensitizers. **Christoph**, I am always amazed by how many new ideas you have for the complexes and I am looking forward to many more to come.

Also, I want to thank everybody that was involved in proofreading my thesis or my manuscript. **Luci**, **Felix**, **Svenja**, **Björn**, **Christina** and **Debi**, thank you for taking your valuable time to read and correct my thesis, for giving me constructive feedback and for countless Zoom meetings to discuss open questions and grammar rules.

Throughout my time as a PhD student I was extremely blessed to get to work with many students. I am grateful to **Dimitri**, **Xavier**, **Raoul**, **Pascal**, **Jessica**, **Jasmin**, **Debi** and **Fabian** who all made a contribution to this thesis either during their Wahlpraktikum and/or their Schlussversuch. I feel very lucky that I was able to work with such talented and motivated students, and I am especially grateful for the many friendships that emerged out of these internships.

I want to thank all the current and former members of the Wenger group for the great working-atmosphere, all the scientific and non-scientific discussions and all the fun we had throughout the last four years. A special thank goes to my lab mates of lab 304, **Patrick**, **Luci**, **Jakob**, **Chris**, **Christina**, **Narayan** and **Han**, as well as of lab 307, **Xingwei** and **Sabine**. I always enjoyed working with you and I will truly miss all the bad jokes and Friday music.

Felix, thank you for being my photocatalysis buddy and for being my personal (F)lexicon and **Luci**, thank you for your constant feedback and for always answering all my questions. **Patrick**, **Christoph**, **Luci, Chris** and **Björn**, thank you for all your help regarding spectroscopy.
Also, I want to thank **Patrick**, **Luci**, **Svenja**, **Chris**, **Christoph**, **Michael** and **Xingwei** for the great time we had during conferences or NCCR related events.
Furthermore, I would like to thank **Linda**, for her constant advices, for our regular lunch meetings and for always being there for me.
Moreover, I would like to thank the entire analytics team (**Sylvie**, **Michael** and **Jonas**) for the great service they provide and especially to **Sylvie** for always taking care of all of us. I want to thank **PD Dr. Daniel Häussinger** and his entire group (**Thomas**, **Daniel**, **Raphael** and **Pascal**) for maintaining the NMRs and for our Thursday lunch meetings. Furthermore, I want to thank **Oli** for all his help, for organizing all our chemicals and materials and in particular for optimizing all the processes regarding the shop. Also, I want to thank the entire Werkstatt (**Markus**, **Hisni**, **Andreas** and **Andres Koller**) for maintaining a great research atmosphere and fixing everything I broke within the last years. I also want to thank the administrative staff, **Brigitte**, **Marina**, **Beatrice** and **Olaf**, for all the work they do in the background to keep the department running.

This long time at the department would not have been the same without the many people I got to know both during my studies and during my PhD. It has been an extreme joy to be surrounded by all of you and to get to know so many different cultural backgrounds. Thanks to all of you for many BBQs, countless discussions and for all the support throughout the last years. Many of you became close friends and I highly appreciate that you have always been there for me; not only in good times, but also whenever I was frustrated or just had a bad day.
Zudem möchte ich mich bei all meinen Freunden von ausserhalb der Universität bedanken. Viele von euch begleiten mich schon während mehr als der Hälfte meines Lebens und ich bin besonders dankbar für die vielen unterhaltsamen Abende, für die gemeinsamen Urlaube, für die langen Telefonate und besonders dafür, dass ihr immer für mich da seid.
Zum Schluss möchte ich mich noch bei meiner gesamten Familie bedanken. Besonders bei meinen Geschwistern, **Lea** und **Simon**; danke, dass ihr immer für mich da seid und dass ihr mich immer zum Lachen bringt. **Simon**, deine Unbeschwertheit und deine Lebensfreude sind beneidenswert und **Lea**, ich wünschte ich besässe nur einen kleinen Teil von deinen Management-Skills und deiner Kreativität. Ich bin unglaublich stolz auf euch beide.
Mami und **Papi**, danke, dass ihr immer hinter uns steht und uns dabei unterstützt unsere Träume zu verwirklichen. Danke, dass ihr uns vorgelebt habt, wie wichtig Nächstenliebe und gegenseitiger Respekt ist, aber auch, wie wertvoll ein erfüllender Beruf sein kann. Ihr seid meine grössten Vorbilder und ohne euch wäre ich nicht der Mensch geworden, der ich heute bin. Danke!

Abstract

Exploiting the ability of visible light to enable new chemical transformations has emerged as an important method in chemistry in recent years since it provides a more sustainable and mild alternative to many thermal processes.[1–3]

To expand the scope of traditional photocatalysis, combining the light-dependent cycle with a second, co-catalytic cycle has proven to be extremely valuable.[4,5] Among the many synergistic strategies, merging photocatalysis with transition metal catalysis has gained particular interest since the activation of the organometallic catalyst via energy or electron transfer enables completely new reactivities.[6] In this thesis, two different approaches for the merger of photocatalysis with metal hydride chemistry are investigated in order to enable new light-dependent reactions.

In the first project (Chapter 3), the two catalytic reactivities are merged within one single-component dual photocatalyst. The investigated iridium hydrides are photoactive[7,8] and can therefore take over the function of the chromophore as well as the metal hydride. While the photohydride[9,10] or photoacid[11] behavior of iridium hydrides has been reported previously, Chapter 3 focuses on their ability to activate olefins via photoinduced hydrogen atom transfer (photo-HAT). The key to this new reactivity is the weak Ir^{II}-H bond (ca. 44 kcal $\cdot$ mol^{-1}),[12] which is formed upon reductive quenching of the triplet-excited Ir(III) hydride in presence of triethylamine. The typical HAT reactivity was observed for a series of 12 different substrates and the radical mechanism was further supported with a radical clock experiment.

The second project (Chapter 4) provides mechanistic insight into the bimolecular processes that are at play when transition metal hydride chemistry is merged with photocatalysis in the context of nucleotide co-factor regeneration. For this purpose, four water-soluble variants of **(*fac*)-[Ir(ppy)$_3$]** (ppyH = 2-phenylpyridine) were developed and characterized by steady-state and time-resolved spectroscopy as well as by cyclic voltammetry. Their excited-state reactivity was exploited for the photochemical regeneration of 1-benzyl-1,4-dihydronicotinamide (**1,4-BNAH**), a commonly employed nucleotide co-factor mimic. The bimolecular processes that govern this light-dependent transformation were analyzed based on the correlation between the efficiency of the reaction and the excited-state properties of the sensitizers. More mechanistic insight was gained by luminescence-quenching experiments and transient absorption spectroscopy.

All in all, this thesis demonstrates how the synergy between photocatalysis and transition metal hydride chemistry can be utilized to enable new light-dependent reactivities and furthermore provides an insight into the bimolecular processes that govern the interplay between the two reactivities.

Table of Contents

Abbreviations

1,4-BNAH	1-benzyl-1,4-dihydronicotinamide
1,4-NADH	1,4-dihydronicotinamide adenine dinucleotide
A	acceptor
AgOTf	silver trifluoromethanesulfonate
aq.	aqueous
BNACl	1-benzyl-3-carbamoylpyridin-1-ium chloride
BDE	bond dissociation enthalpy
BDFE	bond dissociation free energy
bpy	2,2'-bipyridine
calcd.	calculated
Cp*	pentamethylcyclopentadienyl
D	donor
DABCO	1,4-diazabicyclo[2.2.2]octane
DCM	dichloromethane
DFT	density-functional theory
DIPEA	diisopropylethylamine
DMSO	dimethyl sulfoxide
EA	elemental analysis
EI	electron ionization
ESI	electrospray ionization
Et	ethyl
GC/MS	gas chromatography–mass spectrometry
h	hours
HAT	hydrogen atom transfer
HOMO	highest occupied molecular orbital
HRMS	high-resolution mass spectrometry
IC	internal conversion
ISC	intersystem crossing
ISTD	internal standard
LED	light-emitting diode
LUMO	lowest unoccupied molecular orbital
NAD^+	nicotinamide adenine dinucleotide
NMR	nuclear magnetic resonance
Me	methyl
MeCN	acetonitrile
M-H	metal hydride
MHAT	metal hydride catalyzed hydrogen atom transfer
min	minutes

MLCT	metal-to-ligand charge-transfer
PC	photocatalyst
PET	photoinduced electron transfer
PCET	proton-coupled electron transfer
phen	1,10-phenanthroline
photo-HAT	photoinduced hydrogen atom transfer
ppyH	2-phenylpyridine
rt	room temperature
sat.	saturated
SCE	saturated calomel electrode
SET	single electron transfer
TCSPC	time-correlated single photon counting
TEA	triethylamine
TEOA	triethanolamine
TFA	trifluoroacetic acid
TFAA	trifluoroacetic anhydride
Tfen	*N*-(2-aminoethyl)-4-(trifluoro-methyl)benzenesulfonamide
THF	tetrahydrofuran
TOF	turnover frequency
TON	turnover number
ttEnT	triplet-triplet energy transfer
UV	ultraviolet
Vis	visible

1 Perspective

Two of the most crucial problems society is currently facing are climate change and a growing energy demand.[13] Both problems are closely interlinked with fossil fuels, which to date still provide around 80% of the world's energy.[14] However, there are major problems associated with fossil fuels: Due to their finite and non-renewable nature, fossil fuels will at some point in the future no longer be readily accessible. In addition, the combustion of fossil fuels is accompanied by the formation of gases such as CO_2, SO_2 and NO_x; all of which are responsible for anthropogenic climate change.[15–17] Thus, an environmentally friendly and renewable alternative energy source is highly desirable.

Within one hour, the sun provides more energy to the earth than humankind consumes within a year.[16,18,19] Furthermore, this energy is non-polluting and in principle readily available. It is already possible to convert solar energy into electricity (solar cells) and thermal energy (solar heating). However, both strategies are based on secondary conversion of solar energy, which limits the efficiency of these devices.[18,20] Direct conversion of solar energy into chemical energy is thus highly desirable. With natural photosynthesis, nature provides a blueprint for this process. A substantial amount of research has been performed trying to mimic this natural system.[16,21,22] In this context, nucleotide co-factor regeneration has proven to be particularly important since it manages to combine a photocatalytic system with an enzymatic dark reaction, in analogy to natural photosynthesis.[23–25] Other important research fields in terms of solar energy conversion include water splitting[26,27] and CO_2 reduction.[28,29]

Using light as an energy input has not only gained a broad interest regarding solar energy conversion, but more recently, photocatalysis has emerged as an important new strategy in synthetic organic chemistry. Exploiting the excited-state reactivity of photocatalysts enables new chemical transformations, which would not be possible in the absence of light.[1,2,4] Photocatalysis provides a sustainable and mild alternative to traditional thermal methods, enabling reactions with high selectivities and a broad functional group tolerance. Especially in the field of radical chemistry, photocatalysis has gained a lot of attention since it allows the formation of open-shell intermediates under mild reaction conditions and without the need for radical initiators.[1,19,30]

To expand the scope of traditional photocatalysis, combining the light-dependent reaction with a second co-catalytic cycle has proven to be particularly useful.[3–5] Among the various co-catalytic methods, combining photocatalysis with transition metal catalysis has gained specific relevance, since it allows new reactivities of organometallic species by activating them either via energy or electron transfer processes.[6,31,32] In this field, merging photocatalysis with transition metal hydride reactions is particularly interesting since transition metal hydride chemistry is extremely diverse due to the different possible cleavage modes of the metal–hydrogen bond.[33–36]

In the first project (Chapter 3), the ability of iridium hydrides to function both as the photocatalyst and as a hydrogen atom transfer catalyst is exploited to achieve a photoinduced hydrogen atom transfer (photo-HAT) from the metal center to unactivated olefins. This is relevant in the context of photocatalysis since the vast majority of photocatalytic transformations have been dominated by photoinduced electron transfer (PET) processes and as such are strongly dependent on the redox properties of both the photoredox catalyst and the substrate.[1–3,37–40] Photo-HAT is a promising alternative to PET reactions since it allows the activation of substrates regardless of their redox properties.[41,42] In analogy to PET with traditional photoredox catalysts, photo-HAT can in principle take place from either the excited state or on the ground-state potential surface. Despite its potential, photo-HAT is still underexplored in organic synthesis and the key step in the few examples of photo-HAT reactivity always involves hydrogen atom abstraction from an organic substrate by a photoexcited state.[43–47] Hence, this thesis complements these studies, as the contrary reaction, i.e., an overall photo-HAT from a metal complex to a closed-shell organic substrate resulting in the formation of a new C-H bond, is reported.

Transition metal hydrides have a long-standing tradition as redox mediators in the (photo-) catalytic regeneration of nucleotide co-factors.[23,48,49] But even though various examples showcase photocatalytic **1,4-NADH** formation by combining a photocatalyst with rhodium hydride chemistry,[50–52] the knowledge about the interplay between the two catalytic cycles is still limited. In the second project (Chapter 4) new insights into the photophysical mechanisms governing the visible-light driven formation of the rhodium hydride intermediate are gained. The basis of these studies is a set of newly developed water-soluble iridium sensitizers, whose excited-state properties can be used to disentangle the underlying reaction mechanisms.

2 Theoretical Background

2.1 Main Principles for Photocatalysis

2.1.1 The Excited State

Photocatalysis exploits the difference in reactivity of a photocatalyst in its ground state compared to its excited state.[1,2,4] Upon photoexcitation of the photocatalyst, different radiative and non-radiative transitions are involved in the formation and the deactivation of an excited state. These processes can be summarized in a simplified Jablonski diagram (Figure 1). [53–55]

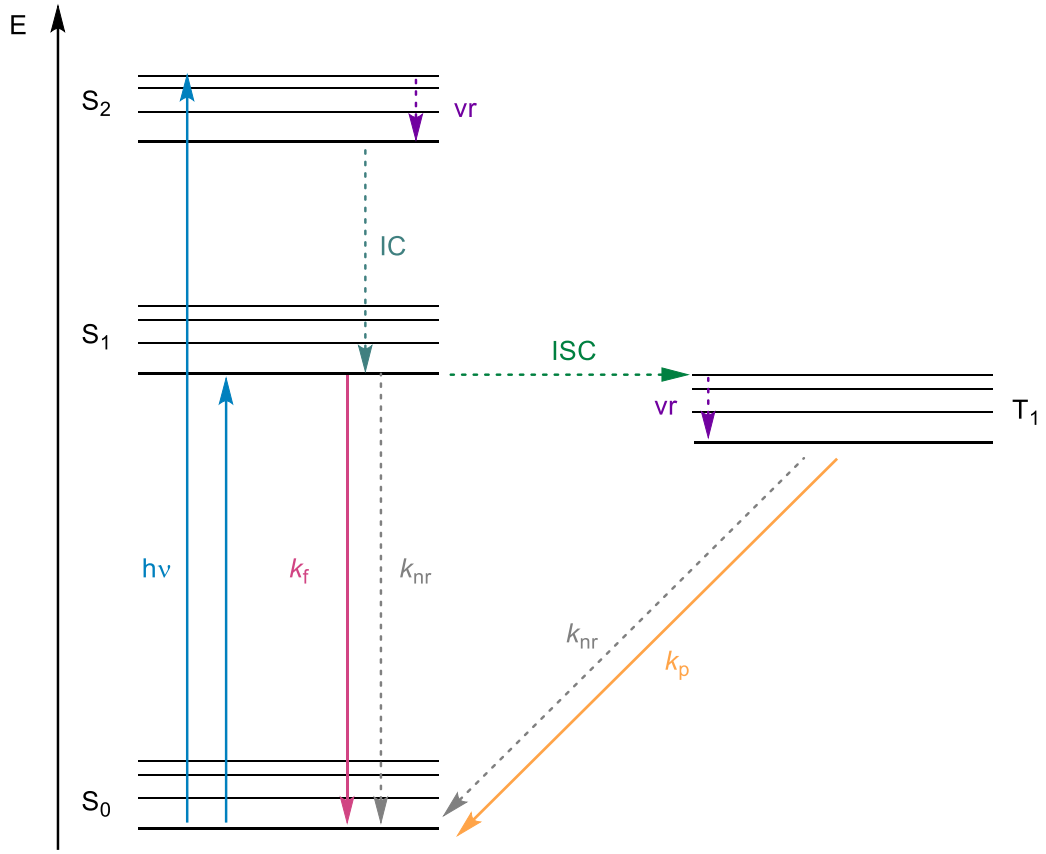

Figure 1: Jablonski diagram depicting absorptions and radiative transitions (solid arrows) as well as non-radiative transitions (dashed arrows) responsible for the formation and the deactivation of an excited state. The involved transitions include absorption ($h\nu$), fluorescence (k_f), phosphorescence (k_p), internal conversion (IC), intersystem crossing (ISC), vibrational relaxation (vr) and non-radiative relaxation (k_{nr}).[53–55]

Upon absorption of a photon ($h\nu$), an electron is excited from the ground state of the molecule (S_0) to a singlet-excited state (S_1 or S_2) in a spin-allowed transition. According to Kasha's rule, luminescence occurs only from the lowest excited state of a certain multiplicity.[55] Hence, when the molecule is promoted into a higher excited state of a given multiplicity (e.g. S_2), it undergoes rapid non-radiative decay via vibrational relaxation (vr, $k_{vr} \approx 10^{12}$-10^{13} s^{-1})[55] and internal conversion (IC, $k_{IC} \approx 10^{6}$-10^{12} s^{-1})[55] to the lowest singlet-excited state (S_1).[53–55] From the S_1-state, the electron can either deactivate to the ground state (S_0) via radiative (fluorescence, k_f) or non-radiative (k_{nr}) decay, or it can populate the

lowest triplet-excited state (T_1) via intersystem crossing (ISC). This non-radiative process is spin-forbidden; however, in the presence of heavy atoms (such as iridium), intersystem crossing is facilitated due to their strong spin-orbit coupling.[56] From the T_1 state, again radiative (phosphorescence, k_p) and non-radiative (k_{nr}) deactivation to the ground state is possible. Since these processes are spin-forbidden, phosphorescence and non-radiative decay from the triplet-excited state are substantially slower compared to fluorescence and non-radiative decay from the singlet-excited state.[53–55] As an example, the rate constant of phosphorescence (k_p) is typically in the range of 10^3 to 10^6 s^{-1},[55] while radiative decay via fluorescence is significantly faster ($k_f \approx 10^7$-10^9 s^{-1}).[55]

2.1.2 Mechanisms in Photocatalysis

If the lifetime of the formed excited state is sufficiently long ($\tau > 1$ ns), the excited molecule is able to encounter a second molecule in solution in a diffusion-controlled process.[53] For cases in which the substrate and the photocatalyst preorganize in solution, even shorter lifetimes can be sufficient for successful photocatalysis.[57,58] Typically, photocatalytic reactions are based on electron transfer or energy transfer pathways.[1,2,53,59] Less frequently, photoexcited states are able to engage in photoinduced hydrogen atom transfer (photo-HAT) reactions.[60]

Photoinduced Electron Transfer

Photoinduced electron transfer (PET) processes in photocatalysis exploit that the formed photoexcited states are both more reducing (higher HOMO) and more oxidizing (lower LUMO) compared to the ground state (Figure 2).[2]

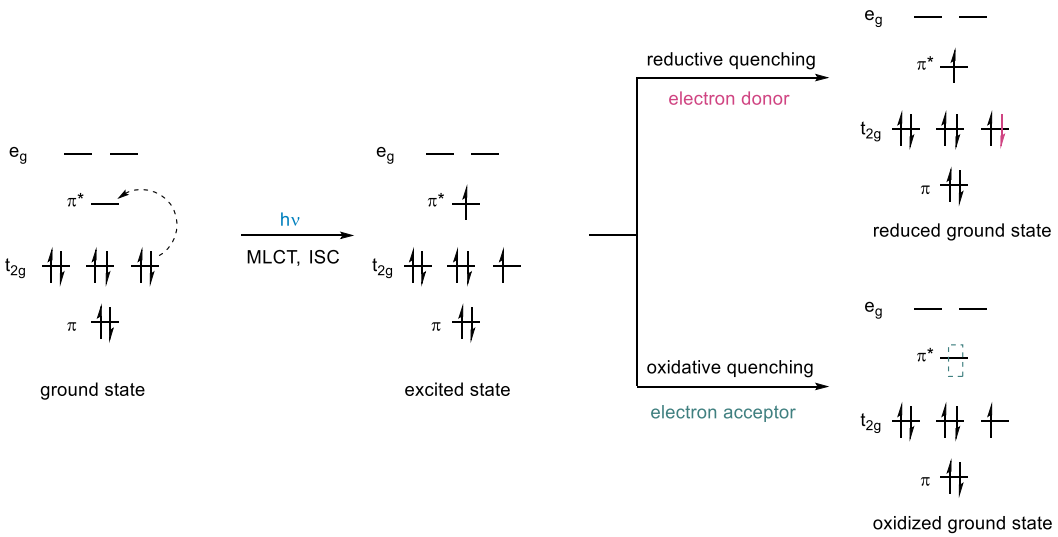

Figure 2: Upon excitation with visible light, photoredox catalysts are both stronger oxidants and stronger reductants compared to their ground state. The relevant processes are exemplified for d^6 metal complexes commonly employed in photoredox catalysis such as **$[Ru(bpy)_3]^{2+}$** and ***fac*-$[Ir(ppy)_3]$**.[1,2] Reproduced from Ref. [1].

The energy difference by which oxidation or reduction is facilitated in the excited state corresponds to the HOMO-LUMO gap of the photocatalyst. Thus, the excited-state redox potentials (E^*_{ox} or E^*_{red}) of photoredox catalysts can be estimated from the ground-state redox

potentials (E^0_{ox} or E^0_{red}) and the HOMO-LUMO gap (E_{00}) of the photocatalyst with the simplified Rehm-Weller equation (eq. 1 and 2), where e is the elementary charge.[61]

$$E^*_{ox} = E^0_{ox} - E_{00} / e \quad (1)$$

$$E^*_{red} = E^0_{red} + E_{00} / e \quad (2)$$

In photocatalysis, two different pathways are usually distinguished for PET processes: after excitation with visible light, the excited photocatalyst (***PC**) can either transfer an electron to the substrate or an electron acceptor (**A**) in an oxidative quenching pathway (Figure 3, left), or it can accept an electron from the substrate or a sacrificial electron donor (**D**) in a reductive quenching pathway (Figure 3, right). In both cases, the ground state (**PC**) needs to be regenerated in a second electron transfer step involving either the substrate or a sacrificial electron donor or acceptor, respectively.[2,3,38]

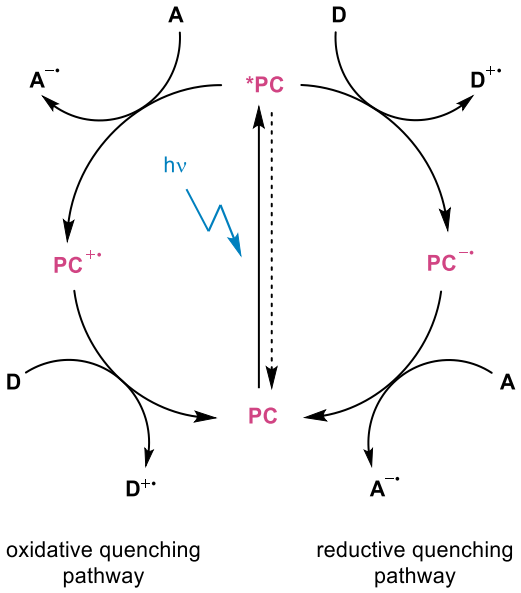

Figure 3: Photoinduced electron transfer processes proceed via oxidative (left) or reductive (right) quenching pathways of the photoexcited state of a photocatalyst (**PC**). **A** = (sacrificial) electron acceptor; **D** = (sacrificial) electron donor.

Depending on the overall change of redox state of the substrate, the photoredox reactions can be denoted as net oxidative, net reductive, and net redox neutral.[2,3,38] Photocatalytic processes that are based on PET are limited by the redox properties of the photocatalyst as well as the substrate. Recent research is eager to enable thermodynamically challenging electron transfer reactions for example by the development of new or modified photocatalysts with properties better suited for the respective reaction.[62–64] Alternative strategies such as two-photon processes[65–68] or merging photocatalysis with electrocatalysis[69–71] have been proven to be promising strategies to extend the intrinsic energetic limitation one visible photon can provide to the photocatalyst in a classical single photon photocatalytic cycle with sacrificial reagents. Alternatively, instead of modulating the photocatalyst and its mechanism, the redox properties of the substrate can be tuned; either by hydrogen bonding in proton-coupled electron transfer (PCET) reactions,[39,72,73] utilizing Lewis acid catalysis,[74,75] or by binding of the substrate to the active site of an enzyme.[76–78]

Triplet-Triplet Energy Transfer

A different approach commonly employed in photocatalysis is based on triplet-triplet energy transfer (ttEnT). In this bimolecular process, the triplet-excited state energy of the photosensitizer is transferred to an acceptor (e.g., the substrate), resulting in the triplet-excited acceptor and the photocatalyst in its ground state (Figure 4).[59] Photocatalytic ttEnT processes proceed via a Dexter energy transfer mechanism, where two electrons are simultaneously exchanged in the ground state and the excited state, respectively (Figure 4, right). Importantly, this mechanism enables the generation of excited states which would hardly or not at all be accessible by direct irradiation due to spin-selection rules. Hence, ttEnT is an important concept in photocatalysis since it allows access to the triplet-excited states of many organic substrates. These states, which are very hard to access via direct irradiation, are of great interest due to their versatile reactivities such as in cyclizations[79] or isomerization reactions.[80] More recently, ttEnT was applied for the sensitization of organometallic reaction intermediates.[32,81] In ttEnT processes, the oxidation states of the sensitizer and the acceptor do not change and are thus independent of the redox properties of the photocatalyst and the substrate. Instead, the triplet energy (E_T) of the substrate and the photosensitizer governs whether energy transfer is feasible.[3,59]

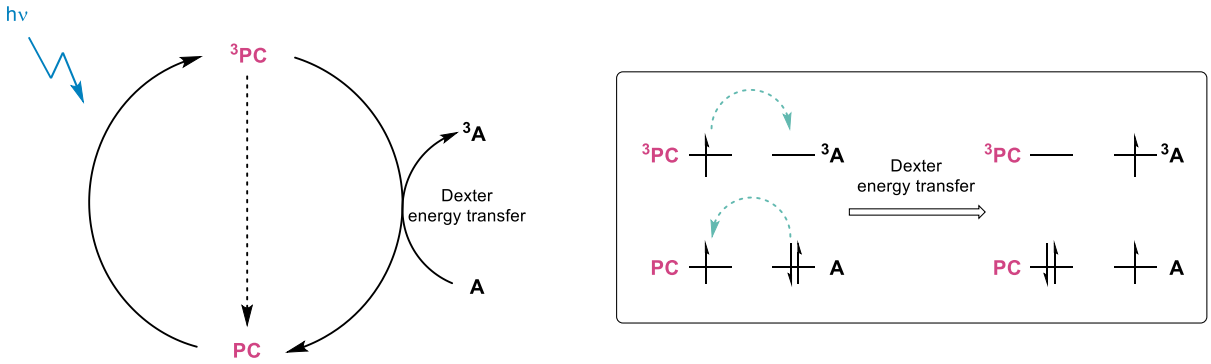

Figure 4: Triplet-triplet energy transfer (ttEnT) processes in photocatalytic reactions (left) are based on a Dexter energy transfer mechanism (right).[59] **PC** = photocatalyst; **A** = energy acceptor.

Photoinduced Hydrogen Atom Transfer

Photoinduced hydrogen atom transfer (photo-HAT) is a third, but vastly underexplored reaction mechanism that enables light-induced chemical transformations.[4,41] While the combination of HAT catalysis with photoredox catalysis is well established in terms of synergistic photocatalysis,[82–84] photo-HAT processes that directly involve the photocatalyst as hydrogen atom transfer (HAT) reagent are rare.[42,46,47,85]

To this date, photo-HAT is based on the ability of certain photoexcited states (**PC***) to abstract hydrogen atoms from an organic molecule (**D-H** in Figure 5).[43,45,60] H-atom abstraction from **PC-H•** by a radical intermediate (**A•**) regenerates the photocatalyst ground state (**PC**). Unlike electron and triplet-triplet energy transfer processes, which depend on the redox properties or the triplet energies of the photocatalyst and the substrate, the feasibility of a photo-HAT is governed by the bond strength of the cleaved **D-H** bond (i.e., the bond dissociation free energy

(BDFE) of the substrate) and the bond strength of the newly formed bond (BDFE(**PC-H•**) in the catalytic cycle depicted in Figure 5).[4,41]

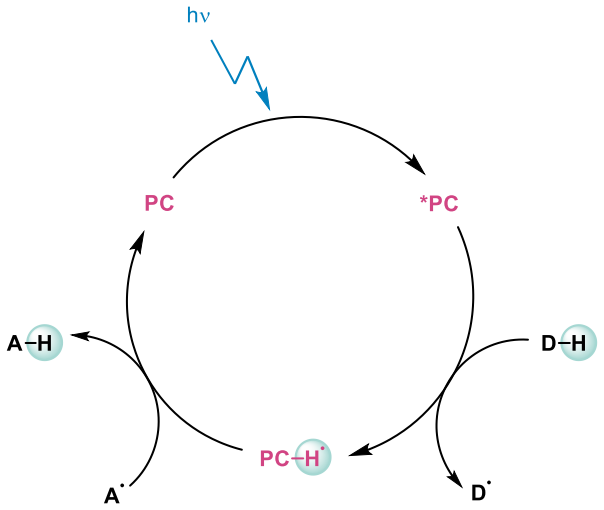

Figure 5: Photocatalytic processes based on photoinduced hydrogen atom transfer (photo-HAT) are to date largely limited to the ability of certain photoexcited states to abstract hydrogen atoms from the substrate.[41] **PC** = photocatalyst; **D-H** = closed-shell hydrogen atom donor; **A•** = open-shell hydrogen atom acceptor.

HAT reactivity is related to proton-coupled electron transfer (PCET), as HAT can be regarded as the concerted transfer of a proton and an electron from one donor to one acceptor.[86,87] Various examples are known for excited-state PCET reactivities; however, the observed PCET is usually limited to polar bonds (such as N-H or O-H) that are able to engage in hydrogen bonding and involves electron and proton transfer from different sites or even different molecules rather than from the same site such as in HAT reactions.[87–91]

2.1.3 Photophysics and Photocatalysis of Cyclometalated Ir(III) Catalysts

Due to their impressive photophysical properties, Ir(III) metal complexes have not only gained broad attention as photocatalysts in electron and energy transfer processes,[31,92–94] but are also applied in OLEDs,[95,96] water-splitting reactions,[97,98] as well as in bioimaging and biosensing and for photodynamic therapy.[99–102] Like the archetypal photoredox catalyst **$[Ru(bpy)_3]^{2+}$** (bpy = 2,2'-bipyridine), Ir(III) complexes belong to the vast family of photoactive d^6 metal complexes. While these complexes, derived from precious metals such as Ru(II) and Ir(III), are well-established,[56,103,104] more recent work has focused on developing photoactive d^6-metal complexes that are more earth-abundant based on Mo(0),[62,105] Cr(0),[106] W(0),[107–109] and Fe(II).[110,111]

Compared to the Ru(II) diimine complexes, most cyclometalated Ir(III) complexes have longer excited-state lifetimes τ_0 (1.9 µs for **(*fac*)-$[Ir(ppy)]_3$** *vs* 0.9 µs for **$[Ru(bpy)_3]^{2+}$**)[112,113] and higher luminescence quantum yields Φ (0.38 for **(*fac*)-$[Ir(ppy)]_3$** *vs* 0.06 for **$[Ru(bpy)_3]^{2+}$**).[113,114] Additional important characteristics of the photoactive Ir(III) complexes are their spectral tunability over the entire visible range of the electromagnetic spectrum and their high photostability.[56,112,114] **(*fac*)-$[Ir(ppy)_3]$** (ppyH = 2-phenylpyridine, referred to as **$Irppy_3$** hereafter) is the most prominent representative among the vast variety of homoleptic and

heteroleptic Ir(III) complexes (Figure 6, left).[114–116] While both geometric isomers are synthetically accessible, the (*fac*)-isomer is commonly employed in photocatalysis due to its more favorable photophysical properties.[112]

The relevant photophysical characteristics of **Irppy$_3$** are summarized in the Latimer diagram in Figure 6. The homoleptic Ir(III) complex is a strong photoreductant, as evidenced by its strongly negative excited-state oxidation potential (E^*_{ox} = –1.73 V *vs* SCE).[61] The excited-state reduction potential is only slightly positive (E^*_{red} = +0.31 V *vs* SCE),[61] which makes **Irppy$_3$** a less potent photooxidant compared to **[Ru(bpy)$_3$]$^{2+}$** (E^*_{red} = +0.73 V *vs* SCE).[61] Since the triplet-excited state cannot be efficiently quenched by many commonly used organic electron donors,[117] most photoredox reactions involving **Irppy$_3$** are based on oxidative rather than reductive quenching.[92]

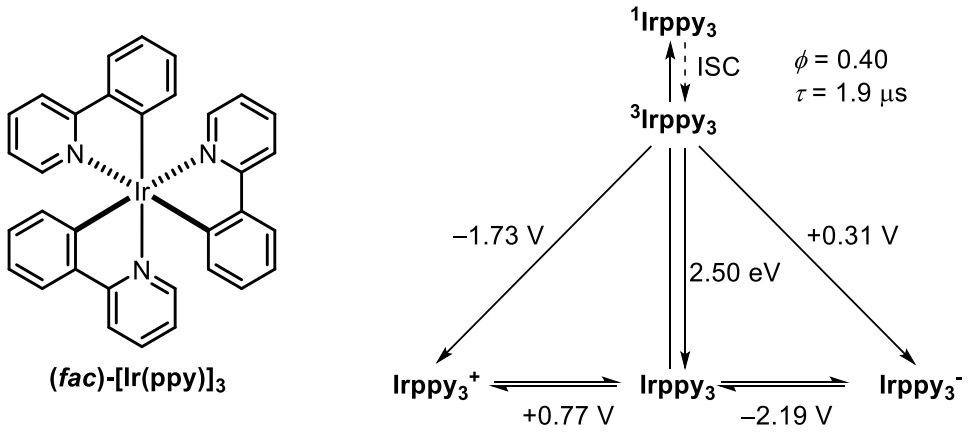

Figure 6: Structure and Latimer-diagram of **Irppy$_3$** (ppyH = 2-phenylpyridine). Data was obtained for CH_3CN and all potentials are given in V *vs* SCE.[61,114]

The photophysical properties of $Irppy_3$ are well-investigated,[112,118] and DFT calculations suggest that the HOMO is delocalized over the Ir-dπ and phenyl-π orbitals, while the LUMO is mostly centered on the heteroaromatic ring.[119] This knowledge can be used to tune the HOMO-LUMO gap E_{00} of Ir(III) complexes. In general, E_{00} is increased when either the HOMO is stabilized and/or the LUMO is destabilized resulting in a blue-shift of the emission and absorption (Figure 7A). In contrast, a smaller E_{00} and thus a red-shift in emission is obtained when the HOMO is destabilized and/or the LUMO is stabilized (Figure 7B).

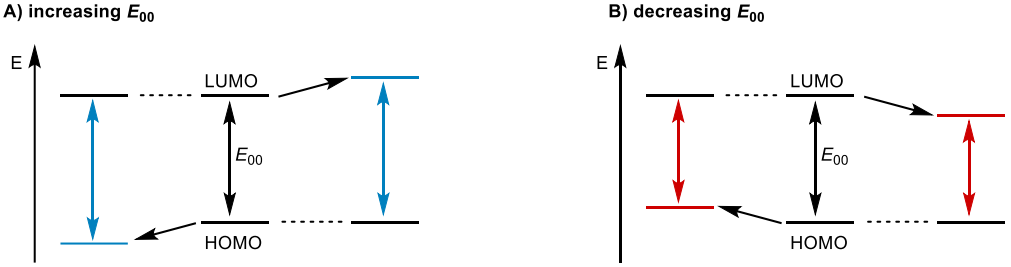

Figure 7: The HOMO-LUMO gap E_{00} of photocatalysts can be tuned by adjusting the HOMO and the LUMO levels of the complexes.

In homoleptic cyclometalated Ir(III) complexes, the energy level of the HOMO can be modified by varying the substituents on the phenyl ring, while the energy level of the LUMO is

influenced by substituents on the heteroaromatic ring.[56] Thus, a common strategy to obtain **Irppy$_3$** derivatives with a high triplet energy is to attach electron-withdrawing substituents such as fluorine or a CF_3 group to the phenyl-ring of 2-phenylpyridine.[112,120] Less frequently, electron-donating groups are introduced on the pyridine-ring of 2-phenylpyridine.[120]
Recently, a water-soluble variant of **Irppy$_3$** was developed in the Wenger group. This photocatalyst can be applied for merging photocatalysis with enzyme catalysis,[121] sensitization of demanding photoreductions using hydrated electrons,[65] or triplet-triplet upconversion,[122] all in the green solvent water. A luminescence quantum yield of 0.73 and a triplet lifetime of 1.6 µs in aqueous solutions as well as a high photostability and an excited-state oxidation potential of –1.89 V *vs* SCE make this complex well suited as a water-soluble analog of **Irppy$_3$**.[65,122]

2.1.4 Synergistic Photocatalysis

To expand the scope of traditional photocatalysis, new concepts, which merge photocatalysis with a second, non-photochemical synthetic strategy, have been developed. This so-called dual catalysis enables new chemical transformations, which would not be possible when using only one of the catalytic systems (Figure 8).[4,5] When merging the two catalytic cycles, two basic concepts have been found to be particularly relevant: i) co-catalysis can allow to activate substrates, which would not be accessible by traditional photocatalysis (Figure 8B) and ii) photocatalysis can generate reactive reaction intermediates, which can react onwards in a second, light-independent catalytic cycle (or vice versa, Figure 8C). As such, combining photocatalysis with a second catalytic cycle allows to access new, unknown reactivities. Furthermore, synergistic photocatalysis broadens the scope of substrates that are accessible by traditional photocatalysis and enhances the control over the selectivity of a light-dependent reaction.[4,5]
Typical co-catalytic strategies include Lewis-acid catalysis,[40,74,75,123,124] Brønsted-acid catalysis,[39,72,125–128] and redox mediation.[129,130] Also, combining photocatalysis with organocatalysis, especially with enamine/imine catalysis,[131–133] and HAT catalysis[82–84] has been found to enable new chemical transformations. Merging photocatalysis with transition metal catalysis further broadens the reaction scope since the resulting organometallic transformations are significantly different from radical chemistry, which typically dominates traditional photocatalysis.[6,31,32,134] Furthermore, photocatalysis can assist organometallic transformations since it can either change the oxidation state of the transition metal catalyst via electron transfer or activate the catalytic intermediate via energy transfer.[6] Merging photocatalysis with enzyme catalysis has gained a lot of attention since it is not only interesting for enabling new reactivities but also in the context of artificial photosynthesis.[24,25,135,136] Especially the photochemical regeneration of nucleotide co-factors was found to be of particular interest.[23,137,138] While in the above-mentioned dual catalytic strategies the light-dependent reaction is mostly based on electron or energy transfer

processes, more recently also photo-HAT catalysis was successfully implemented in synergistic catalysis.[139,140]

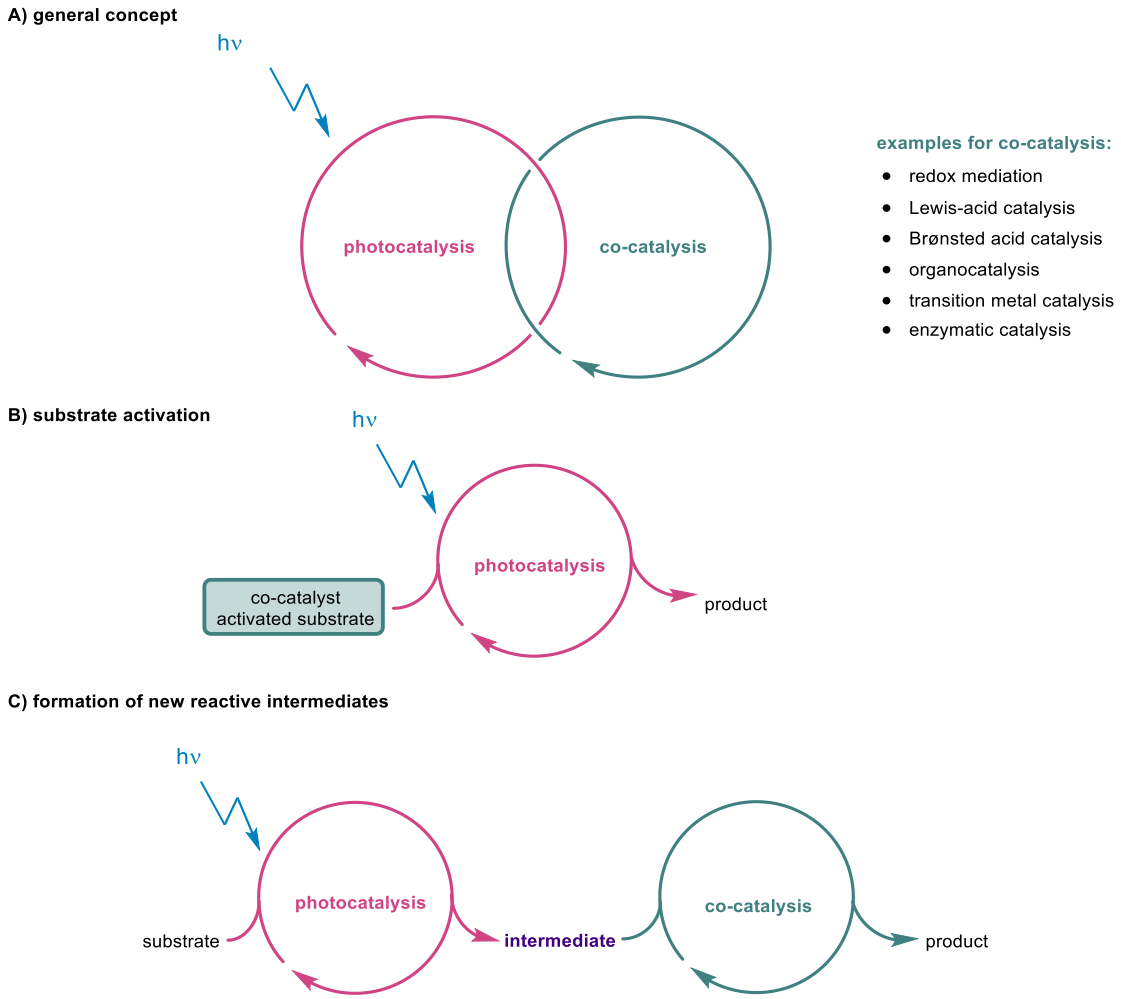

Figure 8: A) Combining photocatalysis with a second co-catalytic cycle enables new chemical transformations. Commonly employed strategies include B) the activation of a substrate for photocatalysis with co-catalysis or C) the formation of new reactive intermediates with photocatalysis that can be transformed in a second, light-independent catalytic cycle.[5]

A special case of merging photocatalysis arises when the photoactive compound is able to perform both the first and the second catalytic reaction (Figure 9). Even though single-component dual catalysis would result in a simplification of multi-component systems, catalysts that combine two or more functionalities are still rare.[141]

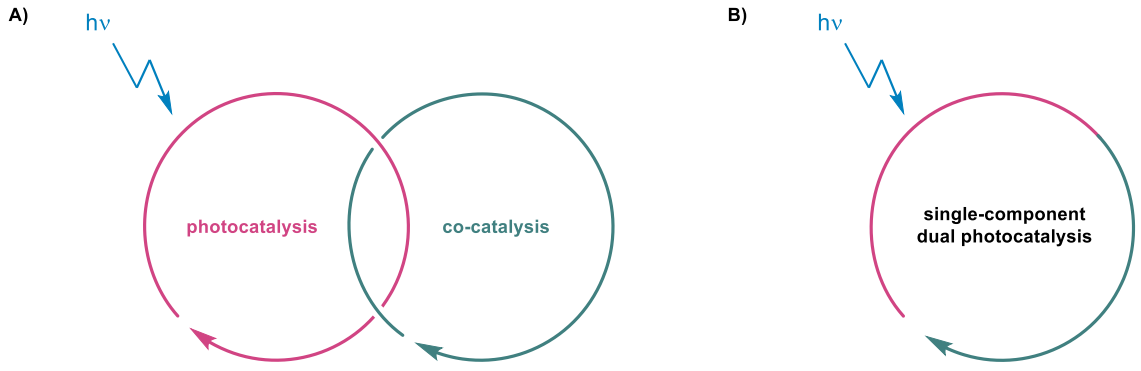

Figure 9: Combining photocatalysis with a second reactivity can either be achieved with two distinct catalytic cycles (A) or it can involve a single-component dual photocatalyst which is able to perform both reactivities (B).

Among the few examples of single-component dual photocatalysts, the copper intermediate which is formed in photoinduced Ullmann coupling reactions serves both as a chromophore and transition metal catalyst.[142–145] Only recently, the ability of certain photoactive compounds to engage consecutively in electro- and photocatalysis was exploited for synthetic photoelectrochemistry[69–71] and for solar energy conversion.[146,147] Bifunctional catalysts, in which a chromophore is covalently linked to an organocatalyst or a hydrogen bonding functional group, were successfully employed in enantioselective photocatalysis.[148–152] In the context of solar energy conversion, single-component dual photocatalysts found applications in dihydrogen production and CO_2 reduction.[141,153,154]

2.2 Transition Metal Hydrides

Transition metal hydrides have found broad applications in organometallic catalysis[155–161] and for the formation of renewable chemical fuels such as H_2[162–164] and carbon-based fuels.[28,29,165–167] The versatility of metal hydride chemistry arises from the three different elementary pathways of metal–hydrogen bond cleavage (Figure 10). Depending on how the metal–hydrogen bond is cleaved, the metal hydride can either serve as a proton source,[11,168] a hydride source,[10,29,34] or as a HAT reagent.[155–157,169] Each pathway can be described with a specific thermodynamic parameter, i.e., the pK_a value for proton transfer reactions, the hydricity $\Delta G°_{H^-}$ for hydride transfer reactions and the BDFE for HAT pathways. The reactivity of one particular metal hydride is thereby not limited to only one specific cleavage mode, but can in some cases even exhibit all three reactivities.[170] Since homolytic bond cleavage of the metal–hydrogen bond is particularly relevant in this thesis, it will be discussed in further detail in the next subsection.

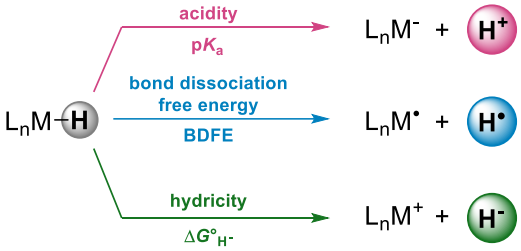

Figure 10: Different reactivities of transition metal hydrides with different coordinating ligands L. Reproduced from Ref. [34].

Homolytic Bond Cleavage of Metal Hydrides

In thermal organometallic chemistry, HAT reactions from transition metal hydrides to organic substrates have enabled various chemical transformations such as hydrogenations,[171] isomerizations,[172,173] and cyclizations.[157,174,175] As mentioned previously, the feasibility of a HAT depends on the BDFE of the employed transition metal hydride.[86] Historically, transition metal–hydrogen bond strengths were often characterized with bond dissociation enthalpies (BDEs) rather than free energies. For cases in which there are no significant entropic effects, the BDFE and BDE values can be interconverted. Depending on the solvent, the BDE value of a given transition metal hydride is ca. 4-5 kcal · mol^{-1} higher than the BDFE of the M–H bond.[86] Typical BDFEs of transition metal hydrides are in the range of 55 to 70 kcal · mol^{-1}.[176]

2.3 Thesis Outline

The aim of this thesis is to gain further understanding of light-dependent reactions that merge photocatalysis with transition metal hydride chemistry in order to broaden the scope of traditional photocatalysis.

The first project (Chapter 3) investigates the photo-HAT reactivity of iridium hydrides upon irradiation with visible light (Figure 11). The employed d^6 transition metal hydride acts as a single-component dual photocatalyst, as it functions both as the chromophore in the light-dependent step (pink trace in Figure 11) and as the HAT catalyst in the light-independent step (green trace in Figure 11). The newly observed overall photo-HAT reactivity, where a hydrogen atom is transferred from an iridium hydride to an unactivated olefin, is investigated by studying the structure-reactivity relationship of various olefins as well as with radical clock and H/D isotope labeling experiments.

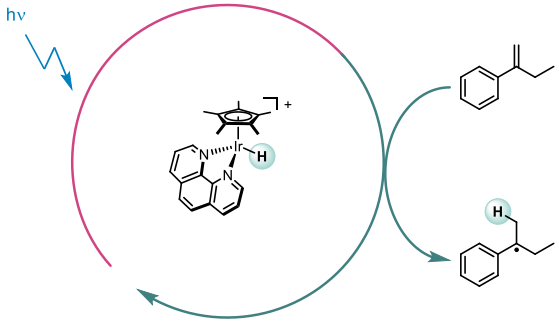

Figure 11: Overall photo-HAT from iridium hydrides to unactivated olefins upon irradiation with visible light.

In the second project (Chapter 4), merging photocatalysis with transition metal hydride chemistry is exploited for nucleotide co-factor regeneration in the context of artificial photosynthesis (Figure 12). Since this requires photocatalysts which can be used under physiological conditions, a series of new water-soluble Ir(III) sensitizers is developed, characterized and studied. The interaction between the photocatalyst and the transition metal hydride is investigated based on the different excited-state reactivities of the synthesized sensitizers and the observed reactivity regarding nucleotide co-factor mimic regeneration. Further insight into the interplay between the two catalysts is gained from luminescence-quenching experiments and transient absorption spectroscopy.

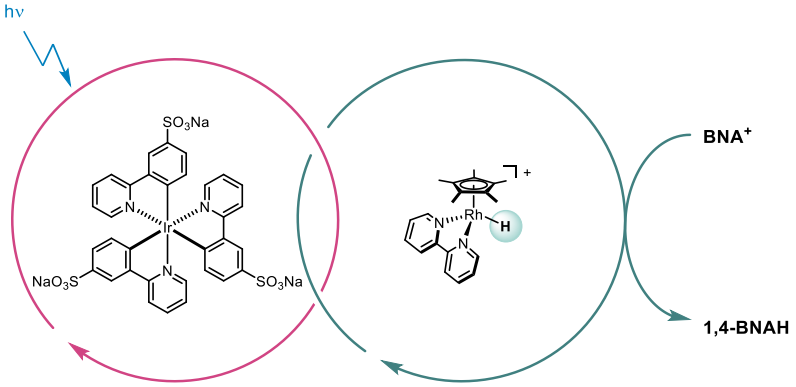

Figure 12: The combination of photocatalysis with rhodium hydride chemistry enables the photochemical regeneration of 1-benzyl-1,4-dihydronicotinamide (**1,4-BNAH**).

3 Photoinduced Hydrogen Atom Transfer from an Iridium Complex to Unactivated Olefins

3.1 Chapter Outline

Photoinduced bimolecular processes between a photocatalyst and a substrate are the basis for the many photocatalytic transformations that emerged in recent years.[1–3] To date, most photocatalytic reactions are governed by electron transfer; however, these processes are limited by the redox properties of both the substrate and the photocatalyst.[2,38] Photo-HAT provides a promising alternative to PET reactions since its reactivity depends on the bond strength of the involved species rather than their redox properties.[41] Nevertheless, photo-HAT has only gained limited attention as a possible activation mode in photocatalysis and the respective examples are based on the ability of certain photoexcited states to abstract hydrogen atoms from a substrate.[42,43,177] Hence, this Chapter provides the missing link for photocatalysis based on photo-HAT, as it shows the contrary reactivity, i.e., an overall photo-HAT from the metal complex to the closed-shell organic substrate resulting in the formation of a new C-H bond.

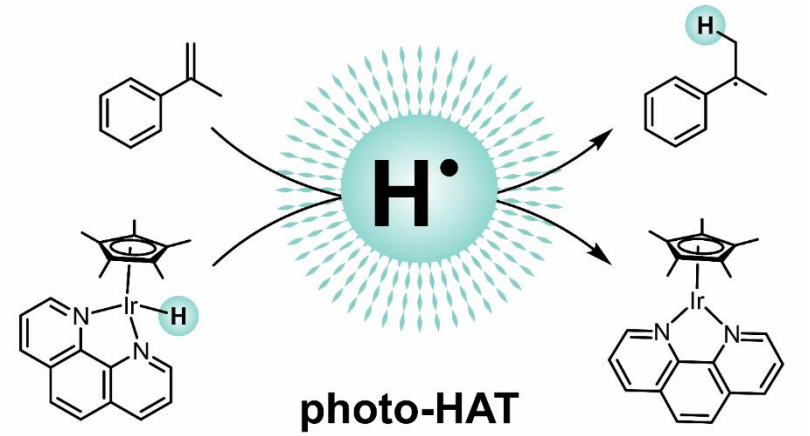

Figure 13: Upon irradiation with visible light, iridium hydrides are able to transfer hydrogen atoms to unactivated olefins.

More precisely, the investigated system takes advantage of the very low BDFE of the iridium(II) hydride (ca. 44 kcal · mol^{-1}),[12] which is formed upon reductive quenching of the respective triplet-excited iridium(III) hydride in presence of triethylamine. In a second, light-independent step, this very weak Ir^{II}-H bond is cleaved and a hydrogen atom is transferred from the metal complex to the unactivated olefin. The investigated olefins are difficult to activate by traditional PET reactions due to their very negative reduction potential (E_{red} < –2.7 V *vs* SCE). Hence, the overall photo-HAT provides an important alternative to circumvent the thermodynamic limitations of PET reactions.

In presence of 50 mM olefin substrate, hydrogenation of the substrate was found to be the primary reaction pathway for aromatic olefins, whereas hydrogen atom abstraction from the radical intermediate was only observed in minor amounts. Structure/reactivity relationships with 12 substrates revealed the typical HAT reactivity, which was further supported by a radical clock experiment. Isolation of the iridium hydride intermediate and experiments with a deuterated substrate allowed to gain further insight into the reaction mechanism.

This Chapter contains a peer-reviewed article, which has been published in Chemical Science (*Chem. Sci.* **2020**, *11*, 8582-8594) and an outlook into possible future research. The supporting information that belongs to this article can be found in Chapter 6.1.

Author Contribution:

- Mirjam Schreier performed the experiments and contributed equally to the design of the experiments and writing the manuscript.
- Xingwei Guo provided guidance and contributed equally to the design of the project.
- Oliver Wenger provided guidance and contributed equally to the design of the project and writing the manuscript.

3.2 Published Article

Chemical Science

ROYAL SOCIETY OF CHEMISTRY

EDGE ARTICLE

View Article Online
View Journal | View Issue

Cite this: *Chem. Sci.*, 2020, **11**, 8582

All publication charges for this article have been paid for by the Royal Society of Chemistry

Photo-triggered hydrogen atom transfer from an iridium hydride complex to unactivated olefins†

Mirjam R. Schreier, Björn Pfund, Xingwei Guo ‡* and Oliver S. Wenger *

Many photoactive metal complexes can act as electron donors or acceptors upon photoexcitation, but hydrogen atom transfer (HAT) reactivity is rare. We discovered that a typical representative of a widely used class of iridium hydride complexes acts as an H-atom donor to unactivated olefins upon irradiation at 470 nm in the presence of tertiary alkyl amines as sacrificial electron and proton sources. The catalytic hydrogenation of simple olefins served as a test ground to establish this new photo-reactivity of iridium hydrides. Substrates that are very difficult to activate by photoinduced electron transfer were readily hydrogenated, and structure–reactivity relationships established with 12 different olefins are in line with typical HAT reactivity, reflecting the relative stabilities of radical intermediates formed by HAT. Radical clock, H/D isotope labeling, and transient absorption experiments provide further mechanistic insight and corroborate the interpretation of the overall reactivity in terms of photo-triggered hydrogen atom transfer (photo-HAT). The catalytically active species is identified as an Ir(II) hydride with an Ir^{II}–H bond dissociation free energy around 44 kcal mol^{-1}, which is formed after reductive ^{3}MLCT excited-state quenching of the corresponding Ir(III) hydride, *i.e.* the actual HAT step occurs on the ground-state potential energy surface. The photo-HAT reactivity presented here represents a conceptually novel approach to photocatalysis with metal complexes, which is fundamentally different from the many prior studies relying on photoinduced electron transfer.

Received 30th March 2020
Accepted 27th July 2020

DOI: 10.1039/d0sc01820a

rsc.li/chemical-science

1 Introduction

Photoinduced electron transfer (PET) can readily be initiated with many photoactive metal complexes, but photo-triggered hydrogen atom transfer (photo-HAT) reactivity of coordination compounds is comparatively rare.[1] Much progress has been made in recent years regarding the development of new photosensitizers, particularly including complexes of Earth-abundant metals[2–6] and purely organic (metal-free) variants,[7] but they all exhibit the well-established PET reactivity. Consequently, the vast majority of current photochemical studies, including most of the work by the photoredox community,[8] still operate on the basis of PET. Even though increasingly thermodynamically challenging PET reactions have been accomplished lately,[9–18] sometimes in combination with an applied electrochemical potential,[19–21] such reactions are limited by the redox properties of the photosensitizer and the substrates. To overcome thermodynamic limitations imposed by PET, proton-coupled electron transfer (PCET)[22] has been exploited successfully in photoredox catalysis for substrates with sufficiently polar functional groups that can form hydrogen bonds.[23] Similarly, the interaction of Lewis acids with polar functional groups can help activate substrates that would be difficult to engage in pure PET chemistry.[24–27]

We hypothesized that the photochemical hydrogenation of olefins would be an ideal test ground for exploring the photo-HAT reactivity of a metal complex. Whilst alkene hydrogenation is of course an extremely well-developed field, photochemical methods are very scarce and largely limited to substrates with strongly electron-withdrawing substituents to permit typical PET chemistry,[28] or to the reduction with solvated electrons.[29,30] For the present work, we chose olefins that do not contain electron-withdrawing groups and which therefore cannot be activated by PET due to their very negative reduction potentials ($E_{red} < -2.7$ V *vs.* SCE[31]). From the perspective of PET, these olefins are unactivated.

HAT is a key process in many photochemical reactions,[32,33] but usually requires auxiliary reagents such as thiols or ascorbate which act as H-atom donors in a secondary, light-independent step that does not involve the photosensitizer.[34–37] Photoreactions, in which a metal complex donates or accepts an H-atom in an electronically excited state, are rare.[33,38–43] For the conceptually related proton-coupled electron transfer (PCET) reactions, there exist numerous compounds which exhibit PCET reactivity from electronically excited states,

Department of Chemistry, University of Basel, St. Johanns-Ring 19, 4056 Basel, Switzerland. E-mail: xingwei_guo@mail.tsinghua.edu.cn; oliver.wenger@unibas.ch

† Electronic supplementary information (ESI) available. See DOI: 10.1039/d0sc01820a

‡ Current address: Center of Basic Molecular Science (CBMS), Department of Chemistry, Tsinghua University, Beijing 100084, China.

but these systems typically rely on polar O–H or N–H groups which can form hydrogen bonds.[44–47]

The HAT reactions considered herein do not proceed directly from an electronically excited state, but instead occur after an initial reductive excited-state quenching process with a tertiary amine. The sequence of reductive excited-state quenching followed by single-electron transfer to the substrate is rather common in organic photoredox catalysis as well as energy-related photochemical research, but here, the situation is conceptually different: reductive quenching leads to an H-atom donor, which can then undergo HAT with olefins. Thermal HAT from metal complexes in their electronic ground state has attracted significant attention[48,49] and homolytic splitting of metal-hydride bonds upon excitation with visible light is known for a few selected examples,[50,51] but we are unaware of prior reports of photo-triggered HAT from metal complexes to unactivated olefins. The reductive excited-state quenching step involved in our photo-triggered HAT gives access to a particularly reactive metal hydride with a very low M–H bond dissociation free energy (BDFE), and this enables uncommon photochemistry that goes beyond the well-established single electron transfer (SET) reactivity. From the synthetic viewpoint, our approach offers the possibility to form C–H bonds, complementing recent work on photo-triggered PCET that focused on the cleavage of C–H bonds.[52,53]

Metal hydride complexes play important roles for proton and CO_2 reduction,[54,55] and recently tungsten hydrides provided fundamental insight into multi-site PCET reactions.[56–58] To some extent their reactivity can be regarded as HAT-like, but with coupled proton and electron transfer reactions occurring

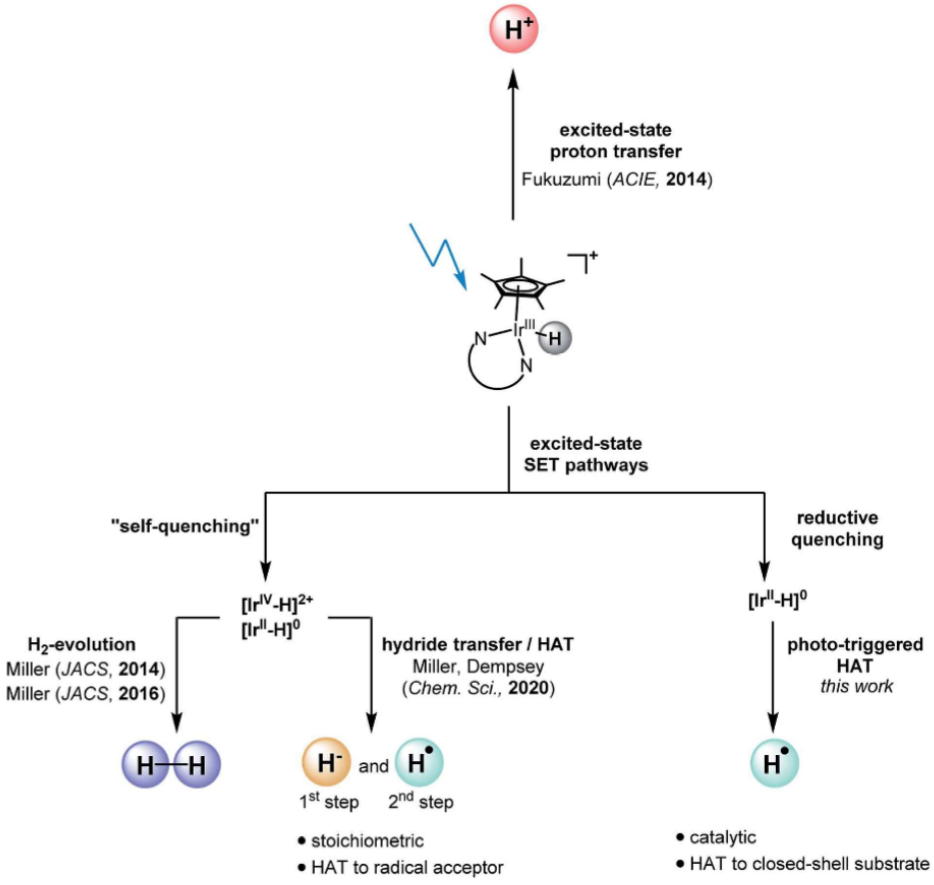

Fig. 1 Different photo-reactivities: iridium hydrides can undergo excited-state proton transfer[60] or photodriven dihydrogen formation.[61,65,67] Herein we demonstrate that photo-HAT represents an additional reaction pathway for iridium hydride complexes, complementing recent work demonstrating sequential hydride and HAT transfer.[64]

to separate base and oxidant molecules.[22] Iridium cyclopentadienyl hydride complexes are a particularly well investigated class of compounds,[59] which have been shown to function as photoacids[60] (Fig. 1). Furthermore, they are able to form H_2 upon irradiation with visible light[61,65] or when used in photo-electrocatalytic settings in water or CH_3CN.[66] "Self-quenching" reactions, in which an electron is transferred from an excited $[Cp^*Ir(\alpha\text{-diimine})H]^+$ complex (Cp^* = pentamethylcyclopentadienyl) to an iridium hydride in the ground state, are responsible for photochemical H_2 formation in water and CH_3CN.[67] By contrast, in neat CH_2Cl_2 the "self-quenching" products (comprised of one oxidized iridium hydride complex and one reduced iridium hydride complex) undergo sequential hydride transfer and HAT, enabling the hydrodechlorination of two equivalents of CH_2Cl_2 to CH_3Cl.[64]

In the present work, $\mathbf{[Cp^*Ir(phen)(H)]^+}$ (phen = 1,10-phenanthroline) was formed *in situ via* photo-irradiation of $\mathbf{[Cp^*Ir(phen)Cl]^+}$ in CH_3CN in presence of excess triethylamine (TEA), which served as a combined electron and proton source. Continued irradiation then promoted $\mathbf{[Cp^*Ir(phen)(H)]^+}$ to its (relatively long-lived) ^{3}MLCT state. In presence of 250 mM TEA, reductive excited-state quenching to form $\mathbf{[Cp^*Ir(phen)(H)]^0}$ rather than "self-quenching" is the dominant reaction pathway. For the closely related $\mathbf{[Cp^*Ir(bpy)(H)]^0}$ complex (bpy = 2,2′-bipyridine), an Ir^{II}–H bond dissociation free energy (BDFE) of 43.9 kcal mol^{-1} was reported previously.[67]

We anticipated that such a low Ir^{II}–H BDFE would make $[Ir^{II}–H]$ complexes suitable for olefin hydrogenation *via* photo-triggered HAT. Activation of olefins by thermal (*i.e.*, not light-driven) metal-hydride catalyzed hydrogen atom transfer (MHAT)[48,68] is typically performed with metal-hydrides that have BDFEs ranging from ≈50 to 60 kcal mol^{-1}.[70,71] Our results presented below indicate that the key-step in our photoinduced hydrogenation of olefins (Fig. 2) is indeed an initial HAT from the $[Ir^{II}–H]$ species to the substrate. After successful activation of the olefin starting material (**SM**) *via* photo-triggered HAT, a radical intermediate (**RI**$^\bullet$) is formed. The latter can undergo two different onward reactions: (i) either **RI**$^\bullet$ can accept a second H-atom to form the hydrogenation product **H**, or (ii) an H-atom can be abstracted from a different position of radical intermediate **RI**$^\bullet$ to give the rearranged products (***E***)-**R** or (***Z***)-**R**.[69,72] In this work, we attempted to maximize the hydrogenation and to minimize the rearrangement yield, but the main point of the study was to establish a new type of photo-reactivity of metal complexes, as noted above.

A very recent study reported on the photoenzymatic hydrogenation of vinyl pyridines, using "ene" reductases in combination with $Ru(bpy)_3Cl_2$ as a catalytic system (with some modest product yields also observable in absence of the enzyme).[73] Mechanistically, this formal hydrogenation proceeded *via* a sequence of reduction, protonation and HAT steps. Such combined enzyme-photoredox catalysis approaches hold much promise for enantioselective conversions, but they are not straightforward to implement.[74–76]

Our iridium complex serves both as photosensitizer and as catalyst of HAT. Due to this dual role, no fine tuning of different catalytic cycles is needed,[77] as is sometimes necessary when merging photoredox chemistry with traditional transition metal catalysis or with enzyme catalysts. The hydride complex is formed *in situ* from a robust Ir(III) precursor complex, and HAT

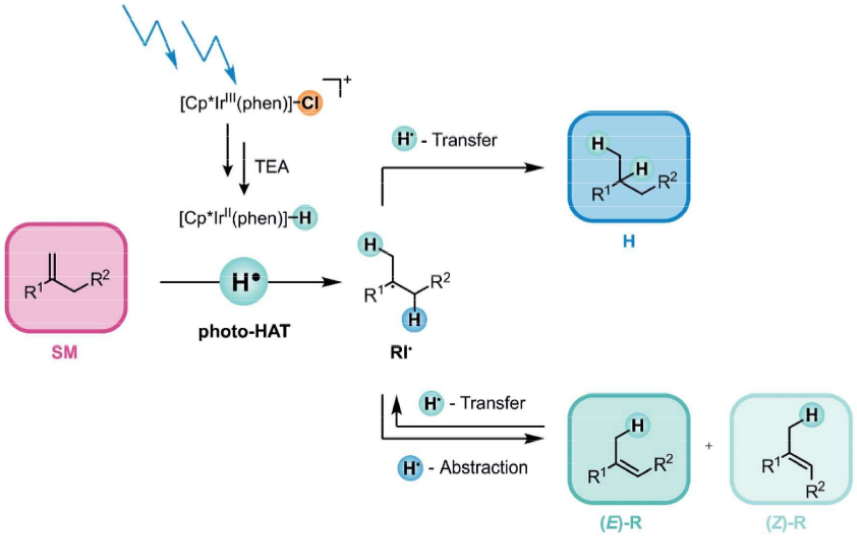

Fig. 2 Visible-light driven catalytic hydrogenation of electron-neutral olefins based on photo-triggered hydrogen atom transfer (photo-HAT) from an iridium(III) hydride (Cp^* = pentamethylcyclopentadienyl; phen = 1,10-phenanthroline), see text for details.

occurs to stable olefin substrates and does not require highly reactive radicals as reaction partners. Thus, alongside the abovementioned very recent study by Miller, Dempsey, and coworkers,[64] our work opens a conceptually new avenue to photoredox chemistry, exploiting visible-light excitation of a simple metal complex for inducing H-atom rather than electron transfer.

2 Results and discussion

2.1 Reaction optimization

We started our reaction screening with (3-methoxyprop-1-en-2-yl)benzene (**1-SM**) as substrate, because geminal disubstituted olefins with aromatic substituents are particularly well-suited acceptors for HAT.[78] In an initial experiment, **[Cp*Ir(phen)Cl]Cl** was used as iridium hydride precursor and diisopropylethylamine (DIPEA) was employed as sacrificial donor. 85% conversion of **1-SM** was observed when irradiating the reaction mixture at 470 nm for 44 h (Table 1, entry 1) under inert atmosphere. However, the chemoselectivity of the reaction was limited, as expressed by a **1-H**/**1-R** product ratio of 2.8 : 1. When the sacrificial donor was changed to triethylamine (TEA), both the conversion (90%) and the chemoselectivity (**1-H**/**1-R** 3.2 : 1) of the reaction were slightly increased (entry 2). Upon addition of excess phenanthroline (30 mol%), the chemoselectivity of the reaction improved drastically in favor of the hydrogenation product **1-H** (**1-H**/**1-R** 14.7 : 1, entry 3) and the conversion further increased (94%). When the reaction was performed in the dark (but otherwise identical conditions), no conversion of **1-SM** was observed (entry 4). Moreover, no conversion of **1-SM** was detected when either the iridium catalyst (entry 5) or the sacrificial donor (entry 6) was absent.

2.2 Substrate scope

As noted in the introduction, the olefin hydrogenation reaction mainly serves as a test ground to establish a new type of metal hydride photo-reactivity, but nevertheless it seemed useful to explore its substrate scope in the interest of gaining a reactivity picture that is as complete as possible. We therefore probed a range of substrates (Fig. 3) and determined hydrogenation and rearrangement product yields by a combination of quantitative NMR and GC/MS analyses in presence of an internal standard. We focused mostly on geminal disubstituted olefins, because the lack of substituents on their terminal olefinic carbon atom permits for faster initial HAT than what would be possible with other olefins.[78] Furthermore, the tertiary radical intermediate formed after initial HAT to this substrate class can be rather stable, particularly when using aromatic geminal disubstituted olefins, which result in benzylic radical intermediates.[78] Consequently, the new method can be applied to a range of substrates of this type (**1-SM**–**5-SM**), tolerating both electron-withdrawing and electron-donating substituents and affording the different hydrogenation products in high yields (88–99%) and with high chemoselectivities (**H**/**R** ratios exceeding 12.7 : 1). Both *para*- and *meta*-substituents on the aromatic ring are well tolerated, and no dehalogenation was observed for both chloro-substituted substrates (**4-SM** and **5-SM**), as opposed to what would be expected for PET with strong photoreductants.[10,79–81]

The conversion of substrate **6-SM** with its free hydroxyl-group was considerably lower, affording the hydrogenation product in only 40% yield. This observation suggests that the catalytic turnover is slowed down by coordinating substituents on the substrate, even if the substrate coordinates only weakly and reversibly, as expected for **6-SM**. When using the mesityl-

Table 1 Reaction optimization and control reactions. For simplicity, only the (*E*)-isomer of the rearranged products (**1-R**) is shown

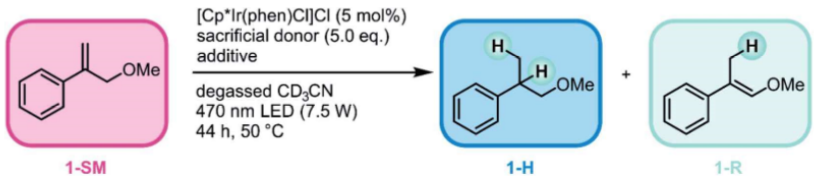

Entry[a]	Catalyst	Sacrificial donor	Additive (mol%)	Conversion[b] [%]	**1-H**/**1-R**[b]
1	**[Cp*Ir(phen)Cl]Cl**	DIPEA	—	85	2.8 : 1
2[c]	**[Cp*Ir(phen)Cl]Cl**	TEA	—	90	3.2 : 1
3[c]	**[Cp*Ir(phen)Cl]Cl**	**TEA**	**phen (30)**	**94**	**14.7 : 1**
4[d]	**[Cp*Ir(phen)Cl]Cl**	TEA	—	0	n.d.
5	—	TEA	—	0	n.d.
6	**[Cp*Ir(phen)Cl]Cl**	—	—	0	n.d.

[a] Reaction conditions: **1-SM** (50 mM), **[Cp*Ir(phen)Cl]Cl** (2.5 mM), sacrificial donor (250 mM) and 1,10-phenanthroline (0 or 15 mM) in 0.5 mL degassed CD_3CN. Irradiation of the sample occurred at 470 nm (7.5 W) for 44 h, while the temperature was kept at 50 °C. See ESI Section 1 for details regarding the photoreactor and ESI Section 3.1 for experimental details. [b] Conversions and **H**/**R** product ratios were determined by ^{1}H-NMR spectroscopy. See ESI Section 3.1.1 for details. [c] Product formation was confirmed by GC/MS spectrometry. See ESI Section 3.1.2 for details. [d] Reaction was performed in the dark.

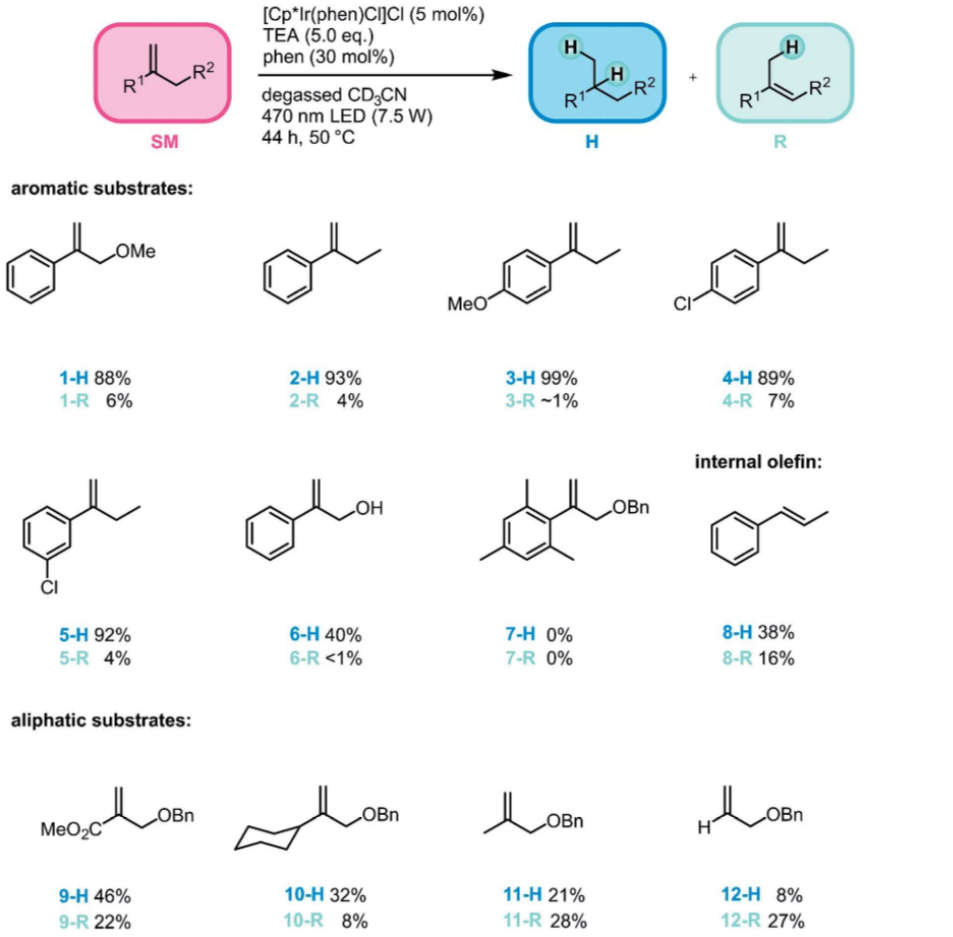

Fig. 3 Substrate scope for the photo-triggered hydrogenation of olefins promoted by an iridium hydride. For simplicity, only one isomer of the rearranged products (R) is shown. Reaction conditions: substrate (50 mM), **[Cp*Ir(phen)Cl]Cl** (2.5 mM), TEA (250 mM) and 1,10-phenanthroline (15 mM) in 0.5 mL degassed CD_3CN. Irradiation of the sample occurred at 470 nm (7.5 W) for 44 h, while the temperature was kept at 50 °C, see Section 1 of the ESI† for details regarding the photoreactor. Yields and conversions were determined by ^{1}H-NMR spectroscopy and the yields of the hydrogenation products (**1-H** to **5-H**, **8-H**, **9-H** and **11-H**) were likewise confirmed by GC-MS spectrometry. See ESI Section 3.2† for details. In the case of product **8-R**, R means isomerization to *cis*-1-phenyl-1-propene. In the case of products **6-H**/**6-R**, **10-H**/**10-R**, and **12-H**/**12-R** the product conversion could not be determined by GC-MS spectrometry. Therefore, the yields for these substrates were determined based on ^{1}H-NMR spectroscopy exclusively.

substituted substrate **7-SM** the reaction was completely shut down. The combined observations made for substrates **6-SM** and **7-SM** suggest that coordination to the Ir center is undesirable, but sterically very demanding substituents can impede HAT completely.

To explore whether our method can also be applied to internal olefins, *trans*-1-phenyl-1-propene (**8-SM**) was tested as substrate, affording propylbenzene (**8-H**) in 38% yield. The lower conversion of this internal olefin in comparison to terminal olefins is in line with prior studies, which found that an additional methyl substituent at the terminal carbon of 1,1-diphenylethylene slows down the thermal HAT from $CpCr(CO)_3H$ to various olefins by about 800 times.[78] Furthermore, with **8-SM** the formation of the hydrogenation product was less favored than for **1-SM–6-SM**. Significant isomerization to *cis*-1-phenyl-1-propene was observed, whereas no isomerization to the thermodynamically less favored terminal olefin (allylbenzene) was detected.

To gain insight into how the stability of the presumed radical intermediates influences the outcome of the overall reaction, a series of terminal olefins (**9-SM–12-SM**) with different non-aromatic substituents at the disubstituted olefinic carbon atom was investigated. The hydrogenation yield decreases along the series **1-SM** > **9-SM** > **11-SM** > **12-SM**, reflecting the stability of the different radicals formed after initial HAT to these substrates along the substituent series Ph > COOMe > CH_3 > H (Fig. 4A).[78] Furthermore, the chemoselectivity of the reaction is highly dependent on the stability of the formed radical intermediate. While the hydrogenation product is the major product for all investigated aromatic substrates (**1-SM–6-SM**), the formation of the rearranged product becomes increasingly important for aliphatic olefins. Specifically, **H**/**R** ratios decrease from *ca.* 15 : 1 for **1-SM** to roughly 2 : 1 for **9-SM**, and finally about 1 : 3 for **12-SM**. This observation reflects the fact that for aliphatic substrates, the newly formed C–H bond in the radical intermediate (**RI**˙ in Fig. 2) is roughly 10 kcal mol^{-1} (ref. 82 and 83) weaker compared to aromatic substrates (see ESI Section 4.1† for details). Consequently, H-atom abstraction to yield rearranged products is faster for aliphatic (*e.g.*, **11-SM** or **12-SM**) than for aromatic substrates (*e.g.*, **1-SM**).

The very good correlation between the reactivity (and chemoselectivity) of the different substrates and the stability of the formed radical intermediates **RI**˙ (Fig. 4A) is fully in line with hydrogenation *via* an initial photo-HAT. The investigated olefin substrates have very negative reduction potentials (below −2.7 V *vs.* SCE)[31] and photoexcited [Cp*Ir(α-diimine)X] species (X = Cl^-, H^-) do not have this much reducing power (see ESI Section 4.1† for details),[67] hence PET is not a viable reaction pathway.

2.3 Monitoring the reaction progress over time

Further mechanistic insight was gained by monitoring the reaction progress at different reaction times of photo-irradiation (Fig. 5A), using the same conditions as for the substrates in Fig. 3. Continuous hydrogenation of the olefin substrate (**1-SM**) was observed over the first 20 h, and a final conversion of 94% was reached after 44 h (Fig. 5B, blue trace). Interestingly, the ratio of the different reaction products (**1-H**/**1-R**) changed over the reaction course. At the beginning of the reaction the **1-H**/**1-R** ratio was only 3 : 1, but then it increased to 14.7 : 1 after 44 h. Moreover, the total amount of rearranged product ((***E***)-**R** + (***Z***)-**R**) even slightly decreased over the reaction course (Fig. 5B, turquoise traces). This is because the rearranged products still contain an olefinic moiety and as such can be hydrogenated over time (leftward arrow in the bottom part of Fig. 2).

2.4 Probing the role of iridium hydride

Next we monitored the reaction progress when using **[Cp*Ir(phen)(H)][PF_6]** instead of **[Cp*Ir(phen)Cl]Cl** as iridium source. With **[Cp*Ir(phen)Cl]Cl**, conversion of **1-SM** was only observed after an initial lag phase of approximately 1 hour, during which essentially no hydrogenation of the substrate was observed (yellow trace in Fig. 6A). This indicates that **[Cp*Ir(phen)Cl]**$^+$ first must be converted to the catalytically

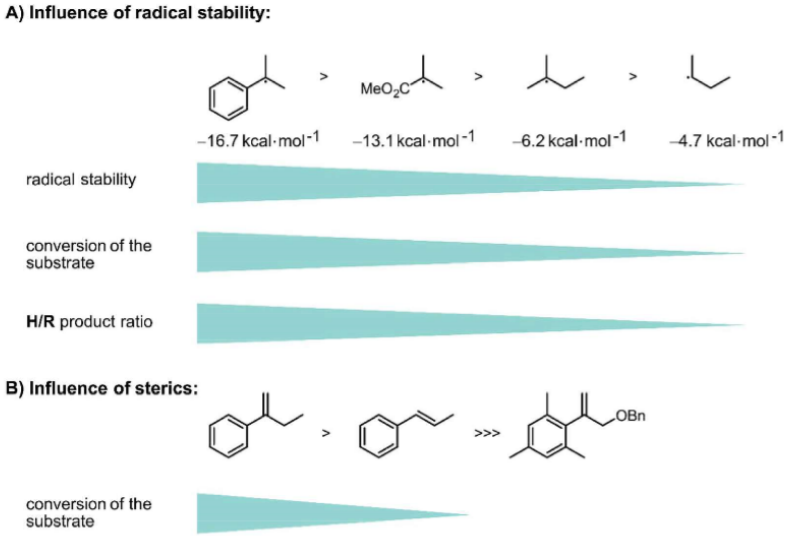

Fig. 4 Influence of radical stability and sterics on reactivity of the substrates and product distribution: (A) the conversion of the substrate decreases with decreasing radical stability (reference value: methyl radical = 0 kcal mol^{-1}).[84] The chemo-selectivity changes towards the rearranged product when aliphatic substrates are used instead of aromatic substrates. (B) Introducing sterics on the substrates hinders the initial HAT and lowers the reactivity of the substrate, see text for details.

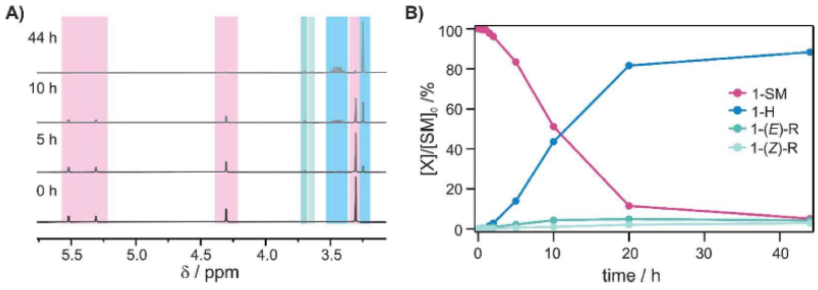

Fig. 5 Reaction progress as a function of time: (A) ^{1}H-NMR spectra of the reaction mixture after different time intervals following irradiation with a 7.5 W 470 nm LED (NMR acquisition occurred in the dark, using 8 aliquots of the same stock solution irradiated in parallel for different amounts of time). The characteristic signals of the starting material (**1-SM**, pink background) disappear, while formation of the hydrogenation product (**1-H**, blue background) and the rearranged products (**1-(*E*)-R** and **1-(*Z*)-R**, turquoise backgrounds) are observable. (B) Conversion of the substrate (**1-SM**, pink trace) and ^{1}H-NMR yields of the different products (**1-H**, blue trace; **1-(*E*)-R** and **1-(*Z*)-R**, turquoise traces) over the reaction course.

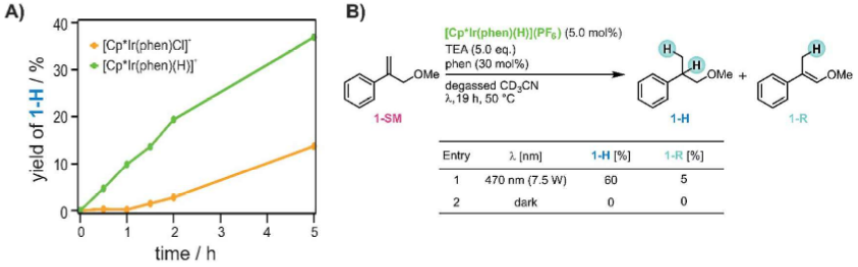

Fig. 6 Role of iridium hydride in the reaction mixture. (A) Comparison of the different reaction time profiles when using **[Cp*Ir(phen)Cl]$^+$** (yellow trace) or **[Cp*Ir(phen)(H)]$^+$** (green trace). (B) Olefin hydrogenation with **[Cp*Ir(phen)(H)](PF$_6$)**, yields determined by ^{1}H-NMR spectroscopy. The yellow trace in panel A is the same data set as the blue trace in Fig. 5B.

active species. When instead using **[Cp*Ir(phen)(H)](PF$_6$)** (see ESI Sections 2.1 and 4.2† for details), no lag phase is observed (green trace in Fig. 6A), and the hydrogenation product **1-H** begins to form without any significant delay. This suggests that the initial lag phase when using **[Cp*Ir(phen)Cl]$^+$** is due to the light-driven conversion of the chloro-complex to **[Cp*Ir(phen)(H)]$^+$** in presence of TEA, and furthermore that **[Cp*Ir(phen)(H)]$^+$** is a catalytically relevant species. However, even with that iridium(III) hydride, no substrate conversion occurred when the reaction mixture was stirred in the dark (entry 2 in Fig. 6B), indicating that **[Cp*Ir(phen)(H)]$^+$** must be activated by visible light in order for the HAT to occur. Evidently, the **[Cp*Ir(phen)(H)]$^+$** complex in its electronic ground state is not a sufficiently good H-atom donor for the olefin substrates considered here (see ESI Section 4.1† for further details).

The electrochemical and chemical conversion of **[Cp*Ir(bpy)Cl]$^+$** to **[Cp*Ir(bpy)(H)]$^+$** is well established,[66,85] but so far does not seem to have been studied in photochemical settings. For related rhodium complexes, the photochemical conversion of chloro- to hydride complexes has been explored to some extent.[86–88] When irradiating a 80 μM solution of **[Cp*Ir(phen)Cl]$^+$** in CH$_3$CN in presence of 1.0 mM TEA with an LED at 455 nm, the UV-Vis absorption spectrum of **[Cp*Ir(phen)Cl]$^+$** converts slowly but steadily to the spectral signature of **[Cp*Ir(phen)(H)]$^+$**. The series of spectra shown in Fig. S33† were recorded after different irradiation times and have an isosbestic point at 375 nm, in line with expectation based on the UV-Vis spectra of neat **[Cp*Ir(phen)Cl]$^+$** and **[Cp*Ir(phen)(H)]$^+$**.

To probe this conversion under conditions resembling more closely those of the reactions in Section 2.2, 3.5 mM **[Cp*Ir(phen)Cl]$^+$** in CD$_3$CN containing 350 mM TEA (but no olefin substrate) was irradiated at 470 nm. The ^{1}H-NMR spectra recorded (in the dark) after photo-irradiation for 2 hours provide clear evidence for the formation of **[Cp*Ir(phen)(H)]$^+$** (ESI, Section 4.2†). This set of experiments furthermore demonstrates that prolonged photo-irradiation leads to dissociation of the phen ligand, which explains why the photochemical hydrogenation proceeds better in the presence of excess phen (Table 1).

Presumably, this photoreaction proceeds *via* an initial reductive dissociation of the chloro-ligand, thereby leading to **[Cp*Ir(phen)]^0**. Protonation of that species (with TEA$^{\bullet+}$ as proton source) can then in principle lead directly to the

formation of **[Cp*Ir(phen)(H)]$^+$**, but this is speculative and our data does not provide insight into the individual elementary steps involved in this conversion. Whilst TEA is principally an electron donor, its one-electron oxidized form TEA$^{\bullet+}$ is competent to act either as acid or H-atom donor.[89]

Having established that **[Cp*Ir(phen)(H)]$^+$** forms from **[Cp*Ir(phen)Cl]$^+$** in the course of continuous photo-irradiation in presence of excess TEA, the next logical step is to elucidate possible onward photochemical reactions of that iridium(III) hydride species. **[Cp*Ir(phen)(H)]$^+$** exhibits ^{3}MLCT photoluminescence with a lifetime (τ) of 148 ns in deaerated CH_3CN at a **[Cp*Ir(phen)(H)]$^+$** concentration of 0.2 mM with 0.6 mM NBu_4PF_6 at room temperature (Fig. S36†). TEA induces reductive ^{3}MLCT quenching with a rate constant of $4.5 \times 10^8\ M^{-1}\ s^{-1}$ according to Stern–Volmer luminescence quenching experiments (inset of Fig. S36†), thereby leading to the respective iridium(II) hydride, **[Cp*Ir(phen)(H)]^0**.

That iridium(II) hydride species cannot be observed directly by transient absorption spectroscopy, because this is a highly reactive species that does not accumulate in detectable concentrations. However, UV-Vis transient absorption spectroscopy provides unambiguous evidence for a follow-up transient species, namely the iridium(I) complex **[Cp*Ir(phen)]^0**, which forms from the iridium(II) hydride **[Cp*Ir(phen)(H)]^0** after H-atom release. This iridium(I) species exhibits diagnostic absorption bands near 600 and 640 nm (Fig. 7C, vertical black lines), which are observable after pulsed 445 nm excitation of **[Cp*Ir(phen)(H)]$^+$** in presence of excess TEA in CH_3CN (Fig. 7A). An analogous experiment with a triarylamine electron donor (TAA-OMe) instead of TEA provides clear evidence for the triarylamine radical cation (absorption band at 720 nm in Fig. 7B/D) superimposed with the spectroscopic signature of the iridium(I) species. Thus, it is clear that both TEA and the triarylamine act as electron donors to the ^{3}MLCT-excited **[Cp*Ir(phen)(H)]$^+$** complex.

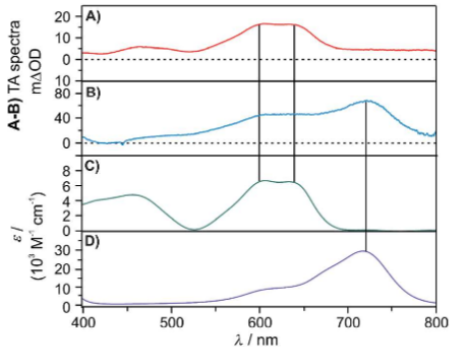

Fig. 7 (A) Transient absorption spectrum of a solution containing **[Cp*Ir(phen)(H)](PF$_6$)** (0.5 mM) and TEA (10 mM). The spectrum was measured at a time delay of 60 ns after excitation at 445 nm (9 mJ) and was time-integrated over 100 ns. (B) Transient absorption spectrum of a solution containing **[Cp*Ir(phen)(H)](PF$_6$)** (0.5 mM) and TAA-OMe (10 mM) in deaerated CH_3CN. The spectrum was measured at a time delay of 10 ns after excitation at 445 nm (9 mJ) and was time-integrated over 100 ns. See ESI Section 2.6† for the molecular structure of TAA-OMe. (C) Absorption spectrum of **[Cp*Ir(phen)]^0** in deaerated CH_3CN at room temperature obtained after deprotonation of **[Cp*Ir(phen)(H)]$^+$** with KO^{t}Bu (1.3 eq.). (D) Absorption spectrum of TAA-OMe$^{\bullet+}$ in deaerated CH_3CN after chemical oxidation of a TAA-OMe solution (31 μM) with $NOBF_4$ (3.0 eq.).

In the presence of the olefin substrates, we expect that **[Cp*Ir(phen)(H)]^0** acts as H-atom donor, leading to the **[Cp*Ir(phen)]^0** complex and the radical intermediates (**RI$^\bullet$** in Fig. 2). In the transient absorption experiments of Fig. 7, where there is no olefin substrate present, **[Cp*Ir(phen)]^0** is expected to form *via* H_2 evolution from two equivalents of **[Cp*Ir(phen)(H)]^0** as illustrated in Fig. S37.† This reaction is exergonic by *ca.* 16 kcal mol^{-1}.[67]

2.5 Radical clock experiment

The reactivity patterns identified above (Fig. 4) are fully compatible with a HAT mechanism. To gain further mechanistic insight, an experiment with (1-(2-phenylcyclopropyl)vinyl)benzene (**13-SM**), a radical clock-type substrate, was performed (Fig. 8). The exact rate constant for the ring-opening of the radical formed after HAT to this particular substrate (**13-RI1$^\bullet$**) is not known, but based on structurally closely related compounds (ESI Section 4.5†) it seems plausible that the rate constant (k_{RO}) for the opening of the cyclopropane-ring in **13-RI1$^\bullet$** (leading to **13-RI2$^\bullet$**) occurs with a rate on the order of $10^8\ s^{-1}$.[90,91] Under our standard reaction conditions (Fig. 8, top left) using **[Cp*Ir(phen)Cl]Cl**, the olefin substrate **13-SM** converts exclusively to the ring-opened product **13-RO** (71% yield after 44 h). No formation of the ring-retention hydrogenation product (**13-RR**) is observed. The observation of the ring-opened product **13-RO** is consistent with a radical mechanism, and furthermore indicates that the intramolecular ring-opening reaction is faster than secondary HAT. Because **13-RO** still contains an olefinic functional group, it reacts onwards to hydrogenation and rearranged products, analogously to substrates **1-SM–12-SM** (ESI Section 4.5†).

2.6 Experiment with a deuterated substrate probing the reversibility of primary HAT

The prior section confirmed the radical nature of the reaction and provided already some insight into the kinetics of secondary HAT to the radical intermediate. By exploring the visible-light induced hydrogenation of deuterated substrate **1-SM-*d*$_4$** we sought to probe the initial HAT step in more detail. After an initial HAT to **1-SM-*d*$_4$** (k_{HAT1} in Fig. 9), the formed radical intermediate (**1-RI$^\bullet$-*d*$_4$**) can in principle directly react onwards to the hydrogenation (**1-H-*d*$_4$**) or the rearranged (**1-R-*d*$_3$**) products. On the other hand also a reverse HAT (H-atom abstraction from **1-RI$^\bullet$-*d*$_4$** to afford **1-SM-*d*$_3$**, k_{-HAT1} in Fig. 9) could occur prior to product formation. Thus, the deuterated substrate is useful to probe the reversibility of initial HAT: if reverse HAT from **1-RI$^\bullet$-*d*$_4$** were kinetically competitive with onward reaction to **1-H-*d*$_4$** or **1-R-*d*$_3$**, there should be proton incorporation into the originally fully deuterated double bond (bond labeled "a" in Fig. 9) and some **1-SM-*d*$_3$** should be formed.

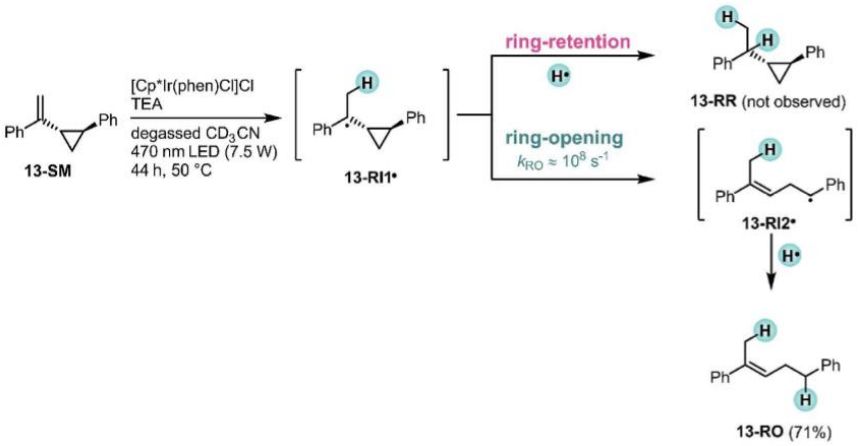

Fig. 8 Radical clock experiment with a cyclopropane substituted olefin confirms that the reaction proceeds *via* a radical intermediate. For simplicity, only the (*E*)-isomer of the ring-opened product **13-RO** is shown.

When the deuterated substrate (**1-SM-d_4**) was subjected to the standard conditions (see Fig. 3) and the reaction mixture was irradiated for 44 h, both hydrogenation (**1-H-d_4**, 87%) and isomerization (**1-R-d_3**, 6%) products were observed. No formation of **1-SM-d_3** was detectable throughout the irradiation process (ESI Section 4.6†). Thus, H-atom abstraction from the radical intermediate (**1-RI$^{\bullet}$-d_4**) to form **1-SM-d_3** can be neglected. Evidently, secondary HAT (k_{HAT2}) yielding the final hydrogenation product **1-H-d_4** as well as isomerization (k_R) leading to the rearranged product **1-R-d_3** are both faster than reverse HAT (k_{-HAT1}). The fast onward reaction to give preferably the hydrogenation product **1-H-d_4** is likely due to the presence of TEA oxidation products such as TEA$^{\bullet+}$ or TEA$^{\bullet}$.[89,92] These highly reactive species presumably serve as the H-atom sources for a secondary HAT to yield the final hydrogenation product.

As noted previously for thermal MHAT, the chemoselectivity of the overall reaction strongly depends on the concentration of the H-atom donor.[72] When the concentration of the H-atom donor is relatively high, such as for a system where $CpCr(CO)_3H$ was readily regenerated under H_2 pressure,[78] hydrogenation products are formed preferably. With lower H$^{\bullet}$ concentrations, however, which was the case in a previously

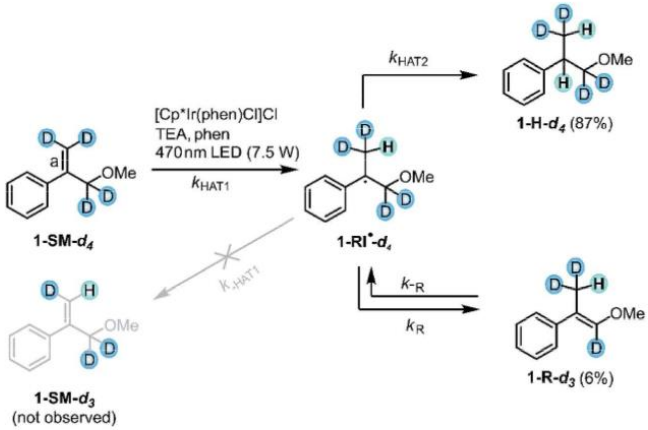

Fig. 9 Experiment with deuterated substrate **1-SM-d_4**: no proton incorporation into the terminal double bond (bond labeled "a") was observed, indicating that H-atom abstraction from **1-RI$^{\bullet}$-d_4** to afford **1-SM-d_3** is negligible (crossed gray leftward arrow labeled k_{HAT1}). For simplicity, only the (*E*)-isomer of the rearranged product **1-R-d_3** is shown.

investigated Co–H/H_2 system,[72] the rearranged products (**1-R-d_3**) are formed preferably. The preferential formation of hydrogenation products in our study therefore indicates an elevated (local) H-atom donor concentration, presumably due to the presence of iridium hydrides and TEA oxidation products in sufficiently close proximity.

2.7 Proposed reaction mechanism

From the various studies in the prior sections, the mechanistic picture in Fig. 10 emerges. Before the actual catalytic cycle initiates, the catalyst precursor **[Cp*Ir(phen)Cl]$^+$** first needs to be converted into **[Cp*Ir(phen)(H)]$^+$** (Section 2.4). The **[Cp*Ir(phen)(H)]$^+$** complex with the metal in its +III oxidation state is not yet reactive enough to catalyze the HAT-step to the olefin substrate (**SM**), as demonstrated by the lack of conversion when the reaction mixture is stirred in the dark (Fig. 6B, entry 2). The Ir^{III}–H BDFE of **[Cp*Ir(phen)(H)]$^+$** is not known, but for a related complex the Ir^{III}–H BDFE is 69 kcal mol^{-1},[93] which is too high for formation of the radical intermediates **RI$^\bullet$** (ESI Section 4.1†).

Photoexcitation of **[Cp*Ir(phen)(H)]$^+$** populates a long-lived ^{3}MLCT excited state (τ of 148 ns at a **[Cp*Ir(phen)(H)]$^+$** concentration of 0.2 mM),[59,67] which is quenched reductively by TEA with a rate constant of $k_q = 4.5 \times 10^8$ M^{-1} s^{-1} to form **[Cp*Ir(phen)(H)]^0** (ESI Section 4.3†). This iridium(II) hydride is likely the key catalytic intermediate, acting as H-atom donor *vis-à-vis* the olefin substrates. At the relevant TEA concentrations for our olefin hydrogenations (250 mM), the rate for reductive ^{3}MLCT excited state quenching exceeds the rate for "self-quenching" by at least one order of magnitude.

Direct detection of **[Cp*Ir(phen)(H)]^0** by transient absorption spectroscopy is not possible, because this is a highly reactive and short-lived species, which does not accumulate in detectable concentrations. Instead, **[Cp*Ir(phen)]^0**, which is formed from **[Cp*Ir(phen)(H)]^0** after H-atom release, is readily detected (Section 2.4).

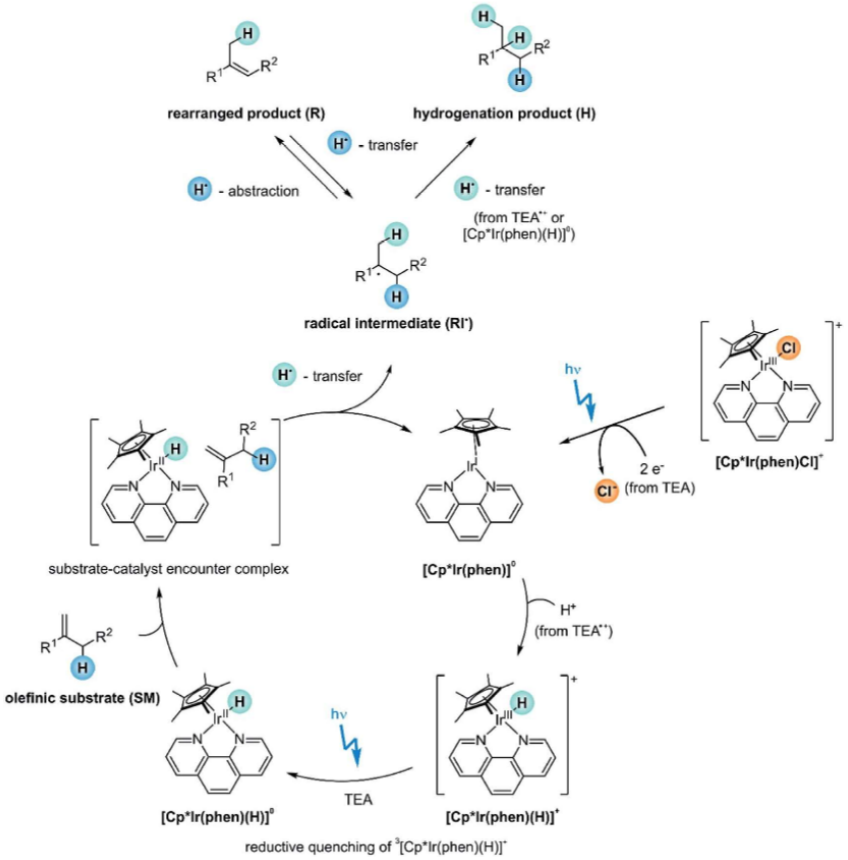

Fig. 10 Proposed reaction mechanism. For simplicity, only the (*E*)-isomer of the rearranged product is shown.

Based on previously determined electrochemical potentials for analogous bpy-based (instead of phen-based) iridium complexes, neither the ^{3}MLCT-excited **[Cp*Ir(phen)(H)]$^+$** ($E^{0\prime}$(IV/III*) ≈ −1.3 *vs.* SCE,[67] ESI Section 4.1†) nor the **[Cp*Ir(phen)(H)]^0** complex ($E^{0\prime}$(III/II) ≈ −1.4 V *vs.* SCE,[67] ESI Section 4.1†) have the reducing power to permit electron transfer to the olefin substrates (E_{red} < −2.7 V *vs.* SCE).[31] Consequently, olefin hydrogenation cannot occur *via* a PET pathway (ESI Section 4.1†).

However, **[Cp*Ir(phen)(H)]^0** exhibits an Ir^{II}–H BDFE of approximately 44 kcal mol^{-1},[67] considerably lower than the M–H BDFEs of common MHAT-catalysts, which are typically in the range of 50–60 kcal mol^{-1}.[70,71] This very weak Ir^{II}–H bond permits an initial HAT to the olefin substrates (ESI Section 4.1†). The achievable hydrogenation yields for the various substrates **1-SM**–**12-SM** reflect the relative stabilities of the involved (charge-neutral) radical intermediates **RI˙** (Fig. 4), as expected for HAT. Furthermore, the radical clock experiment (Fig. 8) underpins the radical pathway and speaks against a mechanism involving olefin insertion into the Ir–H bond.

No conversion at all is observed with the sterically demanding mesityl-substituted olefin **7-SM** (Fig. 3), suggesting that the catalyst and **7-SM** cannot approach sufficiently closely to undergo HAT. The formation of sufficiently intimate contacts, different however from actual substrate ligation to the metal center or olefin insertion into the M–H bond, seems to be a key requirement for successful reaction.

For substrates undergoing successful photo-HAT, the formed radical intermediate (**RI˙**) can either react *via* secondary HAT to yield the hydrogenation product (**H**, top right in Fig. 10) or rearrange to the isomerization product (**R**, top left in Fig. 10). TEA oxidation products such as TEA$^{\bullet+}$ or TEA˙ likely serve as H-atom sources for secondary HAT. Whilst the hydrogenation products (**H**) are inert and do not react onwards, the rearranged products (**R**) can be activated *via* HAT from **[Cp*Ir(phen)(H)]^0** to re-form radical intermediate (**RI˙**). Thus, irradiation over extended time periods drives the overall reaction towards the hydrogenation product (Fig. 5B). Excess phen ligand (30 mol%) in the reaction mixture enhances that **H**/**R** chemoselectivity by decelerating catalyst degradation and enabling photo-reactions over longer irradiation periods (Section 2.4).

3 Conclusions

This work illustrates a new type of photo-reactivity for an archetypal metal hydride complex, complementing prior studies on photoacid and "self-quenching" behavior of this well-known class of compounds.[59–67] From a photochemical perspective, the discovery of photo-HAT from the **[Cp*Ir(phen)(H)]$^+$** complex could represent an important breakthrough, because the vast majority of previously explored metal-based photosensitizers operate on the basis of photoinduced electron transfer. Consequently, photoredox catalysis until now largely relied on single electron transfer, but the possibility of photo-HAT could open completely new perspectives. Our new insights complement recent photophysical and -chemical studies of iridium hydride[59–67] and related complexes.[94,95] In particular, recent work established that the hydrodechlorination of CH_2Cl_2 proceeds *via* excited-state "self-quenching" producing a pair of [Ir^{IV}–H]$^{2+}$ and [Ir^{II}–H]^0 species, which then undergoes (sequential) hydride transfer and HAT to form two equivalents of $CHCl_3$ from two molecules of CH_2Cl_2 solvent. Here, the [Ir^{II}–H]^0 H-atom donor is formed *via* reductive ^{3}MLCT-excited state quenching of the [Ir^{III}–H]$^+$ species, which itself is formed from the robust [Ir^{III}–Cl]$^+$ precursor in photochemical fashion. In our case, the overall HAT reaction is catalytic and occurs to olefin substrates rather than carbon-centered radicals derived from CH_2Cl_2 solvent. Contrary to previously explored polyoxometallate-based photo-HAT systems,[38–43] the iridium hydride explored herein operates under visible-light irradiation.

We focused on the photoinduced hydrogenation of relatively simple olefins as a test ground to explore the reactivity patterns of photo-HAT, but prior studies on thermal (*i.e.*, light-independent) reactions established that metal-catalyzed HAT has numerous applications in organic synthetic chemistry.[68] Compared to thermal HAT, the photo-HAT with **[Cp*Ir(phen)(H)]$^+$** has the advantage that even lower M–H BDFEs (*ca.* 44 kcal mol^{-1} for the reductive quenching product **[Cp*Ir(phen)(H)]^0**) are reachable, which stands in contrast to the traditional thermal manner, where most M–H BDFEs are above 50 kcal mol^{-1}.[70] This gain in driving force of around $\Delta\Delta G$ ≈ 6 kcal mol^{-1} can in principle translate to an approximately 10^4 times faster reaction rate. Very low M–H BDFEs are typically unstable to bimolecular H_2 evolution,[65–67] but in the presence of 50 mM olefin substrate our hydrogenation reactions proceeded well and exhibited the typical reactivity patterns of HAT.

In our reactions, even aliphatic substrates yielding highly reactive radical intermediates were activated successfully. The investigated olefin substrates have strongly negative reduction potentials (<−2.7 V *vs.* SCE)[31] and therefore cannot be activated easily by the traditional path of photoinduced electron transfer.

Conflicts of interest

There are no conflicts to declare.

Acknowledgements

This work was supported by the Swiss National Science Foundation through the NCCR Molecular Systems Engineering. Felix Glaser is thanked for skillful experimental support.

References

1 D. M. Arias-Rotondo and J. K. McCusker, *Chem. Soc. Rev.*, 2016, **45**, 5803–5820.
2 K. S. Kjær, N. Kaul, O. Prakash, P. Chábera, N. W. Rosemann, A. Honarfar, O. Gordivska, L. A. Fredin, K. E. Bergquist, L. Häggström, T. Ericsson, L. Lindh, A. Yartsev, S. Styring, P. Huang, J. Uhlig, J. Bendix, D. Strand, V. Sundström, P. Persson, R. Lomoth and K. Wärnmark, *Science*, 2019, **363**, 249–253.
3 J. D. Braun, I. B. Lozada, C. Kolodziej, C. Burda, K. M. E. Newman, J. van Lierop, R. L. Davis and D. E. Herbert, *Nat. Chem.*, 2019, **11**, 1144–1150.

4 R. Hamze, J. L. Peltier, D. Sylvinson, M. Jung, J. Cardenas, R. Haiges, M. Soleilhavoup, R. Jazzar, P. I. Djurovich, G. Bertrand and M. E. Thompson, *Science*, 2019, **363**, 601–606.
5 C. Förster and K. Heinze, *Chem. Soc. Rev.*, 2020, **40**, 1057–1070.
6 O. S. Wenger, *J. Am. Chem. Soc.*, 2018, **140**, 13522–13533.
7 J. C. Theriot, C. H. Lim, H. Yang, M. D. Ryan, C. B. Musgrave and G. M. Miyake, *Science*, 2016, **352**, 1082–1086.
8 L. Marzo, S. K. Pagire, O. Reiser and B. König, *Angew. Chem., Int. Ed.*, 2018, **57**, 10034–10072.
9 L. Zhang and L. Jiao, *J. Am. Chem. Soc.*, 2019, **141**, 9124–9128.
10 H. Yin, Y. Jin, J. E. Hertzog, K. C. Mullane, P. J. Carroll, B. C. Manor, J. M. Anna and E. J. Schelter, *J. Am. Chem. Soc.*, 2016, **138**, 16266–16273.
11 J. J. Devery, J. D. Nguyen, C. Dai and C. R. J. Stephenson, *ACS Catal.*, 2016, **6**, 5962–5967.
12 P. Herr, F. Glaser, L. A. Büldt, C. B. Larsen and O. S. Wenger, *J. Am. Chem. Soc.*, 2019, **141**, 14394–14402.
13 J. H. Shon, S. Sittel and T. S. Teets, *ACS Catal.*, 2019, **9**, 8646–8658.
14 T. U. Connell, C. L. Fraser, M. L. Czyz, Z. M. Smith, D. J. Hayne, E. H. Doeven, J. Agugiaro, D. J. D. Wilson, J. L. Adcock, A. D. Scully, D. E. Gómez, N. W. Barnett, A. Polyzos and P. S. Francis, *J. Am. Chem. Soc.*, 2019, **141**, 17646–17658.
15 F. Glaser, C. Kerzig and O. S. Wenger, *Angew. Chem., Int. Ed.*, 2020, **59**, 10266–10284.
16 M. Giedyk, R. Narobe, S. Weiß, D. Touraud, W. Kunz and B. König, *Nat. Catal.*, 2020, **3**, 40–47.
17 M. Neumeier, D. Sampedro, M. Májek, V. a. de la Peña O'Shea, A. Jacobi von Wangelin and R. Pérez-Ruiz, *Chem.–Eur. J.*, 2018, **24**, 105–108.
18 J. P. Cole, D.-F. Chen, M. Kudisch, R. M. Pearson, C.-H. Lim and G. M. Miyake, *J. Am. Chem. Soc.*, 2020, DOI: 10.1021/jacs.0c05899.
19 H. Kim, H. Kim, T. H. Lambert and S. Lin, *J. Am. Chem. Soc.*, 2020, 2087–2092.
20 N. G. W. Cowper, C. P. Chernowsky, O. P. Williams and Z. K. Wickens, *J. Am. Chem. Soc.*, 2020, **142**, 2093–2099.
21 J. P. Barham and B. König, *Angew. Chem., Int. Ed.*, 2019, **59**, 2–18.
22 J. W. Darcy, B. Koronkiewicz, G. A. Parada and J. M. Mayer, *Acc. Chem. Res.*, 2018, **51**, 2391–2399.
23 E. C. Gentry and R. R. Knowles, *Acc. Chem. Res.*, 2016, **49**, 1546–1556.
24 M. Kuss-Petermann and O. S. Wenger, *Chem.–Eur. J.*, 2017, **23**, 10808–10814.
25 G. E. M. Crisenza, D. Mazzarella and P. Melchiorre, *J. Am. Chem. Soc.*, 2020, **142**, 5461–5476.
26 T. P. Yoon, *Acc. Chem. Res.*, 2016, **49**, 2307–2315.
27 R. Brimioulle and T. Bach, *Science*, 2013, **342**, 840–843.
28 C. Pac, M. Ihama, M. Yasuda, Y. Miyauchi and H. Sakurai, *J. Am. Chem. Soc.*, 1981, **103**, 6495–6497.
29 R. Naumann, F. Lehmann and M. Goez, *Chem.–Eur. J.*, 2018, **24**, 13259–13269.
30 C. Kerzig, X. Guo and O. S. Wenger, *J. Am. Chem. Soc.*, 2019, **141**, 2122–2127.
31 H. Senboku, H. Komatsu, Y. Fujimura and M. Tokuda, *Synlett*, 2001, 418–420.
32 Y. Y. Loh, K. Nagao, A. J. Hoover, D. Hesk, N. R. Rivera, S. L. Colletti, I. W. Davies and D. W. C. MacMillan, *Science*, 2017, **1187**, 1182–1187.
33 L. Capaldo and D. Ravelli, *Eur. J. Org. Chem.*, 2017, 2056–2071.
34 M. H. Shaw, V. W. Shurtleff, J. A. Terrett, J. D. Cuthbertson and D. W. C. MacMillan, *Science*, 2016, **352**, 1304–1308.
35 J. Twilton, M. Christensen, D. A. DiRocco, R. T. Ruck, I. W. Davies and D. W. C. MacMillan, *Angew. Chem., Int. Ed.*, 2018, **57**, 5369–5373.
36 X. Q. Hu, J. R. Chen and W. J. Xiao, *Angew. Chem., Int. Ed.*, 2017, **56**, 1960–1962.
37 X. Guo and O. S. Wenger, *Angew. Chem., Int. Ed.*, 2018, **57**, 2469–2473.
38 S. Protti, M. Fagnoni and D. Ravelli, *ChemCatChem*, 2015, **7**, 1516–1523.
39 V. De Waele, O. Poizat, M. Fagnoni, A. Bagno and D. Ravelli, *ACS Catal.*, 2016, **6**, 7174–7182.
40 P. J. Sarver, V. Bacauanu, D. M. Schultz, D. A. Dirocco, Y. Lam, E. C. Sherer and D. W. C. MacMillan, *Nat. Chem.*, 2020, **12**, 459–467.
41 J. J. Zhong, W. P. To, Y. Liu, W. Lu and C. M. Che, *Chem. Sci.*, 2019, **10**, 4883–4889.
42 D. M. Schultz, F. Lévesque, D. A. DiRocco, M. Reibarkh, Y. Ji, L. A. Joyce, J. F. Dropinski, H. Sheng, B. D. Sherry and I. W. Davies, *Angew. Chem., Int. Ed.*, 2017, **56**, 15274–15278.
43 G. Laudadio, Y. Deng, K. Van Der Wal, D. Ravelli, M. Nuño, M. Fagnoni, D. Guthrie, Y. Sun and T. Noël, *Science*, 2020, **96**, 92–96.
44 J. J. Concepcion, M. K. Brennaman, J. R. Deyton, N. V. Lebedeva, M. D. E. Forbes, J. M. Papanikolas and T. J. Meyer, *J. Am. Chem. Soc.*, 2007, **129**, 6968–6969.
45 J. C. Lennox, D. A. Kurtz, T. Huang and J. L. Dempsey, *ACS Energy Lett.*, 2017, **2**, 1246–1256.
46 O. S. Wenger, *Chem.–Eur. J.*, 2011, **17**, 11692–11702.
47 Y. Deng, J. A. Roberts, S.-M. Peng, C. K. Chang and D. G. Nocera, *Angew. Chem., Int. Ed.*, 1997, 2124–2127.
48 S. W. M. Crossley, C. Obradors, R. M. Martinez and R. A. Shenvi, *Chem. Rev.*, 2016, **116**, 8912–9000.
49 J. Hartung, M. E. Pulling, D. M. Smith, D. X. Yang and J. R. Norton, *Tetrahedron*, 2008, **64**, 11822–11830.
50 R. N. Perutz and B. Procacci, *Chem. Rev.*, 2016, **116**, 8506–8544.
51 J. A. Bandy, F. G. N. Cloke, G. Cooper, J. P. Day, R. B. Girling, R. G. Graham, J. C. Green, R. Grinter and R. N. Perutz, *J. Am. Chem. Soc.*, 1988, **110**, 5039–5050.
52 C. M. Morton, Q. Zhu, H. Ripberger, L. Troian-Gautier, Z. S. D. Toa, R. R. Knowles and E. J. Alexanian, *J. Am. Chem. Soc.*, 2019, **141**, 13253–13260.
53 M. E. Ener, J. W. Darcy, F. S. Menges and J. M. Mayer, *J. Org. Chem.*, 2020, **85**, 7175–7180.
54 F. Gloaguen and T. B. Rauchfuss, *Chem. Soc. Rev.*, 2009, **38**, 100–108.

55 Y. A. Small, D. L. Dubois, E. Fujita and J. T. Muckerman, *Energy Environ. Sci.*, 2011, **4**, 3008–3020.
56 M. Bourrez, R. Steinmetz, S. Ott, F. Gloaguen and L. Hammarström, *Nat. Chem.*, 2015, **7**, 140–145.
57 T. Liu, M. Guo, A. Orthaber, R. Lomoth, M. Lundberg, S. Ott and L. Hammarström, *Nat. Chem.*, 2018, **10**, 881–887.
58 T. Huang, E. S. Rountree, A. P. Traywick, M. Bayoumi and J. L. Dempsey, *J. Am. Chem. Soc.*, 2018, **140**, 14655–14669.
59 D. Sandrini, M. Maestri and R. Ziessel, *Inorg. Chim. Acta*, 1989, **163**, 177–180.
60 T. Suenobu, D. M. Guldi, S. Ogo and S. Fukuzumi, *Angew. Chem., Int. Ed.*, 2003, **42**, 5492–5495.
61 S. M. Barrett, C. L. Pitman, A. G. Walden and A. J. M. Miller, *J. Am. Chem. Soc.*, 2014, **136**, 14718–14721.
62 K. R. Brereton, C. N. Jadrich, B. M. Stratakes and A. J. M. Miller, *Organometallics*, 2019, **38**, 3104–3110.
63 C. L. Pitman, K. R. Brereton and A. J. M. Miller, *J. Am. Chem. Soc.*, 2016, **138**, 2252–2260.
64 S. M. Barrett, B. M. Stratakes, M. B. Chambers, D. A. Kurtz, C. L. Pitman, J. L. Dempsey and A. J. M. Miller, *Chem. Sci.*, 2020, **11**, 6442–6449.
65 R. Ziessel, *J. Am. Chem. Soc.*, 1993, **115**, 118–127.
66 C. L. Pitman and A. J. M. Miller, *ACS Catal.*, 2014, **4**, 2727–2733.
67 M. B. Chambers, D. A. Kurtz, C. L. Pitman, M. K. Brennaman and A. J. M. Miller, *J. Am. Chem. Soc.*, 2016, **138**, 13509–13512.
68 S. A. Green, S. W. M. Crossley, J. L. M. Matos, S. Vásquez-Céspedes, S. L. Shevick and R. A. Shenvi, *Acc. Chem. Res.*, 2018, **51**, 2628–2640.
69 S. W. M. Crossley, F. Barabé and R. A. Shenvi, *J. Am. Chem. Soc.*, 2014, **136**, 16788–16791.
70 J. Choi, M. E. Pulling, D. M. Smith and J. R. Norton, *J. Am. Chem. Soc.*, 2008, **130**, 4250–4252.
71 R. G. Pearson, *Chem. Rev.*, 1985, **85**, 41–49.
72 G. Li, J. L. Kuo, A. Han, J. M. Abuyuan, L. C. Young, J. R. Norton and J. H. Palmer, *J. Am. Chem. Soc.*, 2016, **138**, 7698–7704.
73 Y. Nakano, M. J. Black, A. J. Meichan, B. A. Sandoval, M. M. Chung, K. F. Biegasiewicz, T. Zhu and T. K. Hyster, *Angew. Chem., Int. Ed.*, 2020, **59**, 10484–10488.
74 X. Guo, Y. Okamoto, M. R. Schreier, T. R. Ward and O. S. Wenger, *Chem. Sci.*, 2018, **9**, 5052–5056.
75 Z. C. Litman, Y. Wang, H. Zhao and J. F. Hartwig, *Nature*, 2018, **560**, 355–359.
76 K. Lauder, A. Toscani, Y. Qi, J. Lim, S. J. Charnock, K. Korah and D. Castagnolo, *Angew. Chem., Int. Ed.*, 2018, **57**, 5803–5807.
77 T. J. Whittemore, C. Xue, J. Huang, J. C. Gallucci and C. Turro, *Nat. Chem.*, 2020, **12**, 180–185.
78 J. Choi, L. Tang and J. R. Norton, *J. Am. Chem. Soc.*, 2007, **129**, 234–240.
79 C. Kerzig and O. S. Wenger, *Chem. Sci.*, 2019, **2**, 11023–11029.
80 A. U. Meyer, T. Slanina, A. Heckel and B. König, *Chem.–Eur. J.*, 2017, **23**, 7900–7904.
81 R. Matsubara, T. Yabuta, U. Md Idros, M. Hayashi, F. Ema, Y. Kobori and K. Sakata, *J. Org. Chem.*, 2018, **83**, 9381–9390.
82 L. Yu-Ran, *Comprehensive Handbook of Chemical Bond Energies*, Taylor & Francis Group, Boca Raton, 2007.
83 D. J. Goebbert and P. G. Wenthold, *Int. J. Mass Spectrom.*, 2006, **257**, 1–11.
84 J. Hioe and H. Zipse, in *Encyclopedia of Radicals in Chemistry, Biology and Materials*, John Wiley & Sons, Ltd, 2012.
85 M. Ladwig and W. Kaim, *J. Organomet. Chem.*, 1992, **439**, 79–90.
86 T. Ghosh, T. Slanina and B. König, *Chem. Sci.*, 2015, **6**, 2027–2034.
87 K. T. Oppelt, E. Wöß, M. Stiftinger, W. Schöfberger, W. Buchberger and G. Knör, *Inorg. Chem.*, 2013, **52**, 11910–11922.
88 L. Zedler, A. K. Mengele, K. M. Ziems, Y. Zhang, M. Wächtler, S. Gräfe, T. Pascher, S. Rau, S. Kupfer and B. Dietzek, *Angew. Chem., Int. Ed.*, 2019, **58**, 13140–13148.
89 P. J. DeLaive, T. K. Foreman, D. G. Whitten and C. Giannotti, *J. Am. Chem. Soc.*, 1980, **102**, 5627–5631.
90 R. Hollis, L. Hughes, V. W. Bowry and K. U. Ingold, *J. Org. Chem.*, 1992, **57**, 4284–4287.
91 J. Masnovi, E. G. Samsel and R. M. Bullock, *J. Chem. Soc., Chem. Commun.*, 1989, 1044–1045.
92 Y. Pellegrin and F. Odobel, *C. R. Chim.*, 2017, **20**, 283–295.
93 J. A. M. Simões and J. L. Beauchamp, *Chem. Rev.*, 1990, **90**, 629–688.
94 J. C. Deaton, C. M. Taliaferro, C. L. Pitman, R. Czerwieniec, E. Jakubikova, A. J. M. Miller and F. N. Castellano, *Inorg. Chem.*, 2018, **57**, 15445–15461.
95 C. L. Pitman and A. J. M. Miller, *Organometallics*, 2017, **36**, 1906–1914.

3.3 Outlook

After a suitable system has been established for the photoinduced hydrogenation of unactivated olefins, future research could focus on exploring new reactivities of this mechanism, in analogy to thermal metal hydride catalyzed hydrogen atom transfer (MHAT).[155,156] However, with the current experimental conditions, secondary HAT to the radical intermediate is fast due to elevated (local) concentrations of the involved H-atom donors (i.e., the oxidation products of TEA and the iridium hydride). It would therefore be interesting to develop variants of the system that circumvent this secondary HAT, for example by finding a suitable e^--donor/H^+-donor combination (e.g. 1,4-BNAH/TsOH)[141] that manages to form and recycle the iridium hydride but without being able to donate a H-atom. With this deviation, other metal hydride reactions such as cycloisomerization,[178] or the reductive coupling of olefins[179] could be tested (Figure 14A). The two mentioned reactions are particularly interesting, since they could take advantage of the different observed reactivities of aromatic and aliphatic olefins in the investigated photo-HAT. Future research could furthermore focus on testing different iridium hydride precursors since the reductive cleavage of the iridium(III) chloride bond was found to be slow.

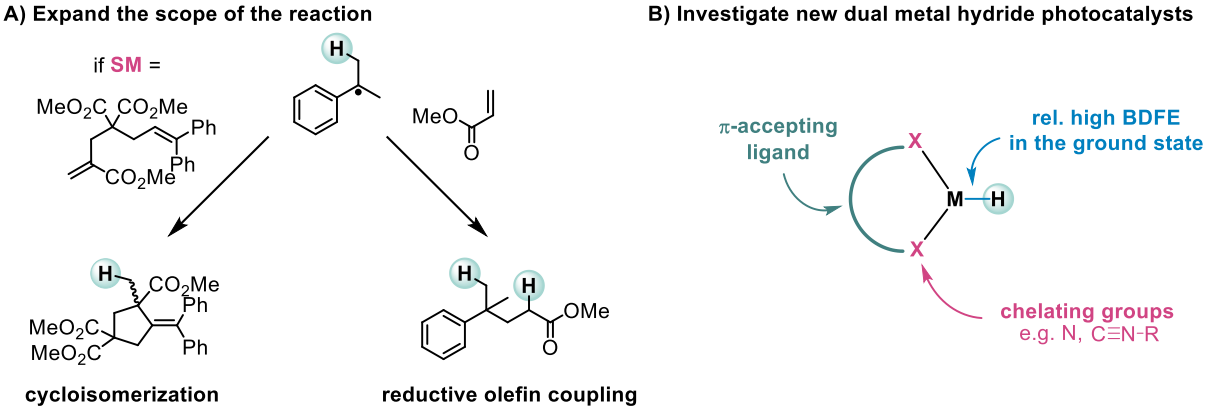

Figure 14: Possible future research of the photo-HAT could focus on A) expanding the scope of the investigated reaction or B) the development of new photoactive metal hydrides.

Moreover, future research could be focusing on expanding the photo-HAT reactivity to other transition metal hydrides. Considering that possible future catalysts need to be able to perform the role of the photocatalyst and as well as being able to transfer H-atoms to the substrate only upon excitation with visible light, two main criteria need to be met: i) the transition metal hydrides need to be photoactive and their excited-state lifetime needs to be long enough to engage in electron transfer processes and ii) the BDFE of the transition metal hydride in the ground state needs to be high enough, so that no or only slow thermal HAT occurs. Since transition metal hydrides with sufficiently long excited-state lifetimes for bimolecular processes are rare, further research could focus on the development of new metal hydride catalysts (Figure 14B).

For example, the introduction of a π-accepting ligand to common transition metal hydrides might enable MLCT states that are sufficiently long-lived for bimolecular processes. Given that

many first row transition metal hydrides such as Co-H, Fe-H, Cr-H and Mn-H are known to be efficient H-atom donors in the ground state,[156,180] future projects should focus on second and third row transition metal hydrides because they tend to have higher ground state BDFEs. Also, it could be tested whether some of the already known photoactive transition metal hydrides such as $[Os(phen)_2(CO)(H)]^+$[181] are able to engage in photo-HAT processes.

4 Water-Soluble Iridium Photosensitizers for the Photochemical Regeneration of Nucleotide Co-Factor Mimics

4.1 Introduction

Photobiocatalysis, i.e. the coupling of a photocatalytic with an enzymatic reaction, has emerged as a powerful method to achieve selective, mild, and environmentally friendly chemical transformations that complement nature's and a chemist's toolbox.[23–25,135,182] Natural photosynthesis is the blueprint for this coupling of a light-dependent reaction with an enzymatic dark reaction. In this natural process, excitation of the photosystem with visible light in presence of water as an electron donor leads to the formation of energy rich molecules such as the nucleotide co-factor **NADPH**, which is ultimately re-oxidized in the enzymatic dark reaction.[22] Hence, the efficient photochemical regeneration of nucleotide co-factors arose as an important concept in mimicking natural photosynthesis (Figure 15).[23,24,135]

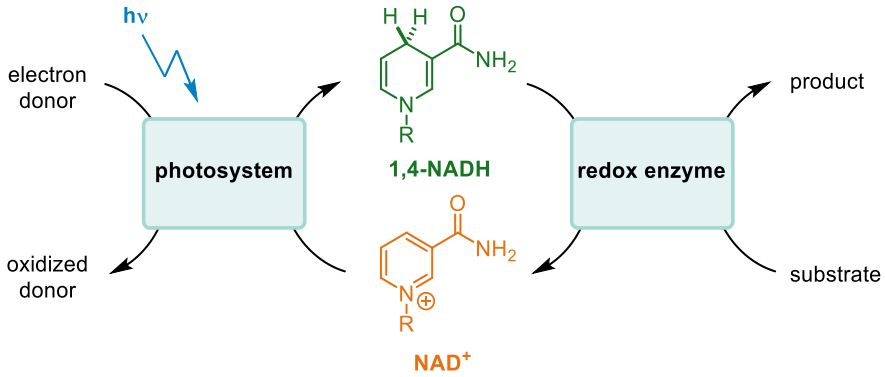

Figure 15: The photochemical regeneration of nucleotide co-factors such as **1,4-NADH** is an attractive strategy to mimic natural photosynthesis since it allows to couple the light-dependent reaction (left) with an enzymatic dark reaction (right).[24,25,135]

Due to its importance as a co-factor in biotransformations, the reduction of **NAD(P)$^+$** to **1,4-NAD(P)H** using easily accessible reductants has been extensively studied in recent years. The advantage of such a system is that it allows to perform enzymatic redox reactions without the need for a stoichiometric co-factor.[23,183,184] Various strategies have been investigated to achieve efficient reduction of **NAD(P)$^+$** or nucleotide co-factor mimics including chemical,[185,186] enzymatic,[187–190] electrochemical,[191,192] and photochemical methods.[23,184] The photochemical nucleotide co-factor regeneration is particularly interesting, not only due to its analogy to natural photosynthesis, but also because light provides a cheap, abundant, and environmentally friendly energy source.[23,184] While a few concepts allow the photochemical reduction of **NAD(P)$^+$** or nucleotide co-factor mimics with a single-component dual photocatalyst,[193–195] merging the photocatalytic

cycle with a second, redox-mediating cycle is the more common strategy for efficient co-factor regeneration. The role of the two distinct catalytic cycles in the regeneration of **1,4-NAD(P)H** will be introduced in further detail in the following sections.

4.1.1 The Redox Mediator

For further applications in photobiocatalysis, the regeneration of **1,4-NADH** from **NAD⁺** must be regiospecific since **1,4-NADH** is the only isomer that can serve as a co-factor in enzymatic dark reactions. However, reduction based on single electron transfer (SET) events (i.e., when using photocatalytic or electrochemical regeneration methods) is often unselective because it involves the formation of a radical intermediate, which is prone to dimerization (Figure 16).[196] Also, reduction in presence of a hydride source such as $NaBH_4$ is often unselective and leads to a mixture of **1,2-**, **1,4-**, and **1,6-NADH** isomers.[196]

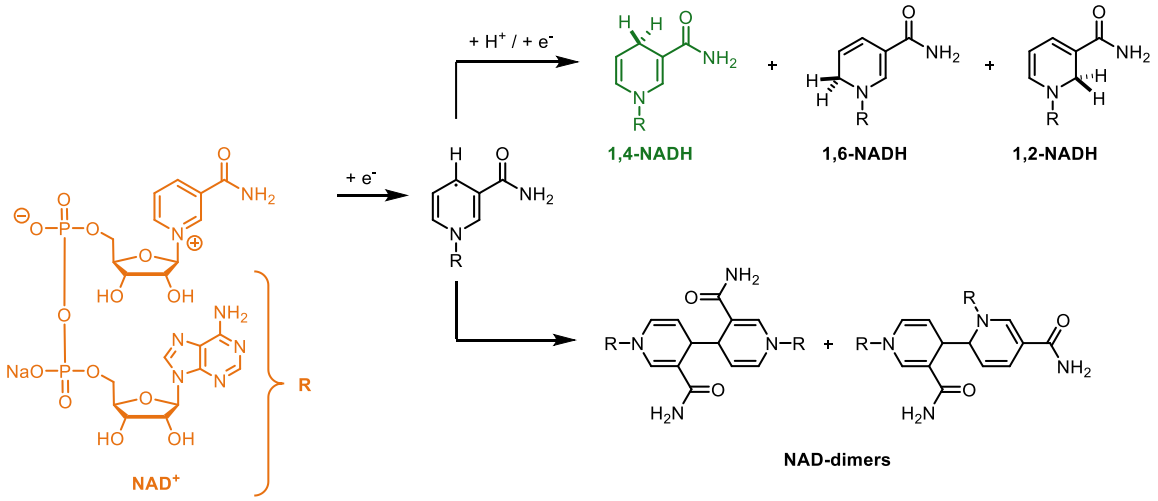

Figure 16: The reduction of **NAD⁺** based on single electron transfer events (SET) suffers from selectivity problems such as the formation of NAD-dimers (bottom) and enzymatically inactive regioisomers (top).

Unspecific and unselective direct reduction of **NAD⁺** can be prevented by using a so-called redox mediator, which aims to transfer the electrons to the substrate in a more controlled manner. Thereby, the electron mediator needs to meet two requirements: i) concerted transfer of two electrons to prevent the formation of NAD-radicals and undesired side-reactions (Figure 16) and ii) regioselective generation of **1,4-NADH**.[23] To this date, the most widely employed electron mediator to catalyze co-factor regeneration is **[Cp*Rh(bpy)(H)]⁺** (Cp* = pentamethylcyclopentadienyl, bpy = 2,2'-bipyridyl) due to its high robustness and selectivity. This Rh(III) hydride is formed in situ from **[Cp*Rh(bpy)(H₂O)]²⁺** in a $2e^-/1H^+$ reduction either in a concerted step in presence of a hydride donor such as formate or via a **[Cp*Rh(bpy)]⁰** intermediate.[49,197,198] Initial studies by the groups of Steckhan and Fish suggest that the regiospecific hydride transfer must occur upon coordination of the substrate to the rhodium metal center and involves a six-membered concerted transition state and an η^5- to η^3- ring slip of the cyclopentadiene ligand (Figure 17, left).[49,198–200] More recent studies by the groups of Miller, Gray, and Blakemore propose that a (Cp*H)Rh(I) intermediate is formed upon reductive elimination

of the Rh(III) hydride.[201,202] Hence, in this pathway the pentamethylcyclopentadienyl ligand is no longer innocent since hydride transfer occurs from the ligand to **NAD⁺** (Figure 17, right).[201] For conciseness, only the transient **[Cp*Rh(bpy)(H)]⁺** intermediate will be considered in the rest of this Chapter.

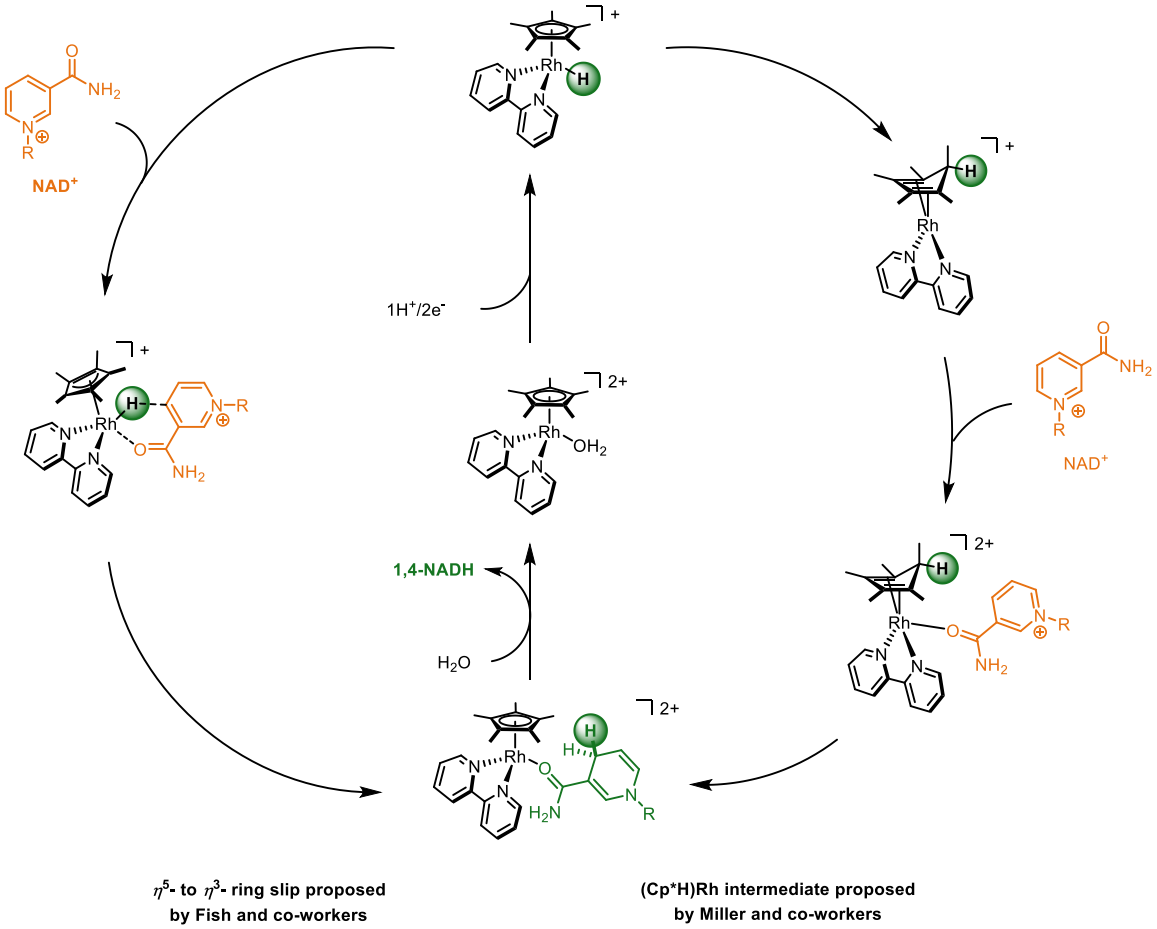

Figure 17 Proposed reaction mechanisms for the regiospecific formation of **1,4-NADH** including either a η^5- to η^3- ring slip (left) or a (Cp*H)Rh(I) intermediate (right).[198–202] See text for details.

In chemical and electrochemical approaches, various redox mediator analogs were synthesized to investigate the influence of different metals and ligand modifications on the nucleotide co-factor regeneration efficiency.[185,191,203–205] In photochemical regeneration systems, these studies are less common and are mainly focusing on optimizing the interaction between the redox mediator and the photocatalyst by Coulombic attraction.[50]

4.1.2 Photochemical NADH-Regeneration

Some of the main challenges for the efficient photochemical regeneration of **1,4-NADH** include the development of new photocatalysts with a high photostability and their applicability under physiological conditions.[23,24] Various efforts have been made towards the development of such photosystems, including both heterogeneous[206,207] and homogeneous photocatalysts (Figure 18).[51,52,208,209]

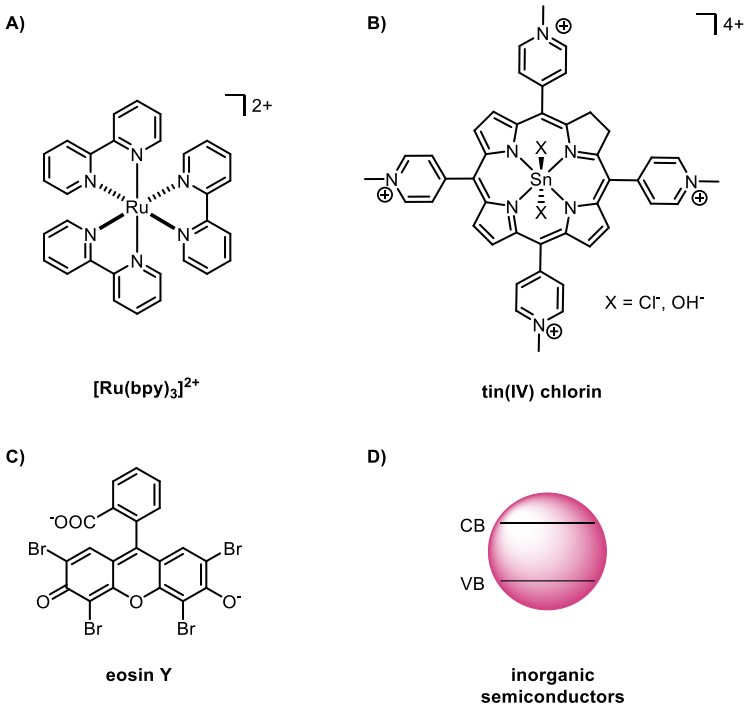

Figure 18: Selected examples of photocatalysts employed for the photochemical regeneration of **1,4-NADH**.

The first report of visible-light driven **1,4-NADH** regeneration dates back to 1983, when Wienkamp and Steckhan reported the regioselective reduction of **NAD⁺** using **[Ru(bpy)$_3$]$^{2+}$** as a photosensitizer and **[Rh(bpy)$_3$]$^{3+}$** as a redox mediator (Figure 18A).[210] More recent examples of photochemical NADH regeneration often rely on **[Cp*Rh(bpy)(H)]⁺** as the redox mediator due to its high robustness and regioselectivity.[23,198] For example, in combination with modified graphene-based materials[211,212] or semiconductors such as $W_2Fe_4Ta_2O_{17}$ and Cd-based nanocrystals,[206,207] the Rh(III) catalyst was able to reduce **NAD⁺** in a regioselective manner (Figure 18B). However, when using semiconductors as photocatalysts, the observed turnover frequency (TOF) for **1,4-NADH** regeneration was rather low (0.12 to 0.55 h^{-1}).[31,32] In homogeneous photocatalysis, Zn-porphyrins were found to enable photoreduction of **NAD⁺** in combination with the commonly used Rh(III) catalyst. Mechanistically, the formation of the Rh(III) hydride intermediate was attributed to a charge transfer from the photocatalyst to the redox mediator, which is bound to the Zn-porphyrin via non-covalent interaction. Despite these favorable interactions, the observed TOF of the photosensitizer was rather low (0.46 h^{-1}).[213] With a related, chlorophyll-like tin-dihydroporphyrin sensitizer, more efficient **1,4-NADH** regeneration (TOF > 20 h^{-1}) was observed using only long-wavelength visible light (λ_{ex} > 610 nm) as an irradiation source (Figure 18B).[52] Interestingly, in this system a tin(IV) chlorin-phlorin anion intermediate is formed upon two-electron reduction of the tin(IV) chlorin photosensitizer. The formed anion serves as the primary hydride source involved in the photoreduction of **NAD⁺**. Whether the hydride transfer from the formed intermediate to the Rh(III) precursor is a concerted step or is based on 2e$^-$ reduction and subsequent protonation was not fully elucidated by the authors.[52] Xanthene dyes such as eosin Y

have proven to be extremely potent photocatalysts for the photochemical regeneration of **1,4-NADH**, reaching TOFs up to 1690 h^{-1} (Figure 18C).[51,208] The authors attribute the extremely high efficiency of xanthene dyes to their ability to coordinate to the Rh(III) metal center, thus enabling efficient intramolecular electron transfer within the photosensitizer-mediator dyad.[51,208] Inspired by these findings, Rau and co-workers investigated a hetero-binuclear dyad in which the photosensitizer is covalently linked to the Rh(III) catalyst, again showing efficient nucleotide co-factor regeneration.[214] These studies therefore manifest the initial finding that the interaction between the photosensitizer and the redox mediator is crucial for the efficient photochemical reduction of **NAD^+**. However, even though photochemical nucleotide co-factor regeneration has proven to be important for various biomimetic transformations in combination with redox enzymes[23,24,135,183] or through its integration into platforms for artificial photosynthesis,[215,216] photophysical studies that examine the interaction between the two key components in more detail are still rare.[217,218]

4.2 Chapter Outline

The second project aimed to develop a new photocatalytic system to regenerate **1,4-NAD(P)H** and to investigate the underlying photophysical processes. Possible future applications in combination with redox enzymes require that the photocatalyst can be employed under physiologically relevant conditions. However, even though substantial progress has been made regarding photocatalysis in the green solvent water,[121,219–222] the number of photosensitizers that can be applied in aqueous solutions[135] is still limited compared to organic solvents.[3,116] Hence, the first part of the project aimed at developing new water-soluble photosensitizers that should enable photocatalytic transformations in aqueous solutions (i.e., in photobiocatalysis). In collaboration with Prof. Dr. Xingwei Guo, two different strategies were pursued to obtain water-soluble variants of **Irppy$_3$**, a potent, well investigated photoreductant in organic solutions (Figure 19).[112]

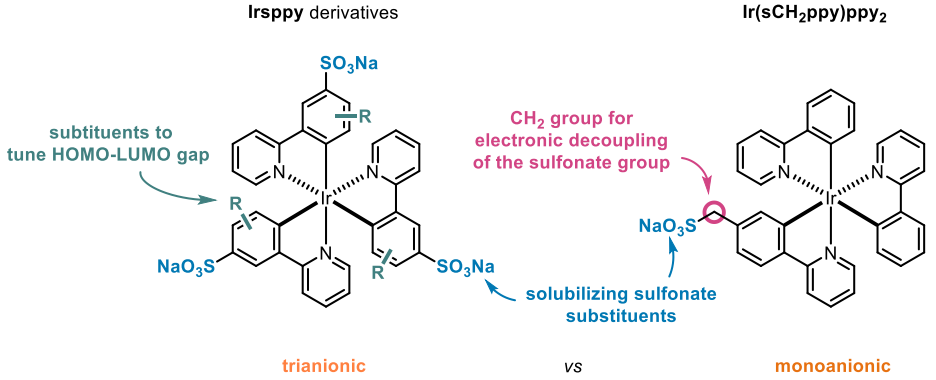

Figure 19: Catalyst design for the synthesis of novel water-soluble Ir sensitizers derived from **Irppy$_3$**. See text for details.

In both cases, sulfonate groups were installed at the cyclometalated ligands to make the Ir complexes water-soluble. A first version of a homoleptic sulfonated Ir complex was obtained by three-fold sulfonation of the lipophilic parent complex (Figure 19, **Irsppy** left). Two additional trianionic variants of **Irsppy** (**IrFsppy** and **IrdFsppy**), which only differed from **Irsppy** regarding the number of fluorine-substituents on the phenylpyridine ligand, were synthesized. The introduction of the additional fluorine atoms intended to tune the HOMO-LUMO gap of the water-soluble photosensitizers, in analogy to the effect that has been found for the parent neutral complexes.[112]

Apart from these three homoleptic Ir complexes, a monoanionic variant (**Ir(sCH$_2$ppy)ppy$_2$**) was developed. In this complex, a CH_2-group was installed between the sulfonate group and the phenylpyridine ligand to electronically decouple the slightly electron-withdrawing sulfonate group from the rest of the ligand. The spectroscopic and electrochemical properties of all four Ir sensitizers were investigated by steady-state and time-resolved spectroscopy as well as cyclic voltammetry.

The second part of the project aimed to employ the newly developed Ir sensitizers for the photochemical regeneration of **1,4-NADH** (Figure 20). To prevent direct reduction of **NAD$^+$** by single electron transfer from the excited state of the Ir sensitizers, Rh catalysts, which

function as hydride mediators and enable the regioselective formation of **1,4-NADH,** were employed.[223,224] Previous studies suggest that the $2e^-/H^+$ reduction, which is required for the formation of **[Cp*Rh(bpy)(H)]$^+$** from **[Cp*Rh(bpy)(H$_2$O)]$^{2+}$**, occurs in an electron transfer process from the photocatalyst to the redox mediator upon excitation with visible light and in presence of a sacrificial electron donor.[23,208]

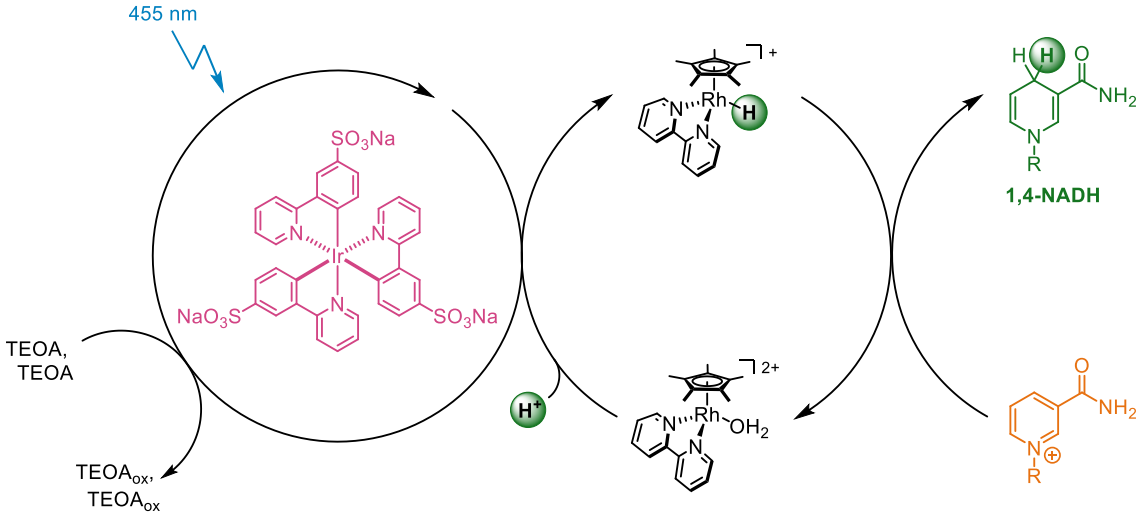

Figure 20: Simplified photocatalytic cycle for the investigated photochemical regeneration of **1,4-NADH**. For simplicity, **Irsppy** and **[Cp*Rh(bpy)(H$_2$O)]$^{2+}$** are depicted as selected examples for the employed Ir sensitizers and Rh catalysts.

Since efficient formation of **1,4-NADH** strongly depends on the interplay of the individual components in the catalytic cycle, the influence of different Ir sensitizers (with different triplet energies and excited-state oxidation potentials) and Rh catalysts on the regeneration of the nucleotide co-factor was tested. The photochemical reaction was monitored by UV-Vis and ^{1}H-NMR-spectroscopy, and luminescence-quenching and transient absorption experiments were performed to gain further insight into the reaction mechanism.

The supporting information that belongs to this research is provided in Chapter 6.2.

4.3 Results and Discussion

4.3.1 Synthesis of the Iridium Photosensitizers

Two different strategies were pursued for the synthesis of the different Ir sensitizers. The synthesis of the trianionic **Irsppy** derivatives was based on direct sulfonation of the respective **Irppy$_3$** derivatives (Figure 21, strategy A), following a procedure that had previously been developed by Prof. Dr. Xingwei Guo.[121] Since a vast variety of homoleptic **Irppy$_3$** analogs are known in the literature,[56] this strategy allows the synthesis of a broad range of water-soluble Ir sensitizers. However, this approach is limited to the synthesis of trianionic complexes, since achieving selective one- or two-fold sulfonation of the parent neutral complexes is difficult. To circumvent this selectivity issue, the synthesis of **Ir(sCH$_2$ppy)ppy$_2$** involved the complexation with ligand **sCH$_2$ppy**, in which the sulfonate group had already been installed prior to complexation (Figure 21, strategy B). This approach allows the selective formation of a monoanionic complex; however, it requires a linear four-step synthesis of the ligand (see below), rendering this strategy less modular.

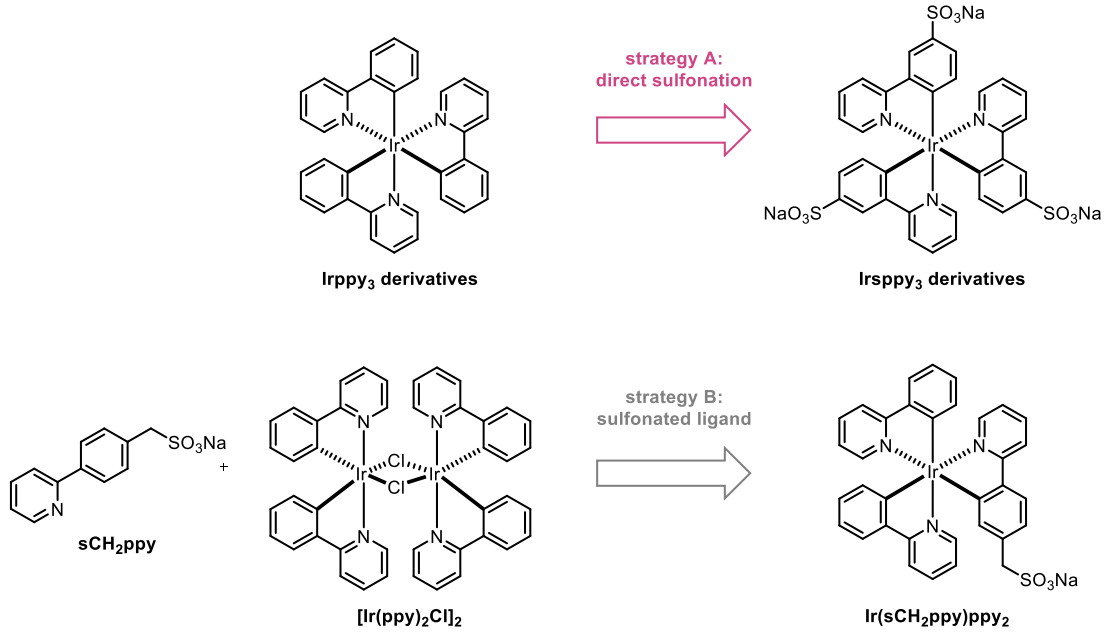

Figure 21: Different strategies for the synthesis of the Ir sensitizers: The trianionic Irsppy derivatives are synthesized via direct sulfonation of the corresponding **Irppy$_3$** derivatives (strategy A), while the synthesis of the monoanionic complex **Ir(sCH$_2$ppy)ppy$_2$** is based on the complexation with a previously sulfonated ligand (strategy B).

In order to obtain the different trianionic, homoleptic Ir complexes (**Irsppy**, **IrFsppy**, and **IrdFsppy**), the respective neutral **Irppy$_3$** analogs were first synthesized (Scheme 1). For this purpose, the two fluorinated phenylpyridine ligands were synthesized in a Suzuki-reaction from 2-bromopyridine (**1**) and the respective fluorinated phenylboronic acid (**2**). The different **Irppy$_3$** derivatives were obtained in a microwave-assisted complexation reaction,[225] starting from $IrCl_3 \cdot H_2O$ as an iridium source. This method is a superior alternative to the commonly used, purely thermal synthesis of **Irppy$_3$**,[112] which requires high reaction temperatures (> 200 °C) to obtain the thermodynamic product **Irppy$_3$**. In the

last step, the desired water-soluble Ir complexes were obtained by direct three-fold sulfonation of the parent neutral complexes. Sulfonation in *para*-position to the cyclometalated bond was achieved using bis(trifluoroacetyl)sulfate as a sulfonation agent,[121] which was prepared in situ from trifluoroacetic anhydride (TFAA) and sulfuric acid.[226] Hydrolysis of the mixed anhydrides in intermediate **3** with sat. aq. $NaHCO_3$ solution afforded the different **Irsppy** derivatives in moderate to high yields (55-88%).

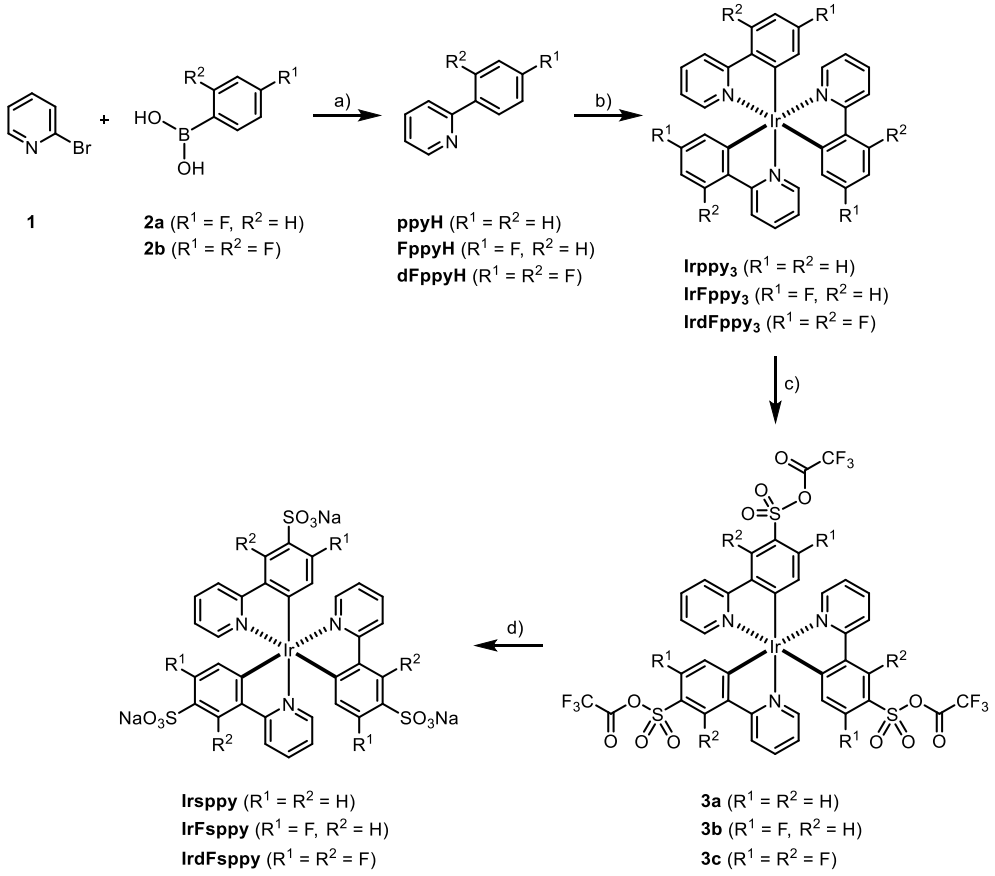

Scheme 1: Synthesis of the different **Irsppy** derivatives: a) for **FppyH**: $Pd(PPh_3)_4$, aq. Na_2CO_3 (1 M), THF, 140 °C, 3 h, 37%; for **dFppyH**: $Pd(PPh_3)_4$, aq. Na_2CO_3 (1 M), THF, microwave, 140 °C, 3 h, 62%; b) $IrCl_3 \cdot H_2O$, ethylene glycol, microwave, 200 °C, 30 min, **Irppy$_3$** = 78%, **IrFppy$_3$** = 72%, **IrdFppy$_3$** = 67%; c) H_2SO_4, TFAA, CH_2Cl_2, 0 °C → rt, overnight; d) sat. aq. $NaHCO_3$, **Irsppy** = 88%, **IrFsppy** = 69%, **IrdFsppy** = 55% (yields given for steps c-d).

As mentioned above, **Ir(sCH$_2$ppy)ppy$_2$** was synthesized based on complexation with a previously sulfonated ligand (**sCH$_2$ppy**, Scheme 2). The ligand synthesis started with a Suzuki coupling[227] of 2-bromopyridine (**1**) and (4-formylphenyl)boronic acid (**4**) affording 4-(pyridine-2-yl)benzaldehyde (**5**) in quantitative yield. The reduction of aldehyde **5** to the corresponding alcohol **6** with $NaBH_4$ and subsequent conversion to the bromide with PBr_3[228] yielded 2-(4-(bromomethyl)-phenyl)pyridine (**7**) in moderate yield (40% over two steps). Substitution of the bromide with SO_3^{2-} (from sodium sulfite) afforded **sCH$_2$ppy** in 27% yield over four steps. **Ir(sCH$_2$ppy)ppy$_2$** was obtained from the reaction of **[Ir(ppy)$_2$Cl]$_2$**[112] and the previously synthesized **sCH$_2$ppy**. AgOTf was added to enhance chloride abstraction, affording **Ir(sCH$_2$ppy)ppy$_2$** in 28% isolated yield.

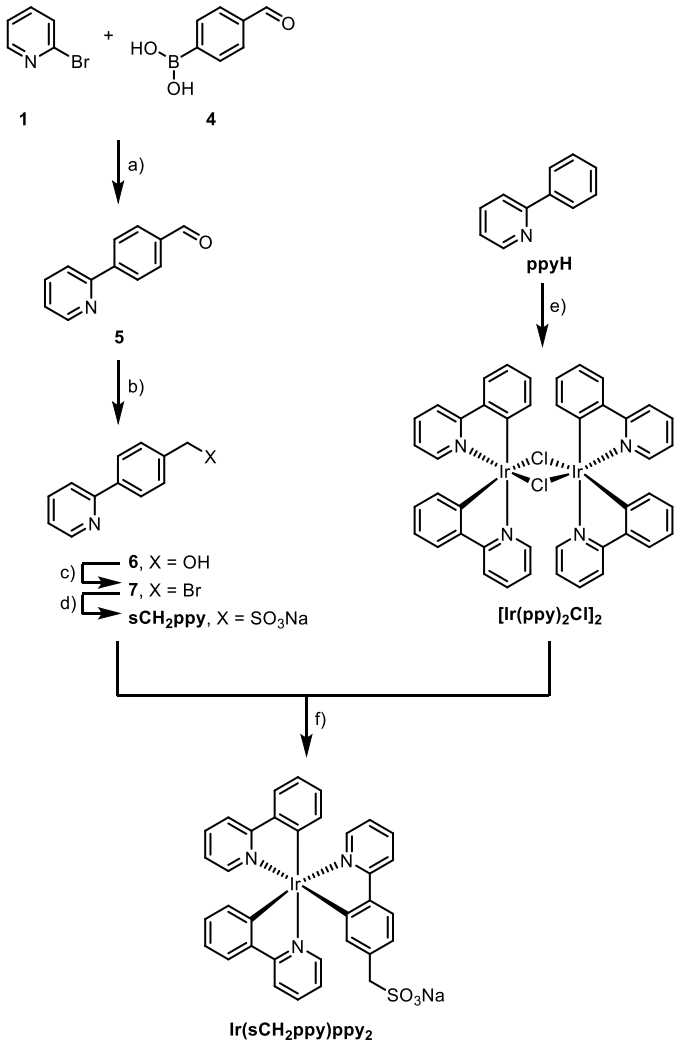

Scheme 2: Synthesis of **Ir(sCH$_2$ppy)ppy$_2$**: a) K_2CO_3, $Pd(PPh_3)_4$, 1,4-dioxane/H_2O 3:1, 100 °C, overnight, quant.; b) $NaBH_4$, EtOH, rt, 2 h, 97%; c) PBr_3, CH_2Cl_2, 0 °C → rt, 7 h, 41%; d) Na_2SO_3, H_2O/acetone 1:2, 80 °C, 40 h, 69%; e) $IrCl_3 \cdot H_2O$, 2-ethoxyethanol/H_2O 3:1, 105 °C, 62 h, 73%; f) AgOTf, 2-ethoxyethanol, 135 °C, overnight, 28%.

4.3.2 Characterization of the Iridium Photosensitizers

The first goal of this project was to obtain a series of water-soluble Ir-based complexes to sensitize challenging photochemical transformations in aqueous solutions. After the successful synthesis of the three new Ir sensitizers, their spectroscopic and electrochemical properties were investigated in collaboration with Björn Pfund and Dr. Christoph Kerzig[122] and compared to their neutral analog **Irppy$_3$**[112,114] as well as the previously characterized **Irsppy**.[121] Concerning future applications in photocatalysis, key requirements of the newly developed water-soluble Ir sensitizers are i) a sufficiently long triplet lifetime to enable bimolecular reactions and ii) either a high triplet energy to sensitize molecules via energy transfer or a strongly negative excited-state oxidation potential $^*E_{ox}$ (i.e., strong reducing power) to enable efficient electron transfer reactions. The UV-Vis and emission spectra of the different sulfonated Ir sensitizers are depicted in Figure 22. All sensitizers exhibit two absorption bands between 220 nm and 280 nm that can be attributed to π → π* transitions, in analogy to the reported **Irppy$_3$**.[112,118] While

the absorption band at 240 nm is similar for all four complexes, the absorption band at ca. 280 nm is blue-shifted when going from **Ir(sCH$_2$ppy)ppy$_2$** (285 nm) to **IrdFsppy** (267 nm). In addition to the π → π* absorption bands, all Ir sensitizers feature a broad MLCT band ranging from ca. 300 nm to 450 nm. This absorption band is blue-shifted upon increasing the number of fluorine substituents on the ligands, with $\lambda_{max,}$ ranging from 375 nm for **Ir(sCH$_2$ppy)ppy$_2$** to 330 nm for **IrdFsppy** (Table 1). For all four Ir sensitizers, significant absorption at the wavelength relevant for the photochemical regeneration of **1,4-BNAH** (455 nm) was observed. However, the extinction coefficients at 455 nm vary from 1910 M^{-1} cm^{-1} for **Ir(sCH$_2$ppy)ppy$_2$** to 230 M^{-1} cm^{-1} for **IrdFsppy** (Table 1). This lower absorbance of the fluorinated Ir sensitizers might influence their performance in further applications as possible photosensitizers.

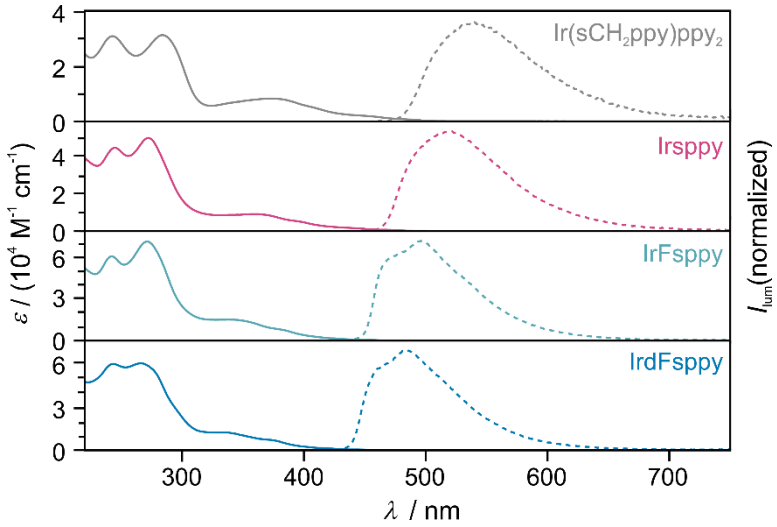

Figure 22: Absorption (solid lines) and normalized luminescence (dashed lines, obtained upon excitation at 400 nm) spectra of the different Ir sensitizers ($2.0 \cdot 10^{-5}$ M) obtained in aq. NaOH solution (50 mM) at room temperature.

All four Ir sensitizers are intensely luminescent. In analogy to the absorption bands, the maxima of the emission bands are blue-shifted upon increasing fluorination (λ_{max} is 540 nm for **Ir(sCH$_2$ppy)ppy$_2$** *vs* 484 nm for **IrdFsppy**). This hypsochromic shift (upon increasing fluorination) has been previously observed for the parent neutral **Irppy$_3$** derivatives.[112] This effect arises due to the electron-withdrawing effect of the fluorine substituents, resulting in the stabilization of the metal- and phenyl-based HOMO compared to the LUMO.[229] This strategy is often exploited for tuning the emission color of luminescent complexes.[56]

The increased stabilization of the HOMO with increasingly electron-withdrawing ligands is directly reflected in the triplet energies (E_T) of the investigated complexes. E_T values were estimated from the blue-edge of the emission band ($\lambda_{10\%}$), where the emission intensity accounts for 10% of the maximal emission intensity (λ_{max}). While **Ir(sCH$_2$ppy)ppy$_2$** has an estimated triplet energy of 2.50 eV, which is identical to its neutral analog **Irppy$_3$**, the triplet energy of **Irsppy** is increased to 2.65 eV (Table 1). A further increase in E_T is observed upon fluorination of the ppy ligands (2.76 eV for **IrFsppy**, 2.81 eV for **IrdFsppy**).

The luminescence quantum yields Φ of the three newly synthesized Ir sensitizers were determined with respect to **Irsppy**.[121] The resulting quantum yields of **IrdFsppy** (0.84) and **IrFsppy** (0.91) are slightly higher in comparison to **Irsppy** (0.73), while the quantum yield of **Ir(sCH$_2$ppy)ppy$_2$** is significantly lower (0.13).

The triplet lifetimes τ_0 of the different Ir sensitizers were determined based on luminescence-decay kinetics. The obtained triplet-excited state lifetimes of the sensitizers vary from ca. 1600 ns to 2200 ns (Table 1) and are thus sufficiently long to enable bimolecular reactions. **IrFsppy** (2165 ns) and **IrdFsppy** (2110 ns) possess slightly longer triplet lifetimes compared to **Irsppy** (1625 ns) and **Ir(sCH$_2$ppy)ppy$_2$** (1560 ns). This increased lifetime might be beneficial for further applications in photocatalysis.

Cyclic voltammograms of the different Ir sensitizers show one reversible oxidation wave for all four Ir sensitizers, with ground-state oxidation potentials E^0_{ox} ranging from +0.56 V *vs* SCE for **Ir(sCH$_2$ppy)ppy$_2$** to +1.05 V *vs* SCE for **IrdFsppy** (Table 1). A shift to more positive ground-state oxidation potentials is observed with increasingly electron-withdrawing ligand substitution (Figure 23), reflecting the reduced electron density on the metal center. Hence, the predominant metal-based HOMO of the Ir sensitizers is stabilized upon increasing fluorination of the ligands. This observation is in agreement with the previously observed blue-shift of the emission band.

The excited-state oxidation potential E^*_{ox} was estimated from the ground-state oxidation potential E^0_{ox} and the triplet energy E_T of the different sensitizers according to the simplified Rehm-Weller equation (eq. 3), with e being the elementary charge.

$$E^*_{ox} = E^0_{ox} - E_T / e \qquad (3)$$

Ir(sCH$_2$ppy)ppy$_2$ was found to be slightly more reducing (E^*_{ox} = –1.94 V *vs* SCE) than the previously characterized **Irsppy** (E^*_{ox} = –1.89 V *vs* SCE). In contrast, the excited states of **IrFsppy** (E^*_{ox} = –1.85 V *vs* SCE) and **IrdFsppy** (E^*_{ox} = –1.76 V *vs* SCE) are slightly less reducing.

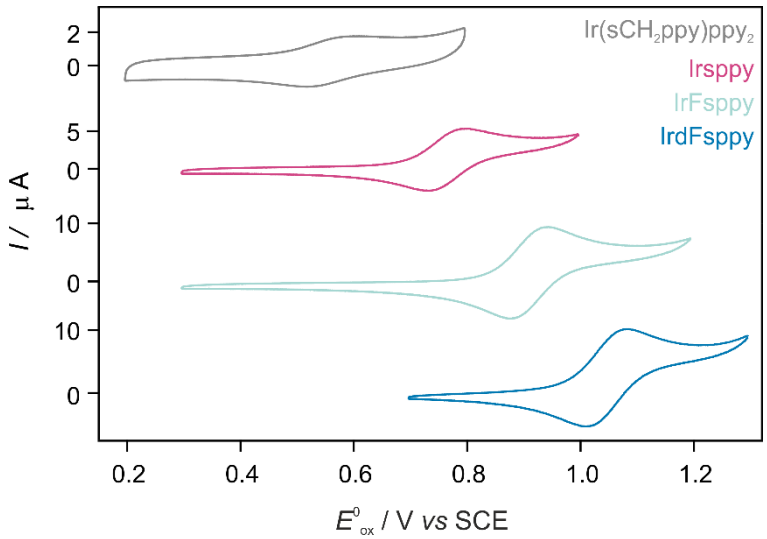

Figure 23: Cyclic voltammograms of 1.0 mM **Ir(sCH$_2$ppy)ppy$_2$** (grey trace), 1.0 mM **Irsppy** (pink trace), 1.0 mM **IrFsppy** (turquoise trace) and 1.0 mM **IrdFsppy** (blue trace) obtained in aq. phosphate buffer (0.1 M, pH 7) with a scan rate of 0.1 V/s.

The spectroscopic and electrochemical properties of the different Ir sensitizers are summarized in Table 1. All four Ir sensitizers have sufficiently long excited-state lifetimes (1.6 – 2.2 µs) for efficient bimolecular reactions. In analogy to their parent neutral complexes,[112] all sulfonated Ir sensitizers were found to be strong photoreductants with excited-state oxidation potentials ranging from –1.74 V *vs* SCE to –1.94 V *vs* SCE. Introduction of fluorine substituents on the phenyl-moiety of the ligand resulted in an increase in triplet energy. This effect is a consequence of the stabilization of the HOMO, which is mainly localized on the metal and the phenyl moieties. Thus, the newly developed water-soluble sensitizers can both be used as strong photoreductants or as energy transfer catalysts for future applications in sustainable photocatalysis in aqueous solutions.

Table 1: Summary of spectroscopic and electrochemical properties of the different Ir sensitizers relevant for this study.

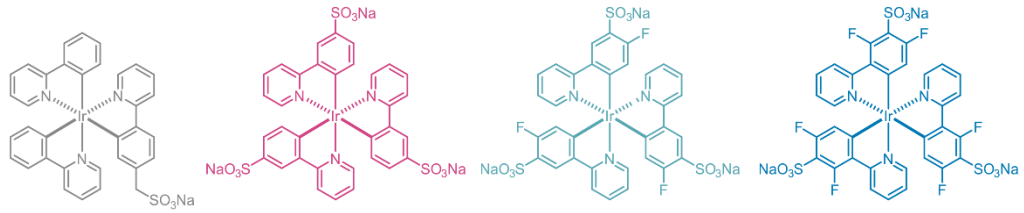

	Absorption[a]		Emission[a]				Electrochemistry	
	λ_{max}[c]	$\varepsilon_{455\ nm}$[d]	λ_{max}[e]	τ_0[f]	Φ[g]	E_T[h]	E^0_{ox}[i]	E^*_{ox}[j]
	/ nm	/ M^{-1} cm^{-1}	/ nm	/ ns		/ eV	/ V *vs* SCE	/ V *vs* SCE
Irppy$_3$[b,112,114]	375	2800	510	1900	0.38	2.50	+0.77	–1.73
Ir(sCH$_2$ppy)ppy$_2$	374	1910	540	1560	0.13	2.50	+0.56	–1.94
Irsppy[121]	360	890	522	1625	0.73	2.65	+0.76	–1.89
IrFsppy	338	500	496	2165	0.91	2.76	+0.91	–1.85
IrdFsppy	330	230	484	2110	0.84	2.81	+1.05	–1.76

[a] All spectroscopic data were obtained in deaerated aq. NaOH solutions (50 mM) at room temperature.
[b] Spectroscopic and electrochemical data for **Irppy$_3$** in acetonitrile and at room temperate. Data was obtained from the literature.
[c] Maxima of the MLCT absorption band of the different Ir sensitizers obtained in aq. NaOH solution (50 mM).
[d] Extinction coefficients of the Ir sensitizers at the wavelength relevant for the photochemical regeneration of **1,4-BNAH**.
[e] Maxima of the ^{3}MLCT emission band obtained after excitation of the Ir sensitizers at 400 nm in aq. NaOH solution (50 mM) at room temperature.
[f] Natural lifetimes of the triplet-excited Ir sensitizers determined based on luminescence decay kinetics measured in aq. NaOH solution (50 mM). Luminescence-decay was detected at 510 nm upon excitation at 420 nm.
[g] Luminescence quantum yields of the ^{3}MLCT emission determined at 400 nm with respect to **Irsppy**[121] as a reference.
[h] Energy of the emissive triplet state estimated from the short-wavelength edge ($\lambda_{10\%}$) of the luminescence spectrum.
[i] Ground-state oxidation potential of the Ir sensitizers determined by cyclic voltammetry in aq. phosphate buffer (0.1 M, pH 7) at a scan rate of 0.1 V/s.
[j] Excited-state oxidation potential of the Ir sensitizers estimated from the ground-state oxidation potential E_{ox}^0 and the triplet energy E_T of the Ir sensitizers based on $E^*_{ox} = E^0_{ox} - E_T/e$.

4.3.3 Photochemical Regeneration of 1,4-BNAH

After the different Ir sensitizers had been synthesized and characterized, we attempted to use the newly developed water-soluble Ir sensitizers for the photochemical regeneration of **1,4-NADH**. Moreover, three different Rh catalysts were synthesized and investigated for the photochemical formation of the nucleotide co-factor. The three catalysts differed regarding their *N*,*N*'-chelate ligand and are known to enable the regioselective reduction of **NAD$^+$** in presence of the chemical reductant formate.[185] For our initial studies we focused on the photochemical formation of 1-benzyl-1,4-dihydronicotinamide (**1,4-BNAH**), a commonly used model system for **1,4-NADH**.[190,196,230,231] In analogy to **NAD$^+$**, 1-benzyl-3-carbamoylpyridin-1-ium chloride (**BNACl**) possesses a pyridinium core structure; however, it differs from the nucleotide co-factor in its *N*-substituent (Figure 24 on the right).

A simplified picture of the investigated catalytic cycle for the photochemical formation of **1,4-BNAH** is depicted in Figure 24. After excitation of the Ir sensitizer with visible light, the Rh(III) aqua complex (**[Cp*Rh(bpy)(H$_2$O)]$^{2+}$**), which is formed upon ligand exchange from the Rh(III) chloro species in aqueous solutions,[217] is transformed into the corresponding Rh(III) hydride (**[Cp*Rh(bpy)(H)]$^+$**) upon two-fold reduction in the presence of a proton source.[197] Regioselective hydride transfer from the Rh(III) hydride to **BNA$^+$** is known to afford **1,4-BNAH** as the major regioisomer.[199]

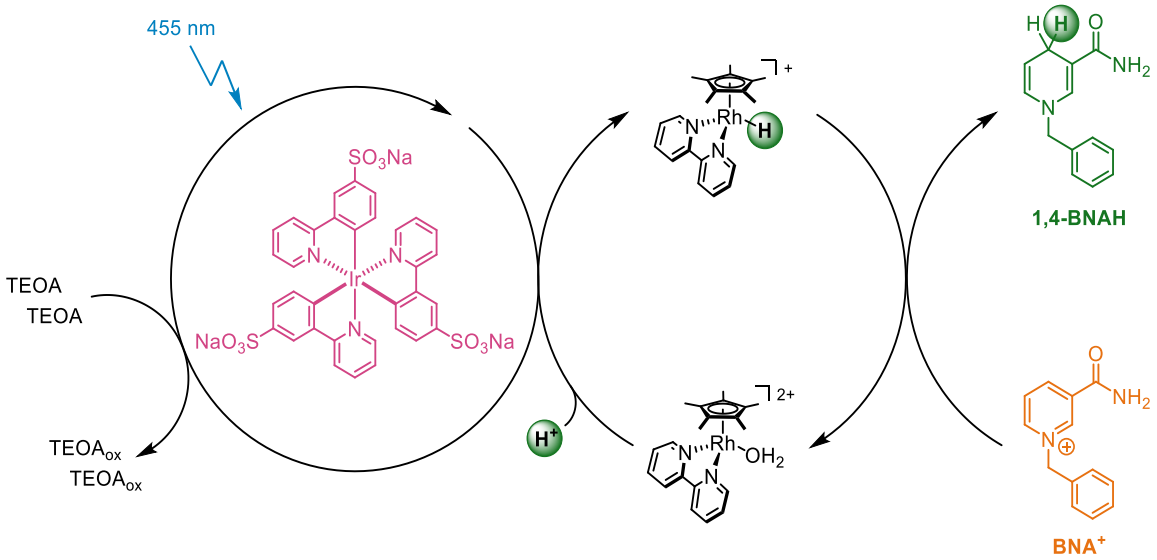

Figure 24: Simplified catalytic cycle for the photochemical regeneration of **1,4-BNAH**. For simplicity, **Irsppy** and **[Cp*Rh(bpy)(H$_2$O)]$^{2+}$** are depicted as representative examples for the different catalysts. See text for details.

UV-Vis Experiments

The investigation of the new photosystem for the photochemical formation of **1,4-BNAH** started with UV-Vis spectrometric monitoring of the reaction progress. This method exploits the different absorption characteristics of the substrate and the product. While both **BNACl** and **1,4-BNAH** show an absorption band below 300 nm, **1,4-BNAH** has a second absorption feature ranging from ca. 320 nm to 420 nm (Figure 25, inset). Hence, the photochemical formation of **1,4-BNAH** can be monitored based on this characteristic absorption band with a maximum at 358 nm.

In an initial experiment, **Irsppy** was tested as a photosensitizer in combination with **[Cp*Rh(bpy)Cl]Cl** as a Rh precursor. The sacrificial electron donor, TEOA, was used in large excess to prevent re-oxidation of **1,4-BNAH** to **BNA$^+$**. To further diminish re-oxidation to **BNA$^+$**, a 455 nm collimated LED was chosen as an irradiation source, because all investigated Ir sensitizers show sufficient absorption at 455 nm (Table 1), while **1,4-BNAH** does not absorb at this wavelength. After irradiation of the reaction mixture at 455 nm, significant formation of **1,4-BNAH** was observed already after 30 minutes as indicated by the characteristic absorption band arising at 358 nm (Figure 25, main plot). Based on the extinction coefficient of **1,4-BNAH** (ε_{358} = 5070 M^{-1} cm^{-1}, see SI section S3.3 for details) the yield of **1,4-BNAH** was determined to be 46% after an irradiation time of 150 minutes.

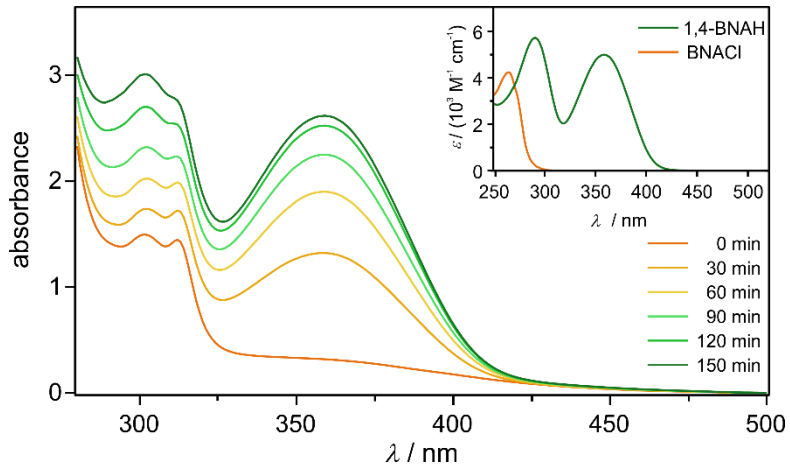

Figure 25: UV-Vis spectra of the visible-light driven **1,4-BNAH** regeneration: The main plot shows the change in absorbance after irradiation of a reaction mixture consisting of **BNACl** (1.0 mM), **Irsppy** (10 µM), **[Cp*Rh(bpy)Cl]Cl** (0.1 mM), and TEOA (0.5 M) in deaerated phosphate buffer (0.1 M, pH 7) at 455 nm at different time points. The inset shows the calibrated absorption spectra of **BNACl** (orange trace) and **1,4-BNAH** (green trace) in deaerated phosphate buffer (0.1 M, pH 7).

When the reaction was performed in the dark, no conversion of **BNACl** was observed, confirming that the formation of **1,4-BNAH** is a light-dependent reaction (Table 2). In the absence of a photosensitizer, only minor amounts (3.5%) of **BNACl** were converted to **1,4-BNAH**, confirming that sensitization via Ir sensitizer is indeed needed for efficient photochemical formation of **1,4-BNAH**.

Table 2: Control reactions for the photochemical regeneration of **1,4-BNAH**.

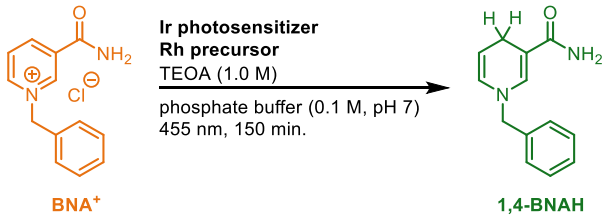

entry[a]	Ir photosensitizer	Rh precursor	Yield of 1,4-BNAH[b] / %
1	**Irsppy**	**[Cp*Rh(bpy)Cl]Cl**	46
2[c]	**Irsppy**	**[Cp*Rh(bpy)Cl]Cl**	0
3	-	**[Cp*Rh(bpy)Cl]Cl**	3.5[d]

[a] A reaction mixture containing **BNACl** (1.0 mM), **Irsppy** (0 or 10 µM), **[Cp*Rh(bpy)Cl]Cl** (0.1 mM), and TEOA (0.1 M) in deaerated aq. phosphate buffer (0.1 M, pH 7) was irradiated at 455 nm for 150 min.
[b] Yield of **1,4-BNAH** formation was determined based on the characteristic absorption band arising at 358 nm (ε_{358} = 5070 M^{-1} cm^{-1}).
[c] The reaction mixture was kept in the dark.
[d] Determined after 160 min.

Since hydride transfer via a Rh catalyst is crucial for the regioselective formation of **1,4-BNAH**, two additional Rh precursors were tested for the photochemical reduction of **BNA⁺**. Previous chemical,[185] electrochemical[191,203] and photochemical regeneration systems[50] suggest that the chelating ligand influences both the selectivity and the reactivity of the Rh catalyst. In both experiments, **Irsppy** was used as a photosensitizer and the reaction progress was monitored by UV-Vis spectrometry. When using **[Cp*Rh(phen)Cl]Cl** (phen = 1,10-phenanthroline) instead of **[Cp*Rh(bpy)Cl]Cl**, a slightly lower yield of **1,4-BNAH** was observed (42% *vs* 46%, Figure 26). This is in agreement with the literature, where the catalytic activity of the Rh catalyst was found to decrease in the order bpy > phen in the transfer hydrogenation of **NAD⁺** in the presence of formate as a hydride source.[185]

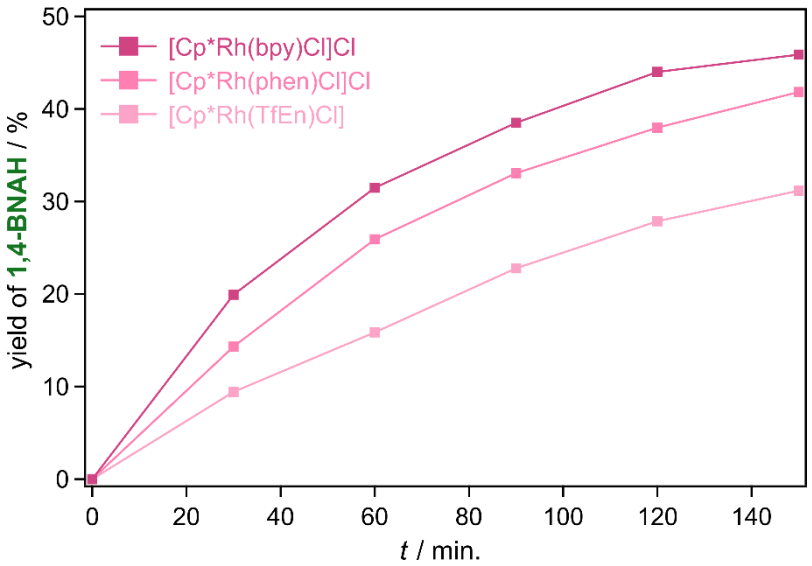

Figure 26: Visible-light driven **1,4-BNAH** regeneration: The different yields were determined by monitoring the formation of **1,4-BNAH** (characteristic absorption band at λ_{max} = 358 nm) by UV-Vis spectroscopy. Irradiation of a mixture consisting of **BNACl** (1.0 mM), **Irsppy** (10 µM), Rh derivative (0.1 mM), and TEOA (0.5 M) in deaerated aq. phosphate buffer (0.1 M, pH 7) at 455 nm.

When using **[Cp*Rh(TfEn)Cl]** (TfEn = *N*-(2-aminoethyl)-4-(trifluoromethyl)benzene-sulfonamide) as a catalyst, the formation of a new absorption band was less pronounced, and the newly formed absorption band was broader compared to the previously studied systems (see SI Figure S4). This different behavior suggests that additional isomers other than the 1,4-dihydropyridine or the BNA-dimers might have been formed upon photochemical reduction of **BNA$^+$**. Since discrimination between the different regioisomers and the BNA-dimers by UV-Vis spectroscopy is difficult,[196] further analysis by ^{1}H-NMR spectroscopy is needed to gain further insight into the reaction progress (see below). Since **[Cp*Rh(bpy)Cl]Cl** performed best out of all three Rh precursors, it was used as a Rh catalyst in all subsequent experiments.

Next, the influence of the different photosensitizers on the photochemical reduction of **BNA$^+$** was tested. For all three tested Ir sensitizers, formation of **1,4-BNAH** was observed when irradiating the reaction mixture at 455 nm (Figure 27). An increase in **1,4-BNAH** formation was observed in the order **Irsppy** < **IrFsppy** < **IrdFsppy** (from 46% for **Irsppy** to 64% for **IrdFsppy**, Table S1). This finding is in conflict with an electron transfer from the Ir sensitizer to the Rh catalyst since **Irsppy** has the most negative excited-state oxidation potential (E^*_{ox} = –1.89 V *vs* SCE, Table 1) and thus would be expected to give the highest yield of **1,4-BNAH** out of the three employed Ir sensitizers. Considering that **IrdFsppy** possesses the lowest extinction coefficient at 455 nm (ε_{455} = 232 M^{-1} cm^{-1}, Table 1), the different reactivities would be even more pronounced when using solutions with equal absorption properties of the Ir sensitizers. Since the formation of **1,4-BNAH** seems not to be governed by the electron transfer rate as was proposed in previous studies,[50,51] further mechanistic investigations are needed to analyze this finding in detail (see section 4.3.4).

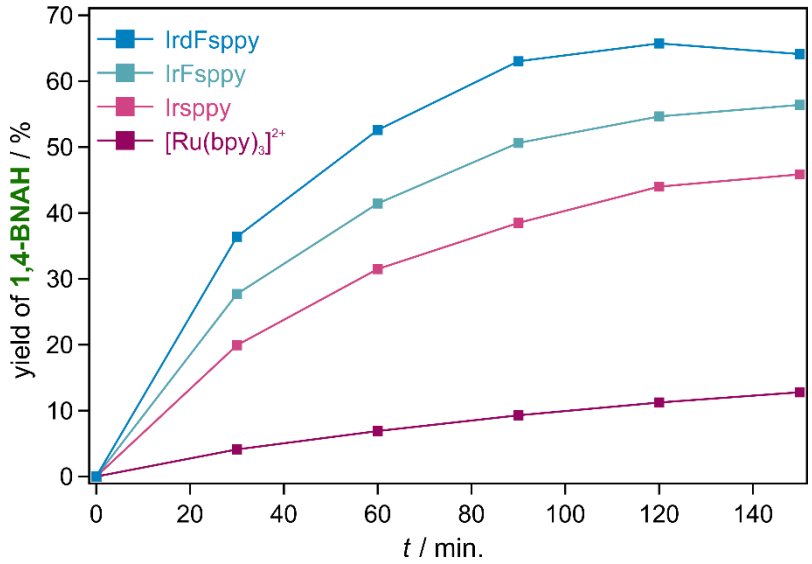

Figure 27: Visible-light driven **1,4-BNAH** regeneration: The different yields were determined by monitoring the formation of **1,4-BNAH** (characteristic absorption band at λ_{max} = 358 nm) by UV-Vis spectroscopy. Irradiation of a mixture consisting of **BNACl** (1.0 mM), photocatalyst (10 µM), **[Cp*Rh(bpy)Cl]Cl** (0.1 mM), and TEOA (0.5 M) in aq. deaerated phosphate buffer (0.1 M, pH 7) at 455 nm.

The efficiency of the newly developed Ir sensitizers was also compared to the well-known photosensitizer **[Ru(bpy)$_3$]$^{2+}$** and all three Ir sensitizers were found to outperform **[Ru(bpy)$_3$]$^{2+}$** in the photochemical formation of **1,4-BNAH** (Figure 27). When comparing the initial turnover frequencies (i.e, the amount of catalytic cycles the sensitizer performs within the first 30 minutes of irradiation), **IrdFsspy** was found to outcompete **[Ru(bpy)$_3$]$^{2+}$** by almost one order of magnitude (the initial TOF was 146 h^{-1} for **IrdFsppy** and 16 h^{-1} for **[Ru(bpy)$_3$]$^{2+}$**, see SI Table S1). The higher conversion of the sulfonated Ir sensitizers compared to **[Ru(bpy)$_3$]$^{2+}$** is not surprising since the investigated Ir sensitizers are both more reducing and have a higher triplet energy compared to **[Ru(bpy)$_3$]$^{2+}$**, making them more efficient catalysts for the photoreduction of **BNA$^+$**. Furthermore, the attractive Coulombic interactions between the trianionic photosensitizers and the dicationic Rh(III) aqua complex (**[Cp*Rh(bpy)(H$_2$O)]$^{2+}$**) might enable a faster quenching of the Ir excited state. These attractive interactions between the photosensitizer and the Rh catalyst are known to be beneficial for the efficient regeneration of nucleotide co-factors.[23,51] In contrast, repulsive Coulombic interactions between the Ru sensitizer and the Rh catalyst diminish efficient formation of **1,4-BNAH**.[50]

When **IrdFsppy** was used as a photosensitizer, a maximal yield of **1,4-BNAH** formation was observed after an irradiation time of 120 minutes (Figure 27). After that time, a slight decrease of the characteristic absorption band at 358 nm was observed. This finding can be attributed to the limited stability of **1,4-BNAH** in water since its natural analog **1,4-NADH** is known to decompose under neutral and acidic conditions at ambient temperatures.[232] Also, **1,4-BNAH** is known to be a potent sacrificial electron donor itself,[117] so that re-oxidation to **BNA$^+$** by quenching of the excited photosensitizer is plausible. Since the development of this photosystem aims at further applications in photobiocatalysis, in which the nucleotide co-factor would be readily consumed in the enzymatic dark reaction, no further optimization of the reaction conditions to increase the stability of **1,4-BNAH** was performed at this stage of the project.

NMR Experiments

The analysis of the regioselective reduction of **BNA$^+$** to **1,4-BNAH** based exclusively on UV-Vis spectrometry is problematic since the other regioisomers and NAD dimers, which are formed upon single electron reduction of **NAD$^+$**, have similar absorption characteristics as the desired 1,4-regioisomer.[196] Thus, an NMR-experiment was designed to confirm the regioselectivity of the photocatalytic reaction. A solution containing **BNACl** (10 mM), the Rh catalyst (1.0 mM), the Ir sensitizer (0.1 mM), and TEOA (1.0 M) was irradiated at 455 nm for 6 hours. To limit deuterium incorporation,[200] a 1:1 mixture of CD_3CN and non-deuterated phosphate buffer (0.1 M, pH 7) was used as a solvent. When irradiating the reaction mixture at 455 nm, the characteristic peaks of

BNACl decreased, while the formation of new peaks was observed that can be attributed to **1,4-BNAH** (Figure 28).

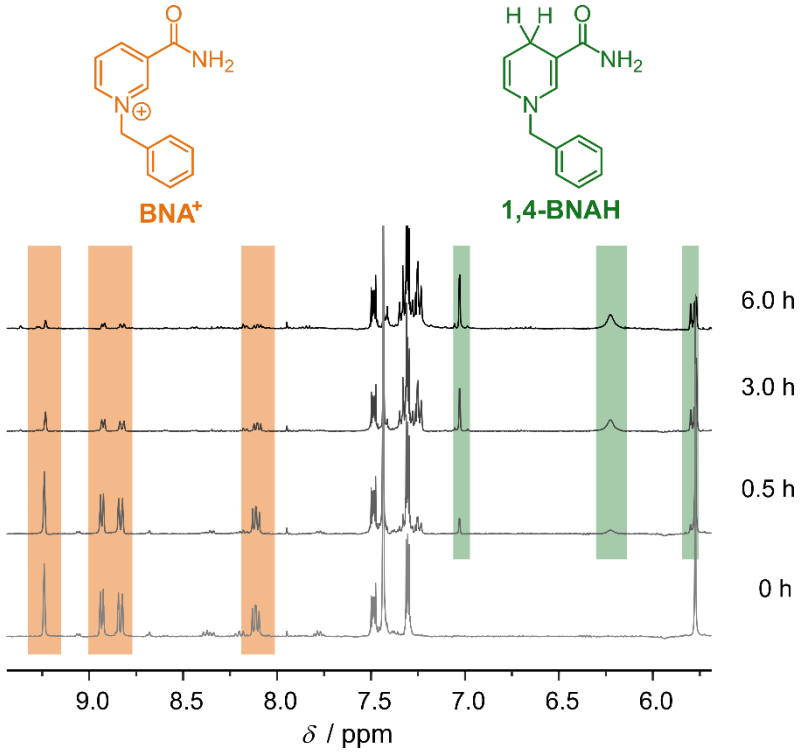

Figure 28: ^{1}H-NMR spectra of the visible-light driven **1,4-BNAH** regeneration obtained after irradiation of a reaction mixture consisting of **BNACl** (10 mM), **Irsppy** (0.1 mM), **[Cp*Rh(bpy)Cl]Cl** (1.0 mM), and TEOA (1.0 M) in a 1:1 mixture of deaerated phosphate buffer (0.1 M, pH 7) and CD_3CN at 455 nm at different time points. The characteristic signals of **BNA$^+$** (orange background) disappear, while formation of **1,4-BNAH** (green background) is observable.

When using **Irsppy** as a sensitizer and **[Cp*Rh(bpy)(H)]$^+$** as a hydride mediator, **1,4-BNAH** was found to be the only regioisomer being formed in 82% yield after 6 hours. Also, when using one of the fluorinated Ir sensitizers as a photocatalyst or **[Cp*Rh(phen)(H)]$^+$** as a hydride mediator, a comparable yield of **1,4-BNAH** was observed (between 82% and 86%, see SI Table S2). When the Rh(III) precursor was changed to **[Cp*Rh(TfEn)Cl]**, formation of **1,4-BNAH** was observed only in minor amounts (6%). The absence of newly formed signals suggests that an insoluble product is formed instead. This finding indicates that **Irsppy** fails to sensitize the Rh catalyst and direct SET from **Irsppy** to **BNA$^+$** takes place instead, leading to the formation of insoluble NAD-dimers.[233] Furthermore, it demonstrates that UV-Vis experiments alone are not sufficient to monitor regiospecific reduction of **BNA$^+$** due to the similar absorption characteristics of the different possible isomers and side products.[196]

4.3.4 Mechanistic Studies

After the photochemical formation of **1,4-BNAH** was confirmed by ^{1}H-NMR-spectroscopy, further mechanistic studies were performed to obtain an insight into the reaction mechanism. Since the interplay between the photosensitizer and the Rh catalyst is known to be crucial for efficient **BNA$^+$** reduction,[50,208] mechanistic studies focused on gaining further insight into this specific interaction. Three different mechanisms are, in theory,

possible for the photochemical regeneration of **1,4-BNAH** (Figure 29A-C): i) the triplet-excited state of the Ir sensitizers is reductively quenched by TEOA, ii) the triplet-excited state of the Ir sensitizers is oxidatively quenched by the Rh-catalyst or iii) a ttEnT mechanism is at play and the Ir sensitizer does only interact with the Rh catalyst and not with the sacrificial donor, as was previously proposed in Figure 20.

Even though the exact excited-state reduction potentials of the Ir sensitizers are unknown, reductive quenching of their excited state by TEOA seems thermodynamically unlikely considering that electron transfer from TEOA (E^0_{ox} = +0.76 V vs SCE)[217] to the neutral analog **Irppy$_3$** (E^*_{red} = +0.31 V vs SCE)[61] is endergonic ($\Delta G_{ET,1}$ = +0.45 eV). Indeed, when quenching experiments were performed with the different Ir sensitizers in presence of TEOA (Figure 29D), reductive excited-state quenching with TEOA was found to be inefficient (η up to 4.9% with **IrdFsppy**, Table 3). In contrast, efficient quenching of the triplet-excited Ir sensitizers with **[Cp*Rh(bpy)Cl]Cl** was observed (η up to 83% with **IrdFsppy**, Figure 29E). This implies that reductive quenching of the triplet-excited state of the Ir complexes with TEOA only plays a minor role in the reaction mechanism (Figure 29A), whereas excited-state quenching with **[Cp*Rh(bpy)Cl]Cl** represents the primary reaction pathway (Figure 29B or C).

When probing the photochemical formation of **1,4-BNAH** with the different Ir sensitizers, it was found that the yields of **1,4-BNAH** formation decrease in the order **IrdFsppy** > **IrFsppy** > **Irsppy** (Figure 27). This finding conflicts with an electron transfer from the triplet-excited state of the Ir sensitizer to the Rh catalyst (Figure 29B), as the excited-state oxidation potential is shifted to less negative potentials (less reducing) when going from **Irsppy** to **IrdFsppy** (Table 1). Thus, the driving force of the electron transfer from the respective Ir complex to **BNA$^+$** is highest for **Irsppy** ($\Delta G_{ET,3}$ = –1.15 eV, see SI section S4.1) and a more efficient formation of **1,4-BNAH** would be expected when using **Irsppy**.

One possible explanation for this counterintuitive finding is that the re-reduction of **IrdFsppy$^+$** is more favored ($\Delta G_{ET,4}$ = –0.29 eV, see SI section S4.1) than re-reduction of **Irsppy$^+$** ($\Delta G_{ET,4} \approx 0$ eV). The more efficient regeneration of the ground state is beneficial for the turnover frequency of the catalyst and might be the reason for the higher yield of **1,4-BNAH** when using **IrdFsppy** as a catalyst.

A different explanation for the observed reactivities can be found when comparing the triplet energies of the employed Ir sensitizers. The observed reactivities of the Ir sensitizers in the photochemical formation of **1,4-BNAH** correlate with the triplet energies of the Ir sensitizers (Table 1). Thus, it seems plausible that the photochemical formation of **1,4-BNAH** proceeds via energy transfer from the excited state of the Ir sensitizer to the Rh catalyst (Figure 29C). The exact triplet energy of **[Cp*Rh(bpy)(H$_2$O)]$^{2+}$** is unknown; however, the triplet energy of a related complex ($[Rh(NH_3)_6]^{3+}$) is 2.51 eV,[234] suggesting that triplet-triplet energy transfer from the three investigated Ir sensitizers to the Rh catalyst is feasible.

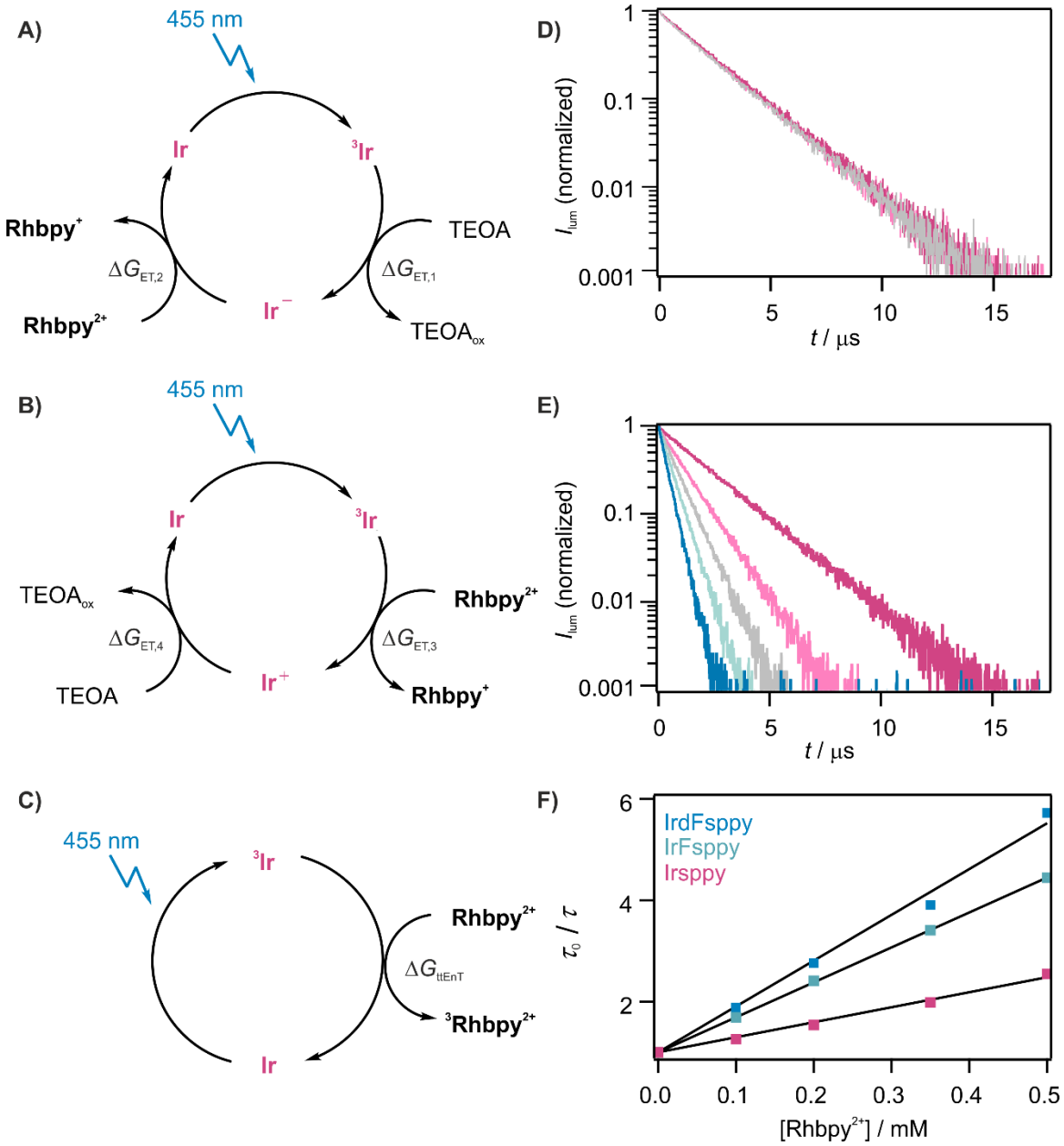

Figure 29: Three types of interactions between the Ir sensitizer and the Rh catalyst are theoretically possible (A-C). For simplicity the Ir catalysts are abbreviated as **Ir** and **[Cp*Rh(bpy)(H₂O)]²⁺** (abbreviated as **Rhbpy²⁺**) is depicted as representative example for the different Rh catalysts. See text for details. D, E) Time-resolved luminescence-quenching experiments of **IrdFsppy** (30 µM) at varying concentrations of D) TEOA or E) **[Cp*Rh(bpy)Cl]Cl**. Measurements were performed using the TCSPC technique in deaerated Tris-buffer (0.1 M, pH 8.8) at 20 °C. Excitation occurred at 405 nm and the luminescence was detected at 500 nm. All decays were normalized to 1.0 at t = 0. F) Stern-Volmer plots obtained from kinetic emission measurements for **Irsppy** (pink data points), **IrFsppy** (turquoise data points) and **IrdFsppy** (blue data points).

To further differentiate between the two mechanisms, the Stern-Volmer constants K_{sv} and the quenching rate constants k_q were determined for all three sensitizers in presence of different concentrations of **[Cp*Rh(bpy)Cl]⁺** (Figure 29C). Excited-state quenching was found to be fast, with rate constants close to the diffusion limit (Table 3, k_{diff} = 6.5·10^9 M^{-1} s^{-1} at 20 °C in water[235]). The quenching rate was found to increase in the order **Irsppy** < **IrFsppy** < **IrdFsppy**, which correlates with the triplet energies of the Ir sensitizers

but opposes the trend observed for the excited-state oxidation potentials (Table 1). Thus, the quenching experiments suggest that excited-state quenching of the Ir sensitizers proceeds via energy transfer from the Ir sensitizer to the Rh catalyst rather than via electron transfer.

Table 3: Stern-Volmer constants (K_{SV}), quenching rate constants (k_q), and quenching efficiencies (η) obtained from quenching experiments with the different Ir sensitizers.

	K_{SV}[a,b] / M^{-1}	k_q[a,b] / 10^9 M^{-1} s^{-1}	η (**[Cp*Rh(bpy)Cl]Cl**)[a,c] / %	η (*TEOA*)[a] / %
Irsppy	2960	2.9	61	n.d.
IrFsppy	6900	3.3	77	0.6
IrdFsppy	9040	4.4	83	4.9

[a] Determined by time-resolved luminescence spectroscopy using the TCSPC technique with solutions containing the Ir sensitizers (30 µM) and either **[Cp*Rh(bpy)Cl]Cl** (0 mM to 50 mM) or TEOA (0 M to 0.5 M) in deaerated Tris-buffer (0.1 M, pH 8.8) at 20 °C.

[b] Determined from Stern-Volmer analysis for the quenching of the excited Ir sensitizer with **[Cp*Rh(bpy)Cl]Cl**. K_{SV} is obtained from the linear fit when plotting τ_0/τ against different concentrations of **[Cp*Rh(bpy)Cl]Cl**. The quenching rate constant k_q is defined as $k_q = K_{SV}/\tau_0$.

[c] The quenching efficiency η was determined based on $\eta=(\tau_0-\tau)/\tau_0$. The quenching efficiency of **[Cp*Rh(bpy)Cl]Cl**) was determined for a solution containing 0.5 mM **[Cp*Rh(bpy)Cl]Cl** and η (TEOA) was determined for a solution containing 0.5 M TEOA.

To further confirm this hypothesis, time-gated transient absorption spectra of a solution containing **Irsppy** (100 µM) and **[Cp*Rh(bpy)Cl]Cl** (2.0 mM) were recorded (Figure 28A). At this Rh concentration, efficient quenching (90%) of the triplet-excited state of **Irsppy** is expected. If an electron-transfer mechanism were at play, one would expect to see a broad, featureless absorption signal with a maximum at 600 nm, arising from the **Irsppy**$^+$ cation (Figure 30C). However, only depletion of the negative signal at around 510 nm, which can be attributed to ^{3}**Irsppy** emission (Figure 30B),[65] was observed. The absence of the absorption feature at 600 nm therefore points towards a triplet-triplet energy transfer mechanism. Since the triplet-excited Rh catalyst has a low extinction coefficient and is lacking any characteristic spectroscopic signature,[217] the absence of a newly formed signal is in good agreement with excited-state quenching via energy transfer. The transient absorption spectra that were obtained of the two fluorinated Ir sensitizers (100 µM) in presence of **[Cp*Rh(bpy)Cl]Cl** (1.0 mM) also lack of a new characteristic absorption signal (SI section S4.2), indicating that the same reaction mechanism is operating for all three Ir sensitizers.

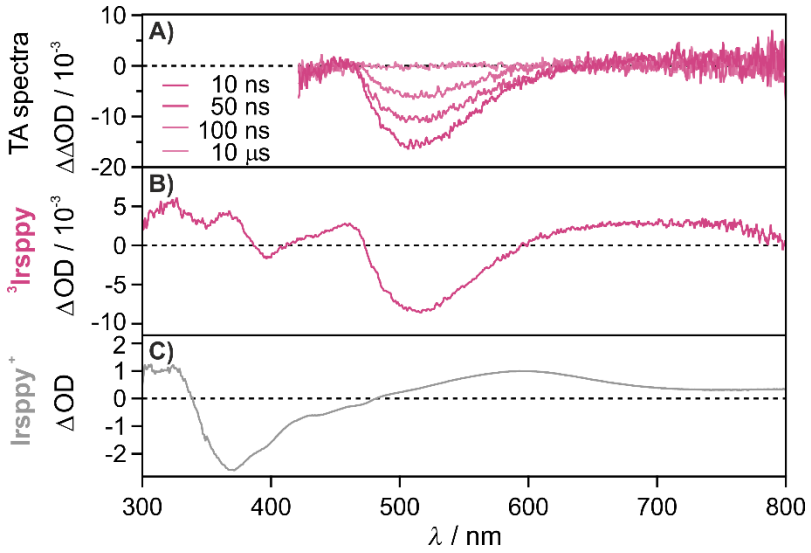

Figure 30: A) Transient absorption spectra of a solution containing **Irsppy** (100 µM) and **[Cp*Rh(bpy)Cl]Cl** (2.0 mM) in deaerated phosphate buffer (0.1 M, pH 7). The spectra were measured at different time delays after excitation at 420 nm (7 mJ) and were time-integrated over 50 ns. B) Transient absorption spectrum of a solution containing **Irsppy** (22 µM) in deaerated NaOH solution (50 mM) depicting the characteristic spectroscopic signature of **^{3}Irsppy**. The spectrum was measured immediately after excitation at 420 nm (14 mJ pulses) and was time-integrated over 100 ns. C) Spectroelectrochemical UV-Vis difference spectrum upon complete oxidation of **Irsppy** (400 µM in deaerated water) to **Irsppy$^+$** when applying a potential of +0.95 V *vs* SCE. The reference spectra (B and C) were obtained from Björn Pfund and Dr. Christoph Kerzig.[65,122]

Hence, the mechanistic studies imply that for cases in which the triplet energy of the photosensitizer is high enough to sensitize the Rh catalyst, the photochemical **1,4-BNAH** regeneration does not necessarily proceed via electron transfer from the sensitizer to the Rh catalyst, as was observed for various previous systems,[50,208] but rather involves a triplet-triplet energy transfer. This allows us to propose a first tentative reaction mechanism for **BNA$^+$** reduction using the newly developed Ir sensitizers as photocatalysts (Figure 31). Upon excitation with visible light, the triplet-excited Ir sensitizer undergoes triplet-triplet energy transfer to **[Cp*Rh(bpy)(H$_2$O)]$^{2+}$**, which is readily formed from the corresponding chloro precursor in aqueous solutions.[185,224] Reductive quenching of **^{3}[Cp*Rh(bpy)(H$_2$O)]$^{2+}$** with TEOA gives the Rh(II) aqua species (**[Cp*Rh(bpy)(H$_2$O)]$^+$**). Subsequent disproportionation and protonation results in the formation of the Rh(III) hydride.[197] The formed **[Cp*Rh(bpy)(H)]$^+$** enables the regioselective formation of **1,4-BNAH** via a hydride transfer, in analogy to the mechanisms that were proposed by the groups of Fish and Miller.[48,236]

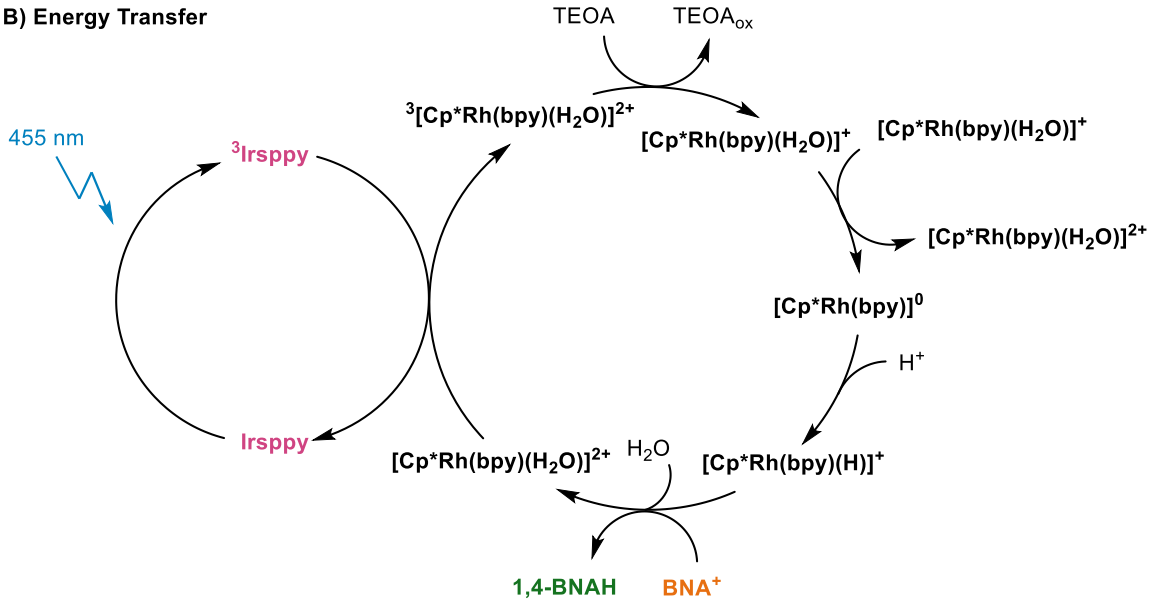

Figure 31: Proposed reaction mechanism. Energy transfer from the excited Ir sensitizer to **[Cp*Rh(bpy)(H$_2$O)]$^{2+}$** gives **^{3}[Cp*Rh(bpy)(H$_2$O)]$^{2+}$**, which is reductively quenched by TEOA to afford **[Cp*Rh(bpy)(H$_2$O)]$^+$**. From **[Cp*Rh(bpy)(H$_2$O)]$^+$**, disproportionation, protonation and regioselective reduction of **BNA$^+$** occurs in analogy to what has been reported previously.[48,197] For simplicity, **Irsppy** and **[Cp*Rh(bpy)(H$_2$O)]$^{2+}$** are depicted as selected examples for the employed Ir sensitizers and Rh catalysts.

4.4 Conclusion and Outlook

A set of newly developed, water-soluble Ir sensitizers set the basis for mechanistic investigations of photochemical nucleotide co-factor mimic regeneration. The four synthesized Ir complexes are derived from the archetypal photocatalyst **Irppy$_3$** and solubility in aqueous solutions was achieved through the introduction of sulfonate groups at the ligand periphery. All sensitizers have luminescence quantum yields in the range of 0.13 to 0.91 and triplet-excited state lifetimes that are sufficiently long to enable bimolecular reactions (1.6 to 2.2 µs, Table 1). Furthermore, these favorable properties are accompanied by very negative excited-state oxidation potentials (E^*_{ox} < –1.76 V *vs* SCE) and high triplet energies (E_T > 2.50 eV, Table 1), allowing applications such as challenging photoreductions[65,121] and triplet-triplet energy transfer[122] in the green solvent water. The introduction of fluorine substituents on the phenylpyridine ligands of the Ir sensitizers offered a straightforward approach to modulate the triplet energy of the sensitizers.

In combination with **[Cp*Rh(bpy)Cl]Cl**, all three trianionic Ir sensitizers were able to efficiently sensitize the photochemical regeneration of the nucleotide co-factor mimic **1,4-BNAH**, with yields ranging from 46% to 64% (Figure 27). The investigated reaction was monitored by UV-Vis spectroscopy and regioselective formation of **1,4-BNAH** was confirmed by ^{1}H-NMR spectroscopy. The yield of **1,4-BNAH** formation correlates with the triplet energies of the Ir sensitizers rather than with their excited-state oxidation potentials. In terms of initial turnover frequencies, the most potent Ir sensitizer for the photochemical regeneration of **1,4-BNAH**, **IrdFsppy**, outcompetes the archetypal **[Ru(bpy)$_3$]$^{2+}$** by almost one order of magnitude (146 h^{-1} *vs* 16 h^{-1}, section S3.2).

Luminescence-quenching experiments and transient absorption measurements were performed to gain further insight into the bimolecular processes involved in photochemical **1,4-BNAH** formation. The triplet-excited state of all three Ir sensitizers is efficiently quenched by **[Cp*Rh(bpy)Cl]Cl** (η ranging from 61 to 83%, Table 3), whereas the inefficient quenching by TEOA suggests that reductive quenching of the excited state by the sacrificial donor is only a minor pathway. The quenching rate constant k_q increases in the order **Irsppy** < **IrFsppy** < **IrdFsppy** (Table 3). The fact that the excited-state quenching rate increases with increasing triplet energy of the sensitizer but does not correlate with its excited-state oxidation potential points towards a triplet-triplet energy transfer. This hypothesis is further supported by the absence of the characteristic spectroscopic signature of **Irsppy$^+$**, which would be expected in an electron transfer pathway. Hence, both the observed reactivities of the photosensitizer in the photochemical regeneration of **1,4-BNAH** and the different mechanistic studies are indicative of energy transfer from the Ir sensitizer to the Rh catalyst. This finding is important since previously studied systems are governed by electron rather than energy transfer.[50,208] Hence, this study underpins that photophysical investigation of the reaction mechanisms that determine the interaction between the photosensitizer and the

transition metal aqua complex are important for the optimization of a given photochemical system. In the context of photochemical **1,4-BNAH** regeneration with an organometallic redox mediator, the triplet energy of the photosensitizer needs to be considered for future catalyst design. While the Ir sensitizers that were developed in the context of this thesis focus on increasing the triplet energy of the sensitizers via stabilization of the HOMO, destabilizing the LUMO of the Ir sensitizer or a combination of the two strategies could be exploited for further modulation of the triplet energy in the future (Figure 32).

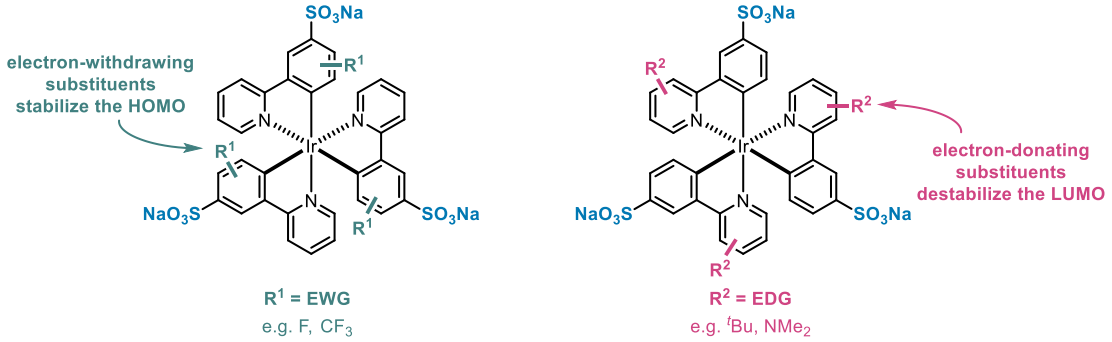

Figure 32: Future studies on water-soluble Ir sensitizers could focus on destabilizing the LUMO by introducing electron-donating groups (EDG) on the pyridine-ring, rather than stabilizing the HOMO with electron-withdrawing substituents on the phenyl-ring.

While the data presented in this thesis is in agreement with an energy transfer from the Ir sensitizer to the Rh catalyst, very recent experiments which were performed during the finalization of this thesis do not completely fit into this picture. Hence, further in-depth analysis of the reaction mechanism is required to fully elucidate the bimolecular processes governing the interaction between the two catalysts. For example, monitoring downstream reaction products has helped to elucidate reaction mechanisms when the product of the photocatalytic key-step is only short-lived.[237] Since the spectroscopic signature of both **[Cp*Rh(bpy)]^0** and **[Cp*Rh(bpy)(H)]$^+$** is known,[197,217] detection of these reaction products by transient absorption spectroscopy after the addition of TEOA seems feasible. However, since this process is irreversible under the experimental conditions, precise optimization of the experimental set-up is required.

Further insight into the reaction mechanism could be gained by investigating **Ir(sCH$_2$ppy)ppy$_2$** as a sensitizer for the photochemical regeneration of **1,4-BNAH**. Since the triplet energy of the monoanionic sensitizer (2.50 eV) is in the range of the expected triplet energy of the Rh catalyst (E_T of a comparable Rh catalyst ($[Rh(NH_3)_6]^{3+}$) is 2.51 eV),[234] triplet-triplet energy transfer between the two species is approximately thermoneutral and thus thermodynamically less favored compared to triplet-triplet energy transfer with the trianionic Ir sensitizers. Moreover, **Ir(sCH$_2$ppy)ppy$_2$** has the most negative excited-state oxidation potential (E^*_{ox} = –1.94 V *vs* SCE), implying that electron transfer from the Ir sensitizer to the Rh catalyst is strongly exergonic ($\Delta G_{ET,3}$ = –1.20 eV,

see SI section S4.1). Hence, examining the photochemical formation of **1,4-BNAH** with **Ir(sCH$_2$ppy)ppy$_2$** might provide new insights into the reaction mechanism.

Furthermore, after thorough investigation of the reaction mechanism, future research could focus on merging the newly developed photocatalytic system with an enzymatic dark reaction. In a preliminary experiment with glutamate dehydrogenase (GDH), regeneration of **1,4-NADH** was observed; however, no formation of the reaction product could be detected. Since mutual deactivation of the Rh catalyst and/or the Ir sensitizer and the enzyme is known,[121,183] further optimization of the reaction conditions is required. In previous studies, compartmentalization of the different reaction partners has helped to overcome such deactivation processes.[121,183]

5 General Summary

In this thesis, two different concepts of how transition metal hydride chemistry can be merged with photocatalysis were investigated to explore new light-induced reactivities and to gain insight into the bimolecular processes that govern the synergy between the two catalytic processes.

In the first project, **[Cp*Ir(phen)(H)]$^+$** was investigated as a photocatalyst that catalyzes the overall photo-HAT to unactivated olefins. In this approach, both the light-dependent reductive quenching step and the light-independent HAT step are performed by the same catalyst, the iridium hydride. The overall photo-HAT therefore represents one of the rare examples of single-component dual photocatalysis (Figure 33). The key for this new reactivity is the formation of a very weak Ir^{II}-H bond in **[Ir-H]^0**, thereby enabling the HAT to unactivated olefins and ultimately resulting in the formation of a new C-H bond.

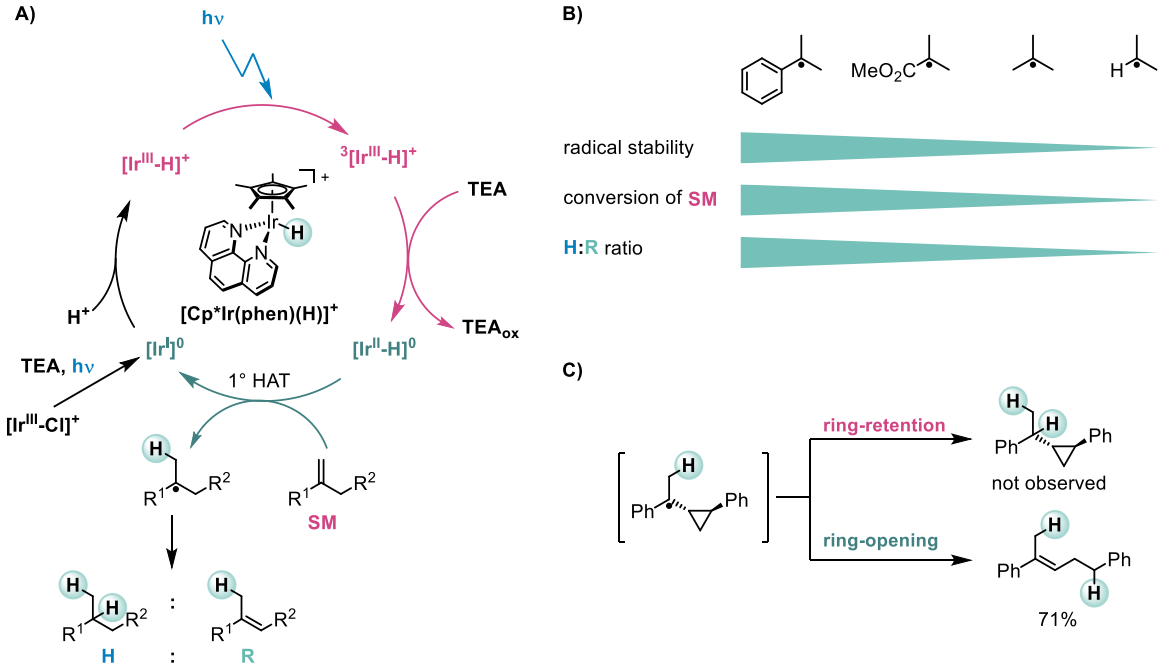

Figure 33: A) The ability of iridium hydrides to function both as the photocatalyst and as a hydrogen atom transfer catalyst is exploited in the investigation of a photo-HAT from a metal complex to unactivated olefins. B) Both the conversion of the olefin substrate and the **H**:**R** chemoselectivity of reaction correlate with the stability of the respective radical intermediate, in line with a photo-HAT mechanism. C) The exclusive formation of the ring-opened product in a radical clock experiment underpins that the reaction proceeds via a radical mechanism.

A simplified mechanism of the investigated photoinduced hydrogenation of olefins is depicted in Figure 33A. Due to the limited stability of the iridium hydride, the corresponding Ir(III) chloride was employed as a catalyst precursor. Upon irradiation with visible light, reductive dissociation of the chloro ligand in presence of triethylamine and rapid protonation of the Ir^I species lead to the formation of the Ir(III) hydride, in analogy to a previously studied related Rh-based system.[218] The viability of this intermediate was validated by the absence of a lag phase when directly using the Ir(III) hydride as a catalyst

in comparison to the time-delayed product formation when using Ir(III) chloride as catalyst precursor.

The weak Ir^{II}-H bond, which is formed upon reductive quenching of the triplet-excited Ir(III) hydride in presence of triethylamine ($k_q = 6.8 \cdot 10^8\ M^{-1} \cdot s^{-1}$), is vital for this new photo-HAT reactivity. While neither the triplet-excited **[Cp*Ir(phen)(H)]$^+$** ($E^{0\prime}$(IV/III*) ≈ –1.3 V *vs* SCE)[12] nor **[Cp*Ir(phen)(H)]^0** ($E^{0\prime}$(III/II) ≈ –1.4 V *vs* SCE)[12] are reducing enough to activate the investigated olefins (E_{red} < –2.7 V *vs* SCE)[238] via a photoinduced electron transfer pathway, the very low Ir^{II}-H BDFE enables a primary HAT (1° HAT in Figure 33A) to the olefin substrate.

The formed radical intermediates can then either react onwards in a secondary HAT to give the hydrogenation product **H**, or a hydrogen atom can be abstracted from the radical intermediate, leading to the rearranged product **R**. Structure-reactivity relationships of 12 investigated olefins support the typical HAT reactivity (Figure 33B): the conversion of the olefin substrate is dependent on the nature of the substituent R^1 and decreases in the order Ph > CO_2Me > Me > H. This correlation between the conversion of the olefin substrate and the stability of the formed radical intermediate is in agreement with thermal HAT reactivities.[180] Furthermore, the decrease in **H**:**R** chemoselectivity from ca. 15:1 to 2:1 when using an aliphatic (R^1 = Me) instead of an aromatic (R^1 = Ph) olefin is in line with a radical mechanism. The observed change in chemoselectivity is based on the weaker C_α-H bond in the aliphatic radical intermediate and hence hydrogen atom abstraction can compete with secondary HAT. The susceptibility of the reaction towards an additional substituent at the terminal carbon atom of the olefin substrate corroborates that the reaction proceeds via photo-HAT.[180] Further substantiation for a photo-HAT mechanism was gained with a radical clock experiment, in which the ring-opened product is formed exclusively, consistent with a radical mechanism (Figure 33C).

The reversibility of the initial HAT was investigated with a deuterated substrate and suggests that secondary HAT outcompetes hydrogen atom abstraction from the radical intermediate. The high chemoselectivity towards the hydrogenation product can presumably be attributed to an elevated (local) concentration of the H-atom donors (i.e., the oxidation products of TEA and the iridium hydride). Furthermore, continuous hydrogenation of the rearranged product and the addition of excess phenanthroline increase the observed chemoselectivity towards the hydrogenation product.

While HAT from transition metal hydrides (with BDFEs exceeding 50 kcal · mol^{-1}) to olefins is well investigated in thermal chemistry,[155,156,169] this study provides the first example of a light-induced HAT from the metal complex to unactivated olefins. Since photo-HATs proceed independent of the redox properties of the substrate and the photocatalyst, this newly investigated overall photo-HAT provides an important new approach for the activation of organic substrates that are difficult to access via the traditional photoinduced electron transfer pathway.

The second project investigated the photochemical formation of the nucleotide co-factor mimic **1,4-BNAH** by merging photocatalysis with rhodium hydride chemistry (Figure 34). A special focus was set on probing the bimolecular processes that are at play when the two catalytic cycles are combined.

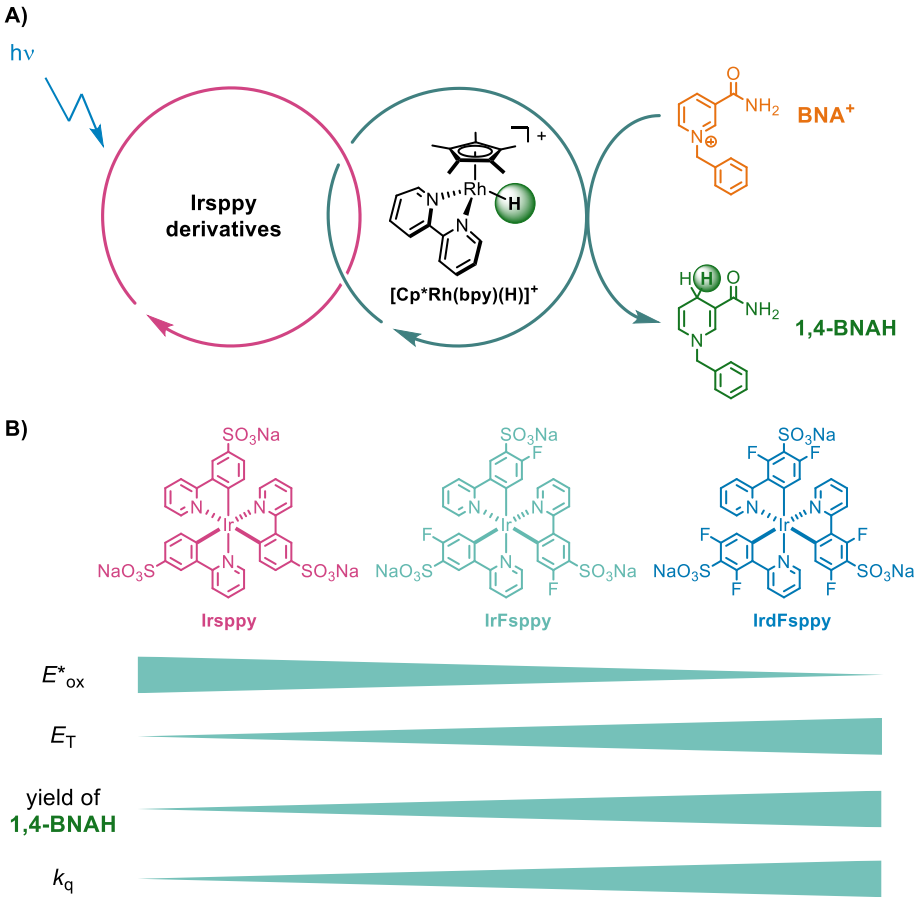

Figure 34: A) Combining photocatalysis with rhodium hydride chemistry enables the photochemical regeneration of **1,4-BNAH**. B) Both the yield of **1,4-BNAH** formation and the quenching rate constant k_q of the luminescence-quenching experiments with different concentrations of **[Cp*Rh(bpy)Cl]Cl** correlate with the triplet energy of the sensitizers and not with their excited-state oxidation potential.

Four new water-soluble analogs of **Irppy$_3$** set the basis for this study. Next to the monoanionic **Ir(sCH$_2$ppy)ppy$_2$**, three trianionic variants of **Irppy$_3$**, which only differed in the number of fluorine substituents on the phenylpyridine ligands, were synthesized. The introduction of additional fluorine atoms aimed at tuning the HOMO-LUMO gap of the Ir sensitizers by stabilizing the HOMO of the investigated complexes. All four sensitizers have a sufficiently long triplet-excited state lifetime (ca. 1.6 to 2.2 µs) for bimolecular reactions and the luminescence quantum yields varies between 0.13 and 0.91. Furthermore, the new Ir sensitizers have highly reducing excited states ($E^*_{ox} < -1.76$ V *vs* SCE) as well as high triplet energies ($E_T > 2.50$ eV). The usefulness of these newly developed water-soluble Ir sensitizers as potent photosensitizers in aqueous solutions has been proven by various applications in the Wenger group. Examples include the synergistic photo- and enzyme catalysis,[121] challenging photoreductions via formation of hydrated electrons,[65] and blue-to-UV upconversion in water.[122]

The three anionic Ir sensitizers were used to catalyze the photochemical regeneration of **1,4-BNAH** in combination with different Rh catalysts. The reaction progress was monitored by UV-Vis spectroscopy and the regioselective formation of the nucleotide co-factor was confirmed by ^{1}H-NMR spectroscopy. The yield of **1,4-BNAH** was found to increase in the order **Irsppy** < **IrFsppy** < **IrdFsppy** and the most efficient photocatalyst, **IrdFsppy**, outcompeted the conventional **[Ru(bpy)$_3$]$^{2+}$** by almost one order of magnitude in terms of initial turnover frequency (146 h^{-1} *vs* 16 h^{-1}). Interestingly, the yield of **1,4-BNAH** formation correlates with the triplet energy of the Ir sensitizers rather than their excited-state oxidation potential. This suggests that the interaction between the two catalysts is dictated by a triplet-triplet energy transfer rather than an electron transfer process, contrary to the findings of previously investigated systems.[50,208] This finding is further substantiated by luminescence-quenching experiments, as the quenching rate constant in presence of different concentrations of **[Cp*Rh(bpy)Cl]Cl** increases in the order **Irsppy** < **IrFsppy** < **IrdFsppy**. Furthermore, the absence of the characteristic spectroscopic signature of **Irsppy^{+}** in transient absorption spectroscopy points towards an energy transfer rather than an electron transfer mechanism.

In summary, this thesis provides new insights into the synergism of photocatalysis with transition metal hydride chemistry and demonstrates that the combination of the two reactivities is an important concept to expand the scope of traditional photocatalysis. Furthermore, the findings of this thesis set the basis for future studies on photo-HAT reactivities and the developed water-soluble Ir sensitizers have emerged as valuable photocatalysts for applications in aqueous solutions.

6 Supporting Information

6.1 Supporting Information for Photoinduced Hydrogen Atom Transfer from Iridium Hydrides (Chapter 3)

Mirjam R. Schreier, Björn Pfund, Xingwei Guo,[*‡] and Oliver S. Wenger[*]
Department of Chemistry, University of Basel, St. Johanns-Ring 19, 4056 Basel, Switzerland
[‡] Current address: Center of Basic Molecular Science (CMBS), Department of Chemistry, Tsinghua University, Beijing 100084, China

Table of Contents

S1 Equipment and Methods

General

Unless stated otherwise, all air- or moisture-sensitive syntheses were performed under inert conditions (N_2 atmosphere). Dry solvents were used as received and if necessary were degassed using the freeze, pump, thaw method. Dry diethyl ether, tetrahydrofuran (THF) and dichloromethane (DCM) were obtained from a commercial solvent purification system by Innovative Technology. Commercially available chemicals were purchased from ABCR, Acros Organics, Fluorochem, or Sigma-Aldrich and used as received.

Chromatography

Column chromatography was performed with silica gel from Silicycle (silica flash, 40-63 µm, (230-400 mesh ASTM) for flash column chromatography). Thin layer chromatography (TLC) was performed with pre-coated aluminium sheets (precoated with silica 60, from Merck, layer thickness of 0.25 mm), coated with fluorescence indicator F254. Visualization of the compounds occurred either under UV light (using either the 254 nm or 365 nm output of a UV lamp) or using a $KMnO_4$-stain.

NMR spectroscopy

NMR spectra were measured on a Bruker Avance III operating at 400 MHz or 500 MHz proton frequencies. All chemical shifts are reported in δ values in ppm and were referenced to the signals of the residual non-perdeuterated solvent used.[239] The deuterated solvents for NMR-spectroscopy were obtained from Cambridge Isotope Laboratories. All coupling constants *J* are given in Hertz (Hz) and the following abbreviations are used to describe their coupling patterns: s (singlet), br s (broad singlet), d (doublet), t (triplet), q (quartet), pent. (quintet), sext. (sextet), m (multiplet), dd (doublet of doublets), dq (doublet of quartets), tq (triplet of quartets), ddd (doublet of doublets of doublets).

GC-MS spectrometry

GC-MS spectrometry was performed using a GC-MS-QP2010 SE gas chromatograph system with a ZB-5HT inferno column (30 m x 0.25 mm x 0.25 mm) that was operated at a 1 mL/min He flow rate (split = 20:1). The different analytes were separated using the methods summarized in Table S1. The retention times (t_R) of the substrates and products are reported in minutes in the experimental sections S2 and S3.

The mass system consisted of a Shimadzu mass detector (EI, 70 eV). The quotients of mass to charge (*m/z*) are given and the relative intensities related to the basis peak (I=100) are reported in brackets.

Table S1. Different methods for analysis by GC-MS spectrometry.

	Oven Temperature Program
Method A	100 °C, 35 °C/min, 200 °C, 100 °C/min, 350 °C
Method B	100 °C, 30 °C/min, 200 °C, 5 °C/min, 230 °C, 100 °C/min, 350 °C

Steady-state absorption spectroscopy

Optical absorption spectroscopy was measured on a Cary 5000 UV-Vis-NIR instrument from Varian.

Time-resolved luminescence spectroscopy

Time-resolved luminescence spectroscopy was performed on a LP920-KS instrument from Edinburgh Instruments. Excitation occurred at 455 nm using a Quantel Brilliant b laser combined with an optical parametric oscillator (OPO) from Opotek as excitation source. The laser pulse duration was ~10 ns and the pulse frequency was 10 Hz. Kinetics at single detection wavelengths were recorded using a photomultiplier tube.

Transient absorption spectroscopy

Transient absorption spectroscopy was performed on a LP920-KS instrument from Edinburgh Instruments. Excitation of the complexes occurred at 445 nm using a frequency-tripled Nd:YAG laser (Quantel Brilliant, ca. 10 ns pulse width) equipped with an OPO from Opotek and the typical pulse energy was ca 9 mJ. A beam expander (GBE02-A from Thorlabs) was used to improve the excitation homogeneity in the detection volume. The transient absorption spectra were detected with an iCCD camera from Andor.

Set-up for photocatalysis

Photoirradiation was performed using a home-built photoreactor (Fig. S1). The setup consists of LED strips (470 nm) that are arranged around the outside of a glass beaker. The photoreactor is divided into 8 compartments, each corresponding to an irradiation power of ca. 7.5 W. The beaker is filled with water and incorporates copper tubing through which water is flowed. The tubes are connected to an external thermostat, enabling a steady temperature throughout the irradiation process. For all experiments, the water temperature was adjusted to 50 °C and the reactions were performed in NMR tubes that were irradiated in individual compartments.

For the UV-Vis irradiation experiment, continuous-wave photo-irradiation of the sample occurred at room temperature using a 455 nm (~1000 mW power output) collimated LED purchased from ThorLabs.

Figure S1. Home-built photoreactor (λ = 470 nm), connected to an external thermostat (left). Different compartments of the photoreactor (viewed from the top), each corresponding to an irradiation power of ca. 7.5 W (right).

S2 Experimental Procedures

S2.1 Catalyst Syntheses

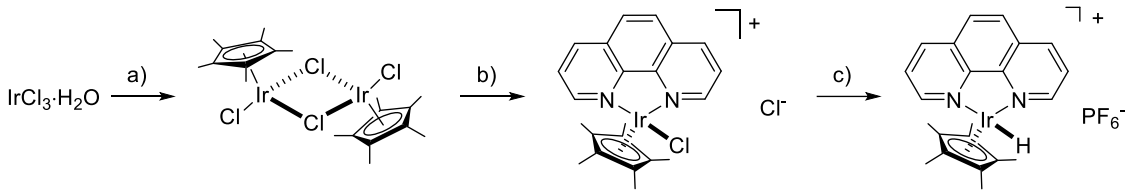

Scheme S1. Synthesis of different iridium complexes: a) C_5Me_5H, MeOH, reflux, 2 days, 80%; b) phen, MeOH, rt, overnight, 70%; c) aq. formic acid (3 M, pH 5), rt, 5 h, then KPF_6, 84%.

[Cp*IrCl₂]₂

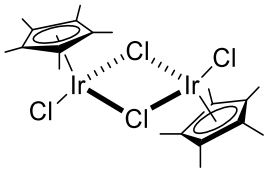

The synthesis of **[Cp*IrCl₂]₂** was adapted from a previously published protocol.[240] Iridium(III) chloride hydrate (501 mg, 1.58 mmol, 2.0 eq.) was dissolved in dry MeOH (10 mL) and pentamethyl-cyclopentadiene (0.40 mL, 2.55 mmol, 3.2 eq.) was added dropwise. The reaction mixture was heated at reflux for 2 days. The resulting suspension was cooled to 0 °C. The formed orange-red precipitate was collected by filtration and washed with cold methanol to afford **[Cp*IrCl₂]₂** (506 mg, 635 µmol, 80%) as an orange solid. Analytical data matches the literature.[240]

$C_{20}H_{30}Ir_2Cl_4$ (797 g/mol):

^{1}H-NMR (400 MHz, 298 K, $CDCl_3$, δ/ppm): 1.59 (s, 30H).

^{13}C-{^{1}H}-NMR (126 MHz, 298 K, $CDCl_3$, δ/ppm): 86.4, 9.5.

[Cp*Ir(phen)Cl]Cl

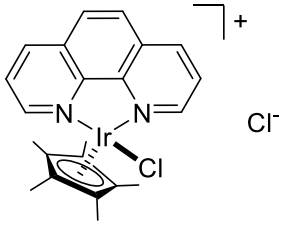

The synthesis of **[Cp*Ir(phen)Cl]Cl** was adapted from a previously published protocol.[241] A round-bottomed flask was charged with **[Cp*IrCl₂]₂** (200 mg, 251 µmol, 1.0 eq.), 1,10-phenanthroline (92.0 mg, 511 µmol, 2.0 eq.) and dry methanol (20 mL). After the reaction mixture was stirred at room temperature overnight, the solvent was evaporated under reduced pressure. The residue was redissolved in DCM and added dropwise to diethyl ether. The formed yellow precipitate was collected by filtration and washed with diethyl ether to afford **[Cp*Ir(phen)Cl]Cl** (203 mg, 351 µmol, 70%) as a yellow solid. Analytical data matches the literature.[242]

$C_{22}H_{23}N_2IrCl_2$ (579 g/mol):
^{1}H-NMR (400 MHz, 298 K, $CDCl_3$, δ/ppm): δ 9.41 (d, *J* = 5.2 Hz, 2H), 8.76 (d, *J* = 8.2 Hz, 2H), 8.32 (dd, *J* = 8.2 Hz, *J* = 5.2 Hz, 2H), 8.17 (s, 2H), 1.85 (s, 15H).
^{13}C-{^{1}H}-NMR (126 MHz, 298 K, $CDCl_3$, δ/ppm): 151.8, 146.6, 139.4, 131.2, 128.4, 128.1, 89.6, 9.2.

[Cp*Ir(phen)(H)](PF$_6$)

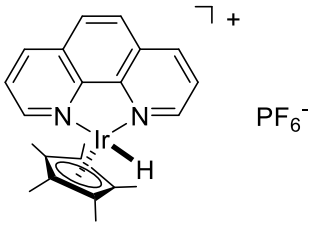

The synthesis of **[Cp*Ir(phen)(H)](PF$_6$)** was adapted from a previously published protocol.[12] The entire synthesis was performed in the dark and under argon atmosphere. **[Cp*Ir(phen)Cl]Cl** (100 mg, 172 µmol, 1.0 eq.) was dissolved in aq. formic acid solution (3 M, 5.7 mL, adjusted to pH 5 by addition of grounded KOH pellets) and the reaction mixture was stirred at room temperature in the dark for 5 hours. The resulting orange solution was filtered over Celite and **[Cp*Ir(phen)(H)](PF$_6$)** was precipitated from the filtrate through the addition of KPF_6 (283 mg, 1.54 mmol, 9.0 eq.). The resulting yellow suspension was filtered over Celite and the formed yellow precipitate was washed with previously degassed water (3 mL) and diethyl ether (3 mL). The residue was eluted with previously degassed MeCN (5 mL) and the filtrate was concentrated under reduced pressure. **[Cp*Ir(phen)(H)](PF$_6$)** (95.0 mg, 146 µmol, 84%) was obtained as a yellow solid. Analytical data is in agreement with the literature data obtained for **[Cp*Ir(phen)(H)](BF$_4$)**.[242]
$C_{22}H_{24}N_2IrPF_6$ (654 g/mol):
^{1}H-NMR (400 MHz, 298 K, CD_3CN, δ/ppm): 9.22 (dd, *J* = 5.4 Hz, 1.2 Hz, 2H), 8.64 (dd, *J* = 8.2 Hz, 1.2 Hz, 2H), 8.15 (s, 2H), 7.96 (dd, *J* = 8.2 Hz, 5.4 Hz, 2H), 1.90 (s, 15H), -11.46 (s, 1H).

[Cp*Ir(phen)]^0

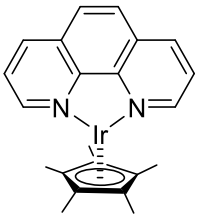

A reference spectrum of **[Cp*Ir(phen)]^0** was obtained after deprotonation of **[Cp*Ir(phen)(H)](PF$_6$)** (3.2 mg, 4.9 µmol, 1.0 eq.) dissolved in CD_3CN (0.5 mL) in presence of KO^{t}Bu (700 µg, 6.25 µmol, 1.3eq.).

^{1}H-NMR (400 MHz, 298 K, CD_3CN, δ/ppm): 9.04 (d, *J* = 6.5 Hz, 2H), 7.48 (s, 2H), 7.37 (d, *J* = 6.9 Hz, 2H), 6.73 (t, *J* = 6.7 Hz, 2H), 1.99 (s, 15H).

S2.2 Substrate Syntheses

S2.2.1 Synthesis of Allylic Ethers

Table S2. Synthesis of different allylic ether substrates (**1-SM**, **7-SM**, **10-SM** and **11-SM**):

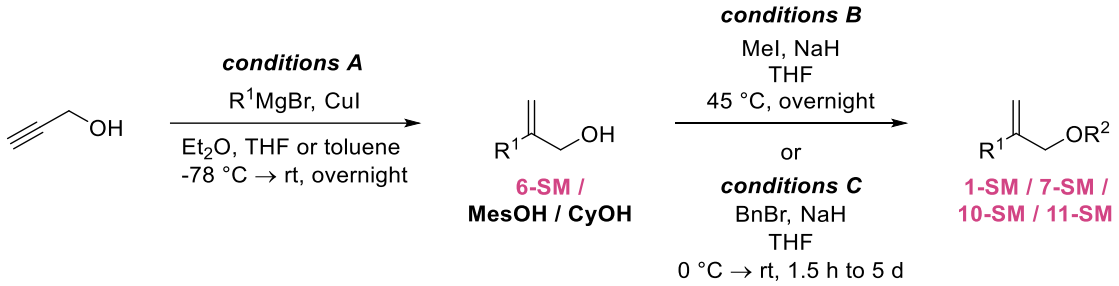

Allylic alcohol	R^1	Conditions	Yield / %	Allylic ether	R^2	Conditions	Yield / %
6-SM	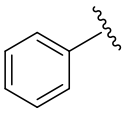	***conditions A*** with Et_2O	91	1-SM	Me	***conditions B***	93
MesOH	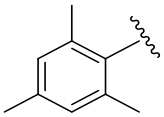	***conditions A*** with THF	69	7-SM	Bn	***conditions C***	69
CyOH		***conditions A*** with toluene/THF	27	10-SM	Bn	***conditions C***	81
	Me	-[a]	-[a]	11-SM	Bn	***conditions C***	89

[a] 2-Methylprop-2-en-1-ol was obtained from commercial sources.

2-Phenylprop-2-en-1-ol (6-SM)

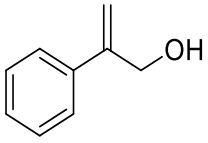

Propargyl alcohol (1.07 g, 19.1 mmol, 1.0 eq.) and CuI (1.66 g, 8.72 mmol, 0.5 eq.) were suspended in dry diethyl ether (25 mL) and the resulting suspension was cooled to −78 °C

with an acetone/dry ice bath. Phenylmagnesium bromide (3.0 M in diethyl ether, 18.0 mL, 54.0 mmol, 2.8 eq.) was added dropwise and the reaction was stirred at −78 °C for 15 minutes. The reaction mixture was then allowed to reach room temperature and was stirred at this temperature overnight. After cooling to 0 °C, the reaction was quenched with sat. aq. NH_4Cl solution (40 mL), the layers were separated, and the aqueous layer was extracted with diethyl ether (3 x 40 mL). The combined organic layers were dried over anhydrous sodium sulfate, filtered and concentrated under reduced pressure. The crude product was purified by flash column chromatography (SiO_2, diethyl ether/pentane 1:5) to afford 2-phenylprop-2-en-1-ol (**6-SM**, 2.34 g, 17.4 mmol, 91%) as a light-yellow liquid. Analytical data matches the literature.[243]

$C_9H_{10}O$ (134 g/mol):

^{1}H-NMR (400 MHz, 298 K, $CDCl_3$, δ/ppm): 7.48-7.43 (m, 2H), 7.39-7.28 (m, 3H), 5.48 (pseudo-q, *J* = 0.9 Hz, 1H), 5.36 (pseudo-q, *J* = 1.3 Hz, 1H), 4.55 (s, 2H), 1.75 (br s, 1H).

^{13}C-{^{1}H}-NMR (101 MHz, 298 K, $CDCl_3$, δ/ppm): 147.4, 138.6, 128.6, 128.1, 126.2, 112.7, 65.2.

2-Mesitylprop-2-en-1-ol (MesOH)

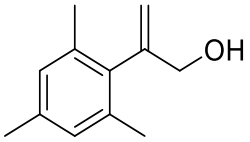

Propargyl alcohol (2.00 g, 35.7 mmol, 1.0 eq.) and CuI (3.40 g, 17.8 mmol, 0.5 eq.) were suspended in dry THF (50 mL) and the resulting suspension was cooled to −78 °C with an acetone/dry ice bath. Mesitylmagnesium bromide [freshly prepared from mesitylbromide (16.5 mL, 108 mmol, 3.0 eq.) and magnesium (3.90 g, 161 mmol, 4.5 eq.) in dry THF (107 mL)] was added dropwise and the reaction was stirred at −78 °C for 15 minutes. The reaction mixture was then allowed to reach room temperature and was stirred at this temperature overnight. After cooling to 0 °C, the reaction was quenched with sat. aq. NH_4Cl solution (40 mL), the layers were separated, and the aqueous layer was extracted with diethyl ether (3 x 40 mL). The combined organic layers were dried over anhydrous sodium sulfate, filtered and concentrated under reduced pressure. The crude product was purified by gradient flash column chromatography (SiO_2, diethyl ether/pentane 1:5 then diethyl ether/pentane 1:3) to afford 2-mesitylprop-2-en-1-ol (**MesOH**, 4.37 g, 24.8 mmol, 69%) as a yellowish liquid. Analytical data matches the literature.[244]

$C_{12}H_{16}O$ (176 g/mol):

^{1}H-NMR (400 MHz, 298 K, $CDCl_3$, δ/ppm): 6.86 (s, 2H), 5.51 (pseudo-q, *J* = 2.1 Hz, 1H), 4.84 (pseudo-q, *J* = 1.8 Hz, 1H), 4.02 (dt, *J* = 6.1 Hz, 1.9 Hz, 2H), 3.06 (t, *J* = 6.1 Hz, 1H), 2.23 (s, 3H), 2.17 (s, 6H).

^{13}C-{^{1}H}-NMR (101 MHz, 298 K, CD_3CN, δ/ppm): 150.3, 137.7, 137.3, 136.4, 128.8, 112.0, 64.9, 21.0, 19.8.

2-Cyclohexylprop-2-en-1-ol (CyOH)

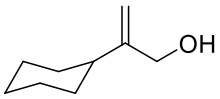

Propargyl alcohol (990 mg, 17.7 mmol, 1.0 eq.) and CuI (1.70 g, 8.93 mmol, 0.5 eq.) were suspended in dry toluene (24 mL) and the resulting suspension was cooled to −78 °C with an acetone/dry ice bath. Cyclohexylmagnesium bromide (1.3 M in toluene/THF (1:1 *v:v*), 40 mL, 52.0 mmol, 2.9 eq.) was added dropwise and the reaction was stirred at −78 °C for 15 minutes. The reaction mixture was then allowed to reach room temperature and was stirred at this temperature overnight. After cooling to 0 °C, the reaction was quenched with sat. aq. NH_4Cl solution (40 mL), the layers were separated, and the aqueous layer was extracted with diethyl ether (3 x 40 mL). The combined organic layers were dried over anhydrous sodium sulfate, filtered and concentrated under reduced pressure. The crude product was purified by gradient flash column chromatography (SiO_2, diethyl ether/pentane 1:10 then diethyl ether/pentane 1:1) to afford 2-cyclohexylprop-2-en-1-ol (**CyOH**, 672 mg, 4.79 mmol, 27%) as a yellowish liquid. Analytical data matches the literature.[243,245]

$C_9H_{16}O$ (140 g/mol):

^{1}H-NMR (400 MHz, 298 K, $CDCl_3$, δ/ppm): 4.94 (pseudo-q, *J* = 1.7 Hz, 1H), 4.81-4.79 (m, 1H), 3.98 (dt, *J* = 5.9 Hz, 1.5 Hz, 2H), 2.76-2.71 (m, 1H), 1.94-1.87 (m, 1H), 1.79-1.72 (m, 4H), 1.70-1.62 (m, 1H), 1.36-1.15 (m, 5H).

^{13}C-{^{1}H}-NMR (126 MHz, 298 K, CD_3CN, δ/ppm): 155.9, 106.5, 64.3, 41.6, 32.9, 27.1, 26.7.

(3-Methoxyprop-1-en-2-yl)benzene (1-SM)

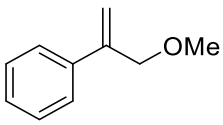

Sodium hydride (95%, 856 mg, 21.4 mmol, 1.2 eq.) was suspended in dry THF (35 mL) and iodomethane (1.6 mL, 25.7 mmol, 1.5 eq.) was added dropwise. After the suspension was heated to 45 °C, 2-phenylprop-2-en-1-ol (**6-SM**, 2.34 g, 17.4 mmol, 1.0 eq.) was added and the reaction mixture was stirred at 45 °C overnight. The crude mixture was cooled to 0 °C and was then quenched with water (25 mL). The layers were separated, and the aqueous layer was extracted with diethyl ether (3 x 50 mL). The combined organic layers were dried over anhydrous sodium sulfate, filtered and concentrated under reduced pressure. The crude product was purified by flash column chromatography (SiO_2, pentane/ethyl acetate 30:1) to afford (3-methoxyprop-1-en-2-yl)benzene (**1-SM**, 2.41 g, 16.3 mmol, 93%) as a colorless liquid. Analytical data matches the literature.[246]

$C_{10}H_{12}O$ (148 g/mol):

^{1}H-NMR (400 MHz, 298 K, $CDCl_3$, δ/ppm): 7.52-7.46 (m, 2H), 7.39-7.27 (m, 3H), 5.52 (s, 1H), 5.31 (pseudo-q, *J* = 1.3 Hz, 1H), 4.31 (s, 2H), 3.30 (s, 3H).
^{13}C-{^{1}H}-NMR (126 MHz, 298 K, CD_3CN, δ/ppm): 145.7, 139.8, 129.3, 128.7, 127.0, 114.8, 75.0, 58.0.
GC (achiral phase, 62.7 kPa He, method A): t_R = 3.62 min.
GC-MS (EI, 70 eV) *m/z* (%): 147 (15), 133 (6), 118 (100), 103 (49), 91 (15), 77 (34), 63 (6).

2-(3-(Benzyloxy)prop-1-en-2-yl)-1,3,5-trimethylbenzene (7-SM)

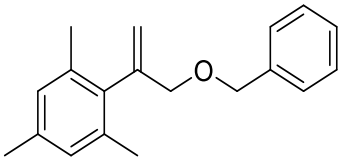

Sodium hydride (60%, dispersed in mineral oil, 500 mg, 12.5 mmol, 1.1 eq.) was suspended in dry THF (15 mL) and the resulting suspension was cooled to 0 °C. 2-Mesitylprop-2-en-1-ol (**MesOH**, 2.01 g, 11.4 mmol, 1.0 eq.) dissolved in dry THF (5 mL) was added dropwise and the reaction mixture was stirred at this temperature for 30 minutes. At 0 °C, benzyl bromide (1.5 mL, 12.5 mmol, 1.1 eq.) was added and the reaction mixture was stirred at room temperature for 1.5 hours. The reaction was quenched with water (50 mL), the layers were separated, and the aqueous layer was extracted with diethyl ether (3 x 100 mL). The combined organic layers were dried over anhydrous sodium sulfate, filtered and concentrated under reduced pressure. The crude product was purified by gradient flash column chromatography (SiO_2, neat pentane then pentane/diethyl ether 30:1) to afford 2-(3-(benzyloxy)prop-1-en-2-yl)-1,3,5-trimethylbenzene (**7-SM**, 2.10 g, 7.88 mmol, 69%) as a colorless liquid.
$C_{19}H_{22}O$ (266 g/mol):
^{1}H-NMR (400 MHz, 298 K, $CDCl_3$, δ/ppm): 7.39-7.32 (m, 4H), 7.31-7.26 (m, 1H), 6.86 (s, 2H), 5.57 (pseudo-q, *J* = 1.8 Hz, 1H), 4.92-4.90 (m, 1H), 4.57 (s, 2H), 4.06 (*t*, J = 1.5 Hz, 2H), 2.23 (s, 3H), 2.17 (s, 6H).
^{13}C-{^{1}H}-NMR (126 MHz, 298 K, CD_3CN, δ/ppm): 146.8, 139.7, 137.5, 137.4, 136.5, 129.3, 128.9, 128.4, 128.4, 114.3, 73.2, 73.1, 21.0, 19.9.
GC (achiral phase, 62.7 kPa He, method A): t_R = 5.96 min.
GC-MS (EI, 70 eV) *m/z* (%): 266 (4, M^+), 235 (9), 175 (16), 160 (100), 157 (54), 145 (69), 129 (35), 120 (27), 115 (22), 105 (21), 91 (75), 77 (11), 65 (16).

(((2-Cyclohexylallyl)oxy)methyl)benzene (10-SM)

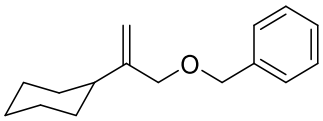

Sodium hydride (60%, dispersed in mineral oil, 420 mg, 10.5 mmol, 1.1 eq.) was suspended in dry THF (15 mL) and the resulting suspension was cooled to 0 °C. 2-Cyclohexylprop-2-en-1-ol (**CyOH**, 1.33 g, 9.48 mmol, 1.0 eq.) dissolved in dry THF (2.5 mL) was added dropwise. The reaction mixture was stirred at this temperature for 30 minutes. At 0 °C, benzyl bromide (1.25 mL, 10.4 mmol, 1.1 eq.) was added and the reaction mixture was stirred at room temperature for 5 days. At 0 °C, the reaction was quenched with water (50 mL), the layers were separated, and the aqueous layer was extracted with diethyl ether (3 x 100 mL). The combined organic layers were dried over anhydrous sodium sulfate, filtered and concentrated under reduced pressure. The crude product was purified by gradient flash column chromatography (SiO_2, neat pentane then pentane/diethyl ether 10:1) to afford (((cyclohexylallyl)oxy)methyl)benzene (**10-SM**, 1.77 g, 7.68 mmol, 81%) as a colorless liquid.

$C_{16}H_{22}O$ (230 g/mol):

^{1}H-NMR (400 MHz, 298 K, CD_3CN, δ/ppm): 7.39-7.32 (m, 4H), 7.31-7.26 (m, 1H), 5.00 (pseudo-q, *J* = 1.6 Hz, 1H), 4.91-4.89 (m, 1H), 4.46 (s, 2H), 3.99 (s, 2H), 2.03-1.95 (m, 1H), 1.82-1.73 (m, 4H), 1.71-1.64 (m, 1H), 1.35-1.12 (m, 5H).

^{13}C-{^{1}H}-NMR (126 MHz, 298 K, CD_3CN, δ/ppm): 152.9, 139.9, 129.3, 128.6, 128.4, 109.9, 73.1, 72.6, 42.1, 33.1, 27.5, 27.1.

GC (achiral phase, 62.7 kPa He, method B): t_R = 8.43 min.

GC-MS (EI, 70 eV) *m/z* (%): 124 (29), 104 (8), 91 (100), 67 (22), 79 (19), 55 (14).

((2-Methylallyloxy)methyl)benzene (11-SM)

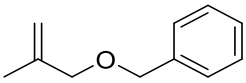

Sodium hydride (60%, dispersed in mineral oil, 1.22 g, 30.5 mmol, 1.1 eq.) was suspended in dry THF (50 mL) and the resulting suspension was cooled to 0 °C. 2-Methylprop-2-en-1-ol (1.96 g, 27.2 mmol, 1.0 eq.) was added and the reaction mixture was stirred at this temperature for 1 hour. At 0 °C, benzyl bromide (3.6 mL, 30.3 mmol, 1.1 eq.) was added dropwise and the reaction was stirred at room temperature for 4 hours. The reaction was quenched with water (50 mL), the layers were separated, and the aqueous layer was extracted with diethyl ether (3 x 100 mL). The combined organic layers were dried over anhydrous sodium sulfate, filtered and concentrated under reduced pressure. The crude product was purified by gradient flash column chromatography (SiO_2, neat pentane then pentane/diethyl ether 30:1) to afford ((2-methylallyloxy)methyl)benzene (**11-SM**, 3.92 g, 24.2 mmol, 89%) as a colorless liquid. Analytical data matches the literature.[247]

$C_{11}H_{14}O$ (162 g/mol):

^{1}H-NMR (400 MHz, 298 K, $CDCl_3$, δ/ppm): 7.38-7.27 (m, 5H), 5.01 (s, 1H), 4.93 (s, 1H), 4.50 (s, 2H), 3.94 (s, 2H), 1.78 (s, 3H).

^{13}C-{^{1}H}-NMR (101 MHz, 298 K, $CDCl_3$, δ/ppm): 142.4, 138.6, 128.5, 127.8, 127.7, 112.5, 74.3, 72.0, 19.7.

GC (achiral phase, 62.7 kPa He, method A): t_R = 3.85 min.

GC-MS (EI, 70 eV) *m/z* (%): 118 (9), 107 (44), 91 (100), 79 (12), 65 (17), 55 (6).

S2.2.2 Synthesis of Terminal Olefins

Table S3. Synthesis of terminal olefins (2-SM to 5-SM) in a Wittig reaction.

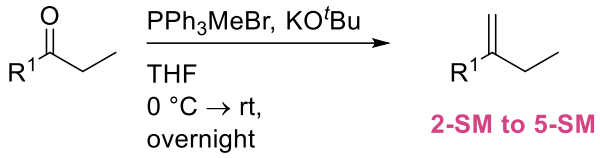

2-SM to 5-SM

Terminal Olefin	R^1	Yield / %
2-SM	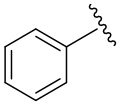	86
3-SM	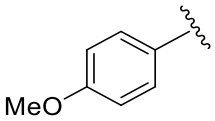	92
4-SM	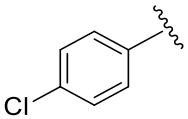	92
5-SM	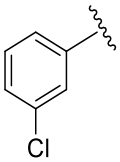	68

General procedure A: Wittig reaction for the synthesis of terminal olefins

Methyltriphenylphosphonium bromide (3.0 eq.) was suspended in dry THF (5 mL per mmol ketone) under a nitrogen atmosphere. At 0 °C, potassium *tert*-butoxide (3.0 eq.) was added and the resulting yellow suspension was stirred at this temperature for 30 minutes. The desired ketone (1.0 eq.) was added at 0 °C and the reaction mixture was stirred at room temperature overnight. The reaction was quenched with water (5 mL per mmol ketone), the layers were separated, and the aqueous layer was extracted with diethyl ether (3 x 10 mL per mmol ketone). The combined organic layers were dried over

anhydrous sodium sulfate, filtered and concentrated under reduced pressure. The crude product was purified by flash column chromatography.

But-1-en-2-ylbenzene (2-SM)

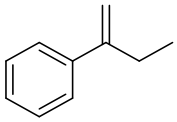

According to general procedure A, methyltriphenylphosphonium bromide (16.1 g, 45.0 mmol, 3.0 eq.) and potassium *tert*-butoxide (5.10 g, 45.5 mmol, 3.0 eq.) in dry THF (75 mL) were stirred at 0 °C for 30 minutes. After the addition of 1-phenyl-propan-1-one (2.00 g, 15.0 mmol, 1.0 eq.), the reaction was stirred at room temperature overnight. The crude product was purified by flash column chromatography (SiO_2, pentane/ethyl acetate 10:1) to afford but-1-en-2-ylbenzene (**2-SM**, 1.70 g, 12.9 mmol, 86%) as a colorless liquid. Analytical data matches the literature.[248]

$C_{10}H_{12}$ (132 g/mol):

^{1}H-NMR (400 MHz, 298 K, $CDCl_3$, δ/ppm): 7.44-7.39 (m, 2H), 7.35-7.30 (m, 2H), 7.28-7.23 (m, 1H), 5.27 (s, 1H), 5.06 (pseudo-q, *J* = 1.5 Hz, 1H), 2.52 (q, *J* = 7.4 Hz, 2H), 1.11 (t, *J* = 7.4 Hz, 3H).

^{13}C-{^{1}H}-NMR (101 MHz, 298 K, $CDCl_3$, δ/ppm): 150.2, 141.7, 128.4, 127.4, 126.2, 111.1, 28.2, 13.1.

GC (achiral phase, 62.7 kPa He, method A): t_R = 3.03 min.

GC-MS (EI, 70 eV) *m/z* (%): 132 (82, M^+), 117 (100), 103 (43), 91 (29), 77 (30), 65 (10), 51 (21).

1-(But-1-en-2-yl)-4-methoxybenzene (3-SM)

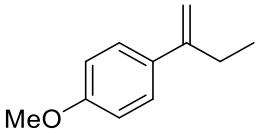

According to general procedure A, methyltriphenylphosphonium bromide (16.1 g, 45.0 mmol, 3.0 eq.) and potassium *tert*-butoxide (5.10 g, 45.5 mmol, 3.0 eq.) in dry THF (75 mL) were stirred at 0 °C for 2 h. After the addition of 1-(4-methoxyphenyl)propan-1-one (2.46 g, 15.0 mmol, 1.0 eq.), the reaction was stirred at room temperature overnight. The crude product was purified by flash column chromatography (SiO_2, pentane/ethyl acetate 10:1) to afford 1-(but-1-en-2-yl)-4-methoxybenzene (**3-SM**, 2.24 g, 13.8 mmol, 92%) as a colorless liquid. Analytical data matches the literature.[249]

$C_{11}H_{14}O$ (162 g/mol):

^{1}H-NMR (400 MHz, 298 K, CD_3CN, δ/ppm): 7.42-7.37 (m, 2H), 6.92-6.86 (m, 2H), 5.22 (s, 1H), 4.99 (pseudo-q, *J* = 1.4 Hz, 1H), 3.79 (s, 3H), 2.50 (q, *J* = 7.4 Hz, 2H), 1.07 (t, *J* = 7.4 Hz, 3H).

^{13}C-{^{1}H}-NMR (126 MHz, 298 K, CD_3CN, δ/ppm): 160.2, 150.4, 134.4, 128.0, 1114.6, 109.8, 55.9, 28.6, 13.5.
GC (achiral phase, 62.7 kPa He, method A): t_R = 4.21 min.
GC-MS (EI, 70 eV) *m/z* (%): 162 (100, M^+), 147 (64), 133 (88), 103 (16), 91 (37), 77 (22), 63 (12).

1-(But-1-en-2-yl)-4-chlorobenzene (4-SM)

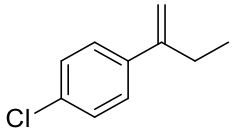

According to general procedure A, methyltriphenylphosphonium bromide (16.1 g, 45.0 mmol, 3.0 eq.) and potassium *tert*-butoxide (5.10 g, 45.5 mmol, 3.0 eq.) in dry THF (75 mL) were stirred at 0 °C for 30 minutes. After the addition of 1-(4-chlorophenyl)propan-1-one (2.54 g, 15.1 mmol, 1.0 eq.), the reaction was stirred at room temperature overnight. The crude product was purified by flash column chromatography (SiO_2, pentane/ethyl acetate 10:1) to afford 1-(but-1-en-2-yl)-4-chlorobenzene (**4-SM**, 2.32 g, 13.9 mmol, 92%) as a colorless liquid. Analytical data matches the literature.[249]
$C_{10}H_{11}Cl$ (167 g/mol):
^{1}H-NMR (400 MHz, 298 K, CD_3CN, δ/ppm): 7.48-7.39 (m, 2H), 7.39-7.30 (m, 2H), 5.31 (s, 1H), 5.12-5.10 (m, 1H), 2.50 (q, *J* = 7.4 Hz, 2H), 1.06 (t, *J* = 7.4 Hz, 3H).
^{13}C-{^{1}H}-NMR (126 MHz, 298 K, CD_3CN, δ/ppm): 150.0, 140.9, 133.6, 129.3, 128.5, 112.2, 28.5, 13.3.
GC (achiral phase, 62.7 kPa He, method A): t_R = 3.93 min.
GC-MS (EI, 70 eV) *m/z* (%): 166 (88, M^+), 151 (46), 131 (100), 115 (65), 102 (40), 91 (28), 75 (26), 63 (13).

1-(But-1-en-2-yl)-3-chlorobenzene (5-SM)

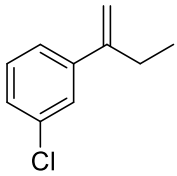

According to general procedure A, methyltriphenylphosphonium bromide (16.1 g, 45.0 mmol, 3.0 eq.) and potassium *tert*-butoxide (5.10 g, 45.5 mmol, 3.0 eq.) in dry THF (75 mL) were stirred at 0 °C for 2 h. After the addition of 1-(3-chlorophenyl)propan-1-one (2.53 g, 15.0 mmol, 1.0 eq.), the reaction was stirred at room temperature overnight. The crude product was purified by flash column chromatography (SiO_2, pentane/ethyl acetate 10:1) to afford 1-(but-1-en-2-yl)-3-chlorobenzene (**5-SM**, 10.2 mmol, 1.70 g, 68%) as a colorless liquid. Analytical data matches the literature.[249]
$C_{10}H_{11}Cl$ (167 g/mol):

^{1}H-NMR (400 MHz, 298 K, $CDCl_3$, δ/ppm): 7.46 (s, 1H), 7.40-7.19 (m, 3H), 5.33 (s, 1H), 5.13 (s, 1H), 2.50 (q, *J* = 7.4 Hz, 2H), 1.07 (t, *J* = 7.4 Hz, 3H).
^{13}C-{^{1}H}-NMR (126 MHz, 298 K, $CDCl_3$, δ/ppm): 150.0, 144.4, 134.8, 130.9, 128.2, 126.9, 125.5, 112.9, 28.5, 13.2.
GC (achiral phase, 62.7 kPa He, method A): t_R = 3.89 min.
GC-MS (EI, 70 eV) *m/z* (%): 166 (72, M^+), 151 (23), 131 (100), 115 (57), 91 (36), 75 (22), 63 (12).

S2.2.3 Synthesis of 9-SM

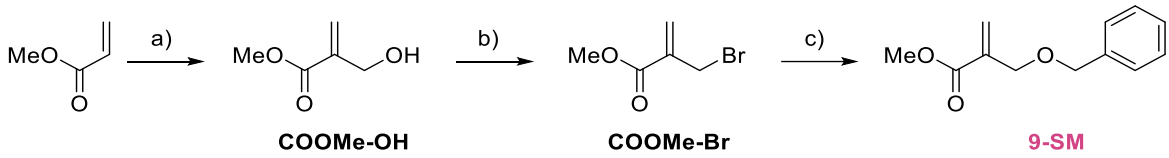

Scheme S2. Synthesis of 9-SM: a) $(CH_2O)_n$, DABCO, dioxane/H_2O (1:1 *v:v*), rt, 4.5 h, quant.; b) PBr_3, Et_2O, rt, 3 h, 97%; c) benzyl alcohol, DABCO, THF, 70 °C, overnight, 78%.

Methyl 2-(hydroxymethyl)acrylate (COOMe-OH)

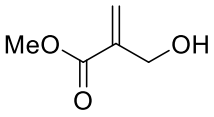

The synthesis of methyl 2-(hydroxymethyl)acrylate (**COOMe-OH**) was adapted from a previously published protocol.[250] Paraformaldehyde (10.2 g, 113 mmol, 1.0 eq.) and 1,4-diazabicyclo[2.2.2]octane (DABCO, 12.6 g, 112 mmol, 1.0 eq.) were suspended in a dioxane/H_2O mixture (20 mL, 1:1 *v:v*). Methyl acrylate (30 mL, 336 mmol, 3.0 eq.) was added and the reaction mixture was stirred at room temperature for 4.5 hours, resulting in full dissolution of the reagents. Water (50 mL) and diethyl ether (50 mL) were added, the layers were separated, and the aqueous layer was extracted with diethyl ether (2 x 100 mL). The combined organic layers were dried over anhydrous sodium sulfate, filtered and concentrated under reduced pressure. The crude product was purified by gradient flash column chromatography (SiO_2, cyclohexane/ethyl acetate 5:1 then neat ethyl acetate) to afford the product (**COOMe-OH**, 13.1 g, 113 mmol, quant.) as a colorless liquid. Analytical data matches the literature.[251]
$C_5H_8O_3$ (116 g/mol):
^{1}H-NMR (400 MHz, 298 K, $CDCl_3$, δ/ppm): 6.04 (pseudo-q, *J* = 1.4 Hz, 1H), 5.67 (pseudo-q, *J* = 1.6 Hz, 1H), 4.09 (s, 2H), 3.86 (br s, 1H), 3.55 (s, 3H).
^{13}C-{^{1}H}-NMR (101 MHz, 298 K, $CDCl_3$, δ/ppm): 166.4, 139.3, 124.8, 60.9, 51.5.

Methyl 2-(bromomethyl)acrylate (COOMe-Br)

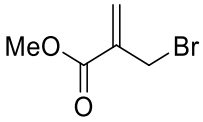

The synthesis of methyl 2-(bromomethyl)acrylate (**COOMe-Br**) was adapted from a previously published protocol.[250] Methyl 2-(hydroxymethyl)acrylate (**COOMe-OH**, 13.0 g, 113 mmol, 1.0 eq.) was dissolved in dry diethyl ether (150 mL) and the solution was cooled to 0 °C. PBr_3 (5.5 mL, 58.5 mmol, 0.5 eq.) was added dropwise and the reaction mixture was stirred at room temperature for 3 hours. At 0 °C, the reaction was quenched with water (50 mL), the layers were separated, and the aqueous layer was extracted with diethyl ether (3 x 100 mL). The combined organic layers were dried over anhydrous sodium sulfate, filtered and concentrated under reduced pressure to afford the product (**COOMe-Br**, 19.7 g, 110 mmol, 97%) as a yellow liquid. Analytical data matches the literature.[251]

$C_5H_7O_2Br$ (179 g/mol):

^{1}H-NMR (400 MHz, 298 K, $CDCl_3$, δ/ppm): 6.34 (d, *J* = 0.7 Hz, 1H), 5.96 (pseudo-q, *J* = 0.9 Hz, 1H), 4.18 (d, *J* = 1.0 Hz, 2H), 3.82 (s, 3H).

^{13}C-{^{1}H}-NMR (101 MHz, 298 K, $CDCl_3$, δ/ppm): 165.4, 137.4, 129.4, 52.4, 29.4.

Methyl 2-((benzyloxy)methyl)acrylate (9-SM)

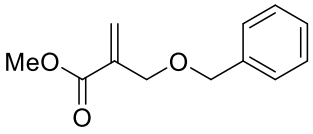

The synthesis of methyl 2-((benzyloxy)methyl)acrylate (**9-SM**) was adapted from a previously published protocol.[252] Methyl 2-(bromomethyl)acrylate (**COOMe-Br**, 5.03 g, 28.1 mmol, 1.0 eq.) and benzyl alcohol (5.2 mL, 50.0 mmol, 1.8 eq.) were dissolved in dry THF (5.0 mL) and the solution was cooled to 0 °C. A solution of 1,4-diazabicyclo[2.2.2]octane (4.62 g, 41.2 mmol, 1.5 eq.) dissolved in THF (30 mL) was added dropwise and the resulting white suspension was heated to 70 °C overnight. The suspension was filtered and the residue was washed with diethyl ether. The filtrate was washed with aq. HCl solution (0.5 M, 50 mL), sat. aq. $NHCO_3$ solution (50 mL) and brine (50 mL). The layers were separated, and the organic layer was dried over anhydrous sodium sulfate, filtered and concentrated under reduced pressure. The crude product was purified by flash column chromatography (SiO_2, neat DCM) to afford the product (**9-SM**, 4.49 g, 21.8 mmol, 78%) as a colorless liquid. Analytical data matches the literature.[252]

$C_{12}H_{14}O_3$ (206 g/mol):

^{1}H-NMR (500 MHz, 298 K, CD_3CN, δ/ppm): 7.39-7.33 (m, 4H), 7.33-7.28 (m, 1H), 6.23 (pseudo-q, *J* = 1.3 Hz, 1H), 5.89 (pseudo-q, *J* = 1.7 Hz, 1H), 4.55 (s, 2H), 4.21 (pseudo-t, *J* = 1.5 Hz, 2H), 3.72 (s, 3H).

^{13}C-{^{1}H}-NMR (126 MHz, 298 K, CD_3CN, δ/ppm): 167.1, 139.5, 138.7, 129.3, 128.6, 128.5, 126.3, 73.2, 69.2, 52.3.
GC (achiral phase, 62.7 kPa He, method A): t_R = 4.99 min.
GC-MS (EI, 70 eV) *m/z* (%): 107 (79), 100 (51), 91 (100), 83 (14), 79 (28), 77 (19), 69 (28), 65 (23).

S2.3 Synthesis of Hydrogenation Products

Table S4. Synthesis of the different hydrogenation products (**1-H** to **5-H** and **9-H** to **12-H**) as a reference for ^{1}H-NMR and GC-MS analysis. Hydrogenation products **6-H** and **8-H** were obtained from commercial sources.

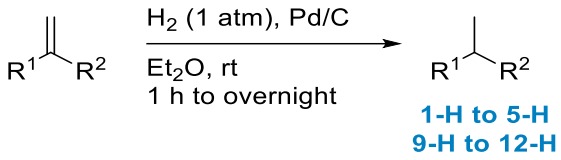

Hydrogenation Product	R^1	R^2	Yield / %
1-H	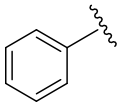	CH_2OMe	94
2-H	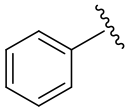	Et	94
3-H	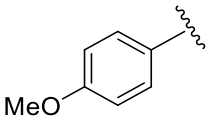	Et	96
4-H	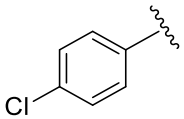	Et	94
5-H	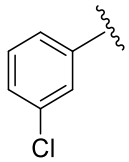	Et	92
9-H	COOMe	CH_2OBn	56
10-H		CH_2OBn	46
11-H	Me	CH_2OBn	89
12-H	H	OBn	74

General procedure B: Hydrogenation of terminal olefins

The terminal olefin was dissolved in dry diethyl ether (3.5 mL per mmol olefin) and Pd/C (10% Pd basis, 10% *w:w* with respect to the terminal olefin) was added. The reaction mixture was stirred under hydrogen atmosphere (1 atm) for several hours. The suspension was filtered over Celite and the filtrate was concentrated under reduced pressure to afford the hydrogenation product. If necessary, the crude product was further purified by flash column chromatography.

2-Phenyl-1-propyl methyl ether (1-H)

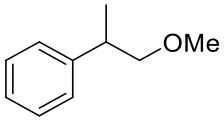

2-Phenyl-1-propyl methyl ether (**1-H**) was synthesized according to general procedure B. (3-Methoxyprop-1-en-2-yl)benzene (**1-SM**, 510 mg, 3.44 mmol, 1.0 eq.) and Pd/C (10% Pd basis, 50.9 mg) in diethyl ether (10 mL) were stirred under hydrogen atmosphere (1 atm) for 4 hours. 2-Phenyl-1-propyl methyl ether (**1-H**, 488 mg, 3.25 mmol, 94%) was obtained as a colorless liquid. Analytical data matches the literature.[253]

$C_{10}H_{14}O$ (150 g/mol):

^{1}H-NMR (400 MHz, 298 K, $CDCl_3$, δ/ppm): 7.34-7.28 (m, 2H), 7.25-7.19 (m, 3H) 3.55-3.40 (m, 2H), 3.34 (s, 3H), 3.03 (sext., *J* = 7.0 Hz, 1H), 1.29 (d, *J* = 7.0 Hz, 3H).

^{13}C-{^{1}H}-NMR (101 MHz, 298 K, CD_3CN, δ/ppm): 146.0, 129.2, 128.3, 127.1, 79.0, 58.7, 40.6, 18.7.

GC (achiral phase, 62.7 kPa He, method A): t_R = 3.53 min.

GC-MS (EI, 70 eV) *m/z* (%): 150 (14, M^+), 118 (6), 105 (100), 91 (7), 79 (14).

***sec*-Butylbenzene (2-H)**

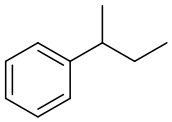

sec-Butylbenzene (**2-H**) was synthesized according to general procedure B. But-1-en-2-ylbenzene

(**2-SM**, 998 mg, 7.55 mmol, 1.0 eq.) and Pd/C (10% Pd basis, 100 mg) in diethyl ether (20 mL) were stirred under hydrogen atmosphere (1 atm) for 3 hours. *sec*-Butylbenzene (**2-H**, 955 mg, 7.13 mmol, 94%) was obtained as a colorless liquid. Analytical data matches the literature.[254]

$C_{10}H_{14}$ (134 g/mol):

^{1}H-NMR (400 MHz, 298 K, CD_3CN, δ/ppm): 7.32-7.26 (m, 2H), 7.23-7.15 (m, 3H), 2.61 (sext., *J* = 7.0 Hz, 1H), 1.60 (pent., *J* = 7.3 Hz, 2H), 1.22 (d, *J* = 7.0 Hz, 3H), 0.80 (t, *J* = 7.3 Hz, 3H).

^{13}C-{^{1}H}-NMR (101 MHz, 298 K, CD_3CN, δ/ppm): 148.7, 129.3, 128.0, 126.8, 42.4, 31.8, 22.3, 12.6.

GC (achiral phase, 62.7 kPa He, method A): t_R = 2.82 min.

GC-MS (EI, 70 eV) *m/z* (%): 134 (25, M^+), 105 (100), 91 (18), 77 (14).

1-(*sec*-Butyl)-4-methoxybenzene (3-H)

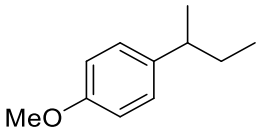

1-(*sec*-Butyl)-4-methoxybenzene (**3-H**) was synthesized according to general procedure B. 1-(But-1-en-2-yl)-4-methoxybenzene (**3-SM**, 998 mg, 6.15 mmol, 1.0 eq.) and Pd/C (10% Pd basis, 100 mg) in diethyl ether (20 mL) were stirred under hydrogen atmosphere (1 atm) for 5 hours. 1-(*sec*-Butyl)-4-methoxybenzene (**3-H**, 967 mg, 5.89 mmol, 96%) was obtained as a colorless liquid. Analytical data matches the literature.[249]

$C_{11}H_{16}O$ (164 g/mol):

^{1}H-NMR (400 MHz, 298 K, CD_3CN, δ/ppm): 7.17-7.08 (m, 2H), 6.89-6.81 (m, 2H), 3.75 (s, 3H), 2.62-2.48 (m, 1H), 1.62-1.49 (m, 2H), 1.19 (d, *J* = 7.0 Hz, 3H), 0.79 (t, *J* = 7.4 Hz, 3H).

^{13}C-{^{1}H}-NMR (126 MHz, 298 K, CD_3CN, δ/ppm): 158.8, 140.6, 128.8, 114.6, 55.8, 41.6, 32.0, 22.4, 12.6.

GC (achiral phase, 62.7 kPa He, method A): t_R = 3.98 min.

GC-MS (EI, 70 eV) *m/z* (%): 164 (18, M^+), 135 (100), 121 (11), 91 (14), 77 (10), 65 (6).

1-(*sec*-Butyl)-4-chlorobenzene (4-H)

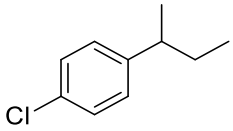

1-(*sec*-Butyl)-4-chlorobenzene (**4-H**) was synthesized according to general procedure B. 1-(But-1-en-2-yl)-4-chlorobenzene (**4-SM**, 998 mg, 5.99 mmol, 1.0 eq.) and Pd/C (10% Pd basis, 100 mg) in diethyl ether (20 mL) were stirred under hydrogen atmosphere (1 atm) for 5 hours. 1-(*sec*-Butyl)-4-chloro-benzene (**4-H**, 953 mg, 5.64 mmol, 94%) was obtained as a colorless liquid. Analytical data matches the literature.[249]

$C_{10}H_{13}Cl$ (169 g/mol):

^{1}H-NMR (400 MHz, 298 K, CD_3CN, δ/ppm): 7.32-7.27 (m, 2H), 7.21-7.17 (m, 2H), 2.61 (sext., *J* = 7.0 Hz, 1H), 1.65-1.49 (m, 2H), 1.20 (d, *J* = 7.0 Hz, 3H), 0.79 (t, *J* = 7.4 Hz, 3H).

^{13}C-{^{1}H}-NMR (126 MHz, 298 K, CD_3CN, δ/ppm): 147.6, 131.8, 129.7, 129.2, 41.8, 31.7, 22.1, 12.4.

GC (achiral phase, 62.7 kPa He, method A): t_R = 3.76 min.

GC-MS (EI, 70 eV) *m/z* (%): 168 (21, M^+), 141 (32), 139 (100), 125 (14), 103 (51), 77 (19).

1-(*sec*-Butyl)-3-chlorobenzene (5-H)

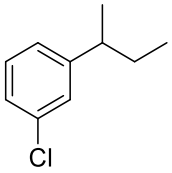

1-(*sec*-Butyl)-3-chlorobenzene (**5-H**) was synthesized according to general procedure B. 1-(But-1-en-2-yl)-3-chlorobenzene (**5-SM**, 998 mg, 5.99 mmol, 1.0 eq.) and Pd/C (10% Pd basis, 100 mg) in diethyl ether (20 mL) were stirred under hydrogen atmosphere (1 atm) for 5 hours. 1-(*sec*-Butyl)-3-chlorobenzene (**5-H**, 937 mg, 5.54 mmol, 92%) was obtained as a colorless liquid. Analytical data matches the literature.[249]

$C_{10}H_{13}Cl$ (169 g/mol):

^{1}H-NMR (400 MHz, 298 K, CD_3CN, δ/ppm): 7.31-7.13 (m, 4H), 2.62 (sext., *J* = 7.0 Hz, 1H), 1.64-1.54 (m, 2H), 1.21 (d, *J* = 7.0 Hz, 3H), 0.79 (t, *J* = 7.4 Hz, 3H).

^{13}C-{^{1}H}-NMR (126 MHz, 298 K, CD_3CN, δ/ppm): 150.8, 134.1, 130.5, 127.6, 126.4, 126.2, 41.8, 31.2, 21.6, 12.0.

GC (achiral phase, 62.7 kPa He, method A): t_R = 3.71 min.

GC-MS (EI, 70 eV) *m/z* (%): 168 (26, M^+), 141 (32), 139 (100), 125 (15), 103 (58), 91 (5), 77 (23).

Methyl 3-(benzyloxy)-2-methylpropanoate (9-H)

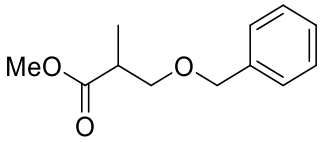

Methyl 3-(benzyloxy)-2-methylpropanoate (**9-H**) was synthesized according to general procedure B. Methyl 2-((benzyloxy)methyl)acrylate (**9-SM**, 994 mg, 4.82 mmol, 1.0 eq.) and Pd/C (10% Pd basis, 101 mg) in diethyl ether (15 mL) were stirred under hydrogen atmosphere (1 atm) for 3 h. The crude product was purified by gradient flash column chromatography (SiO_2, cyclohexane/ethyl acetate 20:1 then cyclohexane/ethyl acetate 5:1) to afford methyl 3-(benzyloxy)-2-methylpropanoate (**9-H**, 559 mg, 2.69 mmol, 56%) as a colorless liquid. Analytical data matches the literature.[255]

$C_{12}H_{16}O_3$ (208 g/mol):

^{1}H-NMR (500 MHz, 298 K, CD_3CN, δ/ppm): 7.43-7.17 (m, 5H), 4.47 (d, *J* = 1.9 Hz, 2H), 3.63 (s, 3H), 3.60 (dd, *J* = 9.2 Hz, 7.2 Hz, 1H), 3.52 (dd, *J* = 9.2 Hz, 5.5 Hz, 1H), 2.80-2.69 (m, 1H), 1.11 (d, *J* = 7.1 Hz, 3H).

^{13}C-{^{1}H}-NMR (126 MHz, 298 K, CD_3CN, δ/ppm): 157.6, 139.2, 128.9, 128.2, 128.1, 73.1, 72.6, 51.7, 40.5, 13.8.

GC (achiral phase, 62.7 kPa He, method A): t_R = 4.83 min.

GC-MS (EI, 70 eV) *m/z* (%): 121 (16), 107 (46), 102 (20), 91 (100), 87 (27), 79 (14), 65 (16).

((2-Cyclohexylpropoxy)methyl)benzene (10-H)

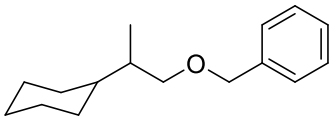

((2-Cyclohexylpropoxy)methyl)benzene (**10-H**) was synthesized according to general procedure B. (((2-Cyclohexylallyl)oxy)methyl)benzene (**10-SM**, 816 mg, 3.55 mmol, 1.0 eq.) and Pd/C (10% Pd basis, 88 mg) in diethyl ether (16 mL) were stirred under hydrogen atmosphere (1 atm) for 1.5 hours. The crude product was purified by gradient flash column chromatography (SiO_2, pentane/diethyl ether 10:1 then pentane/diethyl ether 3:1) to afford ((2-cyclohexylpropoxy)methyl)benzene (**10-H**, 379 mg, 1.63 mmol, 46%) as a colorless liquid. Analytical data matches the literature.[256]

$C_{16}H_{24}O$ (232 g/mol):

^{1}H-NMR (400 MHz, 298 K, CD_3CN, δ/ppm): 7.38-7.14 (m, 5H), 4.45 (s, 2H), 3.42 (dd, *J* = 9.2 Hz, 5.9 Hz, 1H), 3.28 (dd, *J* = 9.2 Hz, 6.7 Hz, 1H), 1.75-1.68 (m, 2H), 1.67-1.55 (m, 4H), 1.40-0.95 (m, 6H), 0.87 (d, *J* = 6.9 Hz, 3H).

^{13}C-{^{1}H}-NMR (101 MHz, 298 K, CD_3CN, δ/ppm): 140.2, 129.2, 128.5, 128.3, 74.6, 73.4, 40.7, 39.4, 31.6, 29.6, 27.6, 27.5, 27.4, 14.3.

GC (achiral phase, 62.7 kPa He, method B): t_R = 8.35 min.

GC-MS (EI, 70 eV) *m/z* (%): 124 (32), 111 (8), 91 (100), 81 (42), 69 (51), 55 (34).

Benzyl *iso*-butyl ether (11-H)

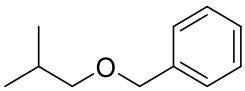

Benzyl *iso*-butyl ether (**11-H**) was synthesized according to general procedure B. ((2-Methylallyloxy)-methyl)benzene (**11-SM**, 1.01 g, 6.23 mmol, 1.0 eq.) and Pd/C (10% Pd basis, 92.5 mg) in diethyl ether (20 mL) were stirred under hydrogen atmosphere (1 atm) for 4 hours. Benzyl *iso*-butyl ether (**11-H**, 905 mg, 5.52 mmol, 89%) was obtained as a colorless liquid. Analytical data matches the literature.[257]

$C_{11}H_{16}O$ (164 g/mol):

^{1}H-NMR (400 MHz, 298 K, CD_3CN, δ/ppm): 7.36-7.33 (m, 4H), 7.31-7.27 (m, 1H), 4.51 (s, 2H), 3.25 (d, *J* = 6.7 Hz, 2H), 1.98-1.85 (m, 1H), 0.93 (d, *J* = 6.7 Hz, 6H).

^{13}C-{^{1}H}-NMR (126 MHz, 298 K, $CDCl_3$, δ/ppm): 140.2, 129.2, 128.5, 128.3, 77.9, 73.4, 29.3, 19.7.

GC (achiral phase, 62.7 kPa He, method A): t_R = 3.70 min.

GC-MS (EI, 70 eV) *m/z* (%): 91 (100), 65 (14).

Benzyl propyl ether (12-H)

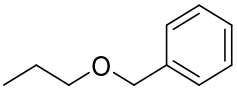

Benzyl propyl ether (**12-H**) was synthesized according to general procedure B. Benzyl allyl ether
(**12-SM**, 514 mg, 3.47 mmol, 1.0 eq.) and Pd/C (10% Pd basis, 51.5 mg) in diethyl ether (10 mL) were stirred under hydrogen atmosphere (1 atm) for 4 hours. Benzyl propyl ether (**12-H**, 386 mg, 2.57 mmol, 74%) was obtained as a colorless liquid. Analytical data matches the literature.[258]
$C_{10}H_{14}O$ (150 g/mol):
^{1}H-NMR (298 K, $CDCl_3$, δ/ppm): 7.37-7.32 (m, 4H), 7.32-7.26 (m, 1H), 4.52 (s, 2H), 3.44 (t, *J* = 6.7 Hz, 2H), 1.72-1.58 (m, 2H), 0.95 (t, *J* = 7.4 Hz, 3H).
^{13}C-{^{1}H}-NMR (101 MHz, 298 K, $CDCl_3$, δ/ppm): 138.9, 128.5, 127.8, 127.6, 73.0, 72.3, 23.1, 10.8.
GC (achiral phase, 62.7 kPa He, method A): t_R = 3.47 min.
GC-MS (EI, 70 eV) *m/z* (%): 107 (11), 91 (100), 79 (16), 65 (17).

S2.4 Synthesis of the Radical Clock Substrate and Reference Products

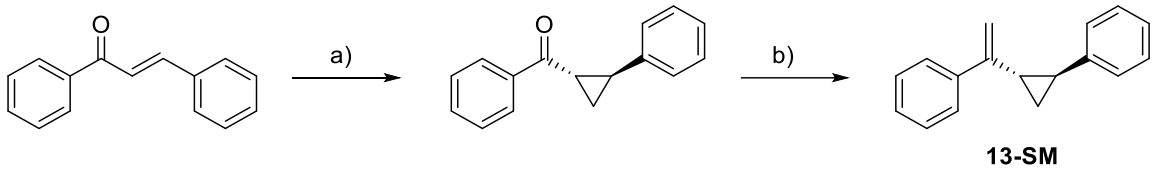

Scheme S3. Synthesis of the cyclopropane substrate (**13-SM**): a) Me_3SOI, NaH, DMSO, 0 °C → rt, 2 days, 76%; b) $MePPh_3Br$, KO^{t}Bu, THF, 0 °C → rt, overnight, 90%.

1-Benzoyl-2-phenylcyclopropane

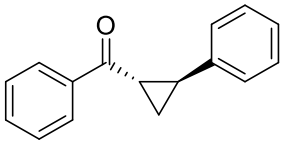

Sodium hydride (60%, dispersed in mineral oil, 1.15 g, 28.8 mmol, 1.2 eq.) and trimethylsulfoxonium iodide (5.88 g, 26.7 mmol, 1.1 eq.) were suspended in dry DMSO (40 mL). After the reaction mixture was cooled to 0 °C, (*E*)-chalcone (5.06 g, 24.3 mmol, 1.0 eq.) in dry DMSO (14 mL) was added and the reaction was stirred at room temperature for 2 days. The reaction was quenched with water (50 mL), the layers were separated, and the aqueous layer was extracted with diethyl ether (3 x 50 mL). The combined organic layers were dried over anhydrous sodium sulfate, filtered and concentrated under reduced pressure. The crude product was purified by flash column chromatography (SiO_2, pentane/diethyl ether 20:1) to afford 1-benzoyl-2-phenylcyclopropane (4.09 g, 18.4 mmol, 76%) as a colorless liquid. Analytical data matches the literature.[259]
$C_{16}H_{14}O$ (222 g/mol):

^{1}H-NMR (400 MHz, 298 K, $CDCl_3$, δ/ppm): 8.02-7.97 (m, 2H), 7.59-7.53 (m, 1H), 7.49-7.43 (m, 2H), 7.34-7.28 (m, 2H), 7.25-7.21 (m, 1H), 7.20-7.16 (m, 2H), 2.91 (ddd, *J* = 8.0 Hz, 5.3 Hz, 4.0 Hz, 1H), 2.70 (ddd, *J* = 9.2 Hz, 6.6 Hz, 4.0 Hz, 1H), 1.93 (ddd, *J* = 9.2 Hz, 5.3 Hz, 4.1 Hz, 1H), 1.56 (ddd, *J* = 8.0 Hz, 6.6 Hz, 4.1 Hz, 1H).
^{13}C-{^{1}H}-NMR (101 MHz, 298 K, $CDCl_3$, δ/ppm): 198.7, 140.6, 137.9, 133.1, 128.7, 128.3, 126.7, 126.4, 30.2, 29.5, 19.4.

(*trans*)-(1-(2-Phenylcyclopropyl)vinyl)benzene (13-SM)

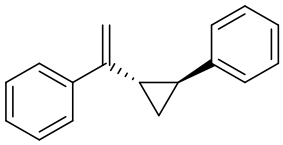

According to general procedure A, methyltriphenylphosphonium bromide (2.42 g, 6.77 mmol, 3.0 eq.) and potassium *tert*-butoxide (762 mg, 6.79 mmol, 3.0 eq.) in dry THF (11 mL) were stirred at 0 °C for 30 minutes. After addition of 1-benzoyl-2-phenylcyclopropane (497 mg, 2.23 mmol, 1.0 eq.) the reaction was stirred at room temperature overnight to afford a racemic mixture of *trans*-**13-SM**. The crude product was purified by flash column chromatography (SiO_2, neat cyclohexane) to afford (1-(2-phenylcyclopropyl)vinyl)benzene (**13-SM**, 444 mg, 2.02 mmol, 90%) as a colorless liquid. Analytical data matches the literature.[259]
$C_{17}H_{16}$ (220 g/mol):
^{1}H-NMR (400 MHz, 298 K, $CDCl_3$, δ/ppm): 7.54-7.49 (m, 2H), 7.34-7.25 (m, 5H), 7.22-7.14 (m, 3H), 5.37 (s, 1H), 5.05 (t, *J* = 1.1 Hz, 1H), 2.04-1.92 (m, 2H), 1.41 (ddd, *J* = 8.7 Hz, 6.2 Hz, 5.0 Hz, 1H), 1.28 (ddd, *J* = 8.5 Hz, 5.8 Hz, 5.0 Hz, 1H).
^{13}C-{^{1}H}-NMR (101 MHz, 298 K, $CDCl_3$, δ/ppm): 148.4, 142.7, 141.2, 128.6, 128.4, 127.7, 126.2, 125.9, 109.5, 28.0, 26.6, 16.0.

GC (achiral phase, 62.7 kPa He, method A): t_R = 5.70 min.
GC-MS (EI, 70 eV) *m/z* (%): 220 (50, M^+), 205 (34), 191 (8), 142 (74), 129 (100), 115 (49), 91 (41), 77 (28), 65 (11).

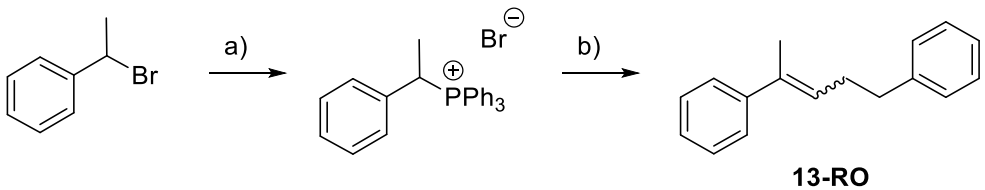

13-RO

Scheme S4. Synthesis of the ring-opened product (**13-RO**): a) PPh_3, toluene, reflux, 3 d, 91%; b) hydrocinnamaldehyde, *n*-BuLi, THF, −78 °C → 0 °C → rt, overnight, 36%.

(1-Phenethyl)triphenylphosphonium bromide

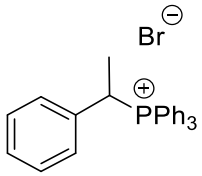

A solution of triphenylphosphane (1.50 g, 5.72 mmol, 1.1 eq.) in dry toluene (6 mL) was treated with (1-bromoethyl)benzene (0.74 mL, 5.42 mmol, 1.0 eq.) and the reaction mixture was stirred at reflux for 3 days. The resulting suspension was allowed to cool to room temperature. The white precipitate was collected by filtration, washed with toluene (10 mL) and dried *in vacuo* to afford (1-phenethyl)triphenylphosphonium bromide (2.20 g, 4.92 mmol, 91%) as a white solid. Analytical data matches the literature.[260]

$C_{26}H_{24}PBr$ (447 g/mol):

^{1}H-NMR (400 MHz, 298 K, $CDCl_3$, δ/ppm): 7.87-7.79 (m, 6H), 7.78-7.72 (m, 3H), 7.67-7.59 (m, 6H), 7.25-7.21 (m, 1H), 7.20-7.12 (m, 4H), 6.84 (dq, *J* = 14.3 Hz, *J* = 7.2 Hz, 1H), 1.82 (dd, *J* = 19.1 Hz, *J* = 7.2 Hz, 3H).

^{31}P-{^{1}H}-NMR (162 MHz, 298 K, $CDCl_3$, δ/ppm): 27.3.

^{13}C-{^{1}H}-NMR (101 MHz, 298 K, $CDCl_3$, δ/ppm): 134.9 (d, *J* = 3.0 Hz), 134.7 (d, *J* = 9.2 Hz), 133.5 (d, *J* = 5.5 Hz), 130.5 (d, *J* = 5.9 Hz), 130.2 (d, *J* = 12.2 Hz), 128.9 (d, *J* = 3.5 Hz), 128.8 (d, *J* = 2.6 Hz), 117.8 (d, *J* = 82.6 Hz), 35.0 (d, *J* = 42.9 Hz), 17.1 (d, *J* = 1.6 Hz).

Pent-3-ene-1,4-diyldibenzene (13-RO)

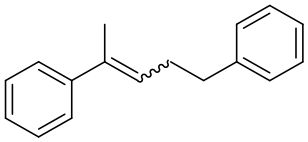

A suspension of (1-phenethyl)triphenylphosphonium bromide (917 mg, 2.05 mmol, 1.1 eq.) in dry THF (2 mL) was cooled to −78 °C. *n*-BuLi (2.5 M in hexanes, 0.93 mL, 2.33 mmol, 1.2 eq.) was added dropwise and the reaction mixture was stirred at 0 °C for 30 minutes. At 0 °C, a solution of hydrocinnamaldehyde (0.25 mL, 1.88 mmol, 1.0 eq.) in dry THF (1 mL) was added dropwise and the reaction mixture was stirred at room temperature overnight. The reaction was quenched with aq. sat. NH_4Cl solution (5 mL), the layers were separated, and the aqueous layer was extracted with diethyl ether (3 x 10 mL). The combined organic layers were dried over anhydrous sodium sulfate, filtered and concentrated under reduced pressure. The crude product was purified and the isomers were separated by gradient flash column chromatography (SiO_2, neat cyclohexane then cyclohexane/ethyl acetate 10:1) to afford (*E*)-pent-3-ene-1,4-diyldibenzene (**(*E*)-13-RO**, 121 mg, 545 µmol, 29%) and (*Z*)-pent-3-ene-1,4-diyldibenzene (**(*Z*)-13-RO** 27.4 mg, 123 µmol, 6.5%) as colorless liquids. Analytical data matches the literature.[261]

$C_{17}H_{18}$ (222 g/mol):

(*E*)-Pent-3-ene-1,4-diyldibenzene

^{1}H-NMR (400 MHz, 298 K, $CDCl_3$, δ/ppm): δ 7.39-7.11 (m, 10H), 5.81 (tq, *J* = 7.1 Hz, 1.4 Hz, 1H), 2.81-2.72 (m, 2H), 2.52 (q, *J* = 7.5 Hz, 2H), 1.97 (q, *J* = 1.0 Hz, 3H).

^{13}C-{^{1}H}-NMR (101 MHz, 298 K, $CDCl_3$, δ/ppm): 144.0, 142.2, 135.6, 128.7, 128.5, 128.3, 127.5, 126.7, 126.0, 125.8, 36.0, 30.9, 15.9.

GC (achiral phase, 62.7 kPa He, method A): t_R = 5.73 min.

GC-MS (EI, 70 eV) *m/z* (%): 222 (6, M^+), 131 (100), 115 (10), 91 (37), 65 (6).

(*Z*)-Pent-3-ene-1,4-diyldibenzene

^{1}H-NMR (400 MHz, 298 K, $CDCl_3$, δ/ppm): 7.36-7.07 (m, 10H), 5.50 (tq, *J* = 7.3 Hz, 1.5 Hz, 1H), 2.64 (dd, *J* = 8.9 Hz, 6.7 Hz, 2H), 2.33-2.24 (m, 2H), 2.02 (q, *J* = 1.3 Hz, 3H).

^{13}C-{^{1}H}-NMR (101 MHz, 298 K, $CDCl_3$, δ/ppm): 142.2, 142.1, 137.1, 128.6, 128.4, 128.2, 128.0, 126.8, 126.6, 125.9, 36.5, 31.1, 25.7.

GC (achiral phase, 62.7 kPa He, method A): t_R = 5.46 min.

GC-MS (EI, 70 eV) *m/z* (%): 222 (7, M^+), 131 (100), 115 (11), 91 (39), 77 (5), 65 (6).

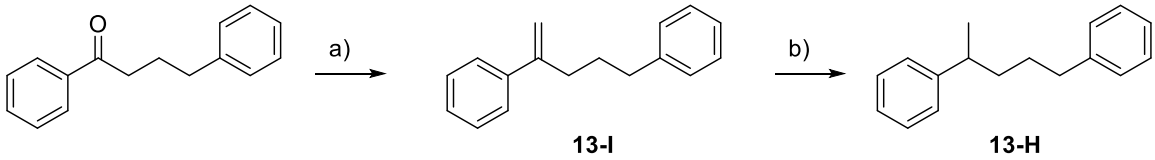

Scheme S5. Synthesis of the isomerization product (**13-I**) and the ring-opened hydrogenation product (**13-H**): a) PPh_3MeBr, KO^{t}Bu, THF, 0 °C → rt, overnight, 91%; b) H_2 (1 atm), Pd/C, Et_2O, rt, 2 h, 97%.

Pent-4-ene-1,4-diyldibenzene (13-I)

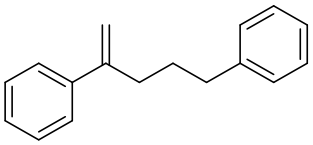

According to general procedure A, methyltriphenylphosphonium bromide (2.41 g, 6.75 mmol, 3.0 eq.) and potassium *tert*-butoxide (752 mg, 6.70 mmol, 3.0 eq.) in dry THF (10 mL) were stirred at 0 °C for 30 minutes. After the addition of 1,4-diphenylbutan-1-one (501 mg, 2.23 mmol, 1.0 eq.), the reaction was stirred at room temperature overnight. The crude product was purified by flash column chromatography (SiO_2, neat petroleum ether) to afford pent-4-ene-1,4-diyldibenzene (**13-I**, 450 mg, 2.03 mmol, 91%) as a colorless liquid. Analytical data matches the literature.[262]

$C_{17}H_{18}$ (222 g/mol):

^{1}H-NMR (400 MHz, 298 K, $CDCl_3$, δ/ppm): 7.41-7.36 (m, 2H), 7.34-7.23 (m, 5H), 7.20-7.12 (m, 3H), 5.32-5.21 (m, 1H), 5.07 (pseudo-q, *J* = 1.4 Hz, 1H), 2.69-2.60 (m, 2H), 2.59-2.49 (m, 2H), 1.84-1.73 (m, 2H).

^{13}C-{^{1}H}-NMR (126 MHz, 298 K, CD_3CN, δ/ppm): 149.5, 143.5, 142.0, 129.3, 129.3, 129.2, 128.4, 127.0, 126.6, 113.0, 35.8, 35.3, 30.9.

GC (achiral phase, 62.7 kPa He, 100 °C, 35 °C/min, 200 °C, 100 °C/min, 350 °C): t_R = 5.64 min.
GC-MS (EI, 70 eV) *m/z* (%): 118 (100), 104 (29), 91 (20), 77 (12), 65 (7).

Pentane-1,4-diyldibenzene (13-H)

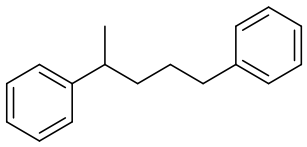

According to general procedure B, pent-4-ene-1,4-diyldibenzene (**13-I**, 221 mg, 994 µmol, 1.0 eq.) and Pd/C (10% Pd basis, 19 mg) in diethyl ether (4 mL) were stirred under hydrogen atmosphere for 2 hours. Pent-4-ene-1,4-diyldibenzene (**13-H**, 215 mg, 960 µmol, 97%) was obtained as a colorless liquid.
$C_{17}H_{20}$ (224 g/mol):
^{1}H-NMR (500 MHz, 298 K, CD_3CN, δ/ppm): 7.34-7.25 (m, 4H), 7.24-7.13 (m, 6H), 2.79-7.71 (m, 1H), 2.66-2.53 (m, 2H), 1.66-1.50 (m, 3H), 1.49-1.41 (m, 1H), 1.23 (d, *J* = 6.9 Hz, 3H).
^{13}C-{^{1}H}-NMR (126 MHz, 298 K, CD_3CN, δ/ppm): 148.7, 143.7, 129.3, 129.3, 129.2, 127.9, 126.8, 126.5, 40.4, 38.6, 36.3, 30.5, 22.6.
GC (achiral phase, 62.7 kPa He, method A): t_R = 5.54 min.
GC-MS (EI, 70 eV) *m/z* (%): 224 (20, M^+), 105 (100), 91 (25), 77 (9), 65 (6).

S2.5 Synthesis of the Deuterated Substrate (1-SM-*d*$_4$)

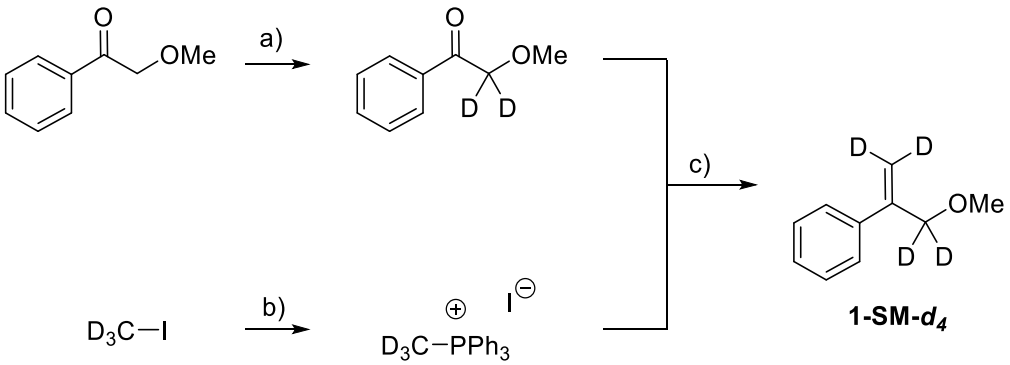

Scheme S6. Synthesis of the deuterated substrate **1-SM-*d*$_4$**: a) NaOH, D_2O, reflux, 1 h, 92%; b) PPh_3, THF, reflux, 45 min., quant.; c) KO^{t}Bu, THF, 0 °C → rt, overnight, 33%.

2-Methoxy-1-phenylethan-1-one-*2,2-d*$_2$

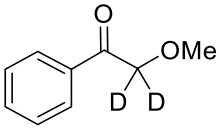

2-Methoxy-1-phenylethan-1-one (499 mg, 3.32 mmol, 1.0 eq.) and grinded NaOH (5.7 mg, 143 µmol, 0.04 eq.) were dissolved in D_2O and stirred under reflux for 1 hour. After cooling to rt, DCM (10 mL) was added, the layers were separated, and the aqueous

layer was extracted with DCM (2 x 10 mL). The combined organic layers were dried over anhydrous sodium sulfate, filtered and concentrated under reduced pressure to afford 2-methoxy-1-phenylethan-1-one-*2,2-d*$_2$ (464 mg, 3.05 mmol, 92%, contains 4.1% of the monodeuterated product) as a yellow liquid. Analytical data matches the literature.[263]
$C_9H_8D_2O_2$ (152 g/mol):
^{1}H-NMR (400 MHz, 298 K, CD_3CN, δ/ppm): 7.94-7.89 (m, 2H), 7.67-7.60 (m, 1H), 7.54-7.48 (m, 2H), 3.41 (s, 3H).
^{13}C-{^{1}H}-NMR (101 MHz, 298 K, CD_3CN, δ/ppm): 197.6, 136.1, 134.3, 129.7, 128.6, 59.3.
The deuterated carbon atom is not visible in the ^{13}C-{^{1}H}-NMR spectrum.

(Methyl-*d*$_3$)triphenylphosphonium iodide

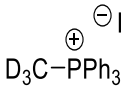

Triphenylphosphane (1.55 g, 5.91 mmol, 1.0 eq.) was dissolved in dry THF (7 mL). Iodomethane-*d*$_3$ (0.43 mL, 6.91 mmol, 1.2 eq.) was added and the reaction mixture was stirred at reflux for 45 minutes. The resulting white suspension was allowed to cool to room temperature. The white precipitate was collected by filtration, washed with toluene (10 mL) and dried *in vacuo* to afford (methyl-*d*$_3$)triphenylphosphonium iodide (2.41 g, 5.91 mmol, quant.) as a white solid. Analytical data matches the literature.[264]
$C_{19}H_{15}D_3PI$ (407 g/mol):
^{1}H-NMR (400 MHz, 298 K, $CDCl_3$, δ/ppm): 7.85-7.65 (m, 15H).
^{31}P-{^{1}H}-NMR (162 MHz, 298 K, $CDCl_3$, δ/ppm): 21.5.
^{13}C-{^{1}H}-NMR (101 MHz, 298 K, $CDCl_3$, δ/ppm): 135.4 (d, *J* = 2.9 Hz), 133.5 (d, *J* = 10.8 Hz), 130.6 (d, *J* = 12.9 Hz), 119.0 (d, *J* = 88.5 Hz).
The deuterated carbon atom is not visible in the ^{13}C-{^{1}H}-NMR spectrum.

(3-Methoxyprop-1-en-2-yl-*1,1,3,3-d*$_4$)benzene (1-SM-*d*$_4$)

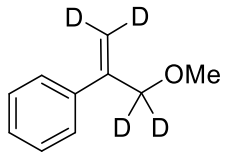

(Methyl-*d*$_3$)triphenylphosphonium iodide (2.76 g, 6.78 mmol, 2.5 eq.) was suspended in dry THF (20 mL). At 0 °C, potassium *tert*-butoxide (608 mg, 5.42 mmol, 2.0 eq) was added and the resulting yellow suspension was stirred at 0 °C for 30 minutes. 2-Methoxy-1-phenylethan-1-one-*2,2-d*$_2$ (412 mg, 2.71 mmol, 1.0 eq.) was added and the reaction mixture was stirred at room temperature overnight. The reaction was quenched with water (20 mL), the layers were separated, and the aqueous layer was extracted with diethyl ether (3 x 20 mL). The combined organic layers were dried over anhydrous sodium sulfate, filtered and concentrated under reduced pressure. The resulting crude product was purified by gradient flash column chromatography (SiO_2, cyclohexane/ethyl acetate

20:1 then cyclohexane/ethyl acetate 10:1) to afford (3-methoxyprop-1-en-2-yl-*1,1,3,3-d*$_4$)benzene (**1-SM-*d*$_4$**, 135 mg, 888 µmol, 33%, contains 6% of non-deuterated olefin) as a light yellow liquid.

$C_{10}H_8D_4O$ (152 g/mol):

^{1}H-NMR (500MHz, 298 K, CD_3CN, δ/ppm): 7.57-7.47 (m, 2H), 7.40-7.33 (m, 2H), 7.32-7.28 (m, 1H), 3.30 (s, 3H).

^{13}C-{^{1}H}-NMR (126 MHz, 298 K, CD_3CN, δ/ppm): 129.3, 128.7, 127.0, 57.9.

The deuterated and the quaternary carbon atoms are not visible in the ^{13}C-{^{1}H}-NMR spectrum.

GC-MS (EI, 70 eV) *m/z* (%): 152 (6), 151 (9), 122 (100), 109 (18), 105 (45), 78 (20), 51 (13).

S2.6 Synthesis of the Triarylamine Donor

Tris(4-anisyl)amine (TAA-OMe)

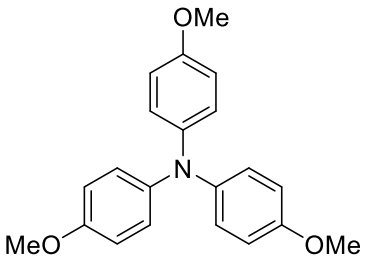

Tris(4-anisyl)amine was synthesized following a previously published protocol.[265] *p*-Anisidine (2.00 g, 16.2 mmol, 1.0 eq.), *p*-bromoanisole (9.09 g, 48.6 mmol, 3.0 eq.) and NaO^{t}Bu (3.89 g, 40.5 mmol, 2.5 eq.) were dissolved in dry toluene and the reaction mixture was degassed by bubbling N_2 through the solution for 15 min. [$Pd_2(dba)_3$] (297 mg, 324 µmol, 2.0 mol%) and SPhos (333 mg, 810 µg, 5.0 mol%) were added and the reaction mixture was degassed for another 10 min. The suspension was heated at reflux for 3 days. After cooling to room temperature, the reaction mixture was filtered over Celite and washed with DCM. The filtrate was concentrated under reduced pressure and the crude product was purified by gradient flash column chromatography (SiO_2, pure pentane then pentane/ethyl acetate 9:1). The resulting yellow liquid was treated with *n*-hexane and the formed precipitate was collected by filtration. Recrystallization from *n*-hexane (150 mL) afforded tris(4-anisyl)amine (4.57 g, 13.6 mmol, 84%) as off-white needles. Analytical data matches the literature.[266]

^{1}H-NMR (500 MHz, 298 K, $CDCl_3$, δ/ppm): 6.97 (d, *J* = 7.1 Hz, 6H), 6.82-6.76 (m, 6H), 3.78 (s, 9H).

^{13}C-{^{1}H}-NMR (126 MHz, 298 K, $CDCl_3$, δ/ppm): 155.1, 142.2, 124.9, 114.6, 55.6.

S3 Visible-Light Driven Hydrogenation of Unactivated Olefins

S3.1 General Procedure and Methods

General procedure C: Light-induced hydrogenation of olefins

The work-flow for the visible-light driven hydrogenation of olefins is depicted in Fig. S2. Degassed stock solutions of the substrate (150 µL, 500mM in CD_3CN, 75.0 µmol, 1.0 eq.), [Cp*Ir(phen)Cl]Cl (375 µL, 10 mM in CD_3CN, 3.75 µmol, 5.0 mol%), 1,10-phenanthroline (150 µL, 150 mM, 22.5 µmol, 30 mol%) and *tert*-butylbenzene (150 µL, 500 mM in CD_3CN, 75.0 µmol, 1.0 eq.) as an internal standard were combined and further diluted with degassed CD_3CN (675 µL). TEA (52 µL, 375 µmol, 5.0 eq.) was added and 0.5 mL of the reaction mixture were transferred to an NMR-tube. The reaction was then irradiated at 470 nm for 44 h, while the temperature was kept at 50 °C using an external thermostat (see section S1 for details about the home-built photoreactor). The conversion was determined both by ^{1}H-NMR spectroscopy (see section S3.1.1 for details) and GC-MS spectrometry (see section S3.1.2 for details). For GC-MS analysis, 200 µL of the reaction mixture were diluted with hexane (2.0 mL) and aq. HCl solution (0.5 M, 1.0 mL) was added. The layers were separated, and the organic layer was dried over anhydrous sodium sulfate, passed through a syringe filter and injected into the GC-MS spectrometer.

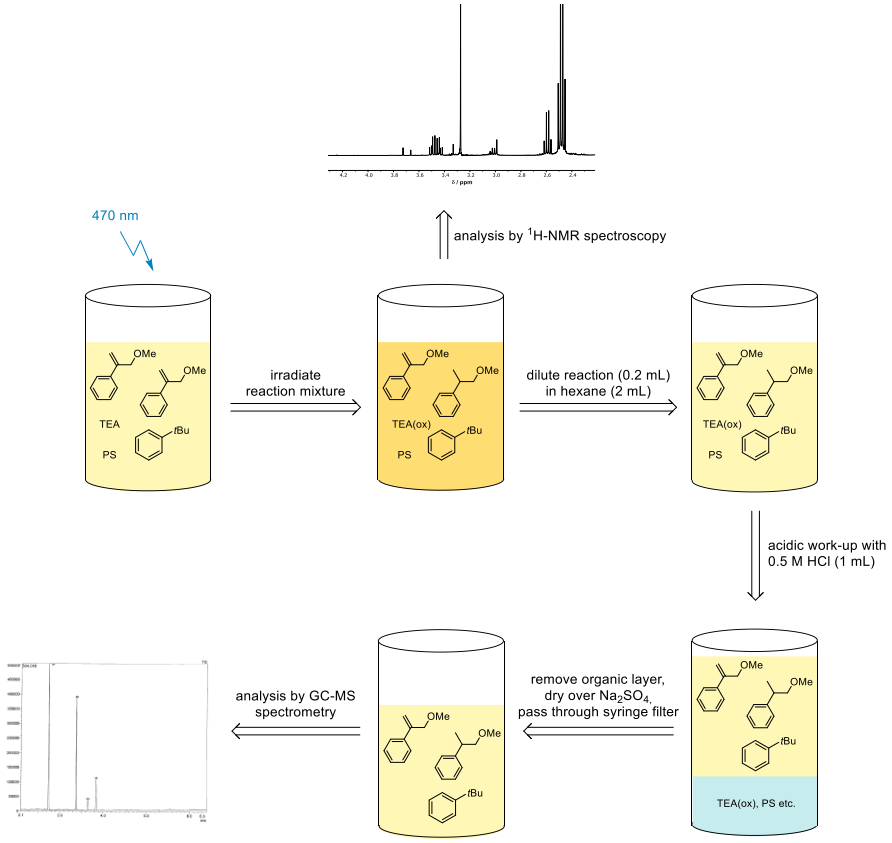

Figure S2. Typical work-flow for the light-induced hydrogenation of unactivated olefins catalyzed by iridium-hydrides. TEA(ox) stands for oxidation products of triethylamine. See text for further details.

S3.1.1 Reaction Monitoring Based on ^{1}H-NMR Spectroscopy

The reaction progress of the visible-light driven hydrogenation of olefins was monitored by ^{1}H-NMR spectroscopy. The conversion was determined by relative integration of the characteristic signals of each compound with respect to *tert*-butylbenzene (9H at 1.31 ppm in CD_3CN) as an internal standard. We estimate that the experimental uncertainty associated with this procedure is on the order of 10%.

S3.1.2 Reaction Monitoring Based on GC-MS Spectrometry

The NMR yield of the hydrogenation product was further confirmed by GS-MS spectrometry (see section S1 for instrumental details and methods). For this purpose, calibration curves were established for the different hydrogenation products (H) with respect to *tert*-butylbenzene as an internal standard (ISTD, t_R = 2.74 min.). To do so, the A_H/A_{ISTD} ratios were plotted against the c_H/c_{ISTD} ratios, where *A* is the area obtained in the GC trace and *c* is the concentration of the analytes. The slope and the intercept of the calibration curves were determined based on linear regression using equation S1.

$$\frac{A_{\mathrm{H}}}{A_{\mathrm{ISTD}}} = a + b\frac{c_{\mathrm{H}}}{c_{\mathrm{ISTD}}} \qquad \text{(eq. S1)}$$

The GC-MS yield of the hydrogenation product was determined based on relative integration of the GC-trace with respect to the area of the ISTD. The concentration of the hydrogenation product (c_H) was then determined by solving the linear equation S1 for C_H:

$$c_{\mathrm{H}} = \frac{({}^{A_{\mathrm{H}}}/_{A_{\mathrm{ISTD}}} - a)/b}{c_{\mathrm{ISTD}}} \qquad \text{(eq. S2)}$$

S3.2 Substrate Scope

S3.2.1 Light-Driven Hydrogenation of (3-Methoxyprop-1-en-2-yl)benzene (1-SM)

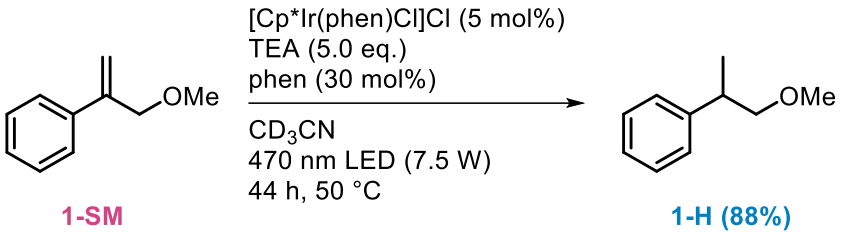

(3-Methoxyprop-1-en-2-yl)benzene (**1-SM**) was reduced to 2-phenyl-1-propyl methyl ether (**1-H**) according to general procedure C. Based on ^{1}H-NMR spectroscopy, the conversion of **1-SM** was determined to be 94%, affording **1-H** in 88% yield. Isomerization to (1-methoxyprop-1-en-2-yl)benzene (**1-R**) was observed in minor amounts (6%). The formation of 2-phenyl-1-propyl methyl ether (**1-H**) was further confirmed by GC-MS spectrometry (90% formation of hydrogenation product **1-H** with respect to *tert*-butylbenzene as an internal standard).

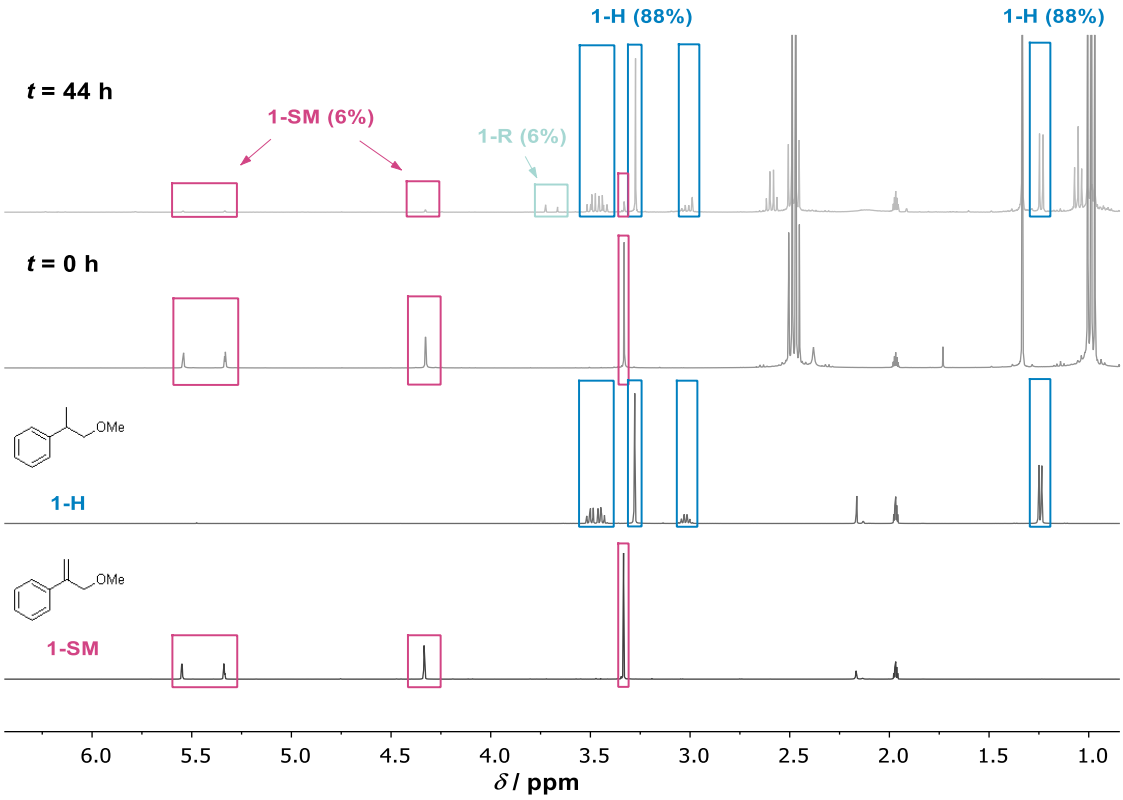

Figure S3. ^{1}H-NMR spectra for the light-driven hydrogenation of (3-methoxyprop-1-en-2-yl)benzene (**1-SM**) in CD_3CN: The ^{1}H-NMR spectra of the reaction mixture before (t = 0 h) and after (t = 44 h) irradiation are shown in comparison to the ^{1}H-NMR spectra of neat (3-methoxyprop-1-en-2-yl)benzene (**1-SM**) and 2-phenyl-1-propyl methyl ether (**1-H**). The triplet at 1.02 ppm and the quartet at 2.56 ppm in the top spectrum are due to diethylamine resulting from TEA oxidation.

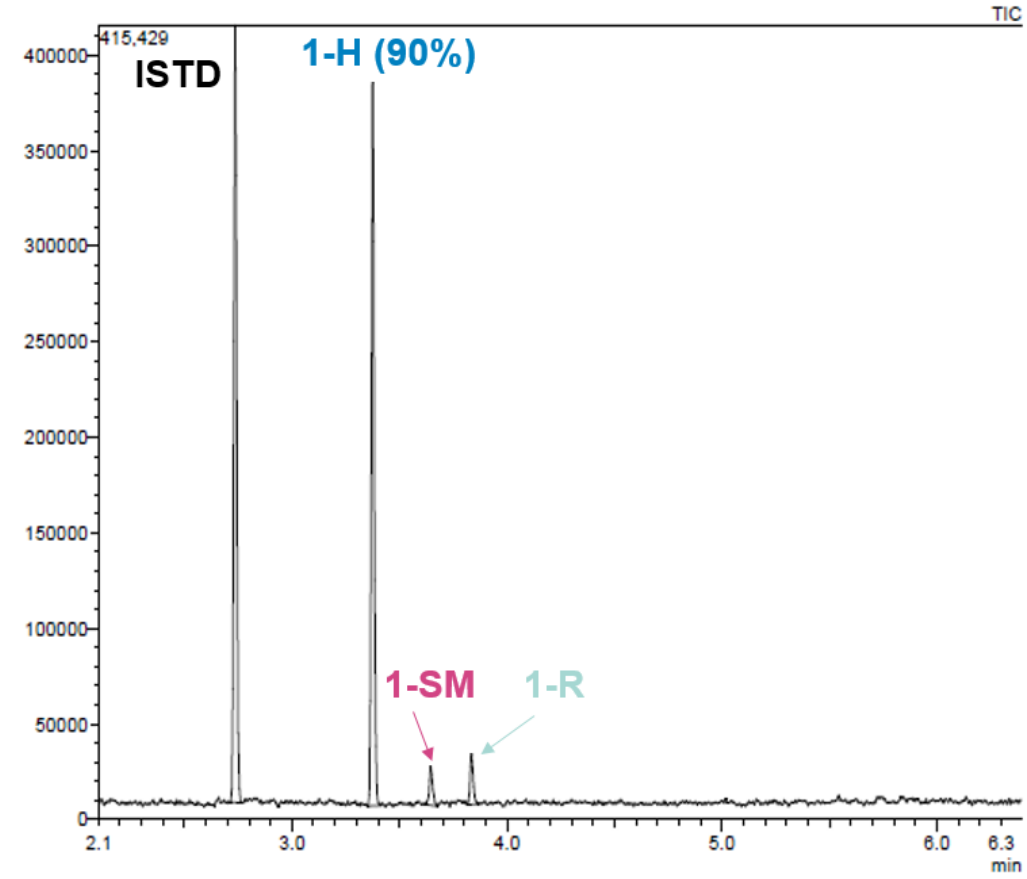

Figure S4. GC-MS trace of the light-induced hydrogenation of (3-methoxyprop-1-en-2-yl)benzene (**1-SM**) to afford 2-phenyl-1-propyl methyl ether (**1-H**) and (1-methoxyprop-1-en-2-yl)benzene (**1-R**). The different analytes were separated using GC method A (see section S1 for details).

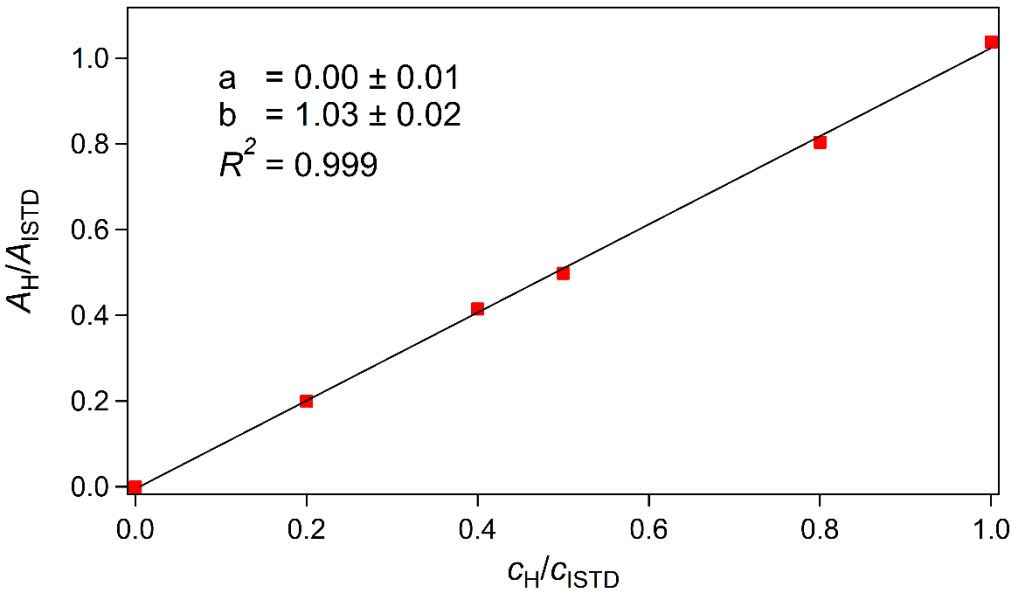

Figure S5. GC-MS calibration curve of 2-phenyl-1-propyl methyl ether (**1-H**) with respect to *tert*-butylbenzene (**ISTD**, 5 mM).

S3.2.2 Light-Driven Hydrogenation of But-1-en-2-ylbenzene (2-SM)

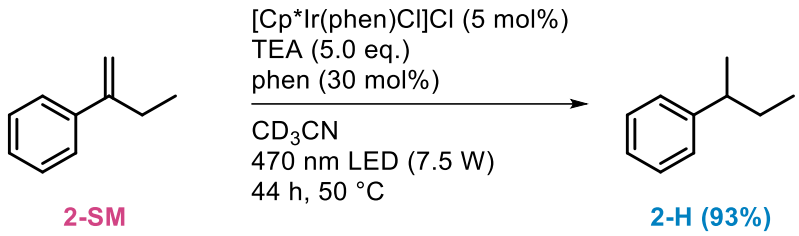

But-1-en-2-ylbenzene (**2-SM**) was reduced to *sec*-butylbenzene (**2-H**) according to general procedure C. Based on ^{1}H-NMR spectroscopy, 97% conversion of **2-SM** was achieved, affording **2-H** in 93% yield. Isomerization to but-2-en-2-ylbenzene (**2-R**) was observed in minor amounts (4%). The formation of *sec*-butylbenzene (**2-H**) was further confirmed by GC-MS spectrometry (92% formation of hydrogenation product **2-H** with respect to *tert*-butylbenzene as an internal standard).

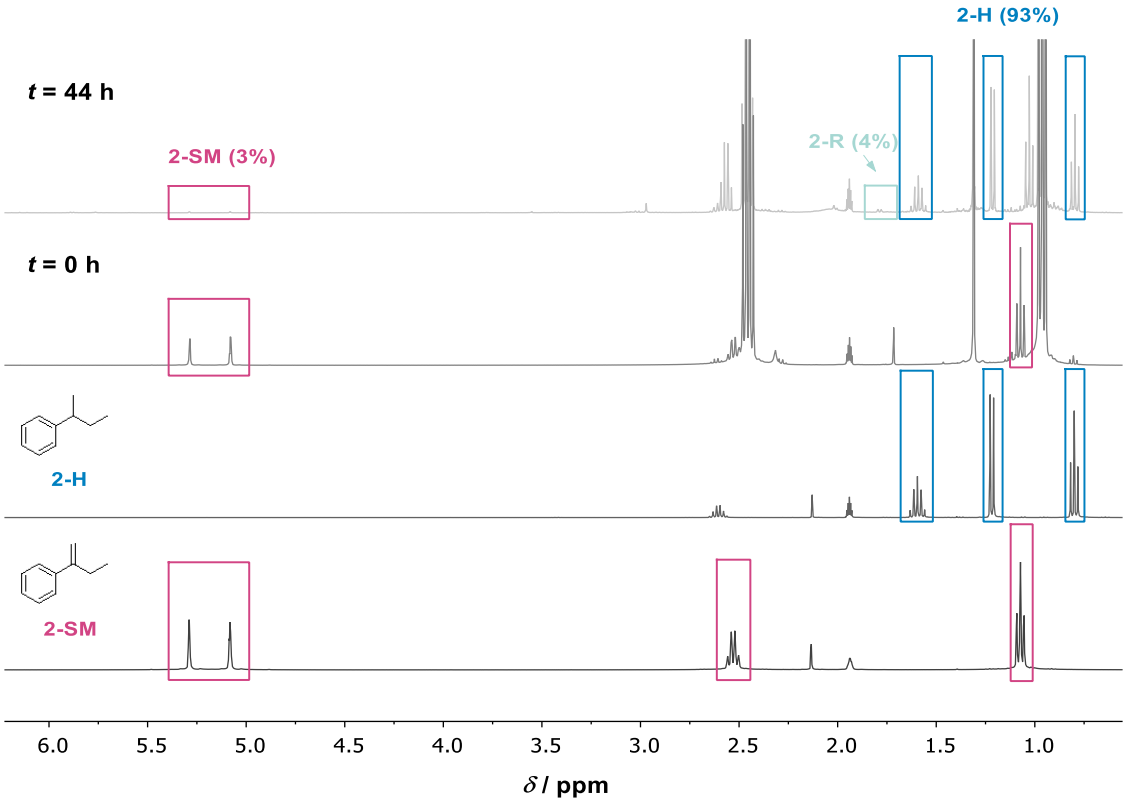

Figure S6. ^{1}H-NMR spectra of the light-driven hydrogenation of but-1-en-2-ylbenzene (**2-SM**) in CD_3CN: The ^{1}H-NMR spectra of the reaction mixture before (t = 0 h) and after (t = 44 h) irradiation are shown in comparison to the ^{1}H-NMR spectra of neat but-1-en-2-ylbenzene (**2-SM**) and *sec*-butylbenzene (**2-H**). The triplet at 1.02 ppm and the quartet at 2.56 ppm in the top spectrum are due to diethylamine resulting from TEA oxidation.

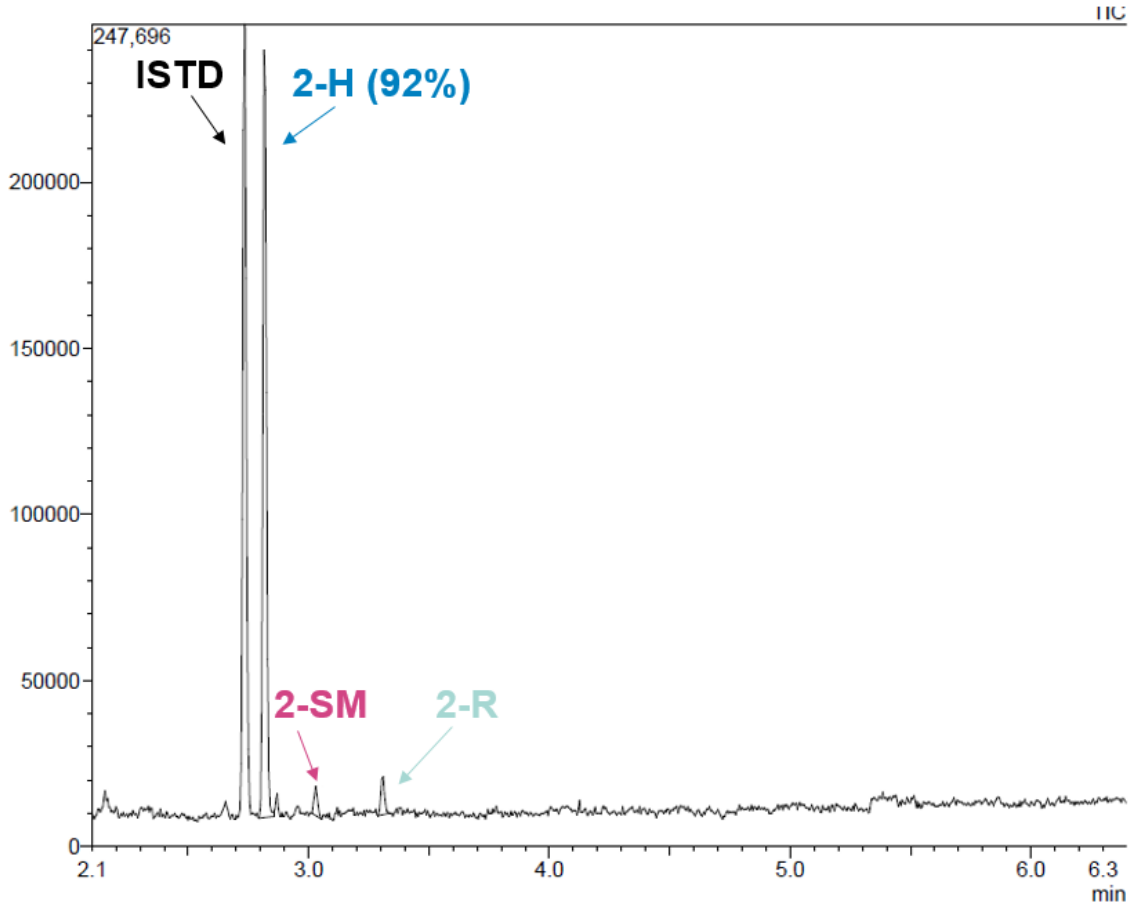

Figure S7. GC-MS trace of the light-induced hydrogenation of but-1-en-2-ylbenzene (**2-SM**) to afford *sec*-butylbenzene (**2-H**) and but-2-en-2-ylbenzene (**2-R**). The different analytes were separated using GC method A (see section S1 for details).

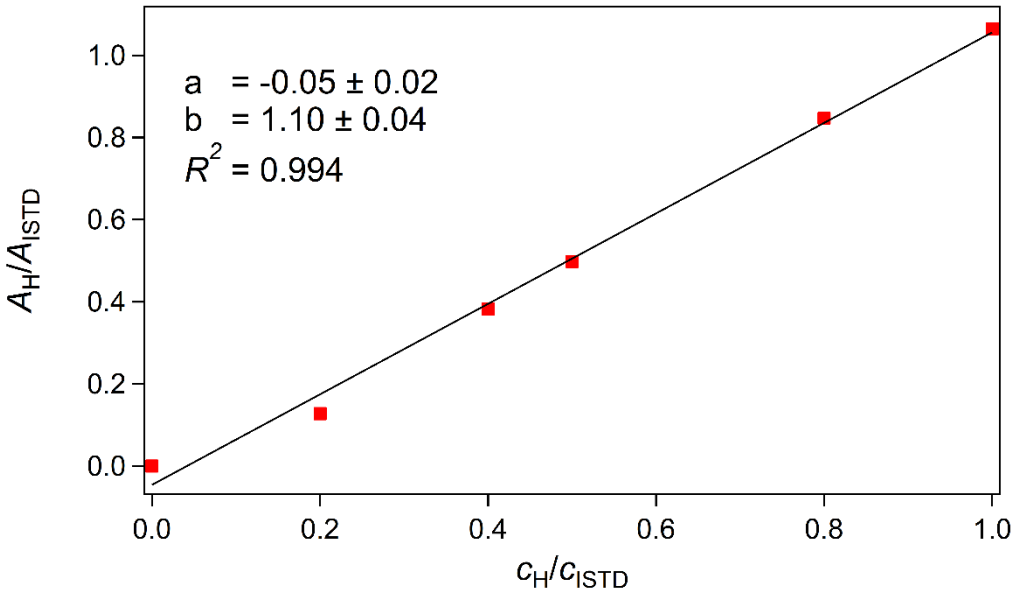

Figure S8. GC-MS calibration curve of *sec*-butylbenzene **(2-H)** with respect to *tert*-butylbenzene (**ISTD**, 5 mM).

S3.2.3 Light-Driven Hydrogenation of 1-(But-1-en-2-yl)-4-methoxybenzene (3-SM)

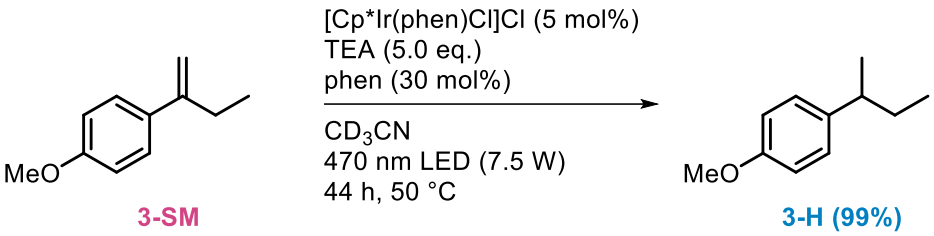

3-SM 3-H (99%)

1-(But-1-en-2-yl)-4-methoxybenzene (**3-SM**) was reduced to 1-(*sec*-butyl)-4-methoxybenzene (**3-H**) according to general procedure C. Based on ^{1}H-NMR spectroscopy, the conversion of **3-SM** was determined to be essentially quantitative, giving hydrogenation product **3-H** in 99% analytical yield. Isomerization to 1-(but-2-en-2-yl)-4-methoxybenzene (**3-R**) was observed in minor amounts (~1%). The formation of 1-(*sec*-butyl)-4-methoxybenzene (**3-H**) was further confirmed by GC-MS spectrometry (95% formation of hydrogenation product **3-H** with respect to *tert*-butylbenzene as an internal standard).

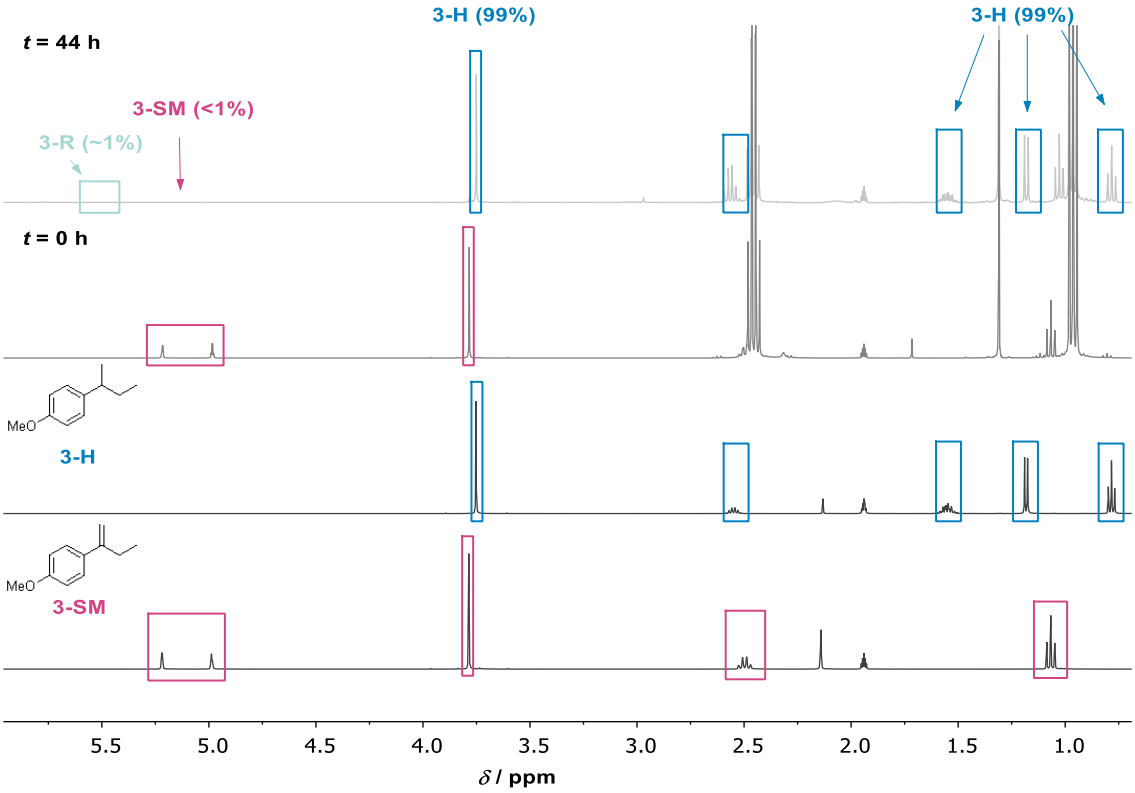

Figure S9. ^{1}H-NMR spectra of the light-driven hydrogenation of 1-(but-1-en-2-yl)-4-methoxybenzene (**3-SM**) in CD_3CN: The ^{1}H-NMR spectra of the reaction mixture before (t = 0 h) and after (t = 44 h) irradiation are shown in comparison to the ^{1}H-NMR spectra of neat 1-(but-1-en-2-yl)-4-methoxybenzene (**3-SM**) and 1-(*sec*-butyl)-4-methoxybenzene (**3-H**). The triplet at 1.02 ppm and the quartet at 2.56 ppm in the top spectrum are due to diethylamine resulting from TEA oxidation.

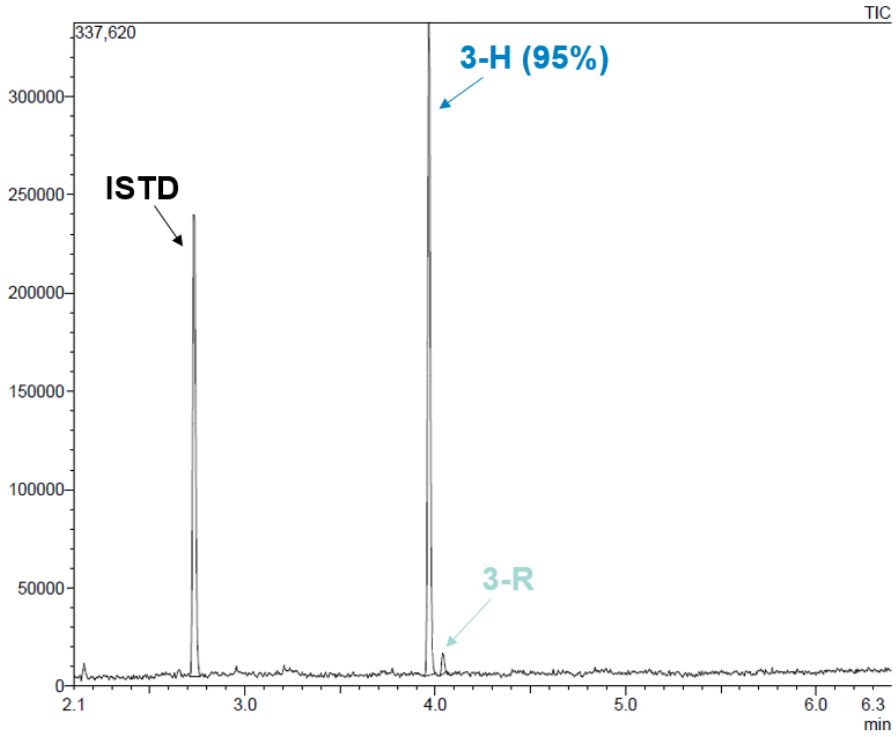

Figure S10. GC-MS trace of the light-induced hydrogenation of 1-(but-1-en-2-yl)-4-methoxybenzene (**3-SM**) to afford 1-(*sec*-butyl)-4-methoxybenzene (**3-H**) and 1-(but-2-en-2-yl)-4-methoxybenzene (**3-R**). The different analytes were separated using GC method A (see section S1 for details).

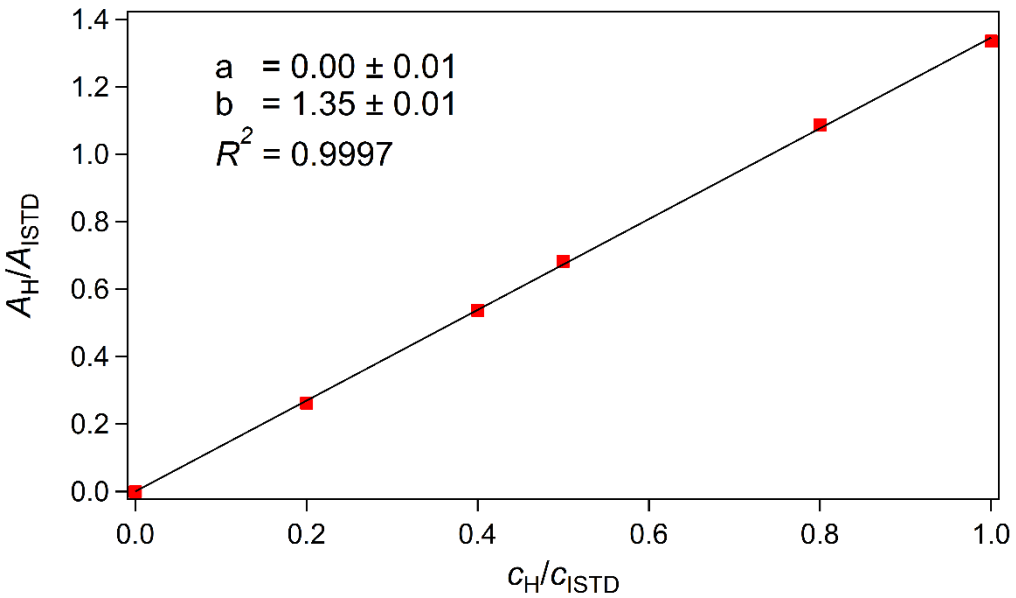

Figure S11. GC-MS calibration curves of 1-(*sec*-butyl)-4-methoxybenzene (**3-H**) with respect to *tert*-butylbenzene (**ISTD**, 5 mM).

S3.2.4 Light-Driven Hydrogenation of 1-(But-1-en-2-yl)-4-chlorobenzene (4-SM)

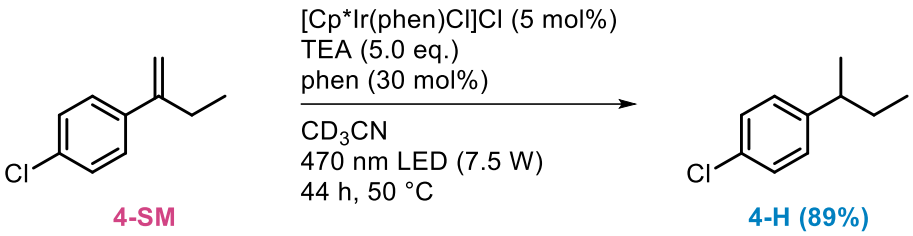

4-SM 4-H (89%)

1-(But-1-en-2-yl)-4-chlorobenzene (**4-SM**) was reduced to 1-(*sec*-butyl)-4-chlorobenzene (**4-H**) according to general procedure C. Based on ^{1}H-NMR spectroscopy, 96% conversion of **4-SM** was achieved, resulting in **4-H** in 89% yield. Isomerization to 1-(but-2-en-2-yl)-4-chlorobenzene (**4-R**) was observed in minor amounts (7%). The formation of 1-(*sec*-butyl)-4-chlorobenzene (**4-H**) was further confirmed by GC-MS spectrometry (91% formation of hydrogenation product **4-H** with respect to *tert*-butylbenzene as an internal standard).

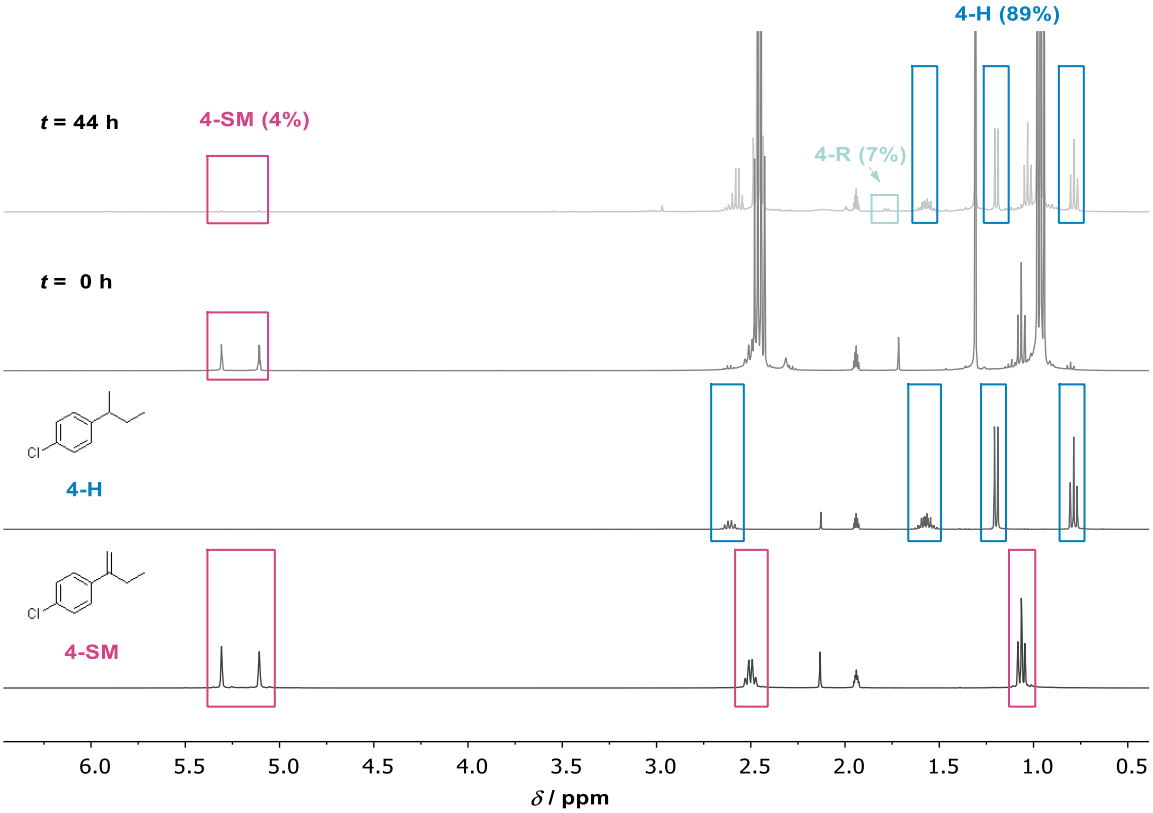

Figure S12. ^{1}H-NMR spectra of the light-driven hydrogenation of 1-(but-1-en-2-yl)-4-chlorobenzene (**4-SM**) in CD_3CN: The ^{1}H-NMR spectra of the reaction mixture before (t = 0 h) and after (t = 44 h) irradiation are shown in comparison to the ^{1}H-NMR spectra of neat 1-(but-1-en-2-yl)-4-chlorobenzene (**4-SM**) and 1-(*sec*-butyl)-4-chlorobenzene (**4-H**). The triplet at 1.02 ppm and the quartet at 2.56 ppm in the top spectrum are due to diethylamine resulting from TEA oxidation.

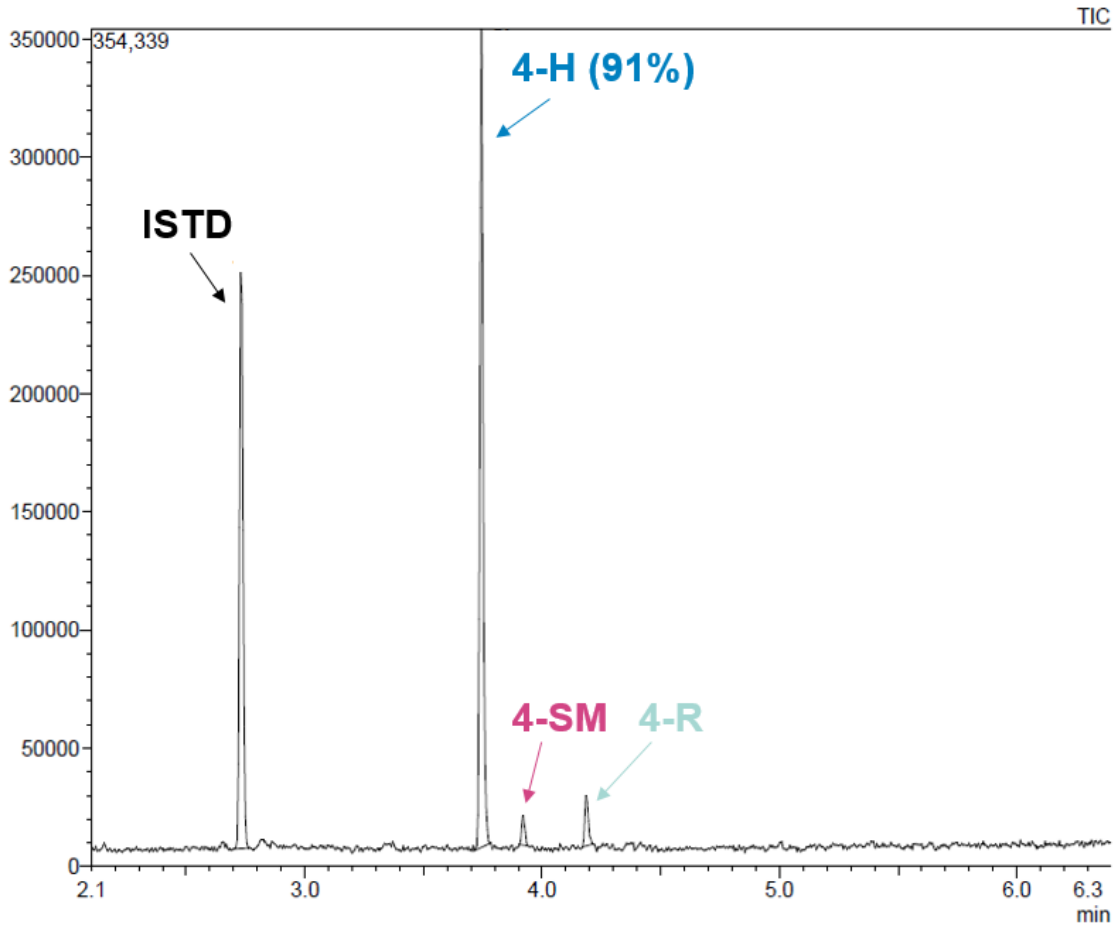

Figure S13. GC-MS trace of the light-induced hydrogenation of 1-(but-1-en-2-yl)-4-chlorobenzene (**4-SM**) to afford 1-(*sec*-butyl)-4-chlorobenzene (**4-H**) and 1-(but-2-en-2-yl)-4-chlorobenzene (**4-R**). The different analytes were separated using GC method A (see section S1 for details).

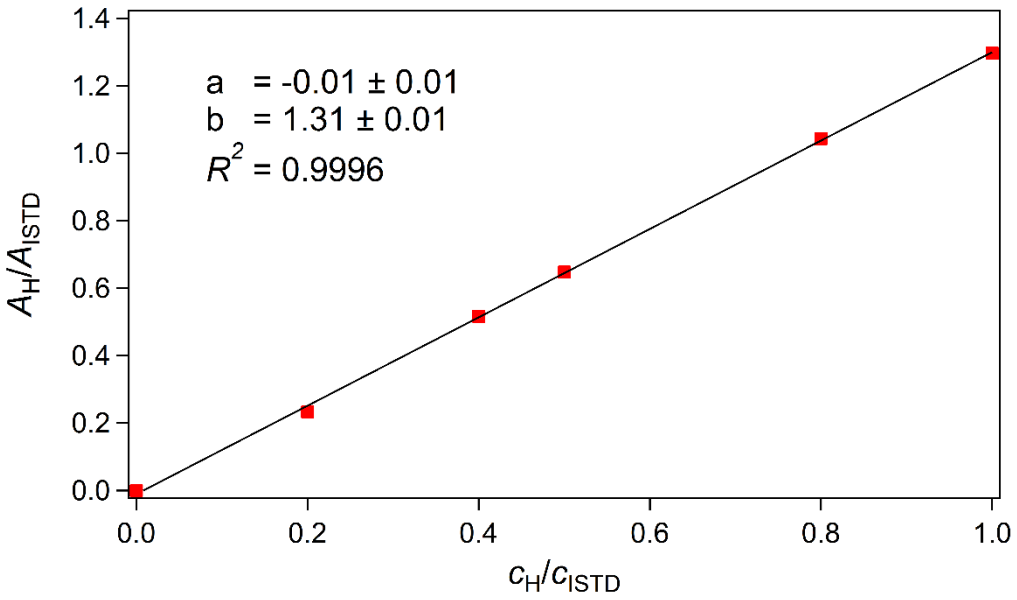

Figure S14. GC-MS calibration curve of 1-(*sec*-butyl)-4-chlorobenzene (**4-H**) with respect to *tert*-butylbenzene (**ISTD**, 5 mM).

S3.2.5 Light-Driven Hydrogenation of 1-(But-1-en-2-yl)-3-chlorobenzene (5-SM)

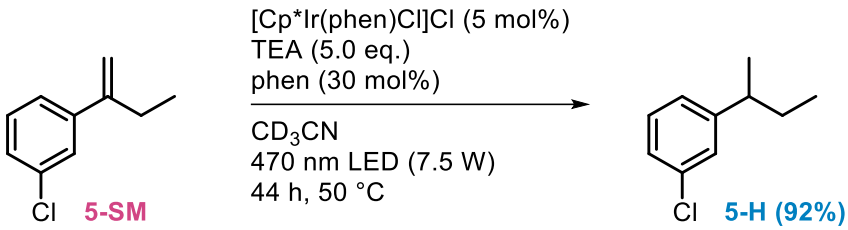

1-(But-1-en-2-yl)-3-chlorobenzene (**5-SM**) was reduced to 1-(*sec*-butyl)-3-chlorobenzene (**5-H**) according to general procedure C. Based on ^{1}H-NMR spectroscopy, the conversion of **5-SM** was 96%, affording **5-H** in 92% analytical yield. Isomerization to 1-(but-2-en-2-yl)-3-chlorobenzene (**5-R**) was observed in minor amounts (4%). The formation of 1-(*sec*-butyl)-3-chlorobenzene (**5-H**) was further confirmed by GC-MS spectrometry (89% formation of hydrogenation product **5-H** with respect to *tert*-butylbenzene as an internal standard).

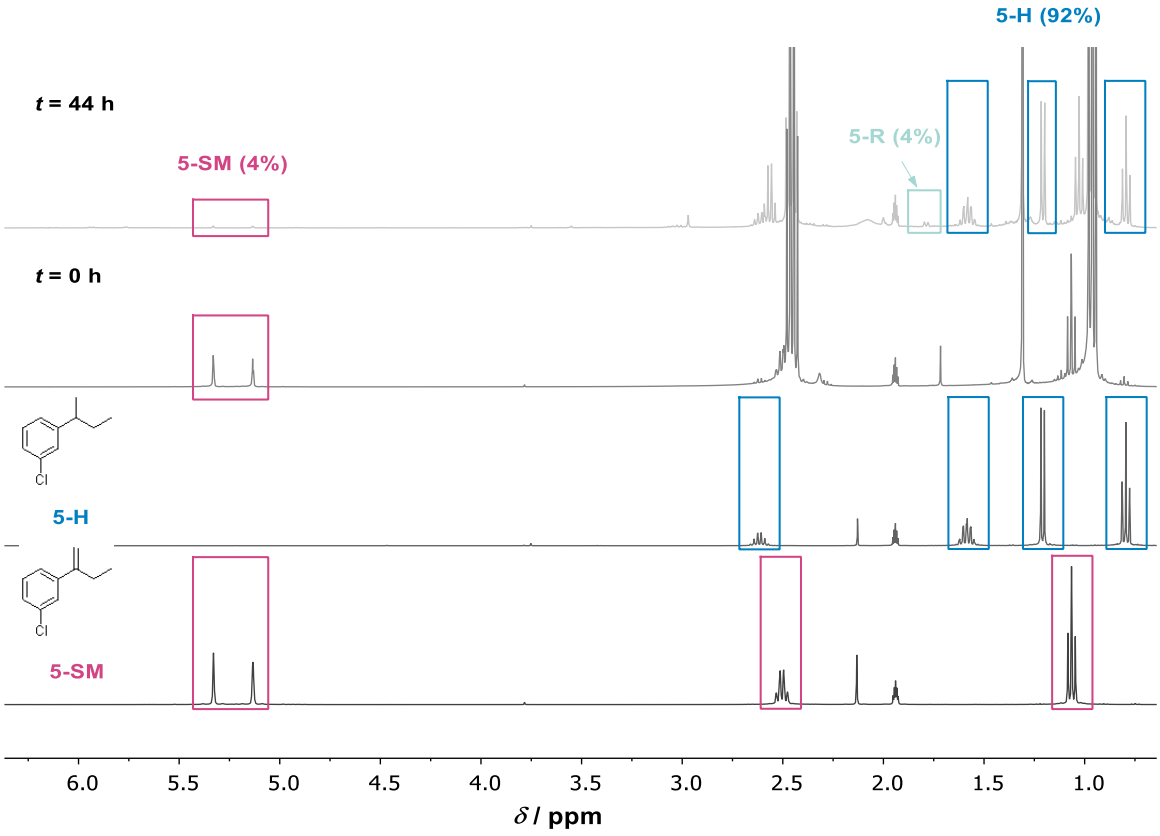

Figure S15. ^{1}H-NMR spectra of the light-driven hydrogenation of 1-(but-1-en-2-yl)-3-chlorobenzene (**5-SM**) in CD_3CN: The ^{1}H-NMR spectra of the reaction mixture before (t = 0 h) and after (t = 44 h) irradiation are shown in comparison to the ^{1}H-NMR spectra of neat 1-(but-1-en-2-yl)-3-chlorobenzene (**5-SM**) and 1-(*sec*-butyl)-3-chlorobenzene (**5-H**). The triplet at 1.02 ppm and the quartet at 2.56 ppm in the top spectrum are due to diethylamine resulting from TEA oxidation.

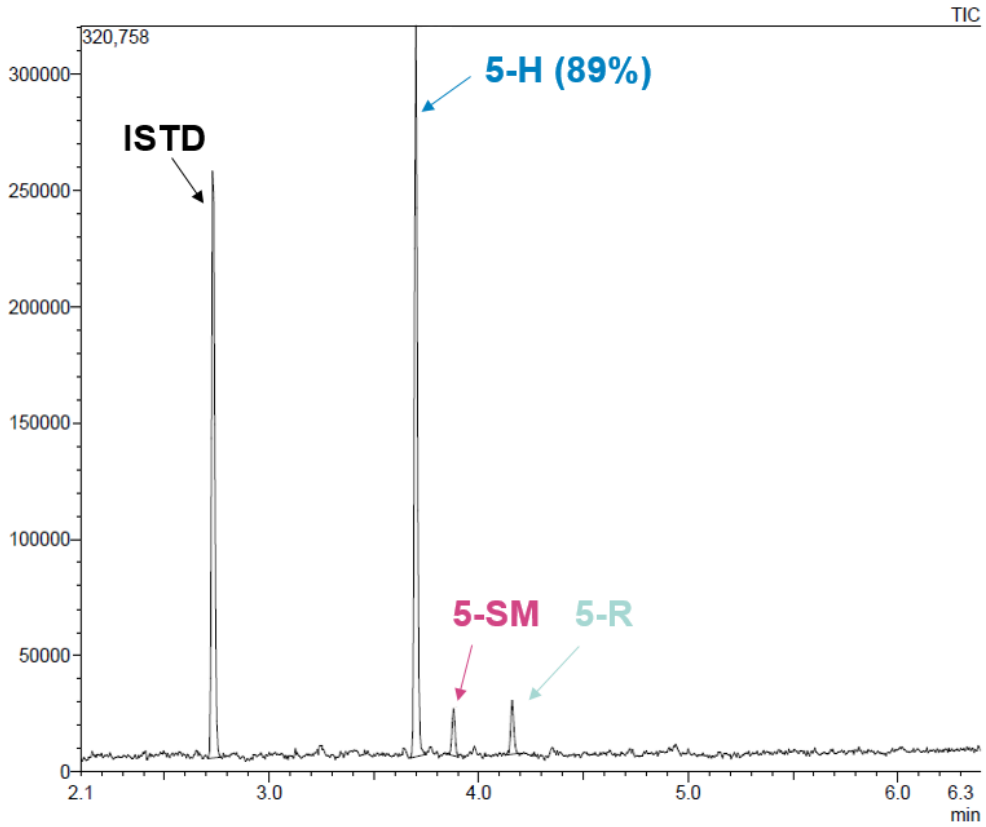

Figure S16. GC-MS trace of the light-induced hydrogenation of 1-(but-1-en-2-yl)-3-chlorobenzene (**5-SM**) to afford 1-(*sec*-butyl)-3-chlorobenzene (**5-H**) and 1-(but-2-en-2-yl)-3-chlorobenzene (**5-R**). The different analytes were separated using GC method A (see section S1 for details).

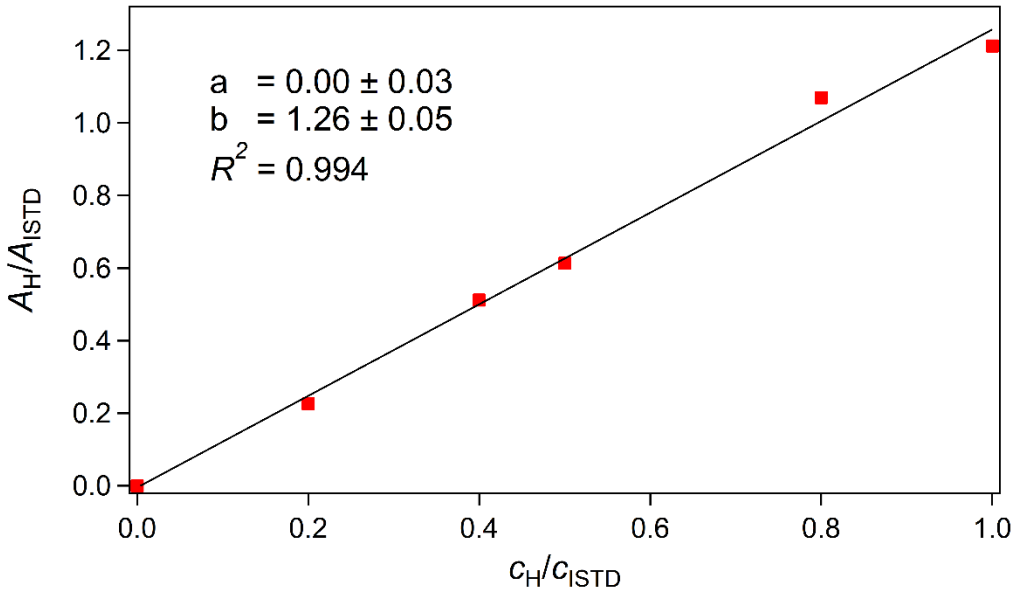

Figure S17. GC-MS calibration curve of 1-(*sec*-butyl)-3-chlorobenzene (**5-H**) with respect to *tert*-butylbenzene (**ISTD**, 5 mM).

S3.2.6 Light-Driven Hydrogenation of 2-Phenylprop-2-en-1-ol (6-SM)

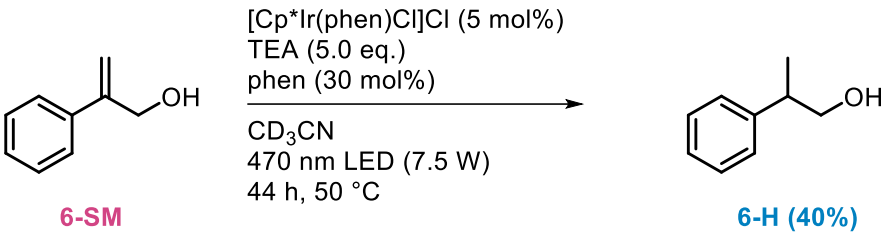

6-SM 6-H (40%)

2-Phenylprop-2-en-1-ol (**6-SM**) was reduced to 2-phenylpropan-1-ol (**6-H**) according to general procedure C. Based on ^{1}H-NMR spectroscopy, the conversion of **6-SM** was 41% affording **6-H** in 40% analytical yield. No significant isomerization of **6-SM** was observed. Since analysis by GC-MS was not possible for substrate **6-SM**, in this particular case the conversions were determined based on ^{1}H-NMR spectroscopy exclusively.

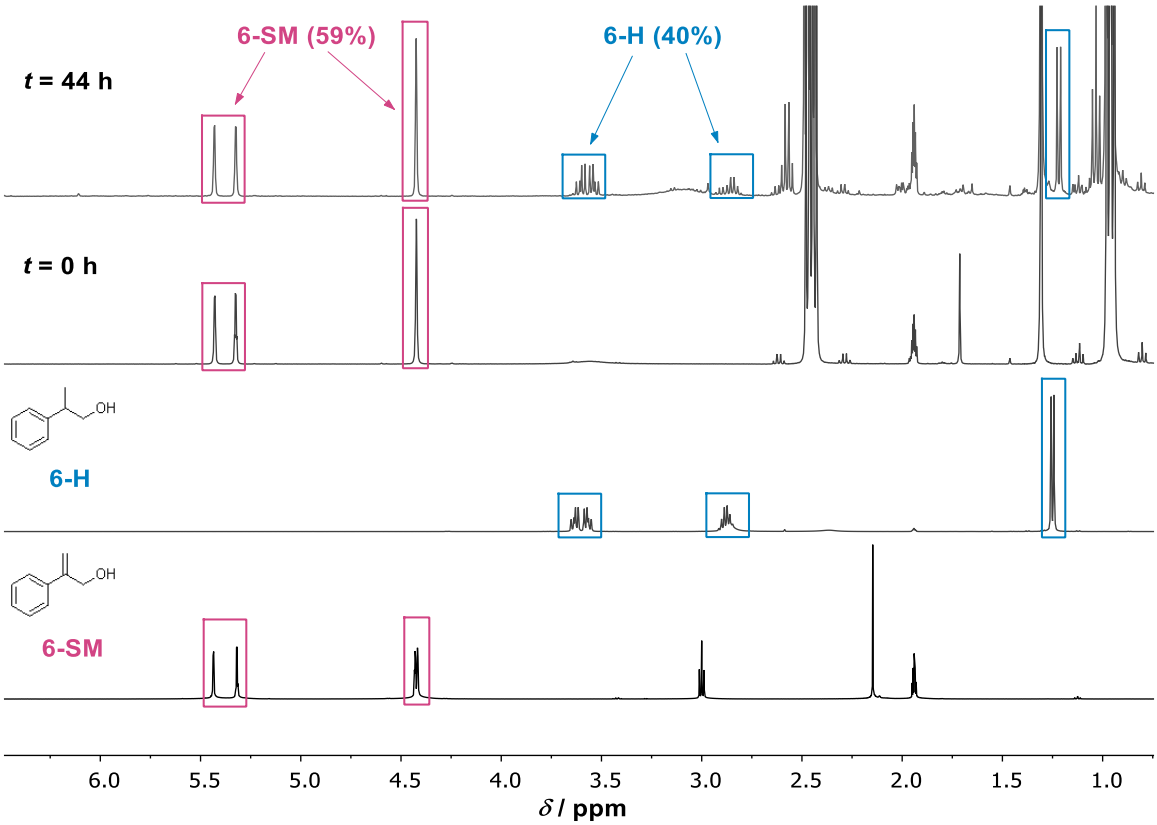

Figure S18. ^{1}H-NMR spectra of the light-driven hydrogenation of 2-phenylprop-2-en-1-ol (**6-SM**) in CD_3CN: The ^{1}H-NMR spectra of the reaction mixture before (t = 0 h) and after (t = 44 h) irradiation are shown in comparison to the ^{1}H-NMR spectra of neat 2-phenylprop-2-en-1-ol (**6-SM**) and 2-phenylpropan-1-ol (**6-H**). The triplet at 1.02 ppm and the quartet at 2.56 ppm in the top spectrum are due to diethylamine resulting from TEA oxidation.

S3.2.7 Light-Driven Hydrogenation of 2-(3-(Benzyloxy)prop-1-en-2-yl)-1,3,5-trimethylbenzene (7-SM)

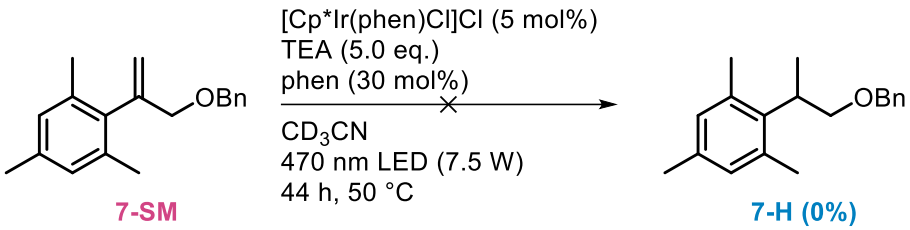

7-SM 7-H (0%)

Hydrogenation of 2-(3-(benzyloxy)prop-1-en-2-yl)-1,3,5-trimethylbenzene (**7-SM**) to 2-(1-(benzyl-oxy)propan-2-yl)-1,3,5-trimethylbenzene (**7-H**) was attempted following general procedure C. However, after irradiating the reaction mixture for 44 h, no conversion of the substrate was observed.

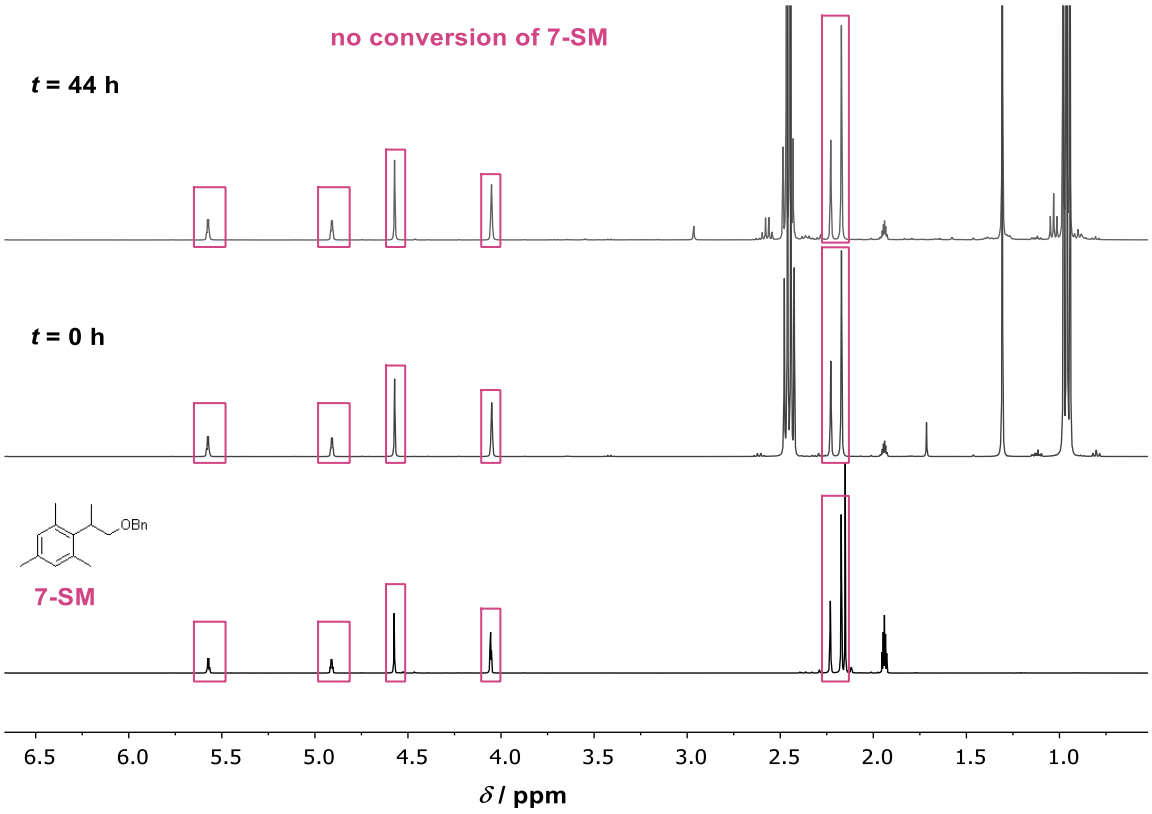

Figure S19. ^{1}H-NMR spectra of the attempted light-driven hydrogenation of 2-(3-(benzyloxy)prop-1-en-2-yl)-1,3,5-trimethylbenzene (**7-SM**) in CD_3CN: The ^{1}H-NMR spectra of the reaction mixture before (t = 0 h) and after (t = 44 h) irradiation are shown in comparison to the ^{1}H-NMR spectrum of neat 2-(3-(benzyloxy)prop-1-en-2-yl)-1,3,5-trimethylbenzene (**7-SM**). The triplet at 1.02 ppm and the quartet at 2.56 ppm in the top spectrum are due to diethylamine resulting from TEA oxidation.

S3.2.8 Light-Driven Hydrogenation of *trans*-1-Phenyl-1-propene (8-SM)

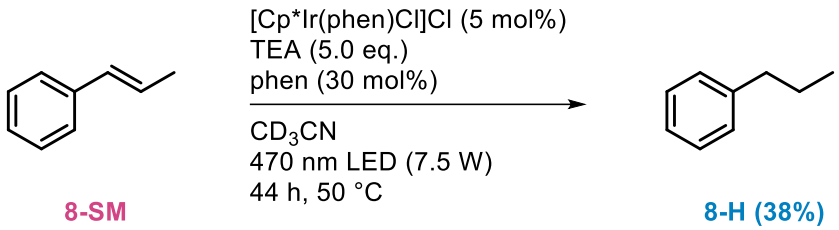

trans-1-Phenyl-1-propene (**8-SM**) was reduced to propylbenzene (**8-H**) according to general procedure C. Based on ^{1}H-NMR spectroscopy, the conversion of **8-SM** was 54%, giving **8-H** in 38% yield. Significant isomerization to *cis*-1-phenyl-1-propene (**8-R**, 16%) was observed. The formation of propylbenzene (**8-H**) was confirmed by GC-MS spectrometry (37% formation of hydrogenation product **8-H** with respect to *tert*-butylbenzene as an internal standard).

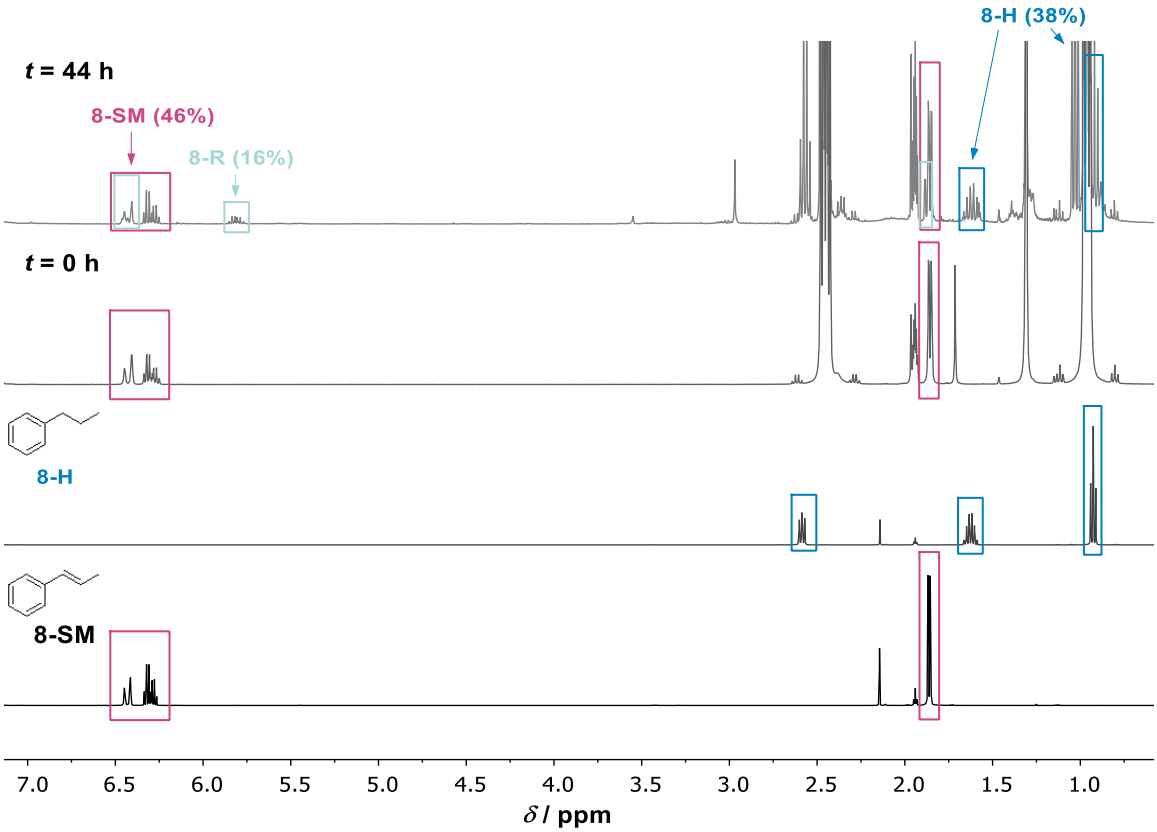

Figure S20. ^{1}H-NMR spectra of the light-driven hydrogenation of *trans*-1-phenyl-1-propene (**8-SM**) in CD_3CN: The ^{1}H-NMR spectra of the reaction mixture before (t = 0 h) and after (t = 44 h) irradiation are shown in comparison to the ^{1}H-NMR spectra of neat *trans*-1-phenyl-1-propene (**8-SM**) and propylbenzene (**8-H**). The triplet at 1.02 ppm and the quartet at 2.56 ppm in the top spectrum are due to diethylamine resulting from TEA oxidation.

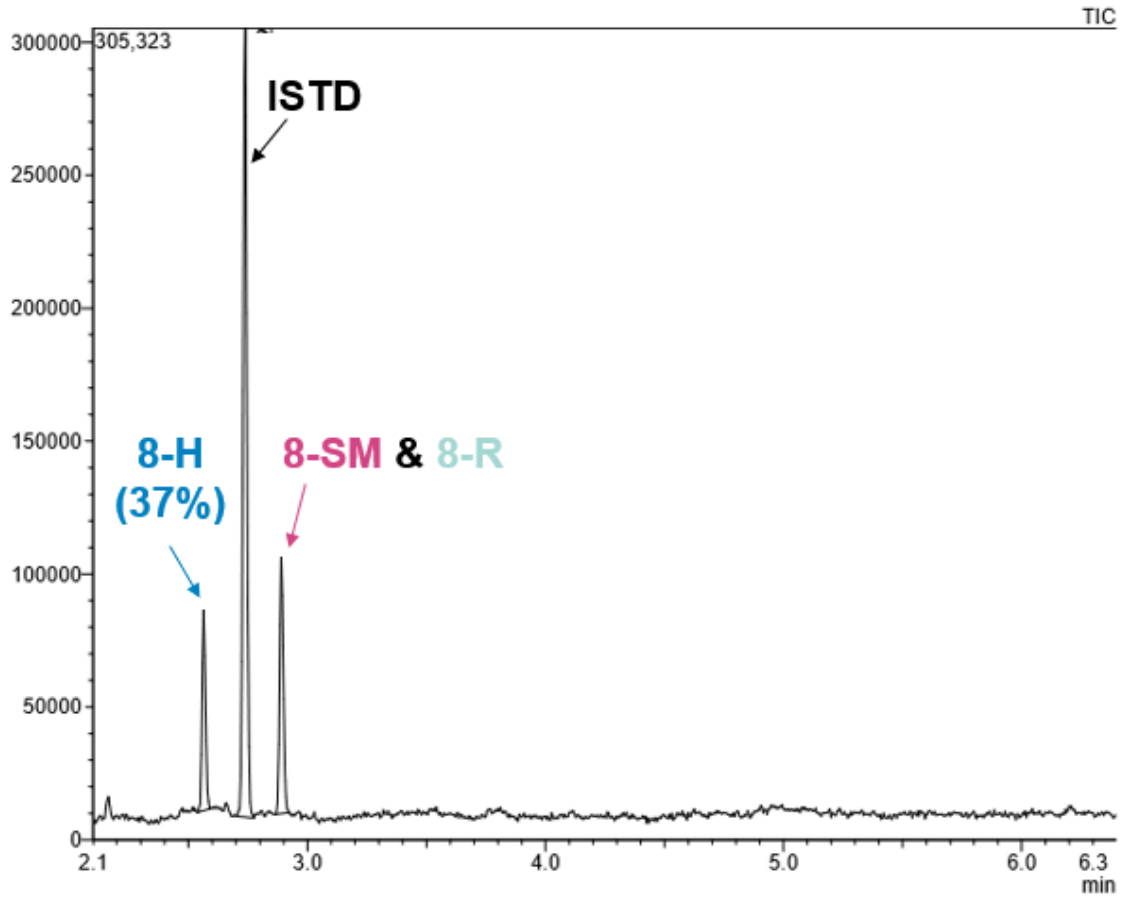

Figure S21. GC-MS trace of the light-induced hydrogenation of *trans*-1-phenyl-1-propene (**8-SM**) to afford propylbenzene (**8-H**) and *cis*-1-phenyl-1-propene (**8-R**). The different analytes were separated using GC method A (see section S1 for details).

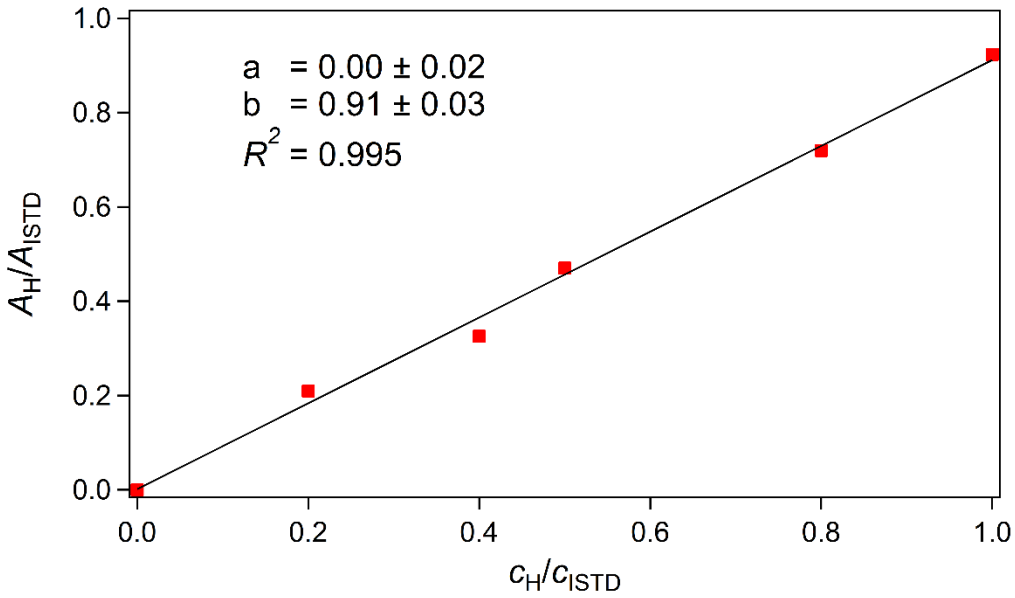

Figure S22. GC-MS calibration curve of propylbenzene (**8-H**) with respect to *tert*-butylbenzene (**ISTD**, 5 mM).

S3.2.9 Light-Driven Hydrogenation of Methyl 2-((benzyloxy)methyl)acrylate (9-SM)

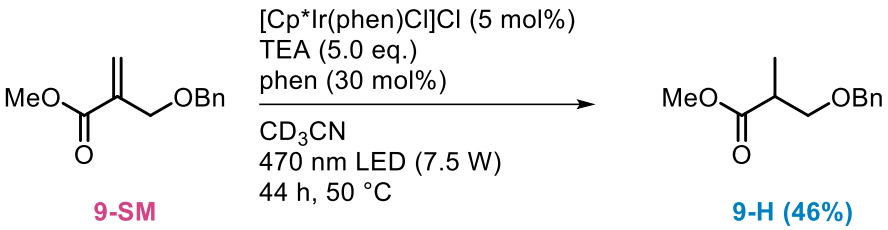

Methyl 2-((benzyloxy)methyl)acrylate (**9-SM**) was reduced to methyl 3-(benzyloxy)-2-methyl-propanoate (**9-H**) according to general procedure C. Based on ^{1}H-NMR spectroscopy, the conversion of the **9-SM** was 71%, affording **9-H** in 46% yield. Significant isomerization to methyl 3-(benzyloxy)-2-methylacrylate (**9-R**, 22%) was detected. In minor amounts, deprotection of the benzylic group (3%) was observed. The formation of methyl 3-(benzyloxy)-2-methyl-propanoate (**9-H**) was further confirmed by GC-MS spectrometry (48% formation of hydrogenation product **9-H** with respect to *tert*-butylbenzene as an internal standard).

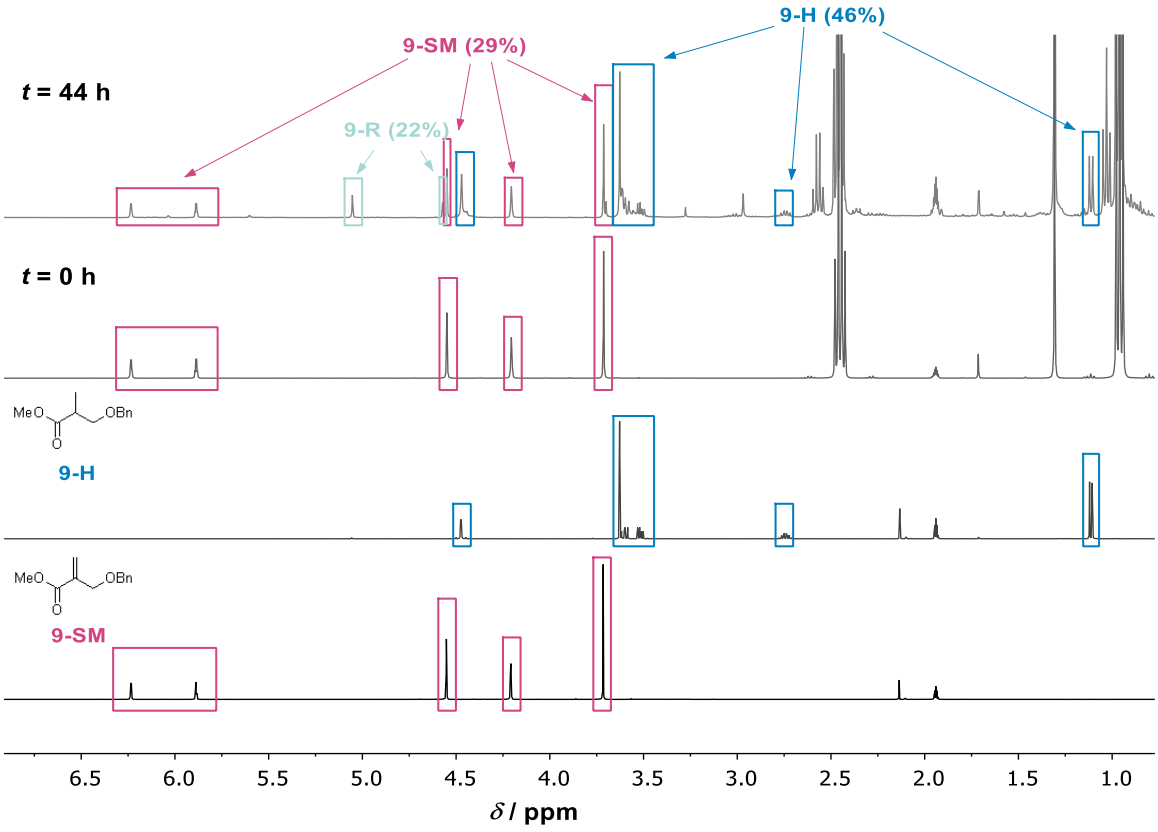

Figure S23. ^{1}H-NMR spectra of the light-driven hydrogenation of methyl 2-((benzyloxy)methyl)acrylate (**9-SM**) in CD_3CN: The ^{1}H-NMR spectra of the reaction mixture before (t = 0 h) and after (t = 44 h) irradiation are shown in comparison to the ^{1}H-NMR spectra of neat methyl 2-((benzyloxy)methyl)acrylate (**9-SM**) and methyl 3-(benzyloxy)-2-methyl-propanoate (**9-H**). The triplet at 1.02 ppm and the quartet at 2.56 ppm in the top spectrum are due to diethylamine resulting from TEA oxidation.

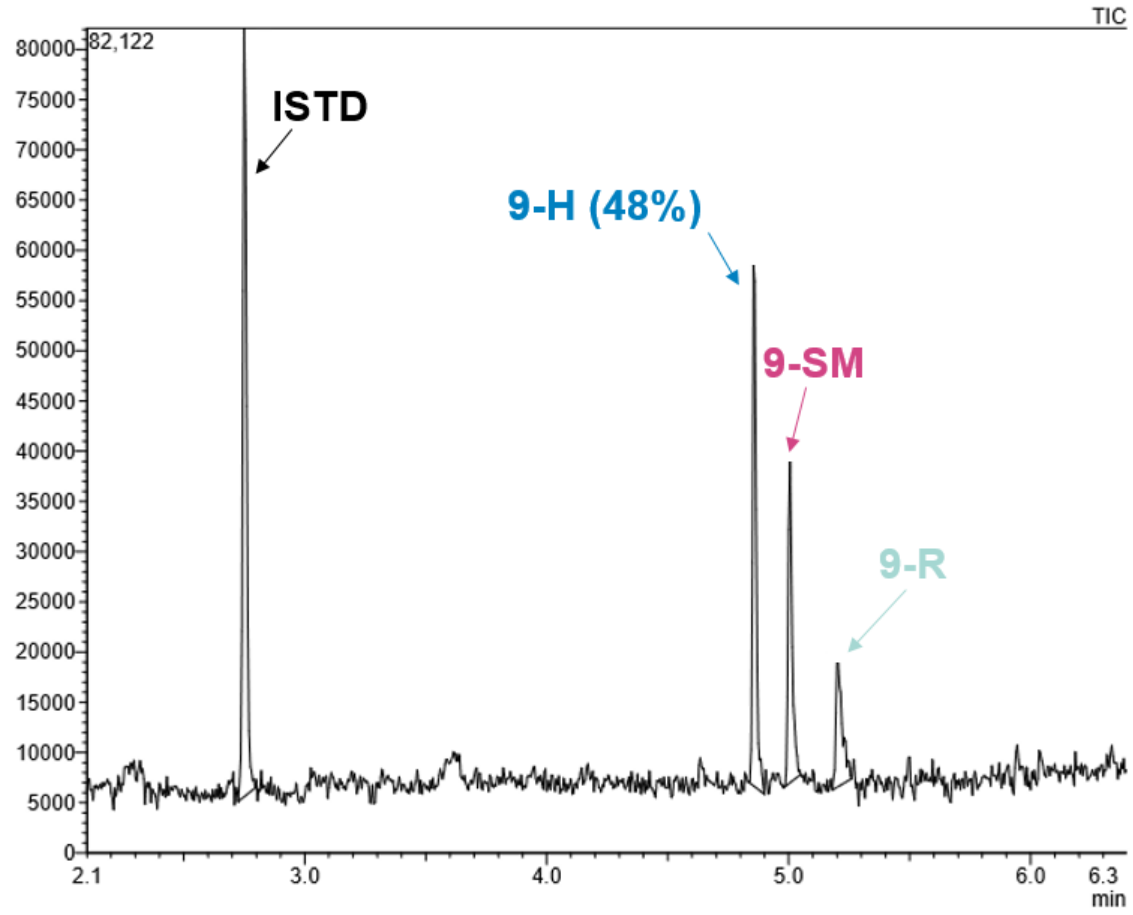

Figure S24. GC-MS trace of the light-induced hydrogenation of methyl 2-((benzyloxy)methyl)acrylate (**9-SM**) to afford methyl 3-(benzyloxy)-2-methyl-propanoate (**9-H**) and methyl 3-(benzyloxy)-2-methylacrylate (**9-R**). The different analytes were separated using GC method A (see section S1 for details).

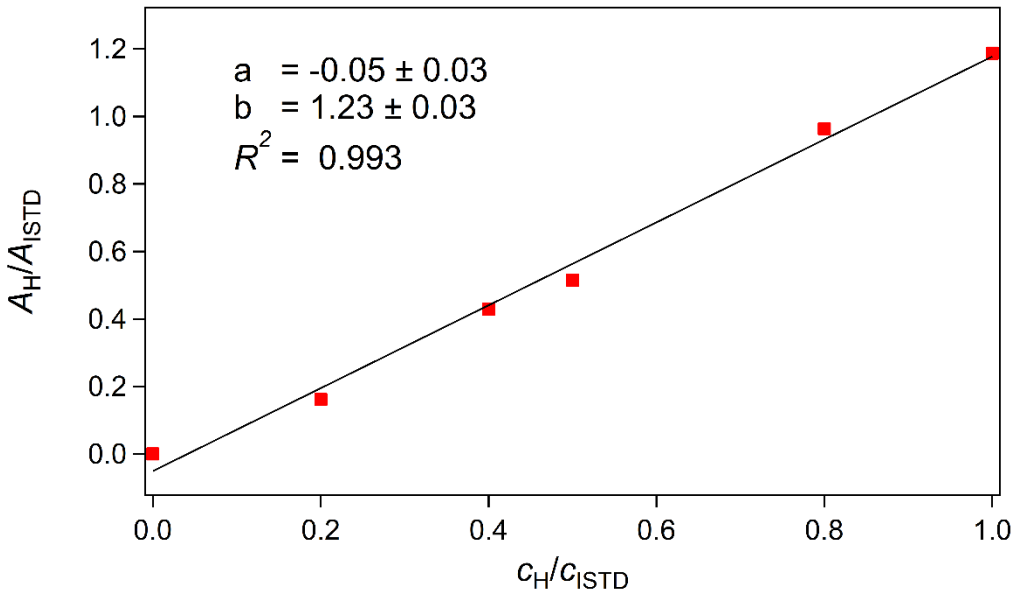

Figure S25. GC-MS calibration curve of methyl 3-(benzyloxy)-2-methyl-propanoate (**9-H**) with respect to *tert*-butylbenzene (**ISTD**, 5 mM).

S3.2.10 Light-Driven Hydrogenation of (((2-Cyclohexylallyl)oxy)methyl)benzene (10-SM)

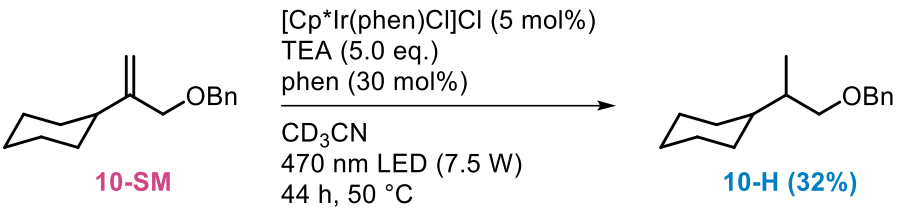

(((2-Cyclohexylallyl)oxy)methyl)benzene (**10-SM**) was reduced to ((2-cyclohexylpropoxy)methyl)-benzene (**10-H**) according to general procedure C. Based on ^{1}H-NMR spectroscopy, the conversion of **10-SM** was 40%, affording **10-H** in 32% yield. Significant isomerization to (((2-cyclohexylprop-1-en-1-yl)oxy)methyl)benzene (**10-R**) was observed (8%).

10-SM and **10-H** could not be separated by GC-MS spectrometry because the retention times of substrate **10-SM** and hydrogenation product **10-H** are too similar. Thus, the conversions were determined by ^{1}H-NMR spectroscopy exclusively.

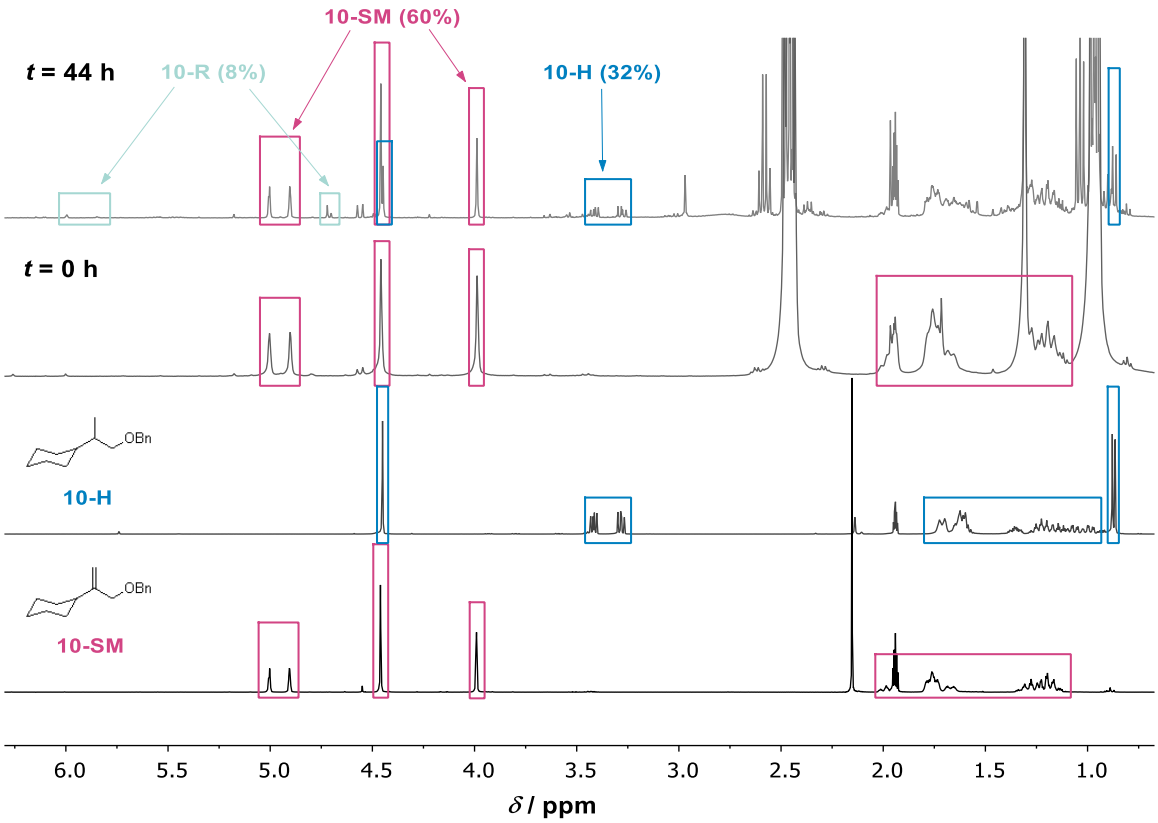

Figure S26. ^{1}H-NMR spectra of the light-driven hydrogenation of (((2-cyclohexylallyl)oxy)methyl)benzene (**10-SM**) in CD_3CN: The ^{1}H-NMR spectra of the reaction mixture before (t = 0 h) and after (t = 44 h) irradiation are shown in comparison to the ^{1}H-NMR spectra of neat (((2-cyclohexylallyl)oxy)methyl)benzene (**10-SM**) and ((2-cyclohexylpropoxy)methyl)-benzene (**10-H**). The triplet at 1.02 ppm and the quartet at 2.56 ppm in the top spectrum are due to diethylamine resulting from TEA oxidation.

S3.2.11 Light-Driven Hydrogenation of ((2-Methylallyloxy)methyl)benzene (11-SM)

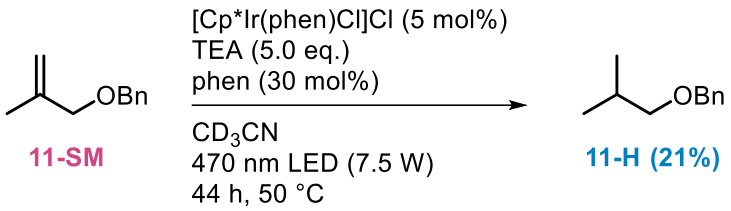

((2-Methylallyloxy)methyl)benzene (**11-SM**) was reduced to benzyl *iso*-butyl ether (**11-H**) according to general procedure C. Based on ^{1}H-NMR spectroscopy, the conversion of **11-SM** was 49%, affording **11-H** in 21% yield. Isomerization to (((2-methylprop-1-en-1-yl)oxy)methyl)benzene (**11-R**, 28%) was found to be the major reaction pathway. The formation of benzyl *iso*-butyl ether (**11-H**) was further confirmed by GC-MS spectrometry (26% formation of hydrogenation product **11-H** with respect to *tert*-butylbenzene as an internal standard).

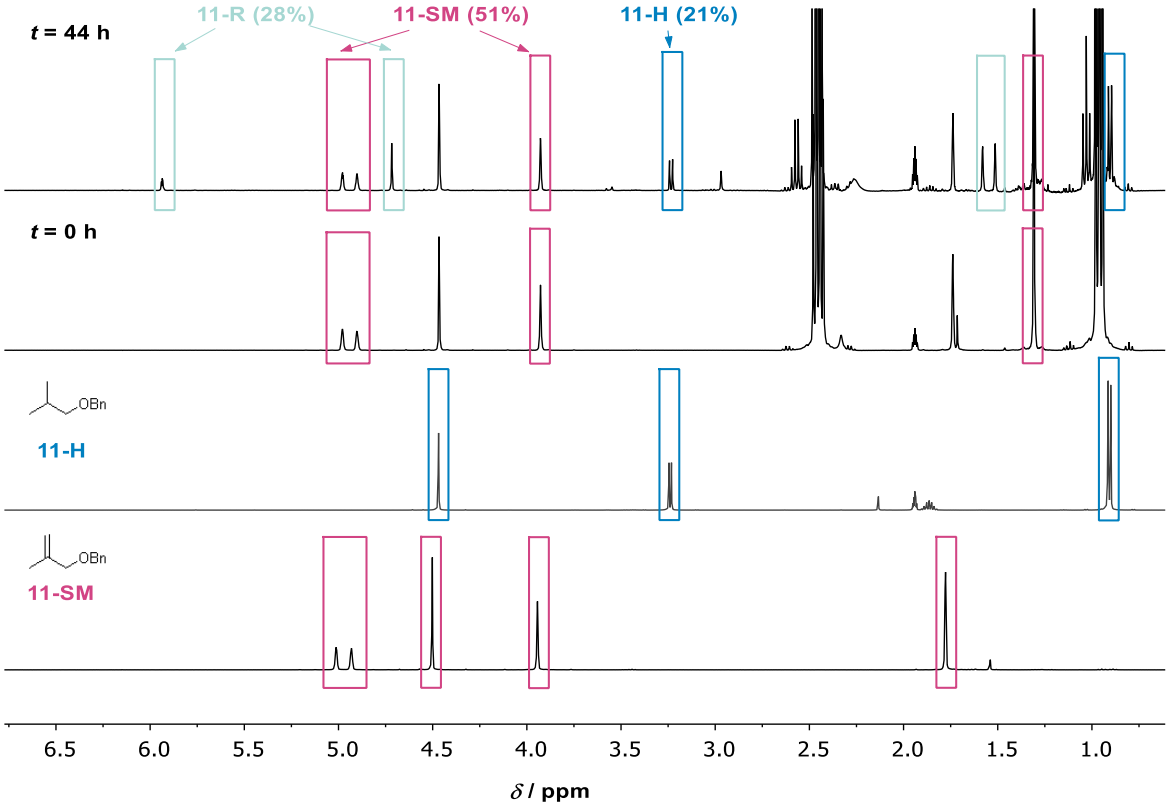

Figure S27. ^{1}H-NMR spectra of the light-driven hydrogenation of ((2-methylallyloxy)methyl)benzene (**11-SM**) in CD_3CN: The ^{1}H-NMR spectra of the reaction mixture before (t = 0 h) and after (t = 44 h) irradiation are shown in comparison to the ^{1}H-NMR spectra of neat ((2-methylallyloxy)methyl)benzene (**11-SM**) and benzyl *iso*-butyl ether (**11-H**). The triplet at 1.02 ppm and the quartet at 2.56 ppm in the top spectrum are due to diethylamine resulting from TEA oxidation.

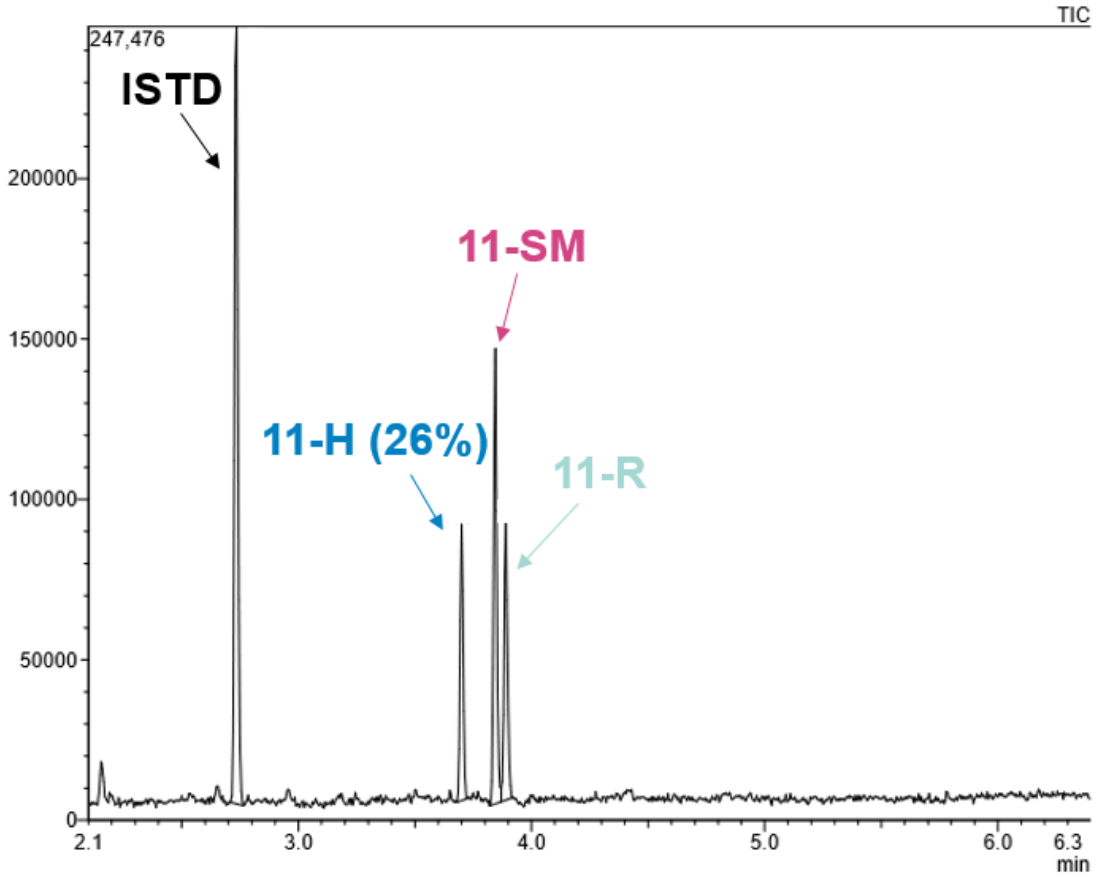

Figure S28. GC-MS trace of the light-induced hydrogenation of ((2-methylallyloxy)methyl)benzene (**11-SM**) to afford benzyl *iso*-butyl ether (**11-H**) and (((2-methylprop-1-en-1-yl)oxy)methyl)benzene (**11-R**). The different analytes were separated using GC method A (see section S1 for details).

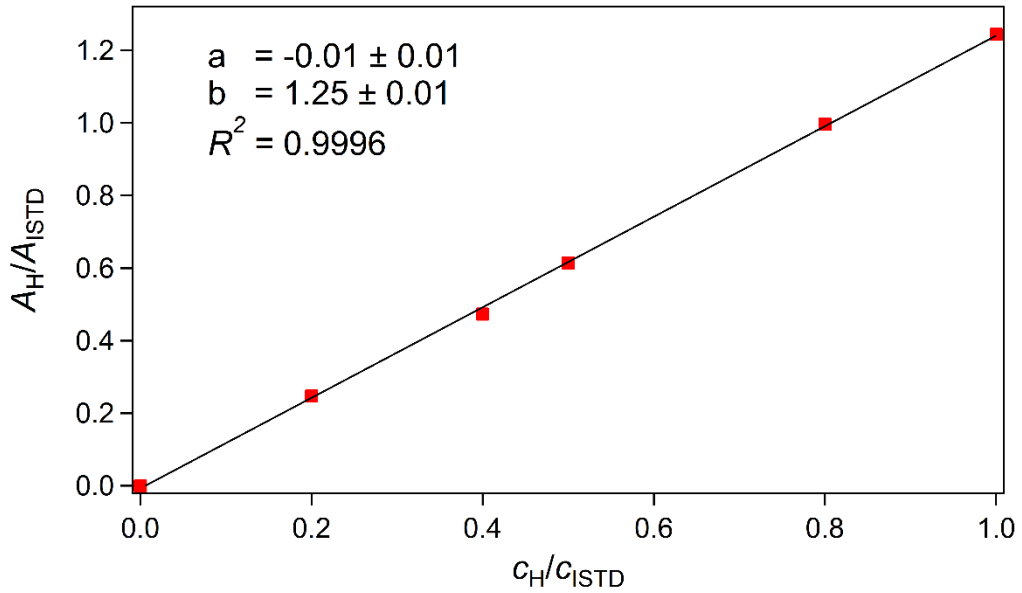

Figure S29. GC-MS calibration curve of benzyl *iso*-butyl ether (**11-H**) with respect to *tert*-butylbenzene (**ISTD**, 5 mM).

S3.2.12 Light-Driven Hydrogenation of ((Allyloxy)methyl)benzene (12-SM)

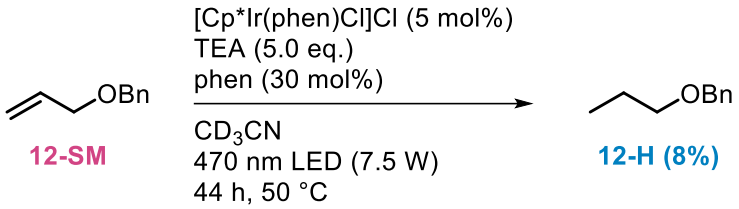

((Allyloxy)methyl)benzene (**12-SM**) was reduced to benzyl propyl ether (**12-H**) according to general procedure C. Based on ^{1}H-NMR spectroscopy, the conversion of **12-SM** was 35%, affording **12-H** in 8% yield. Isomerization to (*E*)-((prop-1-en-1-yloxy)methyl)benzene (**(*E*)-12-R**, 19%) and (*Z*)-((prop-1-en-1-yloxy)methyl)benzene (**(*Z*)-12-R**, 8%) was found to be the major reaction pathway.

12-SM and **12-H** could not be separated by GC-MS spectrometry because the retention times of substrate **12-SM** and hydrogenation product **12-H** are too similar. Thus, the conversions were determined by ^{1}H-NMR spectroscopy exclusively.

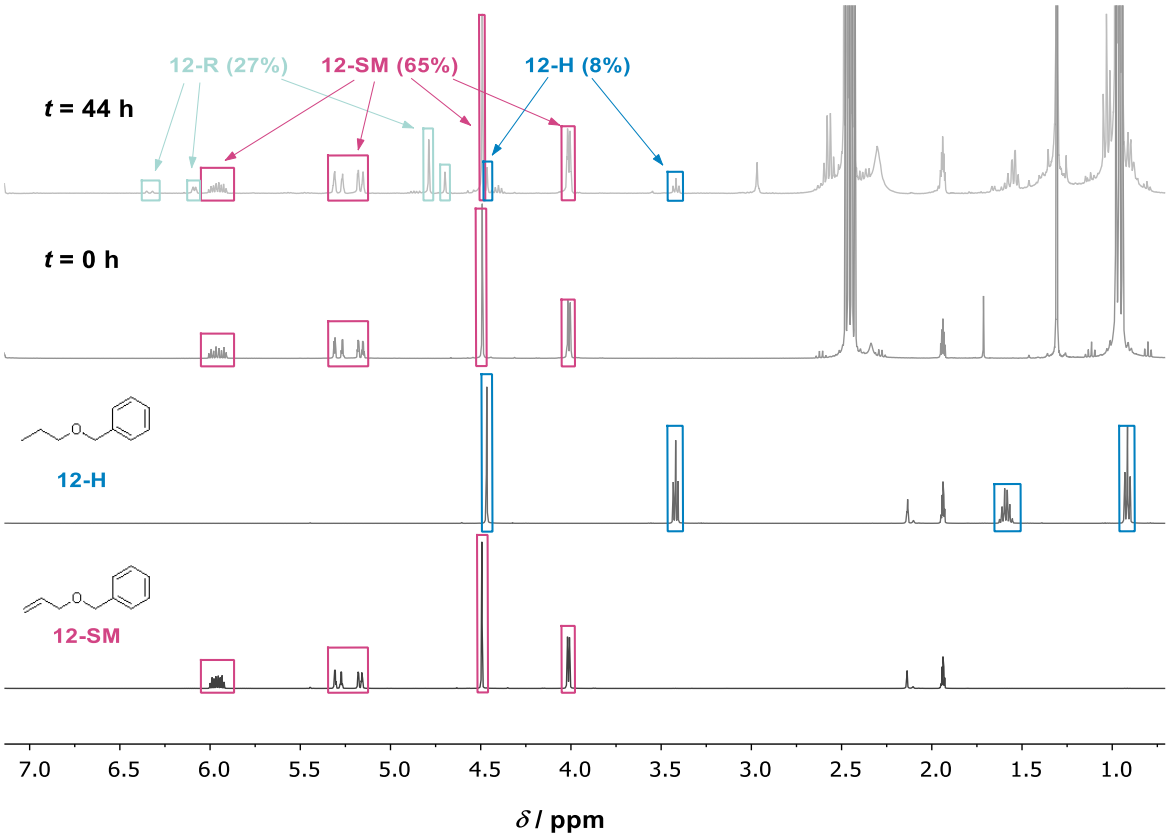

Figure S30. ^{1}H-NMR spectra of the light-driven hydrogenation of ((allyloxy)methyl)benzene (**12-SM**) in CD_3CN: The ^{1}H-NMR spectra of the reaction mixture before (*t* = 0 h) and after (*t* = 44 h) irradiation are shown in comparison to the ^{1}H-NMR spectra of neat ((allyloxy)methyl)benzene (**12-SM**) and benzyl propyl ether (**12-H**). The triplet at 1.02 ppm and the quartet at 2.56 ppm in the top spectrum are due to diethylamine resulting from TEA oxidation.

S4 Mechanistic Studies

S4.1 Thermochemistry of the Photo-Triggered HAT

The Ir^{III}-H BDFE of $[Cp^*Ir(phen)(H)]^+$ is not known, but for the $[Cp^*Ir(PMe_3)(H)_2]$ complex the Ir^{III}-H BDFE is ca. 69 kcal · mol^{-1}. (This BDFE value was estimated based on the published BDE value of the Ir^{III}-H bond for $[Cp^*Ir(PMe_3)(H)_2]$ (74 kcal mol^{-1})[267] taking into account an entropic effect of the solvent (MeCN) of 4.8 kcal · mol^{-1}).[268] By contrast, the Ir^{II}-H BDFE of the $[Cp^*Ir(bpy)(H)]^0$ complex is only 43.9 kcal · mol^{-1}.[12] The only difference of that complex to ours is the presence of a phen instead of a bpy ligand, and it seems plausible that this does not much affect the Ir^{II}-H BDFE. Thus, we assume that our catalytically active $[Cp^*Ir(phen)(H)]^0$ complex has an Ir^{II}-H BDFE of 44±2 kcal · mol^{-1}. On the other hand, the BDFE of the newly formed C-H bond radical intermediates **RI•** bearing an aromatic substituent is on the order of 41±2 kcal · mol^{-1}. That proxy value corresponds to the BDE of the C-H bond formed after H-atom transfer to α-methyl styrene (45.6 kcal mol^{-1}[269]) and takes into account an entropic effect of the solvent (MeCN) of 4.8 kcal · mol^{-1}.[268] The initial photo-HAT from the $[Cp^*Ir(phen)(H)]^0$ complex to our aromatic substrates consequently has $\Delta G_{HAT} \approx 0$ kcal · mol^{-1}, see Fig. S31. Thus, in principle reactants and products of the initial HAT step are in equilibrium, similar to what was found previously for thermal (light-independent) metal-catalyzed HAT reactions.[155] Secondary HAT (with oxidation products of TEA acting as H-atom donors, see main paper) is rapid and drives the overall reaction towards the product side. For aliphatic substrates, the BDFE of C-H bond formed after an initial HAT is around 32±2 kcal · mol^{-1} (corresponding to a C-H BDE of the *tert*-butyl radical of 36.6 kcal · mol^{-1}[270]). For these substrates, initial HAT to the olefin is therefore energetically uphill ($\Delta G_{HAT} \approx +10$ kcal · mol^{-1}) and H-abstraction from the radial intermediate **RI•** gets more favored, leading to a greater proportion of rearranged products in comparison to hydrogenated products.

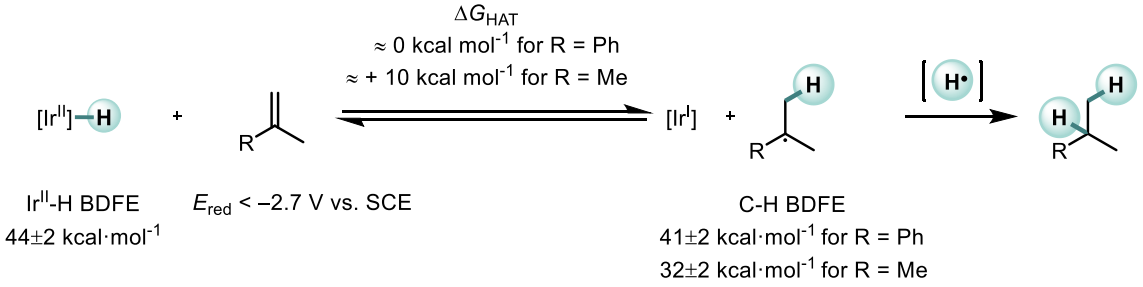

Figure S31. Thermochemistry of the investigated photoinduced HAT.

Aromatic disubstituted germinal olefins have very negative reduction potentials, as illustrated by the reduction potential of α-methyl styrene, which is more negative than −2.7 V vs. SCE (Fig. S31).[238] Thus, electron transfer from $[Cp^*Ir(phen)(H)]^0$ ($E^{0\prime}$(III/II) ≈ −1.4 V vs. SCE[12]) or from ^{3}MLCT-excited $[Cp^*Ir(phen)(H)]^+$ ($E^{0\prime}$(IV/III*) ≈ −1.3 V vs. SCE[12], see Fig. S32) to the investigated olefins is endergonic by at least 1.3 eV. The reduction

potentials included in Fig. S32 were reported for $[Cp^*Ir(bpy)(H)]^+$, but we assume that the reduction potentials of the investigated $[Cp^*Ir(phen)(H)]^+$ complex are similar.

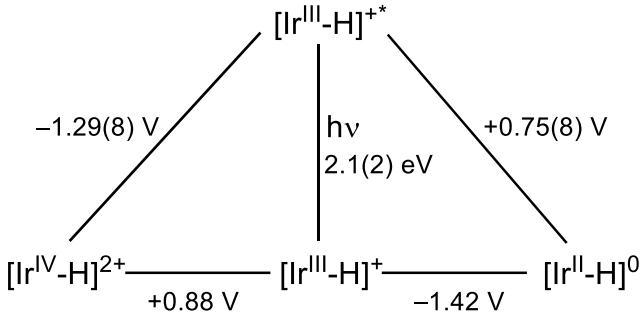

Figure S32. Latimer diagram of $[Cp^*Ir(bpy)(H)]^+$ adapted from Miller and coworkers.[12] All potentials are given in V vs. SCE.

S4.2 Role of Iridium Hydride

Conversion of $[Cp^*Ir(phen)Cl]^+$ (yellow trace, Figure S33) to $[Cp^*Ir(phen)(H)]^+$ (green trace, Figure S33) was monitored by UV-Vis spectroscopy. The increase in absorption at 430 nm and the decrease in absorption at 350 nm as well as the isosbestic point at 375 nm indicate the conversion of [Cp*Ir(phen)Cl]Cl (yellow trace) to $[Cp^*Ir(phen)(H)](PF_6)$ (green trace).

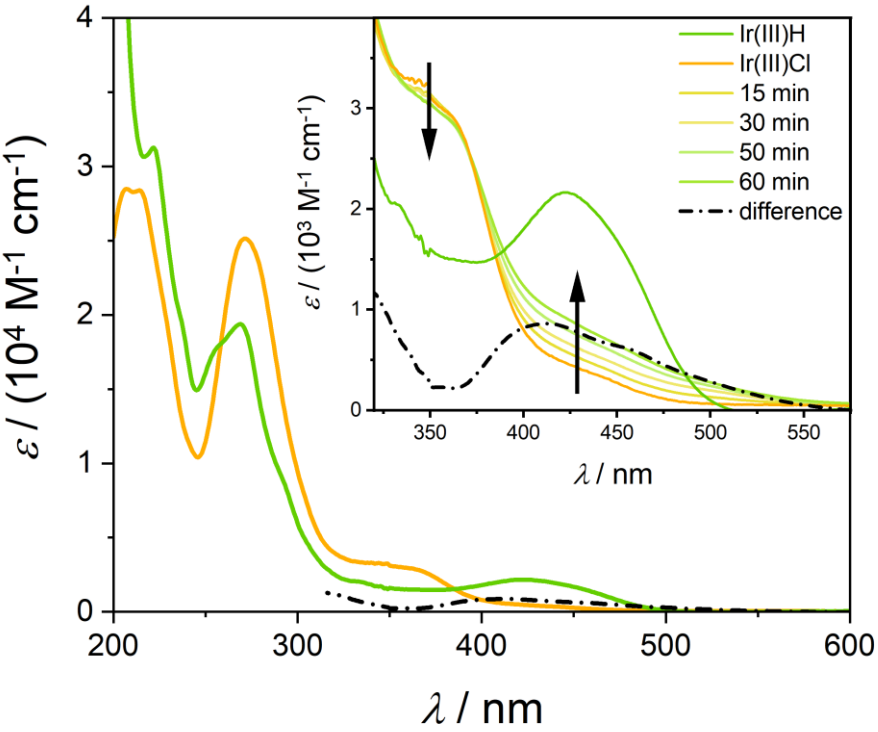

Figure S33. Main plot: Absorption spectra of [Cp*Ir(phen)Cl]Cl (yellow trace) and $[Cp^*Ir(phen)(H)](PF_6)$ (green trace) in CH_3CN at room temperature. Inset: Continuous irradiation of a solution containing [Cp*Ir(phen)Cl]Cl (80 µM) and TEA (1.0 mM) in CH_3CN at 455 nm.

The evidence for the photo-driven conversion of $[Cp^*Ir(phen)Cl]^+$ to $[Cp^*Ir(phen)(H)]^+$ in the UV-Vis data of Figure S33 is further supported by the ^{1}H-NMR data in Figure S34. Clearly, the formation of the iridium(III) hydride species (marked by green boxes) from the iridium(III) chloride (yellow boxes) is very slow, but easily detectable in absence of substrate (panels A and C). In presence of substrate (panels B and D), its detection is difficult, presumably due to its efficient turnover with the substrate.

The grey boxes in Figure S34 mark resonances caused by free (unbound) phen ligand (either added in excess (panels A and B), or form as a result of photo-driven dissociation from the iridium complex.

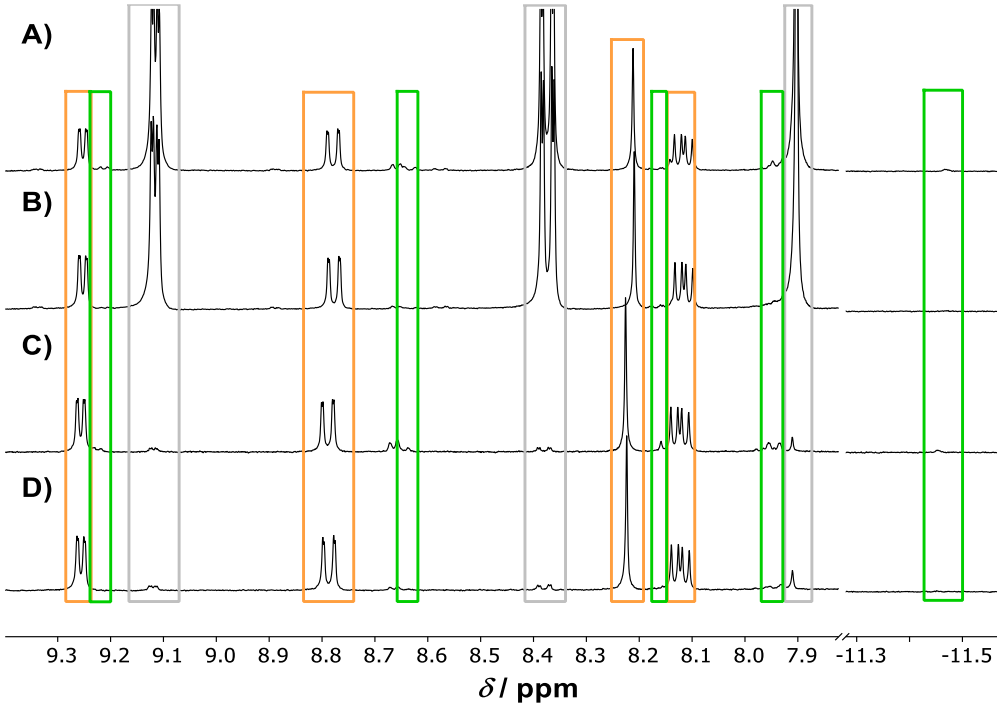

Figure S34: Continuous irradiation of different reaction mixtures containing [Cp*Ir(phen)Cl]Cl] and TEA in deaerated CD_3CN at 470 nm and at 50 °C. A) Reaction mixture containing [Cp*Ir(phen)Cl]Cl] (3.5 mM), phen (21 mM) and TEA (350 mM) in deareated CD_3CN. B) Reaction mixture containing **1-SM** (70 mM), [Cp*Ir(phen)Cl]Cl] (3.5 mM), phen (21 mM) and TEA (350 mM) in deareated CD_3CN. C) Reaction mixture containing [Cp*Ir(phen)Cl]Cl] (3.5 mM) and TEA (350 mM) in deareated CD_3CN. B) Reaction mixture containing **1-SM** (70 mM), [Cp*Ir(phen)Cl]Cl] (3.5 mM) and TEA (350 mM) in deareated CD_3CN.

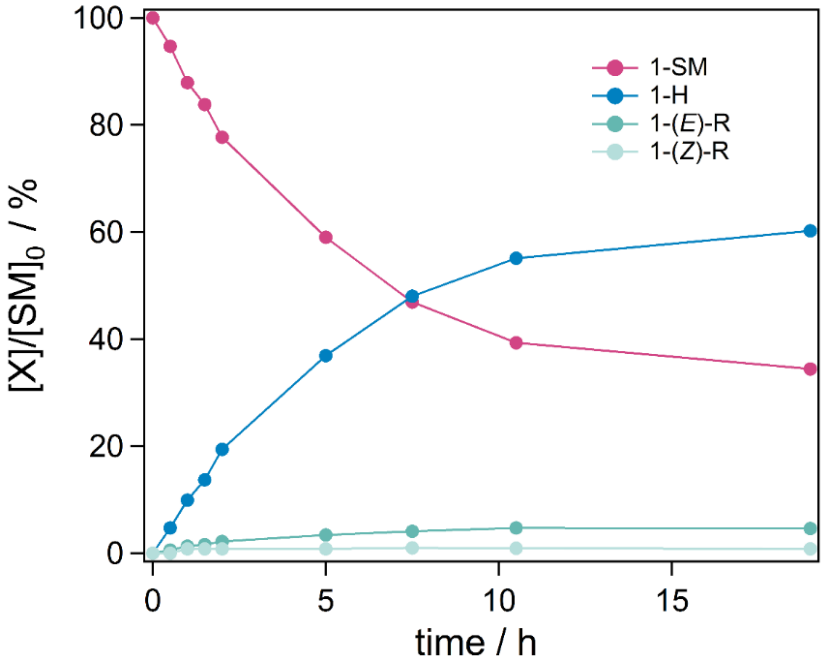

Figure S35. Reaction progress as a function of time when using [Cp*Ir(phen)(H)](PF_6). Conversion of the substrate (**1-SM**, pink trace) and ^{1}H-NMR yields of the different products (**1-H**, blue trace; **1-(*E*)-R** and **1-(*Z*)-R**, turquoise traces) over the reaction course. Monitoring the progress of the reaction mixture containing (3-methoxyprop-1-en-2-yl)benzene (**1-SM**, 50 mM) as a substrate, [Cp*Ir(phen)(H)](PF_6) (2.5 mM), excess 1,10-phenanthroline (15 mM), TEA (250 mM) as sacrificial donor and *tert*-butylbenzene (50 mM) as internal standard while irradiating the reaction mixture at 470 nm (7.5 W). The conversions were determined by ^{1}H-NMR spectroscopy. Acquisition of the NMR spectra occurred in the dark, using 8 aliquots of the same stock solution irradiated in parallel for different amounts of time.

S4.3 Excited-State Quenching Experiments

The MLCT excited-state lifetime τ of $[Cp^*Ir(phen)(H)]^+$ is 148 ns in deaerated CH_3CN containing $[Cp^*Ir(phen)(H)]^+$ (0.2 mM) and NBu_4PF_6 (0.6 mM) at room temperature (Fig. S35), which is in good agreement with the literature,[8] considering that the detected lifetime is concentration dependent.[12] Upon addition of TEA, the emissive MLCT state is quenched with a rate constant of k_q = $4.5 \cdot 10^8$ M^{-1} s^{-1} based on a Stern-Volmer analysis.

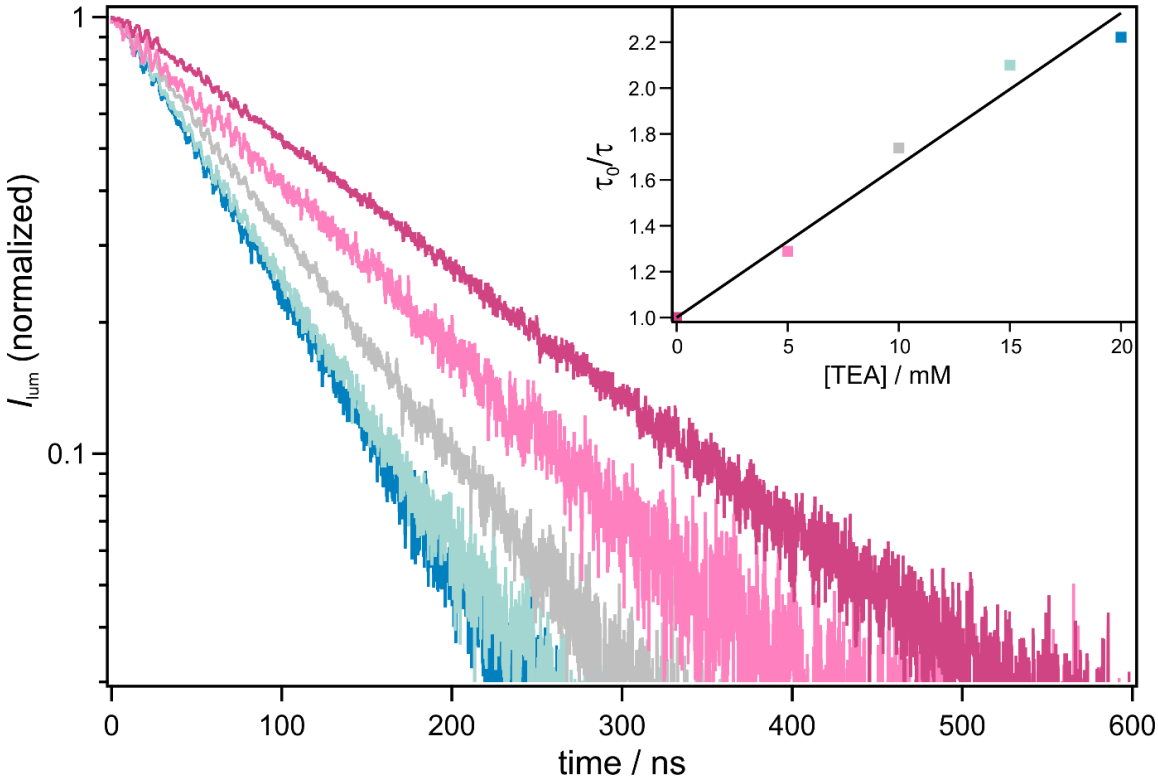

Figure S36. Main plot: Time-resolved luminescence decays of $[Cp^*Ir(phen)(H)](PF_6)$ (0.2 mM) in absence (red trace) and in presence of varying concentrations of TEA. Measurements were performed in deaerated CH_3CN containing NBu_4PF_6 (0.6 mM) at room temperature. Excitation occurred at 455 nm and the luminescence was detected at 700 nm. All decays were normalized to 1.0 at t = 0. Inset: Stern-Volmer plot obtained from the kinetic emission experiments.

Table S5. Lifetime τ at a $[Cp^*Ir(phen)(H)]^+$ concentration of 0.2 mM, Stern-Volmer constant K_{SV} and quenching constant k_q of the reductive quenching of $[Cp^*Ir(phen)(H)](PF_6)$ in presence of TEA in deaerated CH_3CN containing NBu_4PF_6 (0.6 mM) at room temperature.

τ / ns	148
K_{SV} / M^{-1}	66
k_q / M^{-1} s^{-1}	$4.5 \cdot 10^8$

S4.4 Mechanistic Overview

The different possible reaction mechanisms of iridium hydrides are summarized in Figure S37. In absence of both the substrate and a sacrificial donor, iridium(III) hydrides undergo efficient bimetallic "self-quenching" ($k_q = 3.8 \cdot 10^9$ M^{-1} s^{-1})[12] and subsequent H_2-evolution upon irradiation with visible light (Figure S37A), as has been previously reported by the group of Miller.[12] In presence of TEA (250 mM) as a sacrificial donor, reductive quenching becomes the major reaction pathway (Figure S37B), as is evidenced by the higher pseudo first-order rate constant ($1.1 \cdot 10^8$ s^{-1} vs. $9.5 \cdot 10^6$ s^{-1} (for TEA and iridium(III) hydride concentrations of 250 mM and 2.5 mM, respectively)). In absence of a substrate, H_2 evolution from the iridium(II) hydride is expected to be the major reaction product, as H_2 formation is exergonic by 16 kcal/mol. $TEA^{\bullet+}$ serves as a proton source for the regeneration of the iridium(III) hydride. When TAA-OMe is used as a sacrificial donor, reductive quenching of the ^{3}MLCT state is again the major reaction pathway, as was evidenced by the formation of the characteristic $TAA\text{-}OMe^{\bullet+}$ absorption band in the transient absorption experiment (Figures S37C). When an olefin substrate is added to the reaction mechanism, H_2 evolution from the iridium(II) hydride can be avoided and HAT to the olefin substrate is observed instead (Figure S37D).

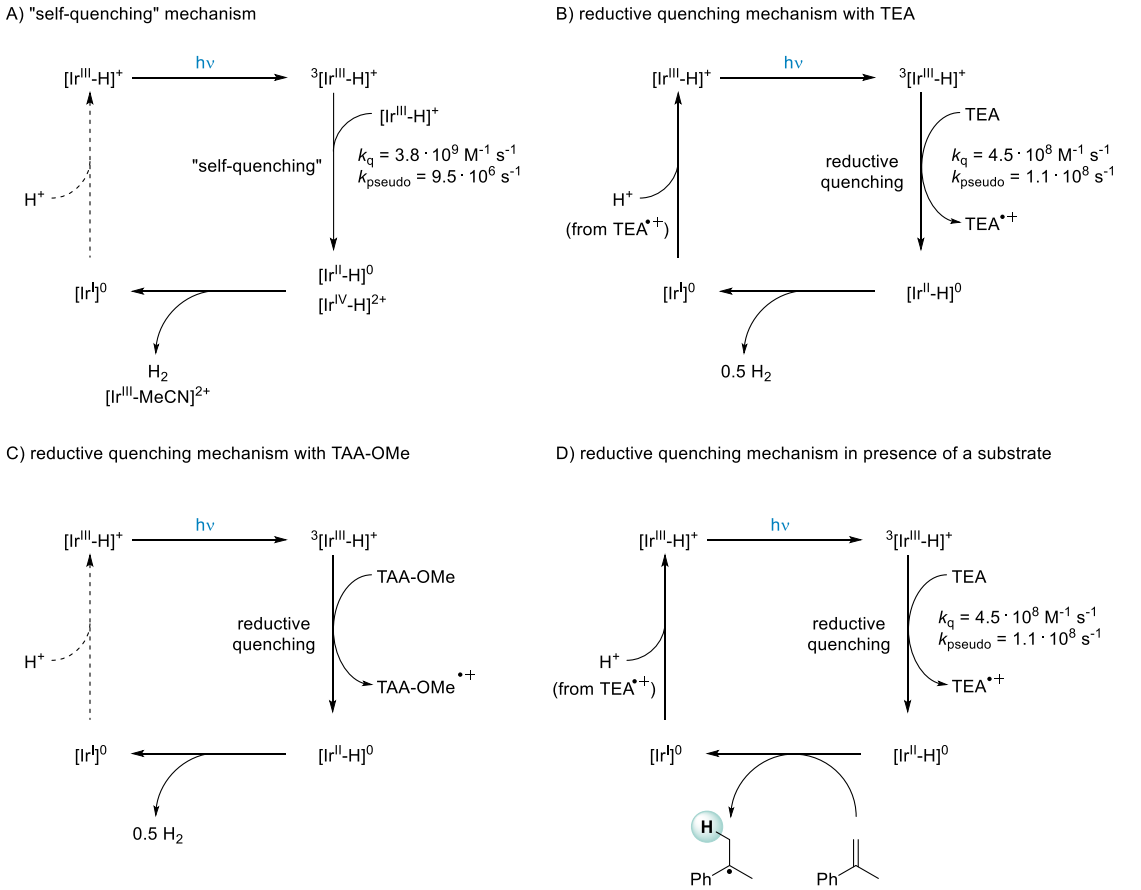

Figure S37. Overview over the different reaction mechanisms of the iridium(III) hydride upon excitation with visible light. A) "Self-quenching" is the dominant reaction pathway in absence of a sacrificial donor.[12] B) and C) Reductive quenching is the major reaction pathway in presence of either B) TEA or C) TAA-OMe as an electron donor. D) In presence of an olefin substrate, HAT to the closed-shell organic substrate takes place.

S4.5 Radical Clock Experiment

Photoinduced H-atom transfer to (1-(2-phenylcyclopropyl)vinyl)benzene (**13-SM**), a radical clock substrate, was investigated to find further evidence for a radical mechanism. The rate constant for the ring opening of this exact substrate is unknown, however, it has been determined for closely related compounds (Table S6). While there is a relatively small difference in the rate constants for the ring opening of secondary and tertiary radicals (compare entry 2 vs. entry 3, Table S6), an additional phenyl substituent on the cyclopropane ring enhances the rate constant k_{RO} (compare entry 2 vs. entry 4, Table S6) by three orders of magnitude. Thus it can be assumed that the rate constant for the ring opening in the structurally related radical intermediate **13-RI1•** (relevant for our studies) occurs with a similar rate constant ($k_{RO} \approx 10^8$ s^{-1}) as in radical intermediate **D** ($3.6 \cdot 10^8$ s^{-1})

Table S6. Rate constants for the ring opening of radical intermediates **A-D** and **13-RI1•**. Whilst the rate constants for radical intermediates **A-D** have been determined previously, the rate constant for the ring opening of radical intermediate **13-RI1•** (relevant for our studies) was estimated by comparison of the different rate constants k_{RO}.

Entry	Radical Intermediate		Rate constant of the ring opening k_{RO} / s^{-1}
1	**A**	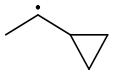	$7 \cdot 10^6$ [271]
2	**B**	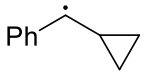	$2.7 \cdot 10^5$ [271]
3	**C**	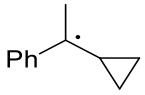	$3.6 \cdot 10^5$ [271]
4	**D**	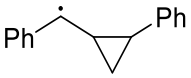	$3.6 \cdot 10^8$ [272]
5	**13-RI1•**	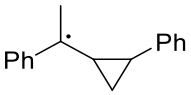	$\approx 10^8$

For the radical clock experiment, degassed stock solutions of (1-(2-phenylcyclopropyl)vinyl)benzene (**13-SM**, 100 µL, 500mM in CD_3CN, 50.0 µmol, 1.0 eq.), [Cp*Ir(phen)Cl]Cl (250 µL, 10 mM in CD_3CN, 2.50 µmol, 5.0 mol%) and *tert*-butylbenzene (100 µL, 500 mM in CD_3CN, 50.0 µmol, 1.0 eq.) as an internal standard were combined and further diluted with degassed CD_3CN (550 µL). TEA (34.7 µL, 250 µmol, 5.0 eq.) was added and 0.5 mL of the reaction mixture were transferred to an NMR-tube. The reaction mixture was then irradiated at 470 nm for 44 h and the conversion was determined both by ^{1}H-NMR spectroscopy and GC-MS spectrometry according to general procedure C.

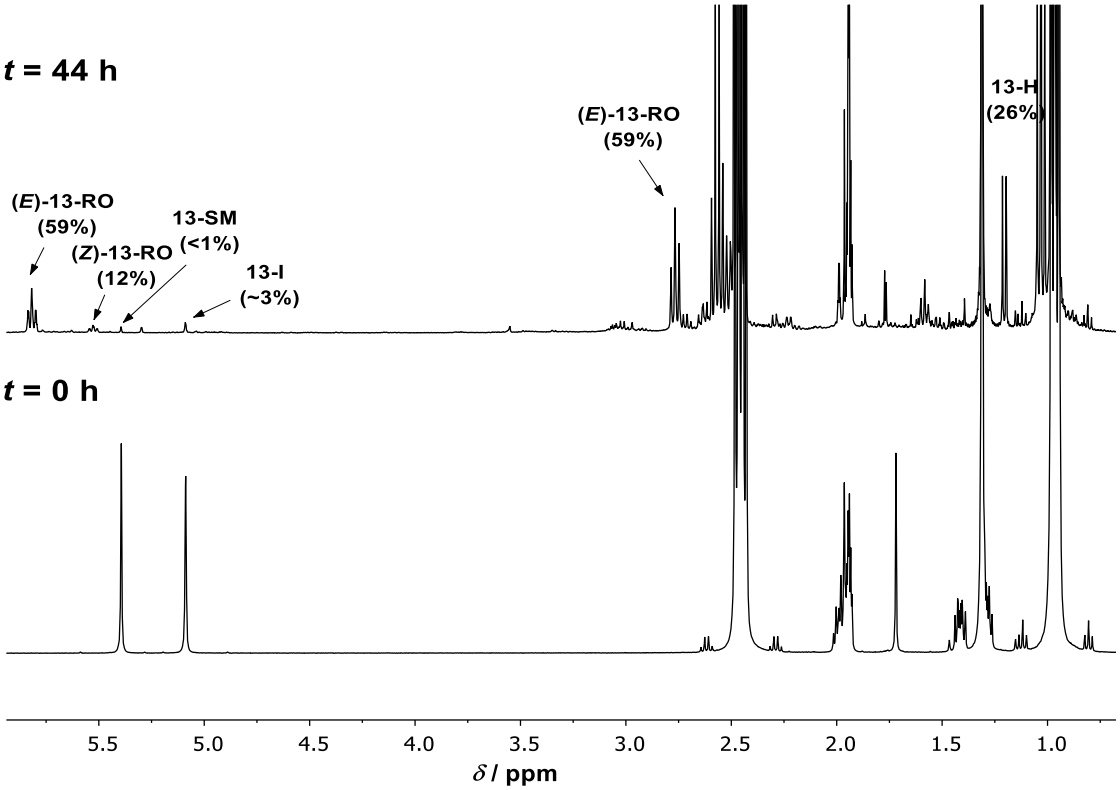

Figure S38. ^{1}H-NMR spectra of the radical clock experiment: The ^{1}H-NMR spectra of the reaction mixture before (*t* = 0 h) and after (*t* = 44 h) irradiation are shown. Visible light-induced hydrogenation of (1-(2-phenylcyclopropyl)-vinyl)benzene (**13-SM**) affords pent-3-ene-1,4-diyldibenzene (**(*E*)-13-RO** and **(*Z*)-13-RO**), pent-4-ene-1,4-diyldibenzene (**13-I**) and pentane-1,4-diyldibenzene (**13-H**).

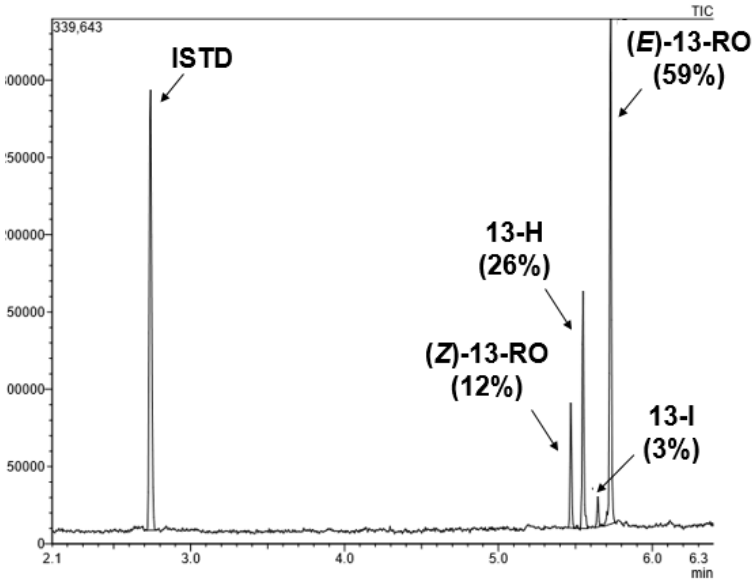

Figure S39. GC-MS trace of the radical clock experiment: Visible light-induced hydrogenation of (1-(2-phenylcyclopropyl)-vinyl)benzene (**13-SM**) affords pent-3-ene-1,4-diyldibenzene (**(*E*)-13-RO** and **(*Z*)-13-RO**), pent-4-ene-1,4-diyldibenzene
(**13-I**) and pentane-1,4-diyldibenzene (**13-H**). The different analytes were separated using GC method A (see section S1 for details).

Analysis of the reaction mixture by ^{1}H-NMR spectroscopy and GC-MS spectrometry indicated that no ring-retention product (**13-RR**) is formed (Fig. S38) and that radical

intermediate **13-RI1•** undergoes fast ring-opening to give the ring-opened product **13-RO** (71%). Thus, secondary HAT to the radical intermediate is slower than the ring-opening reaction ($k_{RO} \approx 10^8$ s^{-1}). However, **13-RO** is not the only product observed after photoinduced hydrogenation of **13-SM**. Since **13-RO** is a suitable substrate for photoinduced H-atom transfer as well, it can further react under the applied conditions, as confirmed by the formation of both the hydrogenation (**13-H**, 26%) and the isomerization (**13-I**, 3%) products (Fig. S38).

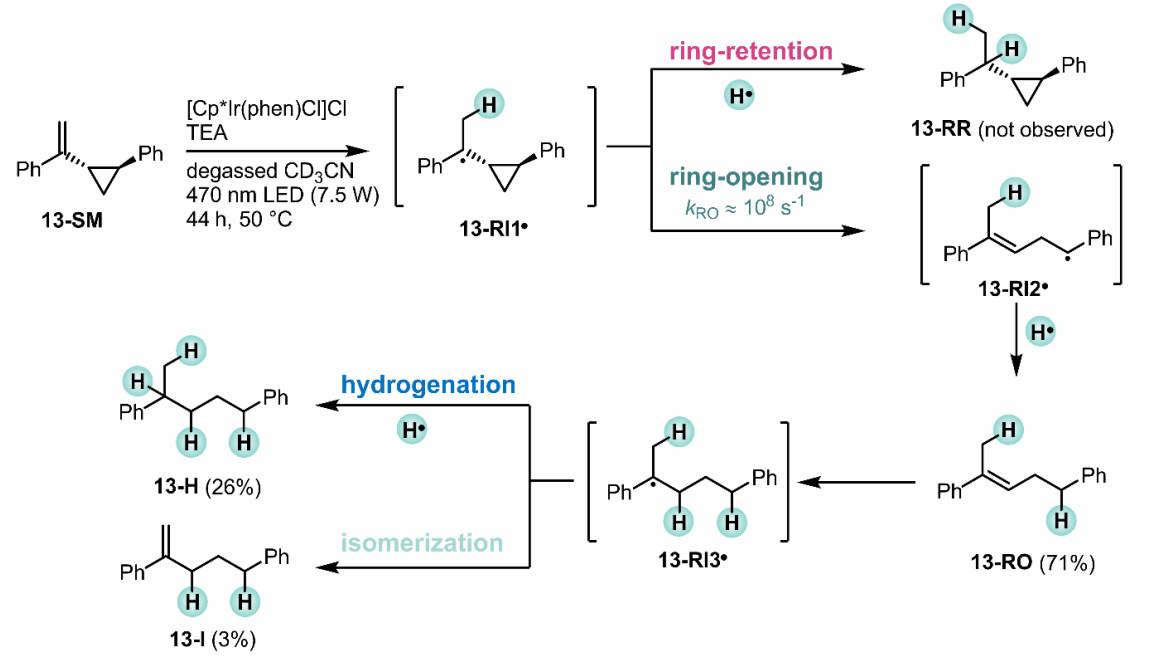

Figure S40. Radical clock experiment with cyclopropane substrate **13-SM** confirms that the reaction proceeds via a radical mechanism. The formed ring-opened product (**13-RO**) can engage in a secondary photoinduced onward reaction to give the hydrogenation (**13-H**) and isomerization (**13-I**) products. For simplicity, only the (*E*)-isomer of the ring-opened product **13-RO** is shown.

S4.6 Experiment with a Deuterated Substrate

To explore the reversibility of the initial photoinduced HAT step, a deuterated substrate ((3-methoxyprop-1-en-2-yl-*1,1,3,3-d*$_4$)benzene, **1-SM-*d*$_4$**) was synthesized and subjected to the reaction conditions. In contrast to traditional studies, where usually a metal-deuteride is used to test the reversibility of hydrogen atoms transfers,[178] we decided to use a deuterated substrate and a non-deuterated hydrogen atom source (TEA). Thus, our method is based on a non-deuterated metal hydride (formed on the basis of the non-deuterated TEA) and a deuterated substrate.

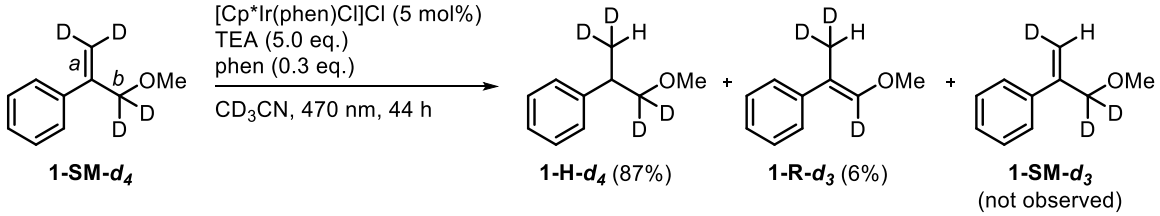

Scheme S7. Experiment with a deuterated substrate **1-SM-*d*$_4$** probing the reversibility of the initial HAT.

(3-Methoxyprop-1-en-2-yl-*1,1,3,3-d*$_4$)benzene (**1-SM-*d*$_4$**) was reduced to (1-methoxy-propan-2-yl-1,1,3,3-*d*$_4$)benzene (**1-H-*d*$_4$**) according to general procedure C. The photochemical reaction was followed by integration of the characteristic singlets of the methoxy-groups in the ^{1}H-NMR spectra of the reaction mixtures. To do so, the chemical shifts of the observable methoxy signals were compared to the corresponding resonance of the non-deuterated substrate **1-SM** (Fig. S39). Based on this, the conversion of **1-SM-*d*$_4$** was determined to be 93%, resulting in 87% of the hydrogenation product **1-H-*d*$_4$**. Throughout the experiment, no proton-incorporation into the initial terminal double bond (bond labeled with "*a*" in Scheme S7) to afford **1-SM-*d*$_3$** was observed, indicating that reverse HAT from radical intermediate **1- RI$^{\bullet}$-*d*$_4$** ($k_{\text{-HAT1}}$ in Fig. 9 in main paper) is kinetically not competitive with onward reaction to **1-H-*d*$_4$** or **1-R-*d*$_3$**. Since the formed rearranged products **1-R-*d*$_3$** can be further hydrogenated to the corresponding hydrogenation product **1-H-*d*$_4$** (*k*$_{\text{-R}}$, Fig. 9 in main paper), proton incorporation at the CD_2 group (position labeled with "*b*" in Scheme S7) is possible. However, the exact amount of proton incorporation at this position could not be determined with the applied analytical methods. Also, further identification of the different formed products by mass spectrometry is not possible due to the identical masses of the different isotopomers. Thus, proton incorporation at the CD_2-position (labeled with "*b*" in Scheme S7) is neglected in the schemes for clarity.

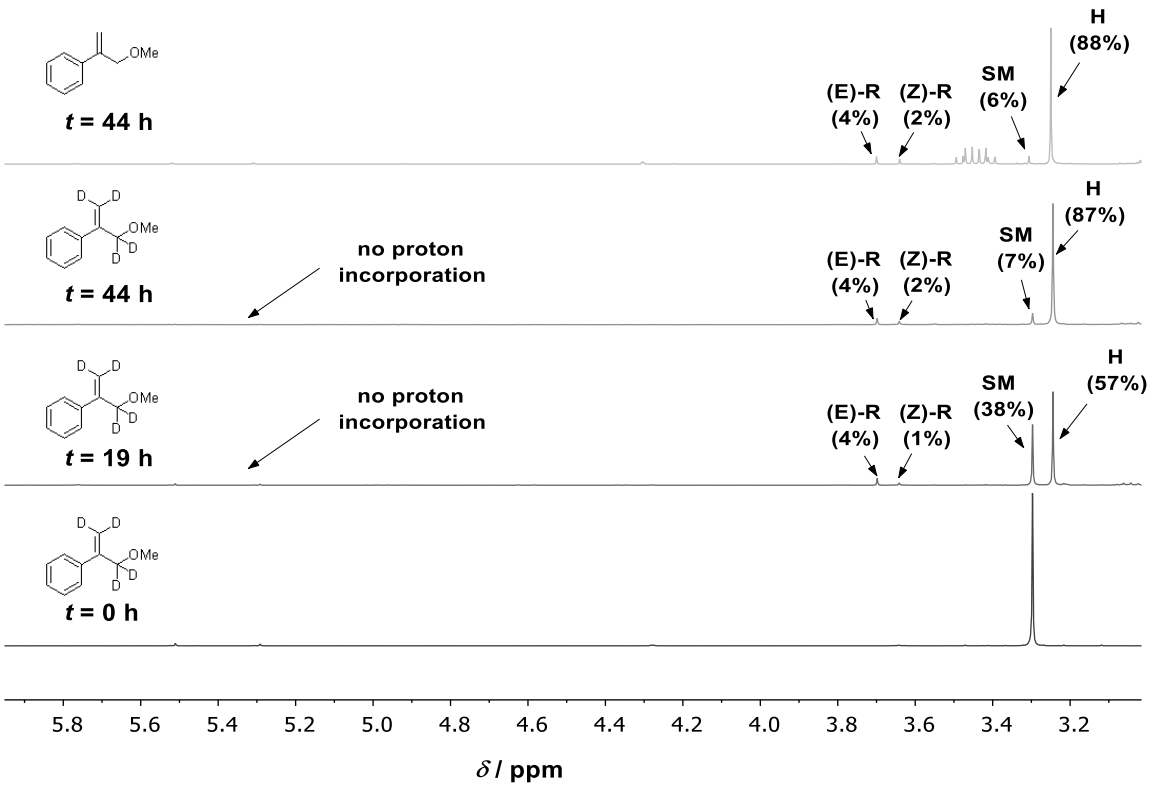

Figure S41. Photochemical experiment with a deuterated substrate: Visible-light driven hydrogenation of (3-methoxyprop-1-en-2-yl-*1,1,3,3-d*$_4$)benzene (**1-SM-*d*$_4$**) at different irradiation times in comparison to the visible-light driven hydrogenation of the non-deuterated substrate **1-SM**.

S5 Spectra of New Compounds

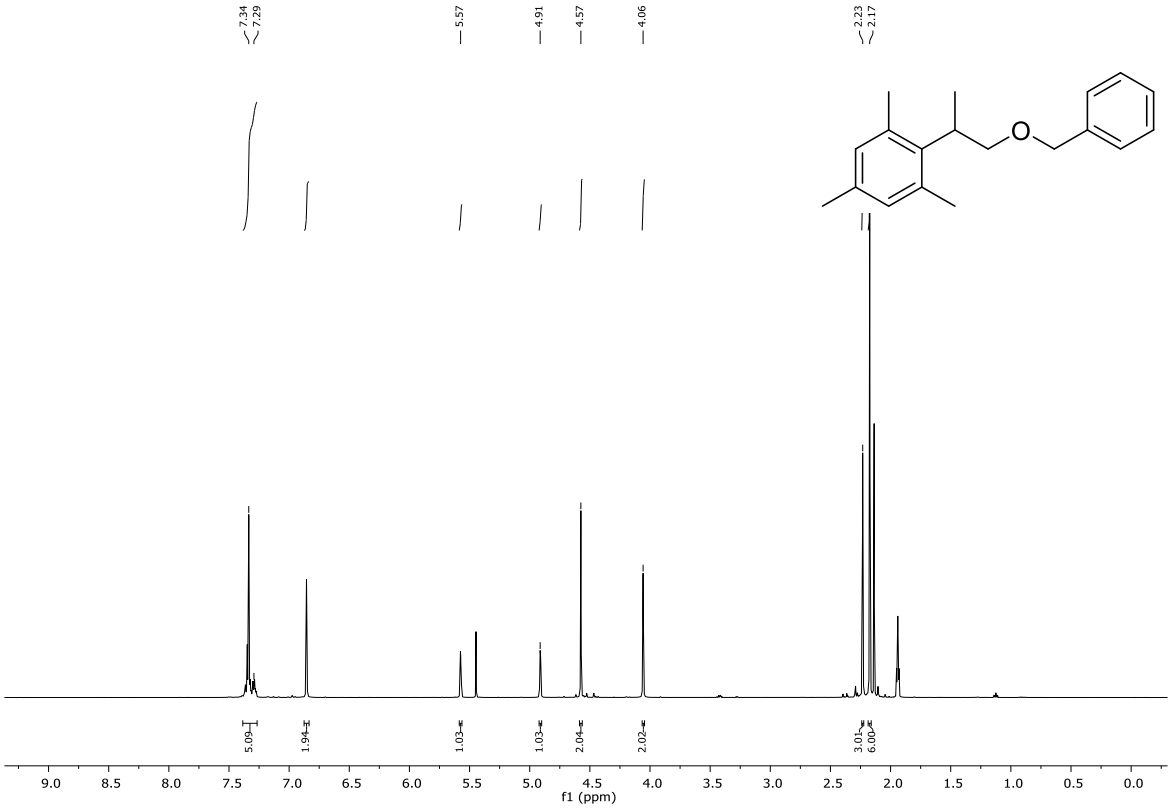

Figure S42. ^{1}H-NMR spectrum of 2-(3-(benzyloxy)prop-1-en-2-yl)-1,3,5-trimethylbenzene (**7-SM**) in CD_3CN.

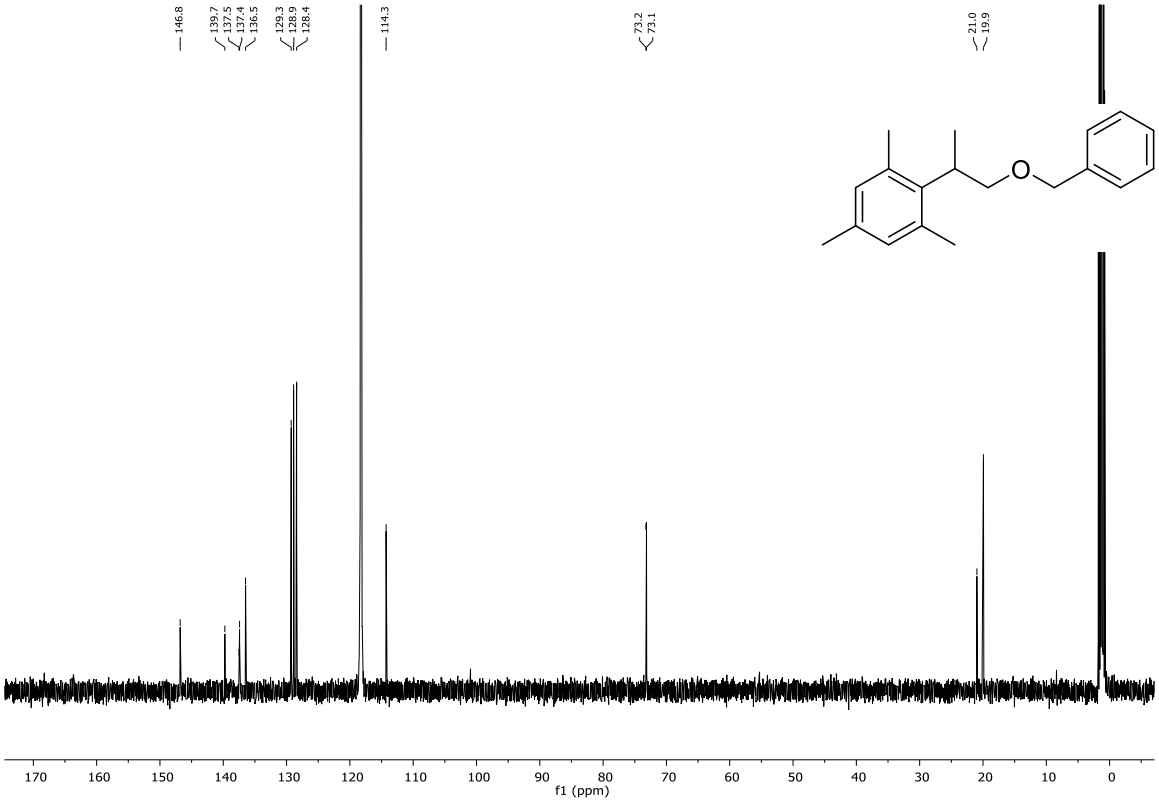

Figure S43. ^{13}C-{^{1}H}-NMR spectrum of 2-(3-(benzyloxy)prop-1-en-2-yl)-1,3,5-trimethylbenzene (**7-SM**) in CD_3CN.

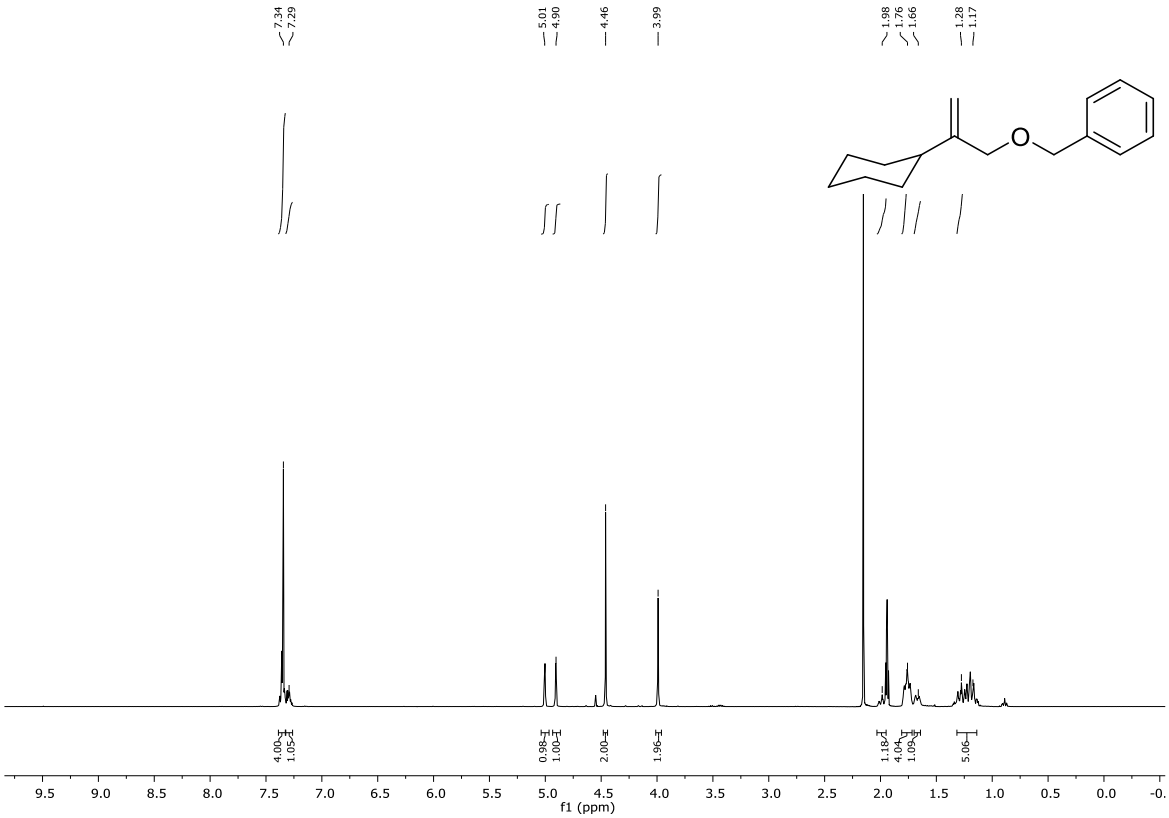

Figure S44. ^{1}H-NMR spectrum of (((2-cyclohexylallyl)oxy)methyl)benzene (**10-SM**) in CD_3CN.

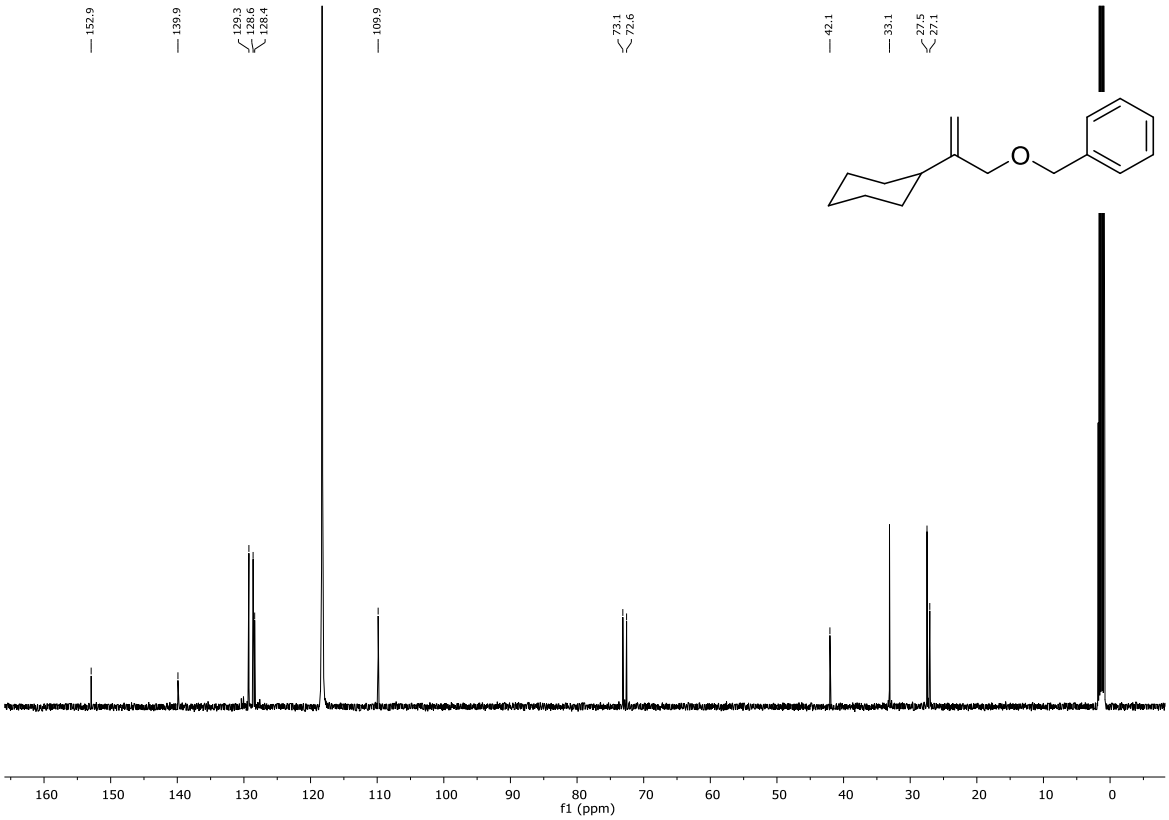

Figure S45. ^{13}C-{^{1}H}-NMR spectrum of (((2-cyclohexylallyl)oxy)methyl)benzene (**10-SM**) in CD_3CN.

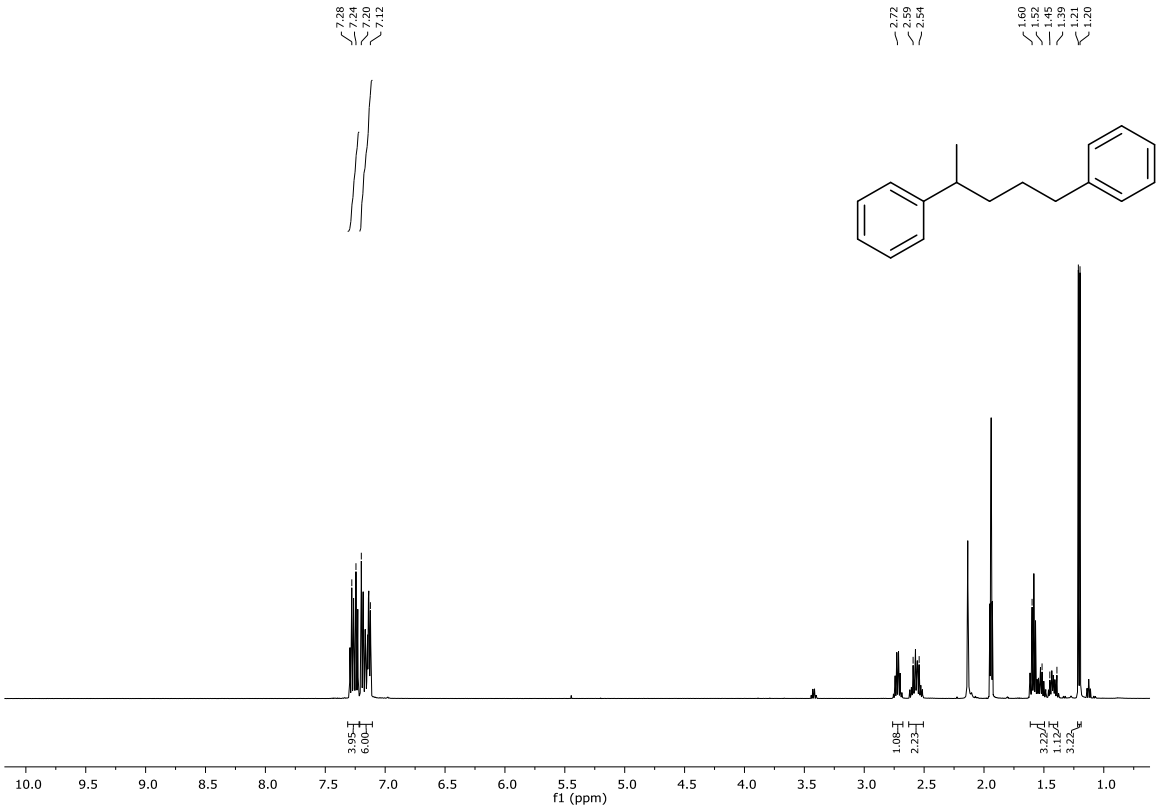

Figure S46. ^{1}H-NMR spectrum of pentane-1,4-diyldibenzene (**13-H**) in CD_3CN.

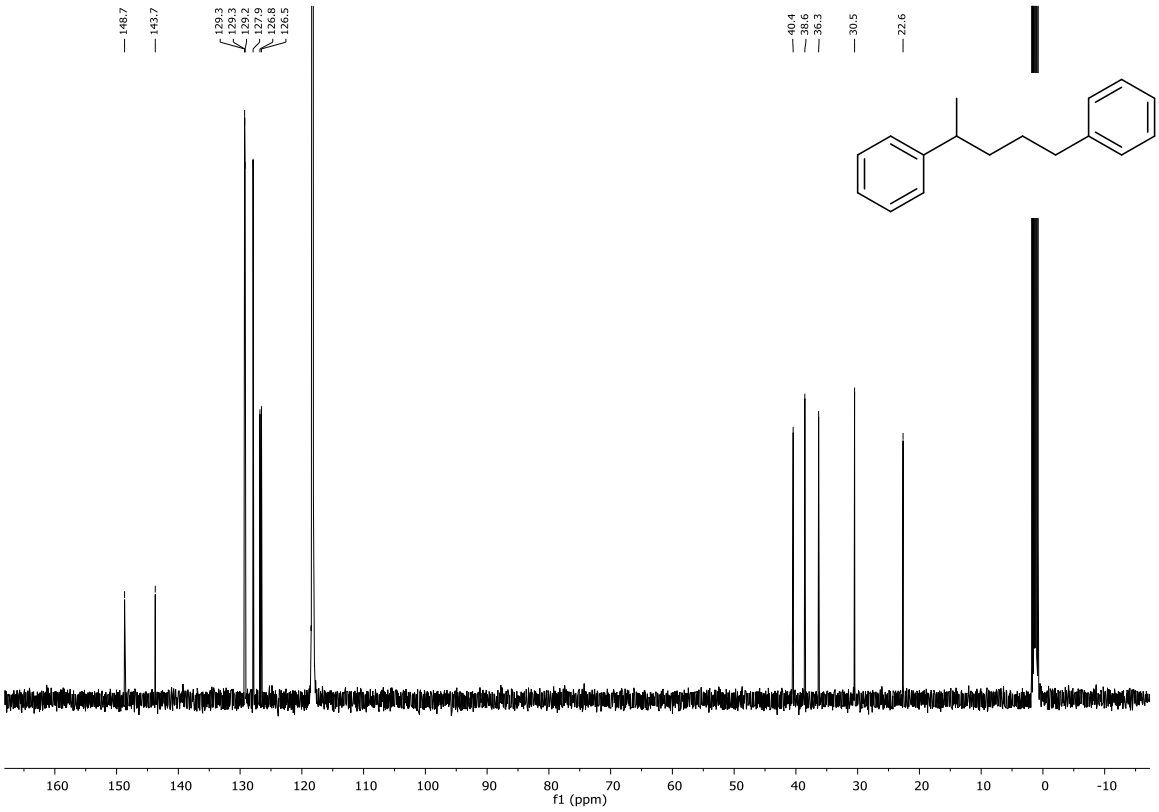

Figure S47. ^{13}C-{^{1}H}-NMR spectrum of pentane-1,4-diyldibenzene (**13-H**) in CD_3CN.

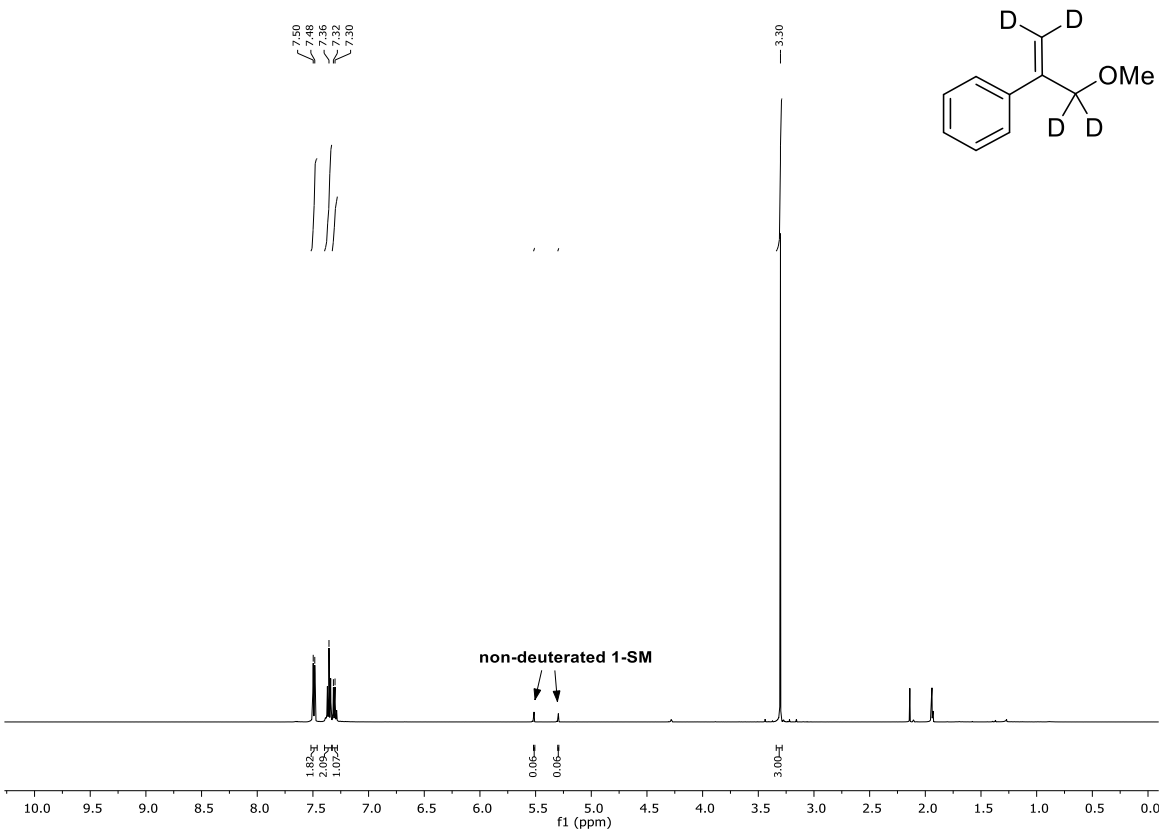

Figure S48. ^{1}H-NMR spectrum of (3-methoxyprop-1-en-2-yl-1,1,3,3-*d*$_4$)benzene (**1-SM-*d*$_4$**) in CD_3CN.

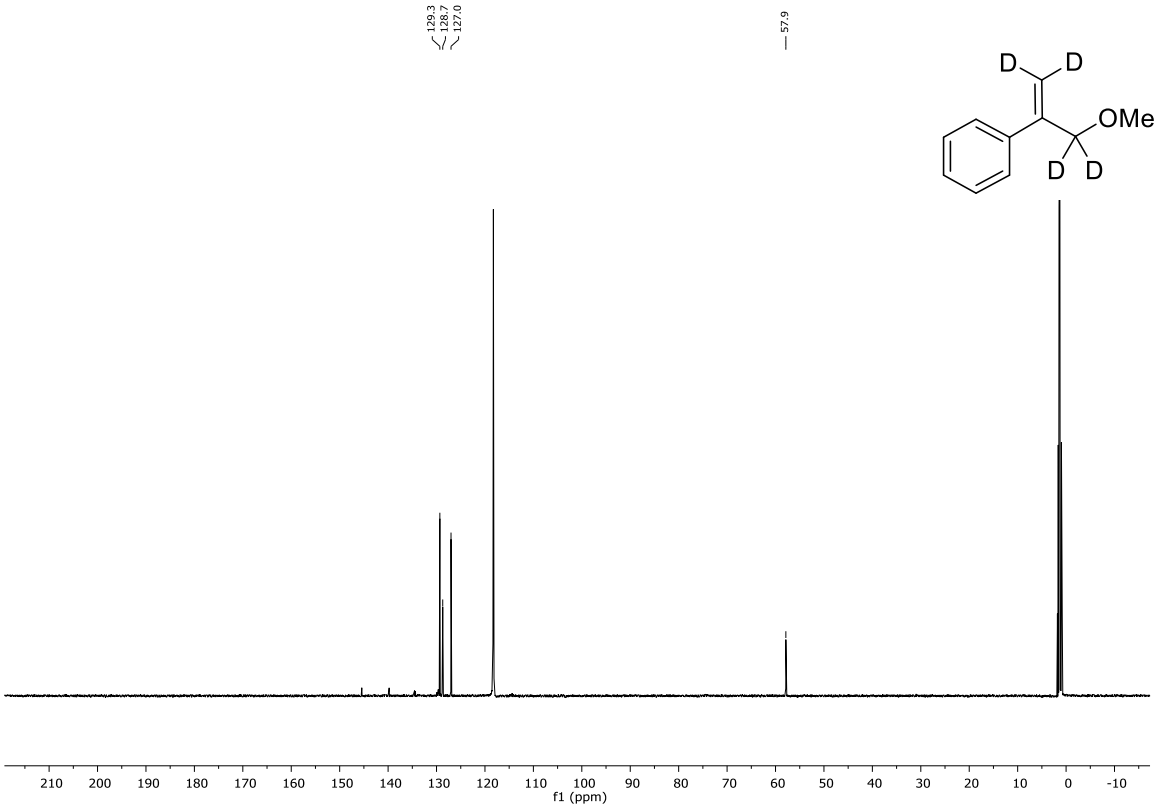

Figure S49. ^{13}C-{^{1}H}-NMR spectrum of (3-methoxyprop-1-en-2-yl-1,1,3,3-*d*$_4$)benzene (**1-SM-*d*$_4$**) in CD_3CN.

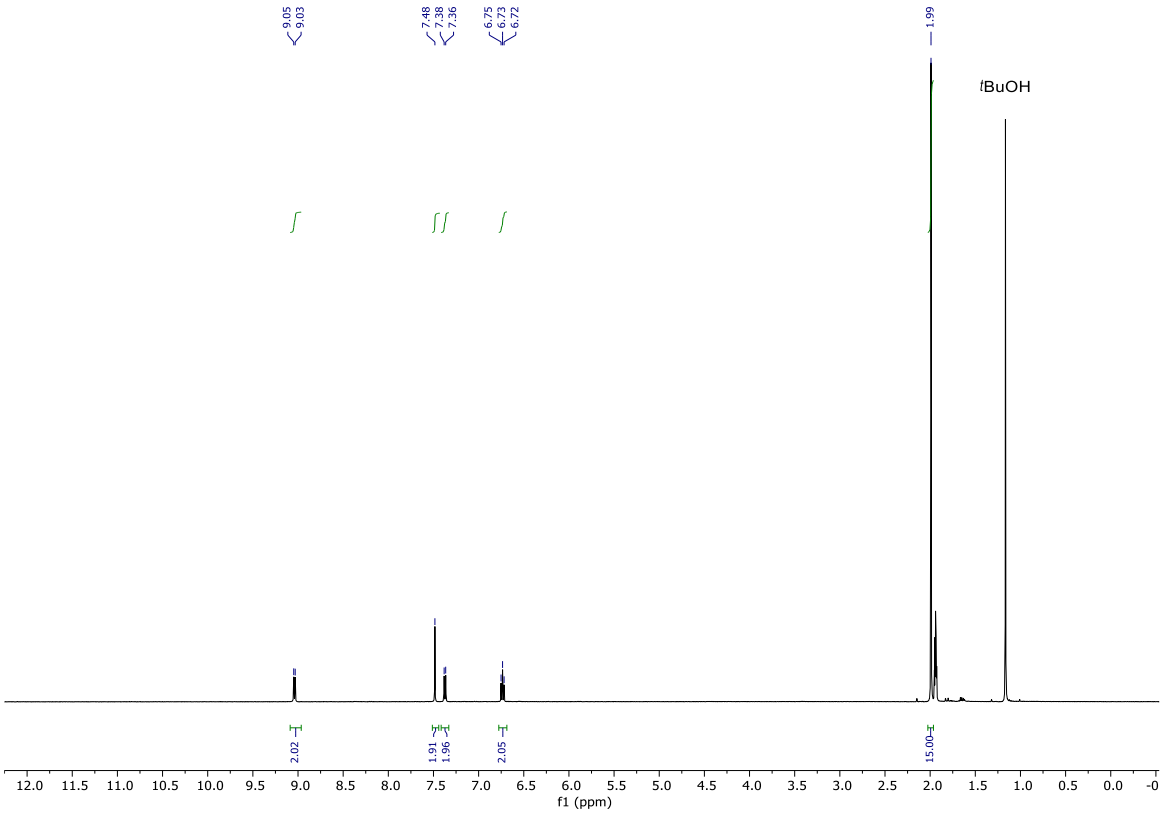

Figure S50. ^{1}H-NMR reference spectrum of $[Cp^*Ir(phen)]^0$ obtained after deprotonation of $[Cp^*Ir(phen)(H)]^+$ in CD_3CN with KO^{t}Bu (1.3 eq.).

6.2 Supporting Information for Photochemical 1,4-BNAH Regeneration with Iridium Sensitizers (Chapter 4)

Table of Contents

S1 Equipment and Methods

General

Unless stated otherwise, all air- or moisture-sensitive syntheses were performed under inert conditions (nitrogen or argon atmosphere). Dry solvents were used as received and dry dichloromethane (DCM) was obtained from a commercial solvent purification system by Innovative Technology. All commercially available chemicals were purchased from ABCR, Acros Organics, Fluorochem or Sigma-Aldrich and used as received. 1-Benzyl-3-carbamoylpyridin-1-ium chloride (**BNACl**) and **[Cp*Rh(bpy)Cl]Cl** were synthesized by Prof. Dr. Xingwei Guo and Dr. Michael Skaisgirski.

Chromatography

Column chromatography was performed with silica gel from Silicycle (silica flash, 40-63 µm, (230-400 mesh ASTM) for flash column chromatography). Thin layer chromatography (TLC) was carried out with pre-coated aluminium sheets (precoated with silica 60, from Merck, layer thickness of 0.25 mm), containing a fluorescence indicator F254. Visualization of the compounds occurred under UV light using either the 254 nm or the 365 nm output of a UV lamp.

Microwave

Microwave-assisted syntheses were performed with a Biotage® Initiator microwave reactor from Biotage at a constant irradiation temperature.

NMR spectroscopy

NMR spectra were measured on a Bruker Avance III operating at 400 MHz, 500 MHz or 600 MHz proton frequencies. All chemical shifts are reported in δ values in ppm and were referenced to the signals of the residual non-perdeuterated solvent used.[239] ^{19}F-{^{1}H}-NMR spectra were referenced to trifluoroacetic acid (–75.3 ppm[273]). The deuterated solvents for NMR-spectroscopy were obtained from Cambridge Isotope Laboratories. All coupling constants *J* are given in Hertz (Hz) and the following abbreviations are used to describe their coupling patterns: s (singlet), d (doublet), t (triplet), q (quartet), dt (doublet of triplets), td (triplet of doublets), ddd (doublet of doublet of doublets), m (multiplet).

High-resolution mass spectrometry

High-resolution mass spectrometry was performed by Dr. Michael Pfeffer on a Bruker maXis 4G QTOF ESI spectrometer in the Department of Chemistry at the University of Basel.

Elemental analysis

Elemental analyses were performed by Ms. Sylvie Mittelheisser on a Vario Micro Cube instrument in the Department of Chemistry at the University of Basel.

Cyclic voltammetry

Cyclic voltammetry was carried out using a Versastat3-200 potentiostat from Princeton Applied Research. A glassy carbon disk was used as working electrode, a silver wire as counter electrode and a SCE as reference electrode.

Steady-state absorption spectroscopy

Optical absorption spectroscopy was measured on a Cary 5000 UV-Vis-NIR instrument from Varian.

Time-resolved luminescence spectroscopy

Time-resolved luminescence spectroscopy was performed on a LP920-KS instrument from Edinburgh Instruments. Excitation occurred at 420 nm using a Quantel Brilliant b laser combined with an optical parametric oscillator (OPO) from Opotek as excitation source. The laser pulse duration was ~10 ns and the pulse frequency was 10 Hz. Kinetics at single detection wavelengths were recorded using a photomultiplier tube.

Further fluorescence lifetime and quenching experiments with the water-soluble Ir complexes were performed on a FLS1000 spectrometer (time-correlated single photon counting (TCSPC) technique) from Edinburgh Instruments using a pulsed LED (ca. 900 ps pulse width) for excitation at 405 nm.

Transient absorption spectroscopy

Transient absorption spectroscopy was performed on a LP920-KS instrument from Edinburgh Instruments. Excitation of the complexes occurred at 420 nm using a frequency-tripled Nd:YAG laser (Quantel Brilliant, ca. 10 ns pulse width) equipped with an OPO from Opotek and the typical pulse energy varied from ca 7 mJ to 14 mJ. A beam expander (GBE02-A from Thorlabs) was used to improve the excitation homogeneity in the detection volume. The transient absorption spectra were detected with an iCCD camera from Andor.

Photoirradiation

Continuous-wave photo-irradiation was carried out at room temperature using a 455 nm (~1000 mW power output) collimated LED purchased from ThorLabs.

S2 Experimental Procedures

S2.1 Synthesis of the Iridium Sensitizers

General procedure A: Microwave-assisted synthesis of (*fac*)-Ir(ppy)$_3$ derivatives

The microwave-assisted synthesis of the **(*fac*)-Ir(ppy)$_3$** derivatives (referred to as **Irppy$_3$** derivatives hereafter) was adapted from a previously published protocol.[225] In a microwave tube, $IrCl_3 \cdot H_2O$ (1.0 eq.) and the **ppyH** ligand (50-100 eq.) were dissolved in ethylene glycol (40 mL per mmol $IrCl_3 \cdot H_2O$) and the reaction mixture was degassed by bubbling nitrogen through the solution for 30 min. The reaction was heated to 200 °C for 30 min under microwave irradiation. After cooling to rt, methanol (40 mL per mmol $IrCl_3 \cdot H_2O$) was added and the resulting suspension was stored in the fridge overnight. The formed precipitate was collected by filtration and washed with methanol to afford the desired **Irppy$_3$** derivative.

General procedure B: Sulfonation of Irppy$_3$ derivatives

The synthesis of the different **Irsppy** derivatives was adapted from a previously published protocol.[121] An emulsion of concentrated H_2SO_4 (3.3 eq.) in trifluoroacetic anhydride (TFAA, 25 mL per mmol of **Irppy$_3$** derivative) was stirred at rt for several hours under nitrogen atmosphere. After complete dissolution (reaction) of the sulfuric acid, a previously prepared solution of the **Irppy$_3$** derivative (1.0 eq.) in dry DCM (100 mL per mmol of **Irppy$_3$** derivative) was slowly added and the reaction mixture was stirred at rt overnight. The solvent was evaporated under reduced pressure. The resulting residue was treated with sat. aq. $NaHCO_3$ solution (20 mL per mmol of **Irppy$_3$** derivative). The solvent was removed under reduced pressure and the crude product was purified by flash column chromatography to afford the desired **Irsppy** derivative.

4-Fluorophenylpyridine (FppyH)

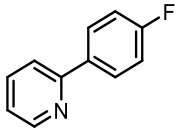

4-Fluorophenylboronic acid (**2a**, 10.6 g, 76.0 mmol, 1.2 eq.) and 2-bromopyridine (**1**, 10.0 g, 63.3 mmol, 1.0 eq.) were dissolved in aq. Na_2CO_3 solution (1 M, 100 mL) and THF (300 mL) under nitrogen atmosphere. The reaction mixture was degassed by bubbling nitrogen through the solution for 30 min. $Pd(PPh_3)_4$ (2.63 g, 2.27 mmol, 3 mol%) was added and the reaction mixture was heated to 140 °C for 3 h. The reaction mixture was allowed to cool to rt, the layers were separated, and the aqueous layer was extracted with DCM (3 × 15 mL). The combined organic layers were dried over anhydrous sodium sulfate, filtered and concentrated under reduced pressure. The crude product was purified by gradient flash column chromatography (SiO_2, pentane/EtOAc 10:1 then pentane/EtOAc

4:1) to afford 4-fluorophenylpyridine (**FppyH**, 4.09 g, 23.6 mmol, 37%) as a yellowish liquid. Analytical data matches the literature.[274]

$C_{11}H_8FN$ (173.2 g mol^{-1}):

^{1}H NMR (400 MHz, 298 K, $CDCl_3$, δ/ppm): 8.67 (d, *J* = 4.9 Hz, 1H), 8.01-7.95 (m, 2H), 7.74 (pseudo-td, *J* = 7.7 Hz, 1.8 Hz, 1H), 7.67 (d, *J* = 8.0 Hz, 1H), 7.22 (ddd, *J* = 7.4 Hz, 4.8 Hz, 1.2 Hz, 1H), 7.18-7.12 (m, 2H).

2-(2,4-Difluorophenyl)pyridine (dFppyH)

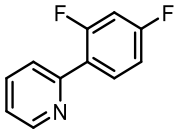

In a microwave vial, 2,4-difluorophenylboronic acid (**2b**, 1.00 g, 6.33 mmol, 1.0 eq.) and 2-bromopyridine (**1**, 1.20 g, 7.06 mmol, 1.2 eq.) were dissolved in aq. Na_2CO_3 solution (1 M, 5.0 mL) and THF (15 mL) under nitrogen atmosphere. The reaction mixture was degassed by bubbling nitrogen through the solution for 30 min. $Pd(PPh_3)_4$ (219 mg, 190 µmol, 3 mol%) was added and the reaction mixture was heated to 140 °C for 3 h under microwave irradiation. The reaction mixture was allowed to cool to rt, the layers were separated, and the aqueous layer was extracted with DCM (3 × 15 mL). The combined organic layers were dried over anhydrous sodium sulfate, filtered and concentrated under reduced pressure. The crude product was purified by flash column chromatography (SiO_2, cyclohexane/EtOAc 4:1) to afford 2,4-difluorophenylpyridine (**dFppyH**, 755 mg, 3.95 mmol, 62%) as a colorless liquid. Analytical data matches the literature.[275]

$C_{11}H_7F_2N$ (191.2 g mol^{-1}):

^{1}H NMR (400 MHz, 298 K, $CDCl_3$, δ/ppm): 8.68 (pseudo-dt, *J* = 4.8 Hz, 1.5 Hz, 1H), 7.98 (pseudo-td, *J* =8.9 Hz, 6.7 Hz, 1H), 7.73-7.68 (m, 2H), 7.21 (ddd, *J* = 6.1 Hz, 4.8 Hz, 2.7 Hz, 1H), 7.00-6.94 (m, 1H), 6.88 (ddd, *J* = 11.3 Hz, 8.8 Hz, 2.5 Hz, 1H).

Irppy$_3$

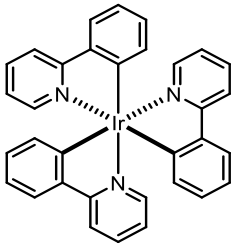

Irppy$_3$ was synthesized according to general procedure A. $IrCl_3{\cdot}H_2O$ (242 mg, 764 µmol, 1.0 eq.) and 2-phenylpyridine (**ppyH**, 11.9 g, 76.4 mmol, 100 eq.) in ethylene glycol (32 mL) were heated to 200 °C for 30 min under microwave irradiation. **Irppy$_3$** (388 mg, 590 µmol, 78%) was obtained as a bright yellow solid. Analytical data matches the literature.[118]

$C_{33}H_{24}IrN_3$ (654.8 g mol^{-1}):
^{1}H NMR (400 MHz, 298 K, CD_2Cl_2, δ/ppm): 7.92 (d, *J* = 7.9 Hz, 3H), 7.71-7.62 (m, 6H), 7.59-7.52 (m, 3H), 6.95-6.84 (m, 6H), 6.82-6.71 (m, 6H).

IrFppy$_3$

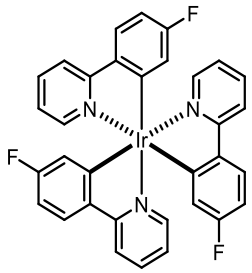

IrFppy$_3$ was synthesized according to general procedure A. $IrCl_3{\cdot}H_2O$ (146 mg, 462 µmol, 1.0 eq.) and 4-fluorophenylpyridine (**FppyH**, 4.00 g, 23.2 mmol, 50 eq.) in ethylene glycol (30 mL) were heated to 200 °C for 30 min under microwave irradiation. **IrFppy$_3$** (237 mg, 334 µmol, 72%) was obtained as a green solid. Analytical data matches the literature.[120]
$C_{33}H_{21}F_3IrN_3$ (708.8 g mol^{-1}):
^{1}H NMR (400 MHz, 298 K, CD_2Cl_2, δ/ppm): 7.87 (pseudo-dt, *J* = 8.2 Hz, 1.0 Hz, 3H), 7.72-7.64 (m, 6H), 7.53 (ddd, *J* = 5.5 Hz, 1.7 Hz, 0.8 Hz, 3H), 6.94 (ddd, *J* = 7.2 Hz, 5.6 Hz, 1.3 Hz, 3H), 6.63 (pseudo-td, *J* = 8.8 Hz, 2.7 Hz, 3H), 6.39 (dd, *J* = 10.3 Hz, 2.7 Hz, 3H).

IrdFppy$_3$

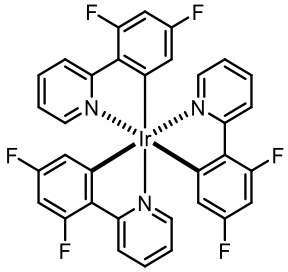

IrdFppy$_3$ was synthesized according to general procedure A. $IrCl_3{\cdot}H_2O$ (166 mg, 524 µmol, 1.0 eq.) and 2-(2,4-difluorophenyl)pyridine (**dFppyH**, 5.00 g, 26.2 mmol, 50 eq.) in ethylene glycol (36 mL) were heated to 200 °C for 30 min under microwave irradiation. **IrdFppy$_3$** (268 mg, 351 µmol, 67%) was obtained as a green solid. Analytical data matches the literature.[120]
$C_{33}H_{18}F_6IrN_3$ (762.7 g mol^{-1}):
^{1}H NMR (400 MHz, 298 K, CD_2Cl_2, δ/ppm): 8.35-8.27 (m, 3H), 7.76-7.71 (m, 3H), 7.51 (ddd, *J* = 5.6 Hz ,1.8 Hz, 0.9 Hz, 3H), 6.98 (ddd, *J* = 7.1 Hz, 5.6 Hz, 1.3 Hz, 3H), 6.42 (ddd, *J* = 13.1 Hz, 9.2 Hz, 2.5 Hz, 3H), 6.24 (dd, *J* = 9.2 Hz, 2.5 Hz, 3H).

Irsppy

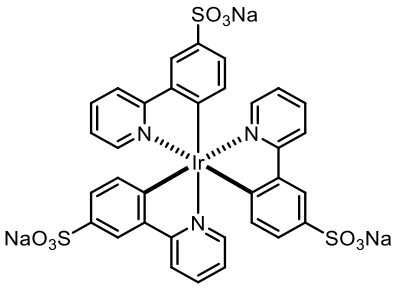

Irsppy was synthesized according to general procedure B. H_2SO_4 (65.8 mg, 670 µmol, 3.3 eq.) and TFAA (5.0 mL) were stirred at rt for 3.5 h, before **Irppy$_3$** (132 mg, 201 µmol, 1.0 eq.) in DCM (20 mL) was added and the resulting yellow solution was stirred at rt overnight. After purification by gradient flash column chromatography (SiO_2, acetonitrile/MeOH/H_2O 50:5:1 then acetonitrile/MeOH/H_2O 50:5:10), **Irsppy** (170 mg, 177 µmol, 88%) was obtained as a yellow solid. Analytical data matches the literature.[121]
$C_{33}H_{21}IrN_3Na_3O_9S_3$ (960.9 g mol^{-1}):
^{1}H NMR (500 MHz, 298 K, D_2O, δ/ppm): 8.18 (s, 3H), 8.15 (d, *J* = 8.3 Hz, 3H), 7.81 (pseudo-t, *J* = 8.2 Hz, 3H), 7.64 (d, *J* = 4.4 Hz, 3H), 7.19 (d, *J* = 8.0 Hz, 3H), 7.05 (pseudo-t, *J* = 5.4 Hz, 3H), 6.85 (d, *J* = 8.0 Hz, 3H).
^{13}C {^{1}H} NMR (126 MHz, 298 K, D_2O, δ/ppm): 165.4, 163.8, 147.7, 145.1, 137.8, 136.2, 135.0, 126.0, 123.8, 120.8, 119.8.

IrFsppy

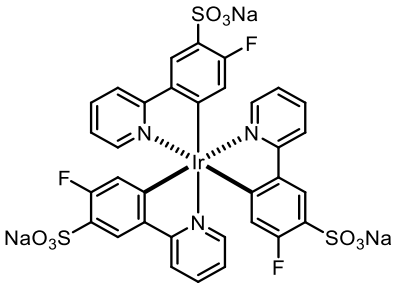

IrFsppy was synthesized according to general procedure B. H_2SO_4 (89.2 mg, 910 µmol, 3.3 eq.) and TFAA (8.0 mL) were stirred at rt for 5.5 h, before **IrFppy$_3$** (193 mg, 272 µmol, 1.0 eq.) in DCM (32 mL) was added and the resulting yellow solution was stirred at rt overnight. After purification by gradient flash column chromatography (SiO_2, acetonitrile/MeOH/H_2O 50:5:1 then acetonitrile/MeOH/H_2O 50:5:10), **IrFsppy** (191 mg, 188 µmol, 69%) was obtained as a yellow solid.
$C_{33}H_{18}F_3IrN_3Na_3O_9S_3$ (1014.9 g mol^{-1}):
^{1}H NMR (400 MHz, 298 K, D_2O, δ/ppm): 8.18 (d, *J* = 7.2 Hz, 3H), 8.10 (d, *J* = 8.2 Hz, 3H), 7.83 (pseudo-td, *J* = 7.9 Hz, 1.6 Hz, 3H), 7.58 (d, *J* = 5.6 Hz, 3H), 7.04 (pseudo-t, *J* = 6.5 Hz, 3H), 6.58 (d, *J* =11.7 Hz, 3H).
^{19}F {^{1}H} NMR (376 MHz, 298 K, D_2O, δ/ppm): –113.1.

^{13}C {^{1}H} NMR (126 MHz, 298 K, D_2O, *δ*/ppm): 168.3 (d, *J* = 6.6 Hz), 162.9, 159.4 (d, *J* = 257.1 Hz), 147.5, 140.9, 137.9, 123.7, 123.6, 122.5 (d, *J* = 17.8 Hz), 122.4 (d, *J* = 18.8 Hz), 119.7.

ESI-HRMS (*m/z*): calcd. for $C_{33}H_{18}F_3IrN_3O_9S_3^{3-}$ [M-3Na]$^{3-}$: 315.3268; found: 315.3273.

EA calcd. for $C_{33}H_{18}F_3IrN_3Na_3O_9S_3 \cdot 2H_2O$: C, 37.72; H, 2.11; N, 4.00; found: C, 37.50; H, 2.42; N, 4.10.

IrdFsppy

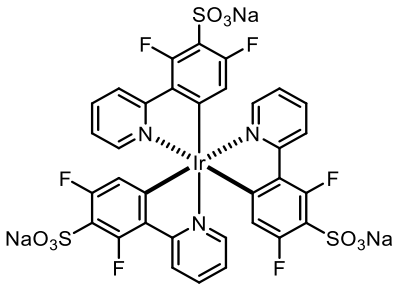

IrdFsppy was synthesized according to general procedure B. H_2SO_4 (97.1 mg, 990 µmol, 3.3 eq.) and TFAA (9.5 mL) were stirred at rt for 5.5 h, before **IrdFppy$_3$** (226 mg, 296 µmol, 1.0 eq.) in DCM (50 mL) was added and the resulting yellow solution was stirred at rt overnight. After purification by gradient flash column chromatography (SiO_2, acetonitrile/MeOH/H_2O 50:5:1 then acetonitrile/MeOH/H_2O 50:5:10), **IrdFsppy** (175 mg, 164 µmol, 55%) was obtained as a yellow solid.

$C_{33}H_{15}F_6IrN_3Na_3O_9S_3$ (1068.9 g mol^{-1}):

^{1}H NMR (400 MHz, 298 K, D_2O, *δ*/ppm): 8.44 (d, *J* = 8.7 Hz, 3H), 7.91 (pseudo-t, *J* = 8.0 Hz, 3H), 7.67 (d, *J* = 5.3 Hz, 3H), 7.14 (pseudo-t, *J* = 6.6 Hz, 3H), 6.42 (d, *J* = 11.2 Hz, 3H).

^{19}F {^{1}H} NMR (376 MHz, 298 K, D_2O, *δ*/ppm): –110.4, –111.6.

^{13}C {^{1}H} NMR (126 MHz, 298 K, D_2O, *δ*/ppm): 168.0 (d, *J* = 7.4 Hz), 160.8 (d, *J* = 6.8 Hz), 157.6 (dd, *J* = 259.1 Hz, *J* = 4.4 Hz), 155.9 (d, *J* = 266.3 Hz, *J* = 4.8 Hz), 147.7, 138.3, 129.2 (dd, *J* = 4.1 Hz, *J* = 1.4 Hz), 123.9 (d, *J* = 22.9 Hz), 123.8, 118.3 (d, *J* = 19.4 Hz), 112.1 (pseudo-t, *J* = 17.7 Hz).

ESI-HRMS (*m/z*): calcd. for $C_{33}H_{15}F_6IrN_3O_9S_3^{3-}$ [M-3Na]$^{3-}$: 333.3173; found: 333.3177.

EA calcd. for $C_{33}H_{15}F_6IrN_3Na_3O_9S_3 \cdot 5H_2O$: C, 34.20; H, 2.17; N, 3.63; found: C, 34.48; H, 2.43; N, 3.66.

4-(Pyridin-2-yl)benzaldehyde (5)

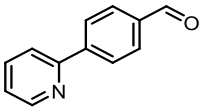

The synthesis of 4-(pyridine-2-yl)benzaldehyde (**5**) was adapted from a previously published protocol.[227] (4-Formylphenyl)boronic acid (**4**, 1.43 g, 9.50 mmol, 1.5 eq.) and potassium carbonate (2.63 g, 19.0 mmol, 3.0 eq.) were dissolved in 1,4-dioxane (60 mL) and water (20 mL). 2-Bromopyridine (**1**, 620 µL, 1.00 g, 6.33 mmol, 1.0 eq.) was added dropwise and the reaction mixture was degassed by bubbling nitrogen through the solution for 30 min. $Pd(PPh_3)_4$ (366 mg, 617 µmol, 5 mol%) was added and the reaction mixture was degassed for additional 10 min. The resulting yellow suspension was heated at reflux overnight. After cooling to rt, the orange suspension was filtered over Celite and the residue was washed with water and dichloromethane. The filtrate was concentrated under reduced pressure and the crude product was purified by gradient flash column chromatography (SiO_2, pentane/ethyl acetate 10:1 then pentane/ethyl acetate 4:1), to afford 4-(pyridine-2-yl)benzaldehyde (**5**, 1.16 g, 6.33 mmol, quant.) as a white solid. Analytical data matches the literature.[227]

$C_{12}H_9NO$ (183.2 g mol^{-1}):

^{1}H NMR (400 MHz, 298 K, $CDCl_3$, δ/ppm): 10.08 (s, 1H), 8.74 (pseudo-dt, J = 4.8 Hz, 1.4 Hz, 1H), 8.20-8.14 (m, 2H), 8.01-7.96 (m, 2H), 7.82-7.79 (m, 2H), 7.34-7.27 (m, 1H).

^{13}C {^{1}H} NMR (101 MHz, 298 K, $CDCl_3$, δ/ppm): 192.1, 156.0, 150.1, 145.1, 137.1, 136.5, 130.3, 127.6, 123.3, 121.3.

(4-(Pyridin-2-yl)phenyl)methanol (6)

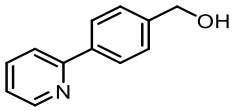

The synthesis of (4-(pyridin-2-yl)phenyl)methanol (**6**) was adapted from a previously published protocol.[228] 4-(Pyridine-2-yl)benzaldehyde (**5**, 1.15 g, 6.28 mmol, 1.0 eq.) was dissolved in dry ethanol (72 mL) under nitrogen atmosphere. Sodium borohydride (549 mg, 14.5 mmol, 2.3 eq.) was added and the colorless solution was stirred at rt for 3 h. The reaction mixture was quenched with sat. aq. NH_4Cl solution (20 mL). Ethanol was removed under reduced pressure and the aqueous layer was extracted with dichloromethane (3 × 20 mL). The combined organic layers were dried over anhydrous sodium sulfate and concentrated under reduced pressure to afford (4-(pyridin-2-yl)phenyl)methanol (**6**, 1.13 g, 6.10 mmol, 97%) as a white viscuous oil. Analytical data matches the literature.[276]

$C_{12}H_{11}NO$ (185.2 g mol^{-1}):

^{1}H NMR (400 MHz, 298 K, $CDCl_3$, δ/ppm): 8.66 (ddd, *J* = 4.9 Hz, 1.8 Hz, 1.0 Hz, 1H), 7.94-7.88 (m, 2H), 7.78-7.67 (m, 2H), 7.44-7.38 (m, 2H), 7.22 (ddd, *J* = 7.2 Hz, 4.9 Hz, 1.5 Hz, 1H), 4.71 (s, 2H), 2.88 (s, 1H).
^{13}C {^{1}H} NMR (101 MHz, 298 K, $CDCl_3$, δ/ppm): 157.4, 149.7, 142.1, 138.6, 137.0, 127.3, 127.2, 122.3, 120.8, 64.9.

2-(4-(Bromomethyl)phenyl)pyridine (7)

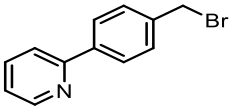

The synthesis of 2-(4-(bromomethyl)phenyl)pyridine (**7**) was adapted from a previously published protocol.[228] (4-(Pyridine-2-yl)phenyl)methanol (**6**, 1.89 g, 10.2 mmol, 1.0 eq.) was dissolved in dry DCM (120 mL) and the solution was cooled to 0 °C. PBr_3 (1.45 mL, 15.4 mmol, 1.5 eq.) was added dropwise. The reaction mixture was stirred at rt for 7 h and was then quenched with H_2O (125 mL) at 0 °C. The layers were separated, and the aqueous layer was extracted with DCM (3 × 120 mL). The combined organic layers were dried over anhydrous sodium sulfate and concentrated under reduced pressure. The crude product was purified by flash column chromatography (SiO_2, pentane/ethyl acetate 4:1) to afford 2-(4-(bromomethyl)phenyl)pyridine (**7**, 1.04 g, 4.19 mmol, 41%) as a yellow oil. Analytical data matches the literature.[228]
$C_{12}H_{10}BrN$ (248.1 g mol^{-1}):
^{1}H NMR (400 MHz, 298 K, $CDCl_3$, δ/ppm): 8.71-8.68 (m, 1H), 8.02-7.95 (m, 2H), 7.80-7.70 (m, 2H), 7.53-7.47 (m, 2H), 7.26-7.22 (m, 1H), 4.55 (s, 2H).
^{13}C {^{1}H} NMR (101 MHz, 298 K, $CDCl_3$, δ/ppm): 156.8, 149.9, 139.6, 138.6, 137.0, 129.6, 127.5, 122.5, 120.7, 33.3.

Sodium (4-(pyridine-2-yl)phenyl)methanesulfonate (sCH$_2$ppyH)

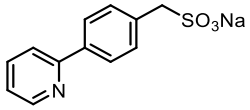

2-(4-(Bromomethyl)phenyl)pyridine (**7**, 1.04 g, 4.19 mmol, 1.0 eq.) and Na_2SO_3 (583 mg, 4.63 mmol, 1.1 eq.) were dissolved in a H_2O/acetone mixture (21 mL, 1:2). The solution was heated to 80 °C for 40 h. After cooling to rt, the solvent was evaporated. The crude product was recrystallized from EtOH (80 °C), collected by filtration and washed with EtOH (3 × 5 mL) to afford sodium (4-(pyridine-2-yl)phenyl)methanesulfonate (**sCH$_2$ppyH**, 781 mg, 2.88 mmol, 69%) as a white solid.
$C_{12}H_{10}NSO_3Na$ (271.3 g mol^{-1}):
^{1}H NMR (500 MHz, 298 K, DMSO-*d*$_6$, δ/ppm): 8.65 (d, *J* = 4.3 Hz, 1H), 7.97 (d, *J* = 8.2 Hz, 2H), 7.93 (d, *J* = 7.8 Hz, 1H), 7.86 (pseudo-td, *J* = 7.5 Hz, 1.8 Hz, 1H), 7.40 (d, *J* = 8.2 Hz, 2H), 7.32 (ddd, *J* = 7.4 Hz, 4.8 Hz, 1.2 Hz, 1H), 3.76 (s, 2H).

^{13}C {^{1}H} NMR (126 MHz, 298 K, DMSO-d_6, δ/ppm): 156.2, 149.5, 137.1, 136.7, 136.6, 130.6, 125.7, 122.3, 120.0, 57.3.
ESI-HRMS (*m/z*): calcd. for $C_{12}H_{10}NSO_3NaH$ $[M+H]^+$: 272.0352; found: 272.0355.

$[Ir(ppy)_2Cl]_2$

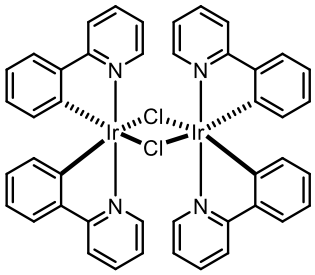

The synthesis of **$[Ir(ppy)_2Cl_2]$** was adapted from a previously published protocol.[112] $IrCl_3 \cdot H_2O$ (2.24 g, 7.07 mmol, 1.0 eq.) and 2-phenylpyridine (**ppyH**, 2.41 g, 15.5 mmol, 2.2 eq.) were dissolved in 2-ethoxyethanol (100 mL) and H_2O (33 mL) under nitrogen atmosphere. The reaction mixture was degassed for 10 min and heated to 105 °C for 3 days. The formed yellow precipitate was collected by filtration and washed with H_2O (3 × 10 mL) and Et_2O (3 × 10 mL) to afford **$[Ir(ppy)_2Cl]_2$** (2.78 g, 2.59 mmol, 73%) as a yellow solid. Analytical data matches the literature.[277]
$C_{44}H_{32}Cl_2Ir_2N_4$ (1072.1 g mol^{-1}):
^{1}H NMR (400 MHz, 298 K, CD_2Cl_2, δ/ppm): 9.30-9.22 (m, 4H), 7.94 (d, *J* = 8.0 Hz, 4H), 7.80 (pseudo-td, *J* = 7.7 Hz, 1.6 Hz, 4H), 7.56 (dd, *J* = 7.8 Hz, 1.4 Hz, 4H), 6.88-6.78 (m, 8H), 6.61 (pseudo-td, *J* = 7.5 Hz, 1.4 Hz, 4H), 5.88 (dd, *J* = 7.8 Hz, 1.2 Hz, 4H).
^{13}C {^{1}H} NMR (101 MHz, 298 K, CD_2Cl_2 δ/ppm): 168.6, 152.0, 145.4, 144.6, 137.2, 130.9, 129.6, 124.2, 123.2, 121.9, 119.3.

$Ir(sCH_2ppy)ppy_2$

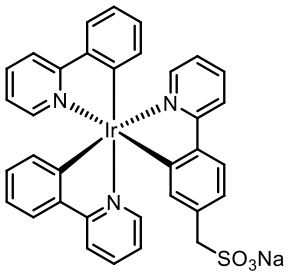

$[Ir(ppy)_2Cl]_2$ (100 mg, 92.3 µmol, 0.6 eq.), sodium (4-(pyridine-2yl)phenyl)methane-sulfonate (**sCH_2ppyH**, 42.2 mg, 155 µmol, 1.0 eq.) and AgOTf (59.9 mg, 233 µmol, 1.5 eq.) were suspended in 2-ethoxyethanol (1.5 mL) under nitrogen atmosphere. The mixture was stirred at 135 °C for 19 h. The solvent was evaporated under reduced pressure and the crude product was purified by two gradient flash columns (first column: SiO_2, DCM/MeOH, 20:1 then pure MeOH, second column: SiO_2, acetonitrile/H_2O/MeOH 50:5:1) to afford **$Ir(sCH_2ppy)ppy_2$** (33.8 mg, 43.9 µmol, 28%) as a yellow solid.

$C_{34}H_{25}IrN_3SO_3Na$ (770.8 g mol^{-1}):

^{1}H NMR (600 MHz, 298 K, CD_3OD, δ/ppm): 8.00-7.96 (m, 3H), 7.69-7.65 (m, 6H), 7.54-7.52 (m, 2H), 7.50 (ddd, *J* = 5.6 Hz, 1.7 Hz, 0.8 Hz, 1H), 7.13 (dd, *J* = 8.1 Hz, 1.9 Hz, 1H), 6.96-6.91 (m, 3H), 6.83-6.78 (m, 3H), 6.77 (d, *J* = 1.8 Hz, 1H), 6.74 (dd, *J* = 7.6 Hz, 1.3 Hz, 1H), 6.72-6.65 (m, 2H), 3.83 (d, *J* = 13.5 Hz, 1H), 3.77 (d, *J* = 13.5 Hz, 1H).

^{13}C {^{1}H} NMR (151 MHz, 298 K, CD_3OD, δ/ppm): 168.1, 168.1, 167.9, 162.4, 162.1, 148.3, 148.3, 148.2, 145.3, 145.2, 144.6, 140.6, 138.4, 138.1, 137.4, 137.4, 137.4, 134.9, 130.4, 130.3, 125.1, 124.9, 124.8, 123.0, 123.0, 123.0, 122.8, 120.8, 120.7, 120.0, 119.9, 199.8, 118.2, 58.9.

ESI-HRMS (*m/z*): calcd. for $C_{34}H_{25}IrN_3SO_3H$ $[M\text{-}Na+H]^+$; $C_{34}H_{25}IrN_3SO_3Na$ $[M]^+$; $C_{34}H_{25}IrN_3SO_3Na_2$ $[M+Na]^+$: 749.1319; 771.1138; 794.1036; found: 749.1315; 771.1134; 794.1036.

EA calcd. for $C_{34}H_{25}IrN_3SO_3Na{\cdot}7H_2O$: C, 45.53; H, 4.38; N, 4.68; found: C, 45.83; H, 3.98; N, 4.94.

S2.2 Synthesis of the Rh Derivatives

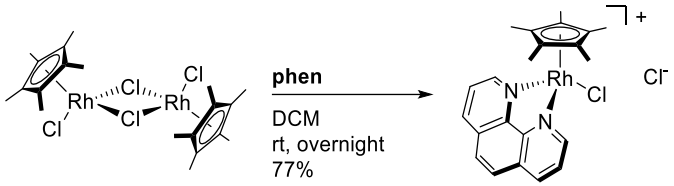

8 **[Cp*Rh(phen)Cl]Cl**

Scheme S1. Synthesis of **[Cp*Rh(phen)Cl]Cl**.

[Cp*Rh(phen)Cl]Cl

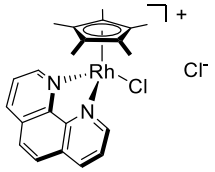

$[Cp^*RhCl_2]_2$ (**8**, 100 mg, 162 µmol, 0.5 eq.) and 1,10-phenantroline (**phen**, 78.2 mg, 437 µmol, 1.4 eq.) were dissolved in dry DCM (6.0 mL). The red solution was stirred at rt overnight under nitrogen atmosphere. The solvent was evaporated under reduced pressure. The crude product was redissolved in minimal amounts of DCM and added dropwise to Et_2O. The formed orange precipitate was collected by filtration and washed with Et_2O to afford **[Cp*Rh(phen)Cl]Cl** (121 mg, 241 µmol, 77%) as an orange-yellowish solid. Analytical data matches the literature.[197]

$C_{22}H_{23}Cl_2N_2Rh$ (489.3 g mol^{-1}):

^{1}H-NMR (400 MHz, 298 K, $CDCl_3$, δ/ppm): 9.43 (d, *J* = 5.1 Hz, 2H), 8.71 (dd, *J* = 8.2 Hz, 1.3 Hz, 2H), 8.29 (dd, *J* = 8.2 Hz, 5.1 Hz, 2H), 8.11 (s, 2H), 1.88 (s, 15H).

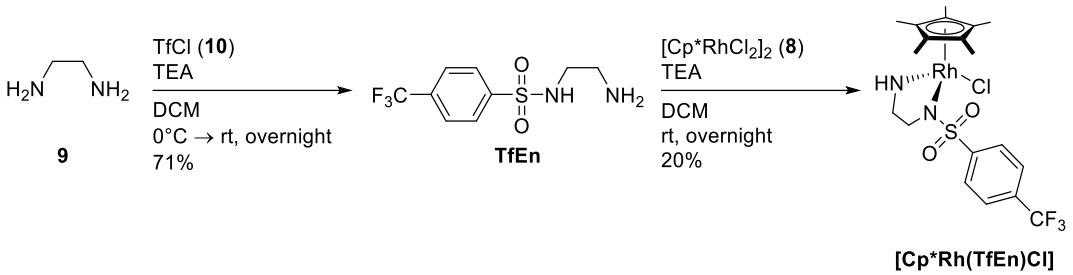

Scheme S2. Synthesis of **[Cp*Rh(TfEn)Cl]**.

N-(2-Aminoethyl)-4-(trifluoromethyl)benzenesulfonamide (TfEn)

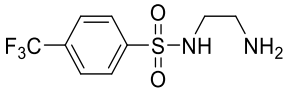

The synthesis of *N*-(2-aminoethyl)-4-(trifluoromethyl)benzenesulfonamide (**TfEn**) was adapted from a previously published protocol.[278] A solution of ethylenediamine (**9**, 2.00 g, 33.3 mmol, 2.0 eq.) and triethylamine (5.05 g, 49.9 mmol, 3.0 eq.) in dry DCM (60 mL) was cooled to 0 °C and stirred at this temperature for 15 min. 4-(Trifluoromethyl)-benzylsulfonyl chloride (**10**, 4.07 g, 16.6 mmol, 1.0 eq.) in dry DCM (6.0 mL) was added dropwise, the reaction was allowed to warm to rt and was stirred at this temperature overnight. Aq. sat. Na_2CO_3 solution (60 mL) was added, and the layers were separated. The organic layer was washed with H_2O (3 × 20 mL), dried over anhydrous sodium sulfate and the solvent was evaporated under reduced pressure to afford **TfEn** (3.16 g, 11.8 mmol, 71%) as a white solid. Analytical data matches the literature.[278]

$C_9H_{11}F_3N_2O_2S$ (268,3 g mol^{-1}):

^{1}H-NMR (400 MHz, 298 K, $CDCl_3$, δ/ppm): 8.01 (d, *J* = 8.0 Hz, 2H), 7.78 (d, *J* = 8.0 Hz, 2H), 3.18–2.92 (m, 2H), 2.92–2.73 (m, 2H), 2.54 (s, 3H).

[Cp*Rh(TfEn)Cl]

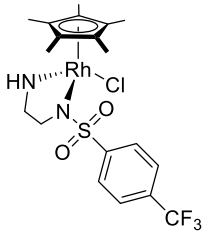

The synthesis of **[Cp*Rh(TfEn)Cl]** was adapted from a previously published protocol.[186] $[Cp^*RhCl_2]_2$ (**8**, 100 mg, 162 µmol, 1.0 eq.) and *N*-(2-aminoethyl)-4-(trifluoromethyl)-benzenesulfonamide (**TfEn**, 86.8 mg, 324 µmol, 2.0 eq.) were dissolved in dry DCM (50 mL). Triethylamine (90.0 µL, 65.6 mg, 647 µmol, 4.0 eq.) was added and the solution was stirred at rt overnight under nitrogen atmosphere. Brine (15 mL) was added and the layers were separated. The organic layer was washed with brine (15 mL), dried over anhydrous sodium sulfate, and the solvent was evaporated under reduced pressure. The

crude product was recrystallized from MeOH to afford **[Cp*Rh(TfEn)Cl]** (34.5 mg, 63.9 µmol, 20%) as orange crystals. Analytical data matches the literature.[186]

$C_{19}H_{24}ClF_3N_2RhSO_2$ (539.8 g mol^{-1}):

^{1}H-NMR (400 MHz, 298 K, $CDCl_3$, δ/ppm): 8.06 (d, *J* = 8.1 Hz, 2H), 7.60 (d, *J* = 8.1 Hz, 2H), 3.25 (s, 2H), 2.65 (m, 3H), 1.76 (s, 15H).

S2.3 Synthesis of 1,4-BNAH

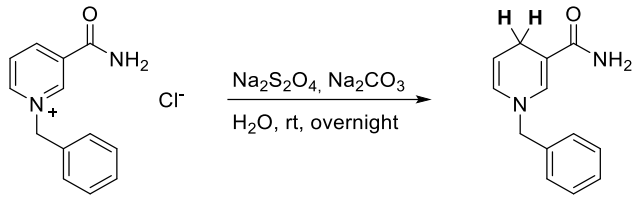

BNACl **1,4-BNAH**

Scheme S3. Chemical reduction of **BNACl** to **1,4-BNAH**.

1-Benzyl-1,4-dihydronicotinamide (1,4-BNAH)

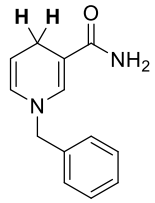

1-Benzyl-3-carbamoylpyridin-1-ium chloride (**BNACl**, 500 mg, 2.01 mL, 1.0 eq.) was dissolved in H_2O (10 mL) and the solution was degassed by bubbling nitrogen through the solution for 15 min. Na_2CO_3 (1.09 g, 10.3 mmol, 5.1 eq.) was added and the reaction mixture was stirred at rt for 30 min. $Na_2S_2O_4$ (1.40 g, 8.04 mmol, 4.0 eq.) was added and the resulting suspension was stirred at rt overnight. The formed yellow precipitate was collected by filtration, washed with water (10 mL) and dried *in vacuo* to afford 1-benzyl-1,4-dihydronicotinamide (**1,4-BNAH**, 323 mg, 1.51 mmol, 75%) as a light yellowish solid. Analytical data matches the literature.[279]

$C_{13}H_{14}N_2O$ (214.3 g mol^{-1}):

^{1}H NMR (400 MHz, 298 K, $CDCl_3$, δ/ppm): 7.50-7.18 (m, 5H), 7.15 (d, *J* = 1.7 Hz, 1H), 7.52 (pseudo-dq, *J* = 8.0 Hz, 1.7 Hz, 1H), 5.65-5.40 (m, 2H), 4.74 (dt, *J* = 8.0 Hz, 3.4 Hz, 1H), 4.28 (s, 2H), 3.16 (dd, *J* = 3.4 Hz, 1.7 Hz, 2H).

S3 Photochemical Regeneration of 1,4-BNAH

S3.1 General Procedures

General Procedure for the Photochemical Regeneration of 1,4-BNAH - UV-Vis Experiment

To determine the photochemical formation of **1,4-BNAH** by UV-Vis spectrometry, **BNACl** (1 mM, 1.0 eq.), the Rh catalyst (100 µM, 10 mol%), the photocatalyst (10 µM, 1 mol%), and TEOA (0.5 M) were dissolved in aq. phosphate buffer (0.1 M, pH 7). 3.0 mL of the reaction mixture were transferred to a Schlenk-cuvette and the solution was degassed using the freeze-pump-thaw technique and set under argon atmosphere. The reaction mixture was irradiated at 455 nm using a collimated LED (see section S1 for details about the LED) and the UV-Vis spectrum of the reaction mixture was measured after different time intervals. The formation of **1,4-BNAH** was determined based on the characteristic absorption band of **1,4-BNAH** arising at 358 nm (ε_{358} = 5070 M^{-1} cm^{-1}, see section S3.3).

General Procedure for the Photochemical Regeneration of 1,4-BNAH - NMR Experiment

To determine the photochemical formation of **1,4-BNAH** by ^{1}H-NMR spectroscopy, **BNACl** (10 mM, 1.0 eq.), the Rh catalyst (1 mM, 10 mol%), the Ir sensitizer (0.1 mM, 1 mol%), and TEOA (1.0 M) were dissolved in a 1:1 mixture of aq. phosphate buffer (0.1 M, pH 7) and CD_3CN. The solution was degassed using the freeze-pump-thaw technique and 0.5 mL of the reaction mixture were transferred to an NMR-tube while maintaining an argon atmosphere. The reaction mixture was then irradiated at 455 nm for 6 h at rt using a collimated LED (see section S1) and the conversion was determined by ^{1}H-NMR spectroscopy.

S3.2 Turnover Numbers and Turnover Frequencies

The turnover number (TON) describes the amount of cycles a catalyst can perform before it gets deactivated, i.e the amount of the product being formed divided by the amount of the catalyst in the reaction mixture. Note that for the photocatalysts this ratio was multiplied with 2, because it undergoes two cycles per equivalent of **1,4-BNAH** being formed. In the UV-Vis experiments, this catalyst characteristic can be determined from the change in absorbance at 358 nm (A_{358}), the extinction coefficient of **1,4-BNAH** (ε_{358}), the path length (d) and the concentration of the photocatalyst (c(PC)). This results in the following equations to determine the TON of the Ir sensitizer (eq. S1) and the TON of the Rh catalyst (eq. S2)

$$\text{TON (PC)} = \frac{2 \cdot c(\text{1,4-BNAH})}{c(\text{PC})} = \frac{2 \cdot A_{358}}{\varepsilon_{358} \cdot d \cdot c(\text{PC})} \quad \text{(S1)}$$

$$\text{TON (Rh)} = \frac{c(\text{1,4-BNAH})}{c(\text{Rh})} = \frac{A_{358}}{\varepsilon_{358} \cdot d \cdot c(\text{Rh})} \quad \text{(S2)}$$

The initial turnover frequency was determined as the amount of cycles that the catalyst could perform within the first 30 min. of the experiment:

$$\text{initial TOF (PC)} = \frac{2 \cdot c(\text{1,4-BNAH})}{c(\text{PC}) \cdot t} = \frac{2 \cdot A_{358}}{\varepsilon_{358} \cdot d \cdot c(\text{PC}) \cdot t} \quad \text{(S3)}$$

$$\text{initial TOF (Rh)} = \frac{c(\text{1,4-BNAH})}{c(\text{Rh}) \cdot t} = \frac{A_{358}}{\varepsilon_{358} \cdot d \cdot c(\text{Rh}) \cdot t} \quad \text{(S4)}$$

Table S1. Summary of the different yields, turnover numbers (TONs) and initial turnover frequencies (TOFs) obtained with the different photocatalysts and Rh catalysts in the photochemical formation of **1,4-BNAH**.[a]

Photocatalyst (PC)	Rh catalyst	Yield of 1,4-BNAH[b] / %	TON[c] (PC)	TON[c] (Rh)	Initial TOF[d] (PC) / h^{-1}	Initial TOF[d] (Rh) / h^{-1}
Irsppy	**[Cp*Rh(bpy)Cl]Cl**	46	92	5	80	4
Irsppy	**[Cp*Rh(phen)Cl]Cl**	42	84	4	57	3
Irsppy	**[Cp*Rh(TfEn)Cl]**	31	62	3	38	2
IrFsppy	**[Cp*Rh(bpy)Cl]Cl**	56	113	6	111	6
IrdFsppy[e]	**[Cp*Rh(bpy)Cl]Cl**	64	128	6	146	7
$[Ru(bpy)_3]^{2+}$	**[Cp*Rh(bpy)Cl]Cl**	13	26	1	16	1

[a] A reaction mixture containing **BNACl** (1.0 mM), an Ir sensitizer (10 µM), a Rh derivative (0.1 mM) and TEOA (0.1 M) in deaerated aq. phosphate buffer (0.1 M, pH 7) was irradiated at 455 nm for 150 min.

[b] The yield of photochemical **1,4-BNAH** formation was determined by UV-Vis spectroscopy based on the characteristic absorption band arising at 358 nm (ε_{358} = 5070 M^{-1} cm^{-1}).

[c] The different turnover numbers (TONs) were determined based on the yield of **1,4-BNAH** obtained after an irradiation time of 150 min.

[d] The different initial turnover frequencies (TOFs) were determined based on the yield of **1,4-BNAH** obtained after an irradiation time of 30 min.

[e] A slightly higher yield and higher TONs were obtained for **IrdFsppy** after an irradiation time of 120 min: yield (**1,4-BNAH**) = 66%, TON (**IrdFsppy**) = 131, TON (**[Cp*Rh(bpy)Cl]Cl**) = 7.

S3.3 Determination of Extinction Coefficient of 1,4-BNAH

The extinction coefficient ε_{358} of **1,4-BNAH** was determined by measuring UV-Vis spectra at varying BNAH concentrations. The absorbance of **1,4-BNAH** at λ_{max} = 358 nm was plotted against the concentration of **1,4-BNAH** and the extinction coefficient could be determined from the slope of the linear fit (ε_{358} = 5.070 mM^{-1} cm^{-1} = 5070 M^{-1} cm^{-1}).

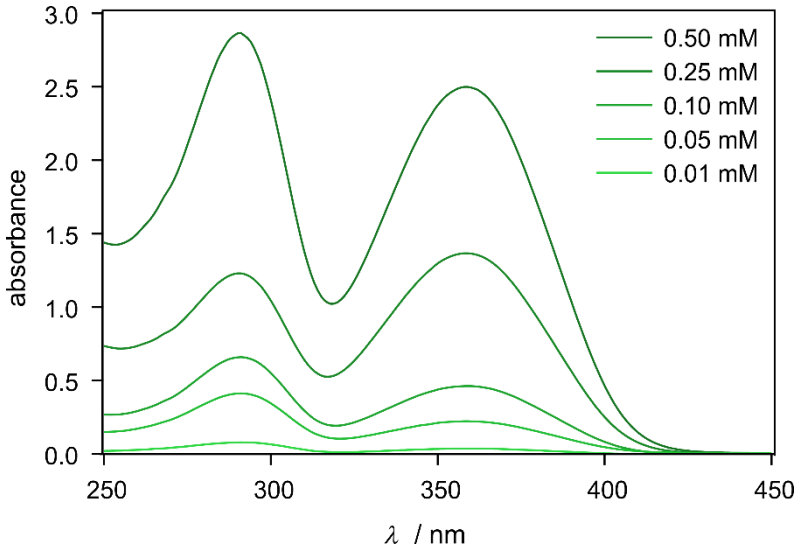

Figure S1. UV-Vis spectra of **1,4-BNAH** in deaerated phosphate buffer (0.1 M, pH 7) at varying concentrations of **1,4-BNAH**.

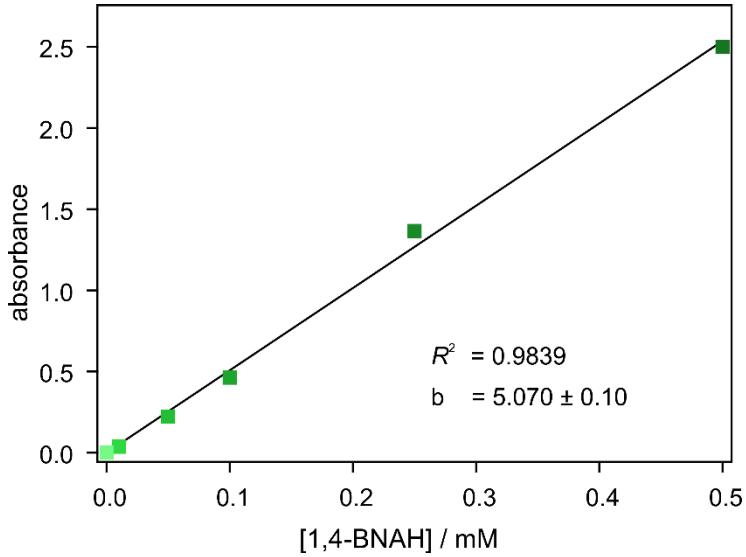

Figure S2. Plot of the absorption of **1,4-BNAH** at 358 nm in aq. deaerated phosphate buffer (0.1 M, pH 7) vs. the concentration of the sample. The extinction coefficient was determined to be ε_{358} = 5070 M^{-1} cm^{-1} from the slope of the linear fit.

S3.4 Additional UV-Vis Spectra

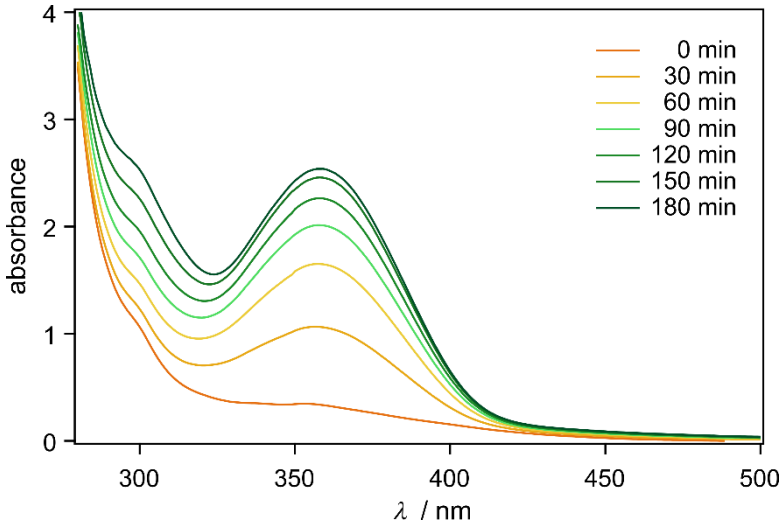

Figure S3. UV-Vis spectra of the visible-light driven **1,4-BNAH**-regeneration: Irradiation of a mixture consisting of **BNACl** (1.0 mM), **Irsppy** (10 µM), **[Cp*Rh(phen)Cl]Cl** (0.1 mM), and TEOA (0.5 M) in deaerated phosphate buffer (0.1 M, pH 7) at 455 nm.

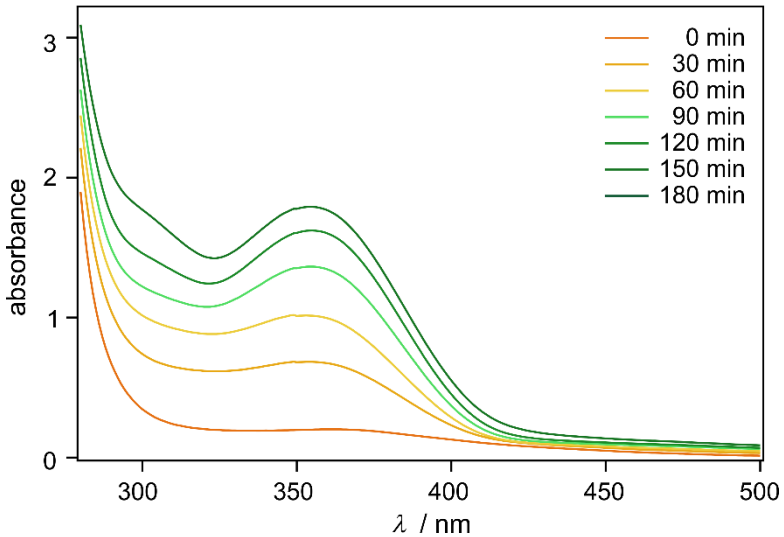

Figure S4. UV-Vis spectra of the visible-light driven **1,4-BNAH**-regeneration: Irradiation of a mixture consisting of **BNACl** (1.0 mM), **IrFsppy** (10 µM), **[Cp*Rh(TfEn)Cl]** (0.1 mM), and TEOA (0.5 M) in deaerated phosphate buffer (0.1 M, pH 7) at 455 nm.

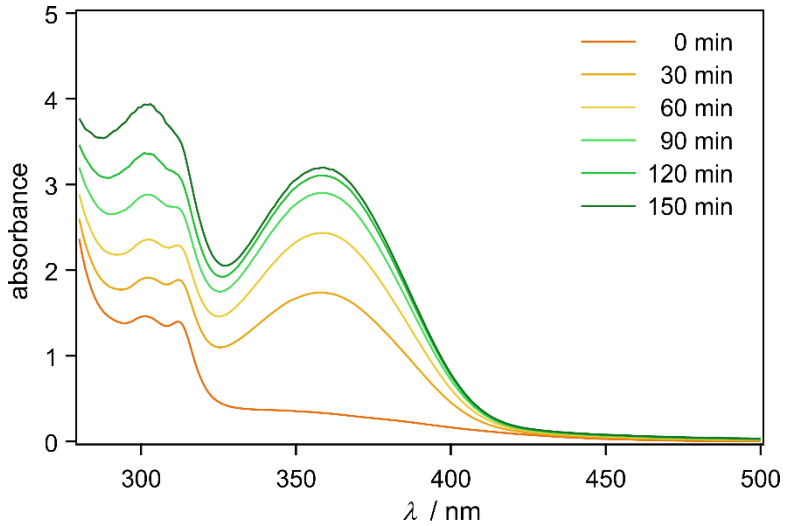

Figure S5. UV-Vis spectra of the visible-light driven **1,4-BNAH**-regeneration: Irradiation of a mixture consisting of **BNACl** (1.0 mM), **IrFsppy** (10 µM), **[Cp*Rh(bpy)Cl]Cl** (0.1 mM), and TEOA (0.5 M) in deaerated phosphate buffer (0.1 M, pH 7) at 455 nm.

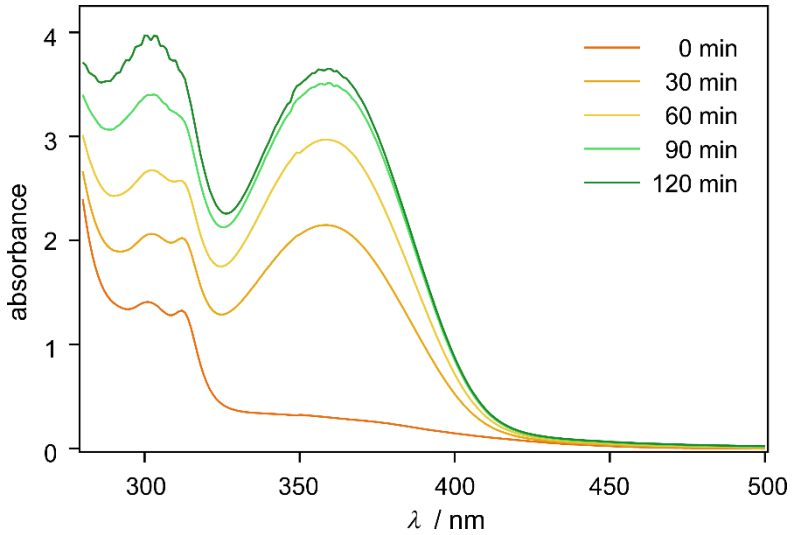

Figure S6. UV-Vis spectra of the visible-light driven **1,4-BNAH**-regeneration: Irradiation of a mixture consisting of **BNACl** (1.0 mM), **IrdFsppy** (10 µM), **[Cp*Rh(bpy)Cl]Cl** (0.1 mM), and TEOA (0.5 M) in deaerated phosphate buffer (0.1 M, pH 7) at 455 nm.

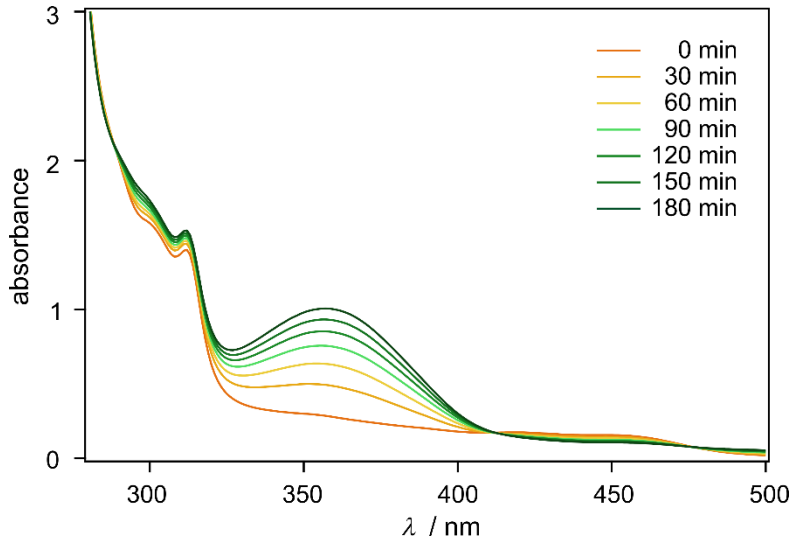

Figure S7. UV-Vis spectra of the visible-light driven **1,4-BNAH**-regeneration: Irradiation of a mixture consisting of **BNACl** (1.0 mM), **[Ru(bpy)$_3$]Cl$_2$** (10 µM), **[Cp*Rh(bpy)Cl]Cl** (0.1 mM), and TEOA (0.5 M) in deaerated phosphate buffer (0.1 M, pH 7) at 455 nm.

S3.5 NMR Experiments

Table S2. Photochemical formation of **1,4-BNAH** analyzed by ^{1}H-NMR spectroscopy.

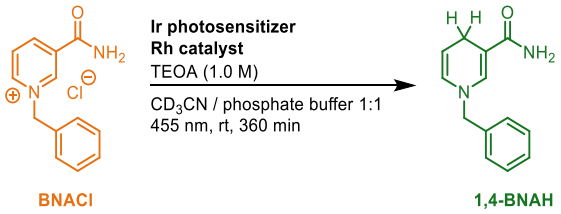

entry[a]	Ir photosensitizer	Rh catalyst	Yield of 1,4-BNAH / %
1	**Irsppy**	**[Cp*Rh(bpy)Cl]Cl**	82
2	**IrFsppy**	**[Cp*Rh(bpy)Cl]Cl**	86
3	**IrdFsppy**	**[Cp*Rh(bpy)Cl]Cl**	83
4	**Irsppy**	**[Cp*Rh(phen)Cl]Cl**	84
5	**Irsppy**	**[Cp*Rh(Tfen)Cl]**	6

[a] A reaction mixture containing **BNACl** (10 mM), the Ir sensitizer (0.1 mM), the Rh catalyst (1.0 mM), and TEOA (1.0 M) in a deaerated 1:1 mixture of phosphate buffer (0.1 M, pH 7) and CD_3CN was irradiated at 455 nm for 6 h. The different yields were determined based on relative integration of the different characteristic signals.

S4 Mechanistic Studies

S4.1 Thermodynamic Considerations

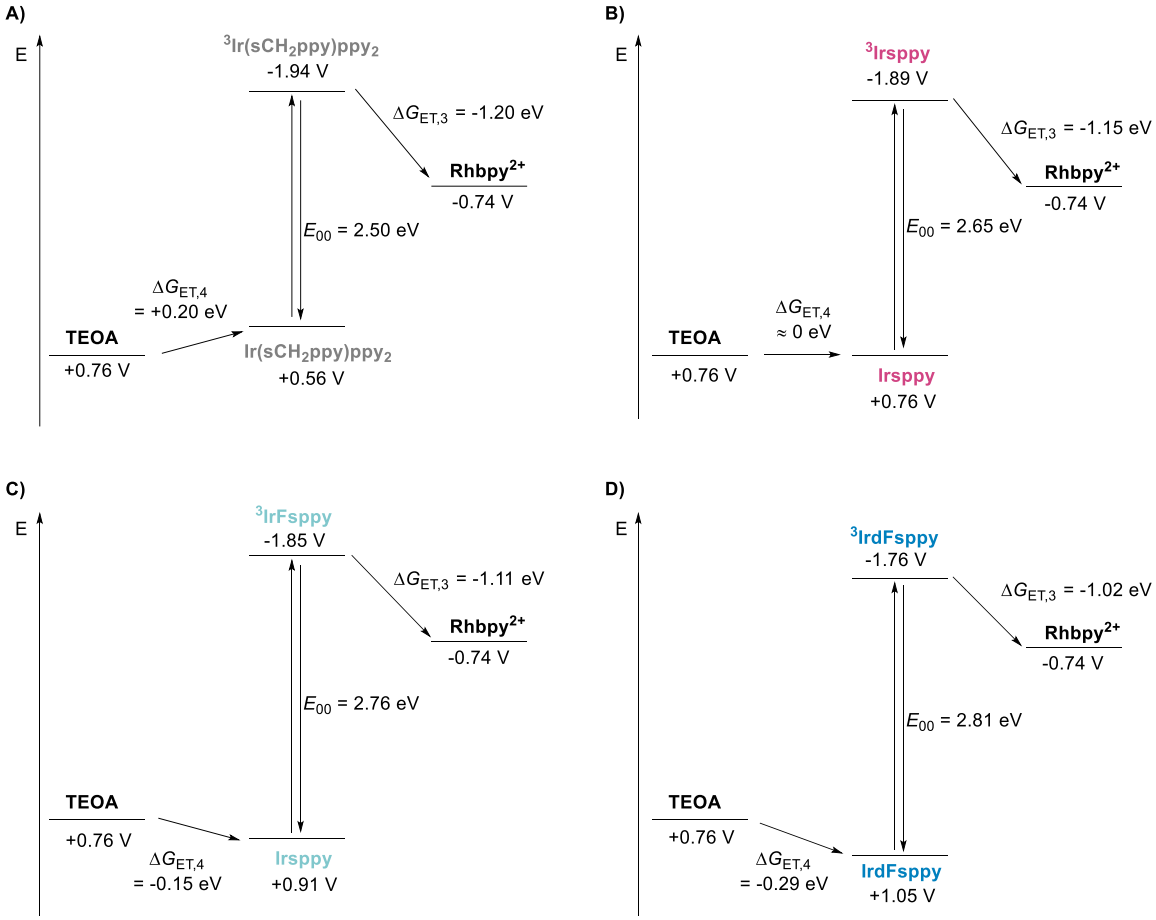

Figure S8. Thermodynamic considerations for the photochemical regeneration of **1,4-BNAH** based on electron transfer processes. The different energy diagrams are shown for A) **Ir(sCH$_2$ppy)ppy$_2$**, B) **Irsppy**, C) **IrFsppy** and D) **IrdFsppy** in combination with **[Cp*Rh(bpy)(H$_2$O)]$^{2+}$** as a Rh precursor and TEOA as a sacrificial donor. The driving forces $\Delta G_{ET,3}$ for the electron transfer from the excited states of different Ir sensitizers to **[Cp*Rh(bpy)(H$_2$O)]$^{2+}$** (**Rhbpy**) are strongly exergonic. The driving forces $\Delta G_{ET,4}$ for the reductive quenching of **Irsppy*** with TEOA range from +0.20 eV to -0.29 eV depending on the Ir sensitizer. All potentials are given in V *vs* SCE.

According to one possible scenario, the photochemical reduction of **BNA**$^+$ can take place via electron transfer from the excited Ir sensitizer to the Rh catalyst (main part, Figure 29B). To gain further insight into the plausibility of the proposed mechanism, the driving forces of the different electron transfer steps involved in the catalytic cycle were calculated for all four Ir sensitizers (Figure S8).

Calculations were based on general equation S5, where ΔG is the Gibbs free energy (i.e., the driving force) of the reaction, e is the elementary charge, E^0_{red} is the redox potential of the reduction half-reaction and E^0_{ox} is the redox potential of the oxidation half-reaction.

$$\Delta G = -e \cdot (E^0_{red} - E^0_{ox}) \quad \text{(S5)}$$

Based on the general equation, the driving force $\Delta G_{ET,3}$ for the electron transfer from the excited Ir sensitizer to the Rh catalyst ($E^0(Rh^{III}/Rh^{II})$ = –0.74 V *vs* SCE)[50] can be determined as follows:

$$\Delta G_{ET,3} = -e \cdot (E^0(Rh^{III}/Rh^{II}) - E^0(Ir^{IV}/{}^*Ir^{III})) \quad \text{(S6)}$$

Accordingly, the driving force $\Delta G_{ET,4}$ for the electron transfer from TEOA ($E^0(TEOA^+/TEOA)$ = +0.76 V *vs* SCE)[217] to the oxidized Ir sensitizer is defined as:

$$\Delta G_{ET,4} = -e \cdot (E^0(Ir^{IV}/Ir^{III}) - E^0(TEOA^+/TEOA)) \quad \text{(S7)}$$

S4.2 Additional Transient Absorption Spectra

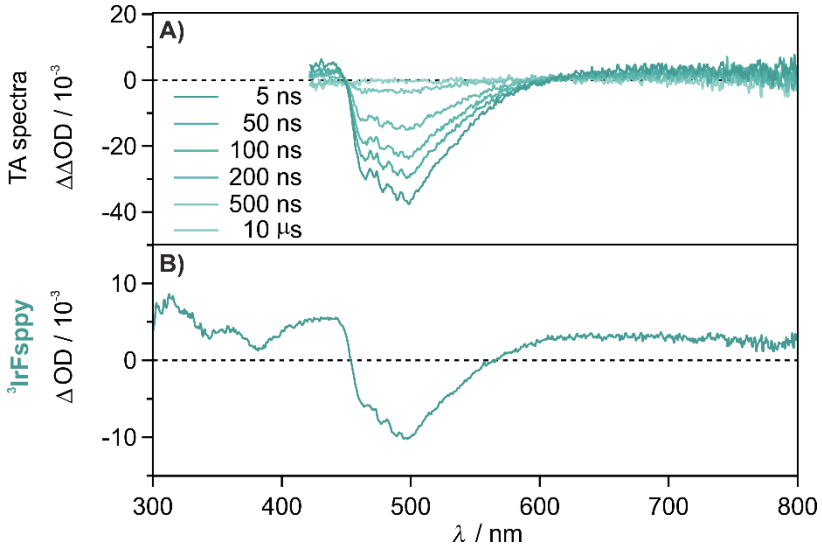

Figure S9. A) Transient absorption spectra of a solution containing **IrFsppy** (100 µM) and **[Cp*Rh(bpy)Cl]Cl** (1.0 mM) in deaerated phosphate buffer (0.1 M, pH 7). The spectra were measured at different time delays after excitation at 420 nm (7 mJ) and were time-integrated over 50 ns. B) Transient absorption spectrum of a solution containing **IrFsppy** (30 µM) in deaerated NaOH solution (50 mM) depicting the characteristic spectroscopic signature of **^{3}IrFsppy**. The spectrum was measured immediately after excitation at 420 nm (14 mJ pulses) and was time-integrated over 100 ns.

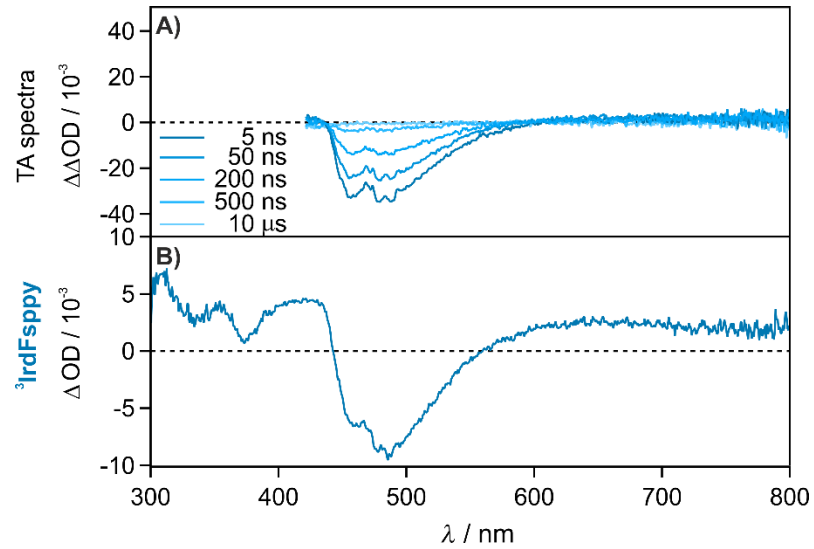

Figure S10. A) Transient absorption spectra of a solution containing **IrdFsppy** (100 µM) and **[Cp*Rh(bpy)Cl]Cl** (1.0 mM) in deaerated phosphate buffer (0.1 M, pH 7). The spectra were measured at different time delays after excitation at 420 nm (7 mJ) and were time-integrated over 50 ns. B) Transient absorption spectrum of a solution containing **IrdFsppy** (42 µM) in deaerated NaOH solution (50 mM) depicting the characteristic spectroscopic signature of **^{3}IrdFsppy**. The spectrum was measured immediately after excitation at 420 nm (14 mJ pulses) and was time-integrated over 100 ns.

S5 Spectra of New Compounds

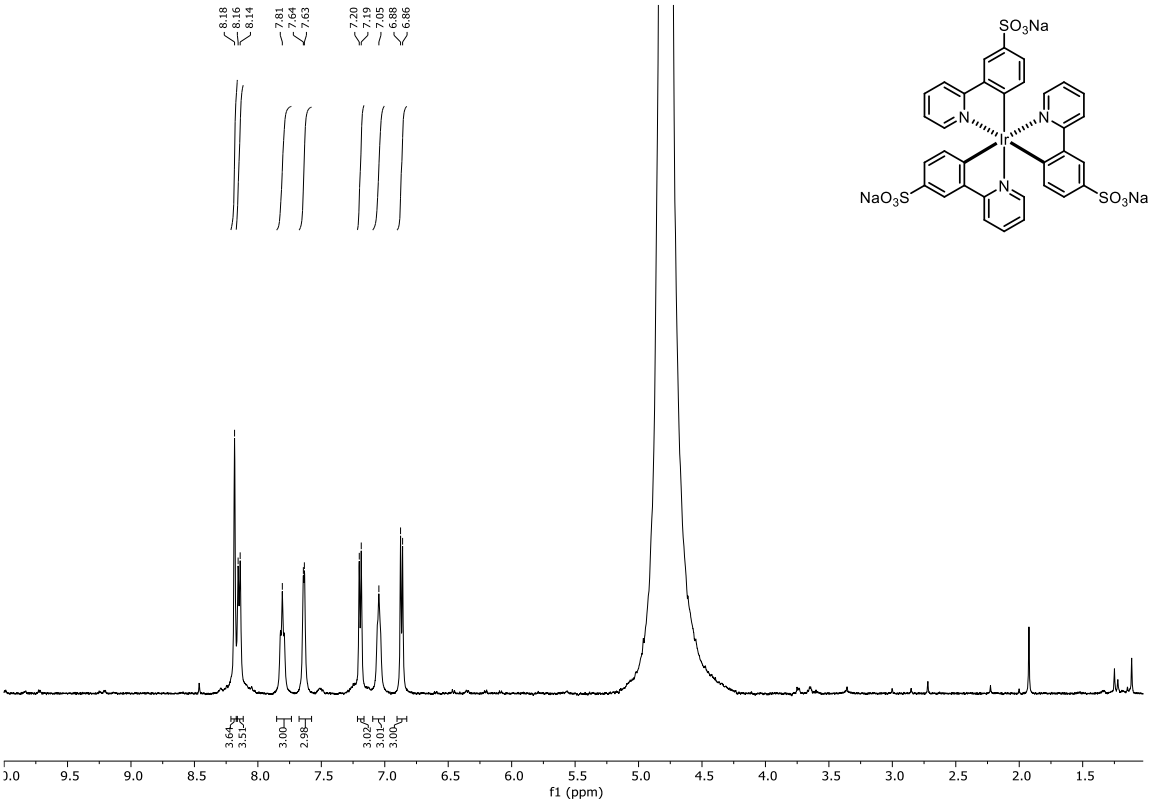

Figure S11. ^{1}H NMR spectrum of **Irsppy** in D_2O.

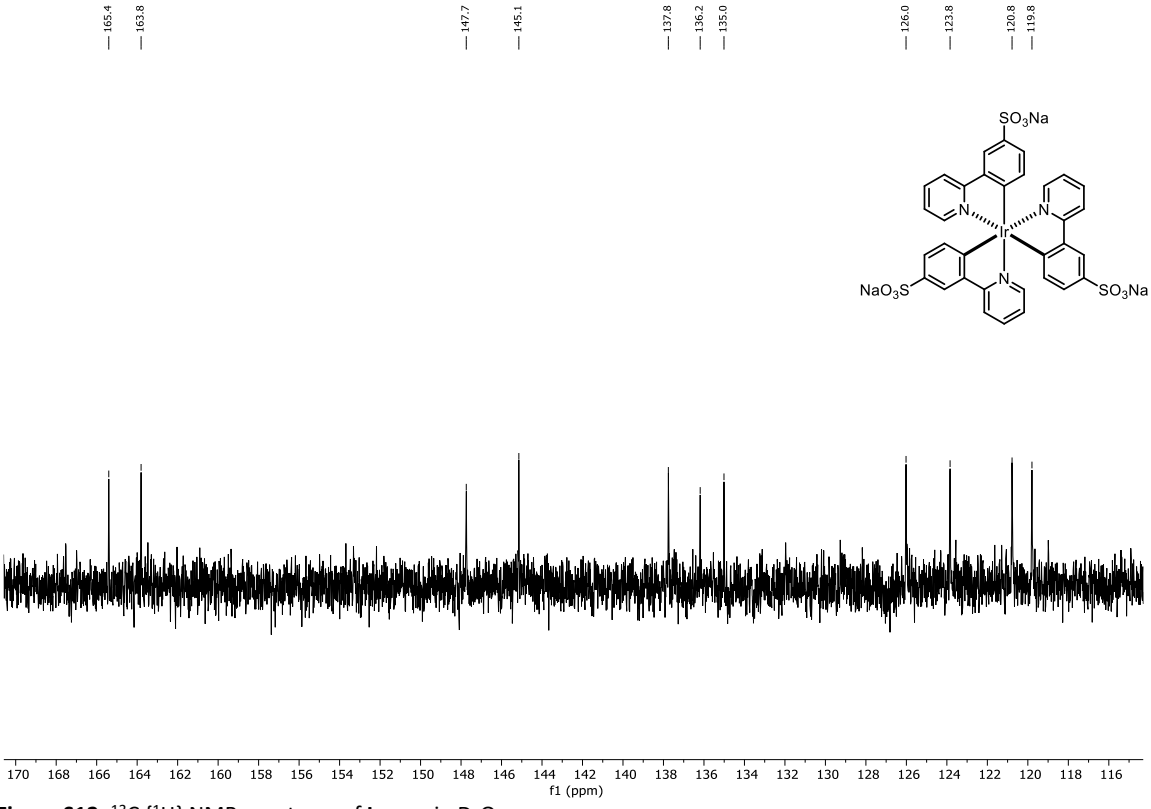

Figure S12. ^{13}C {^{1}H} NMR spectrum of **Irsppy** in D_2O.

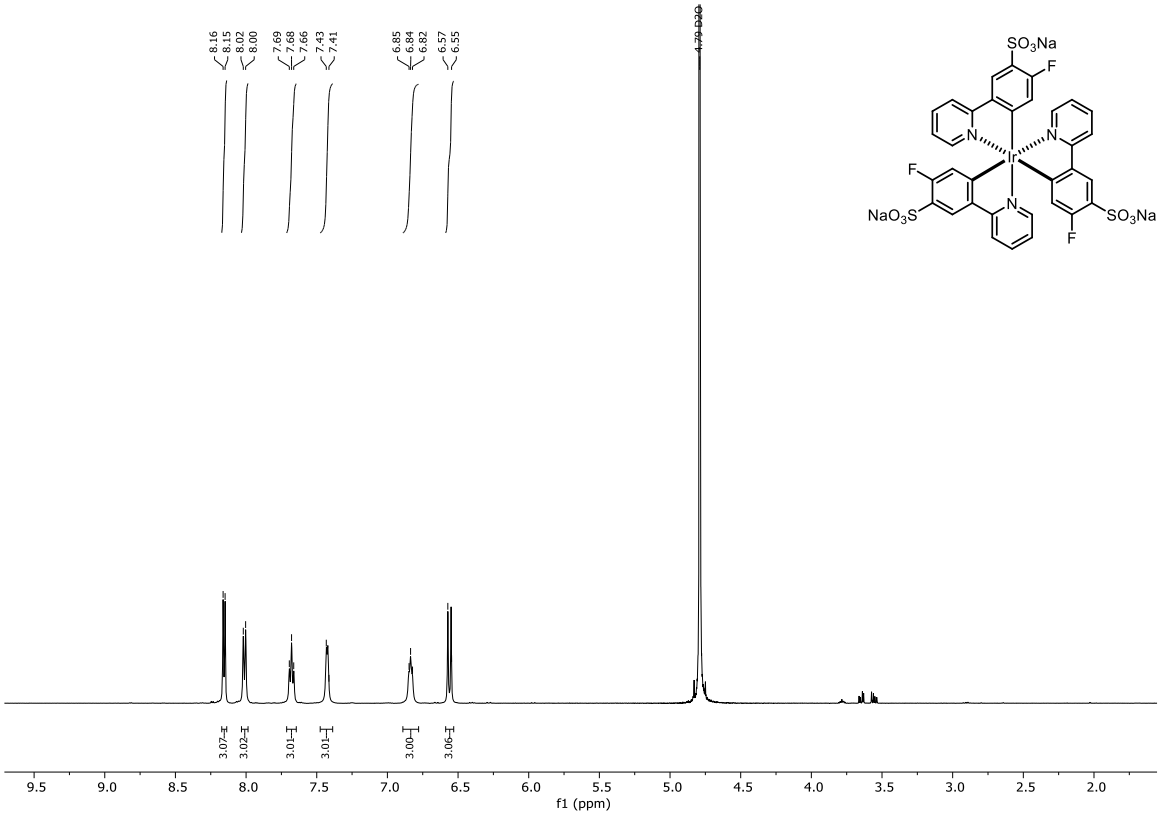

Figure 35: ^{1}H NMR spectrum of **IrFsppy** in D_2O.

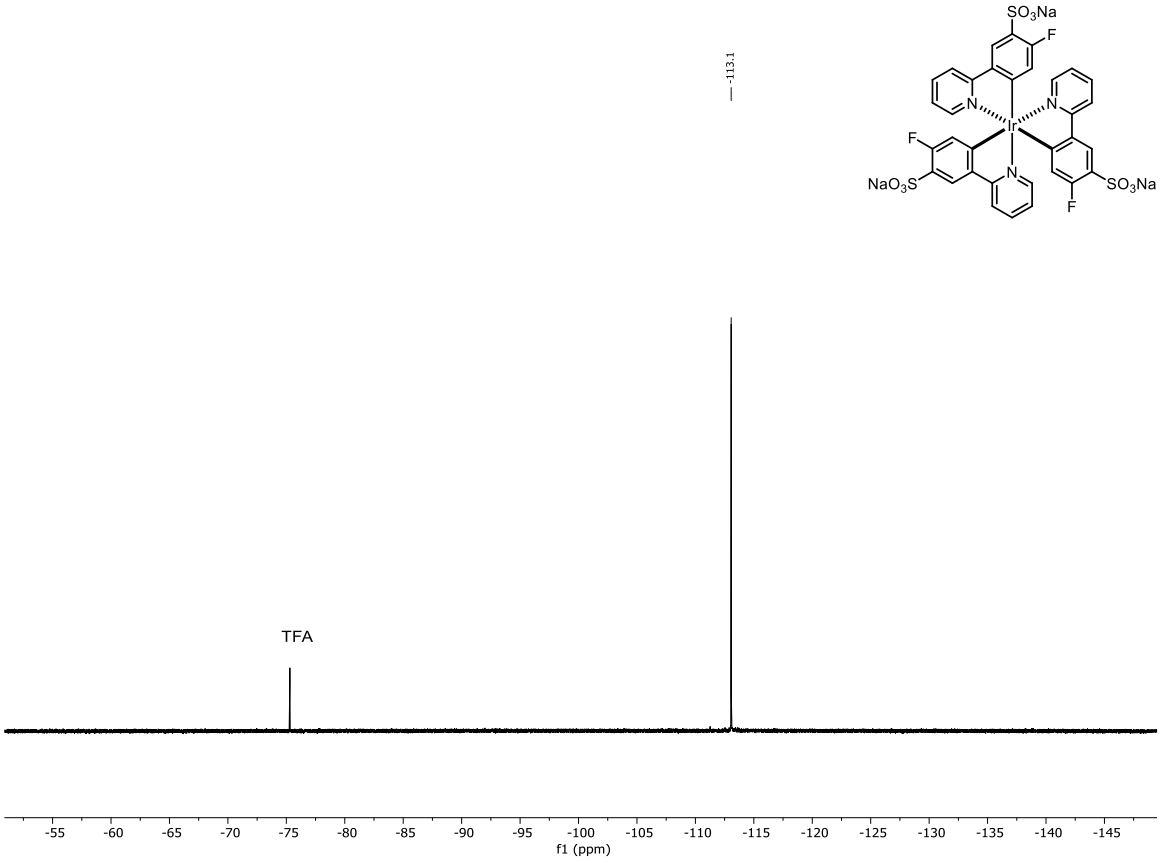

Figure S13. ^{19}F $\{^{1}$H$\}$ NMR spectrum of **IrFsppy** in D_2O.

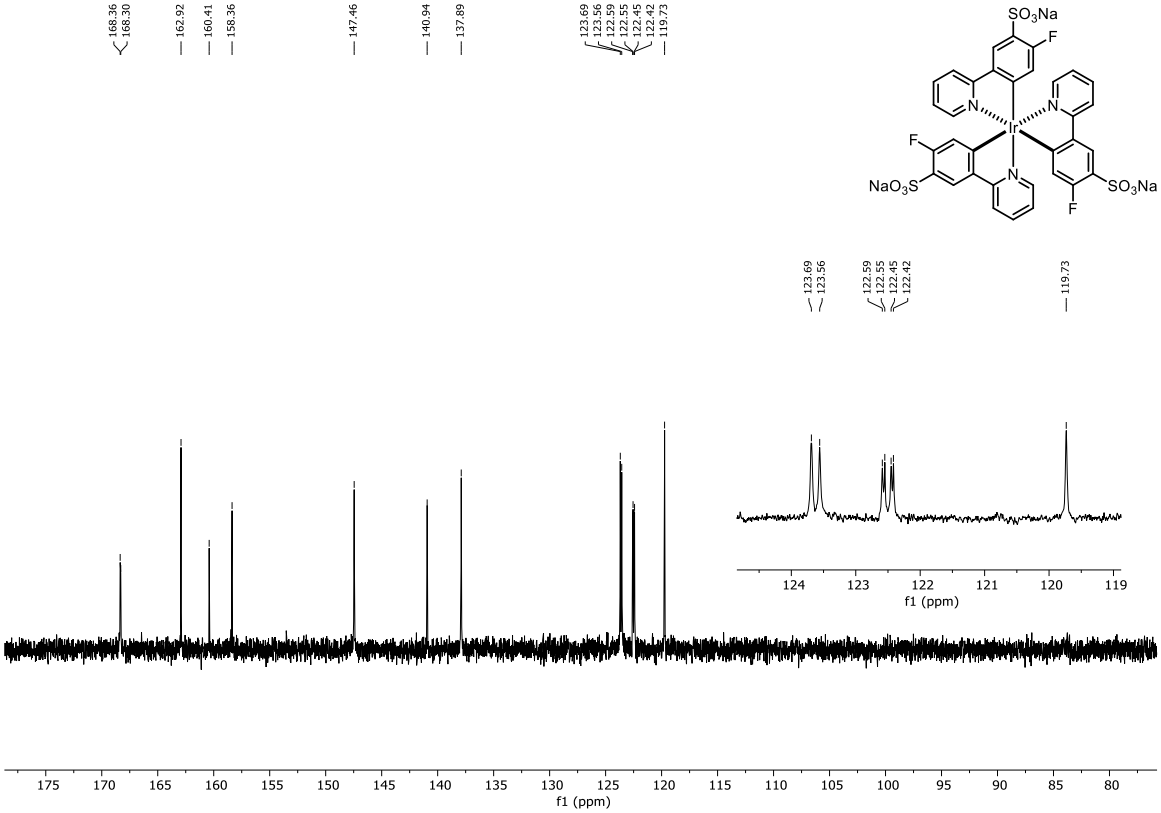

Figure S14. ^{13}C {^{1}H} NMR spectrum of **IrFsppy** in D_2O.

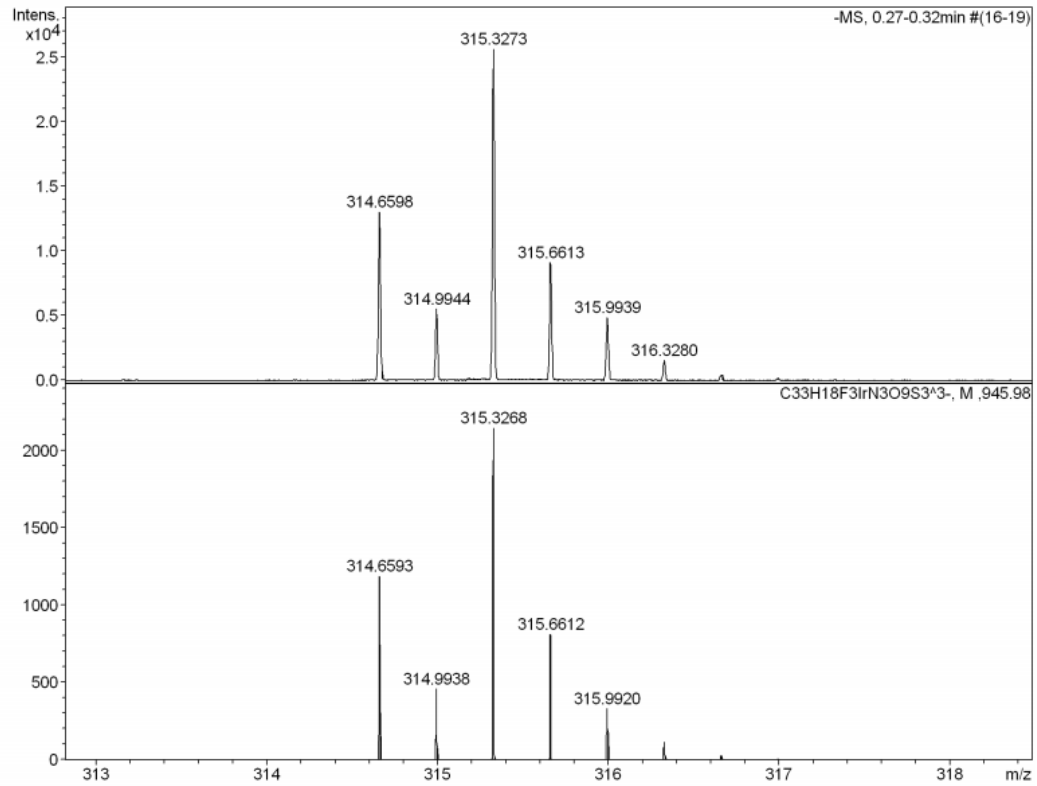

Figure S15. High-resolution ESI mass spectrum of **IrFsppy** (top) in comparison to the calculated spectrum (bottom).

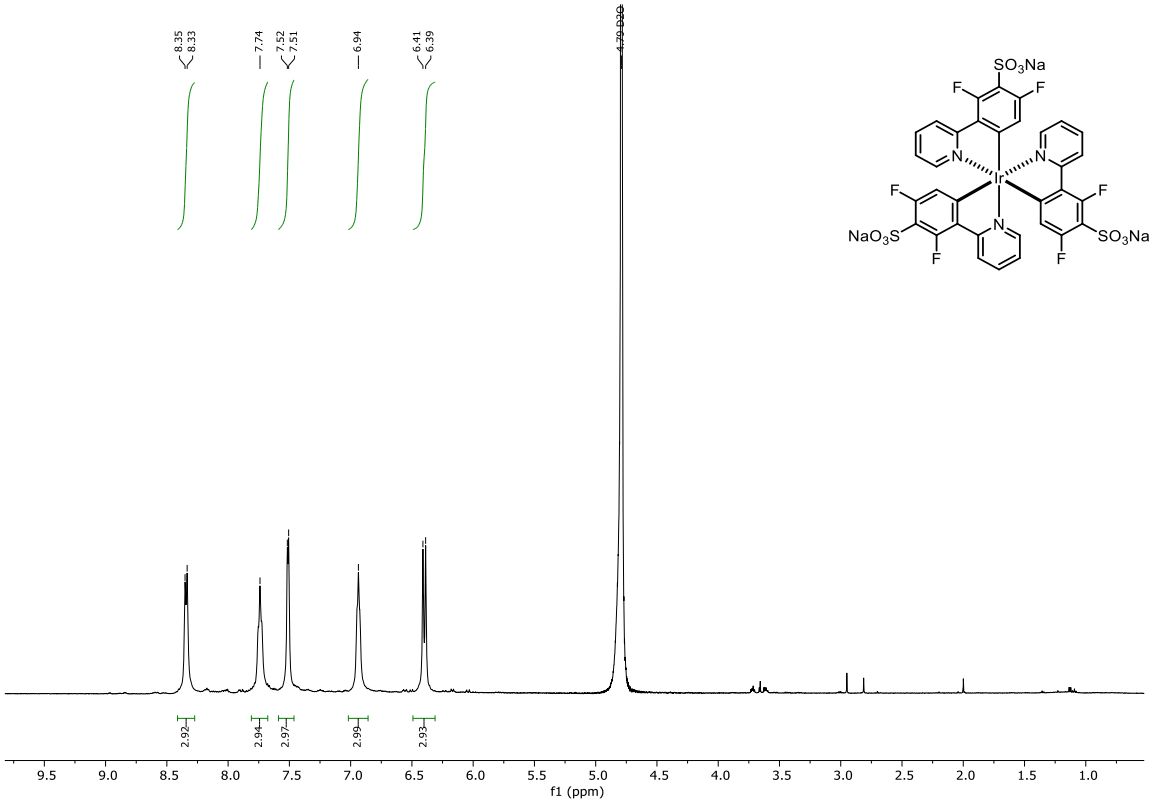

Figure S16. ^{1}H NMR spectrum of **IrdFsppy** in D_2O.

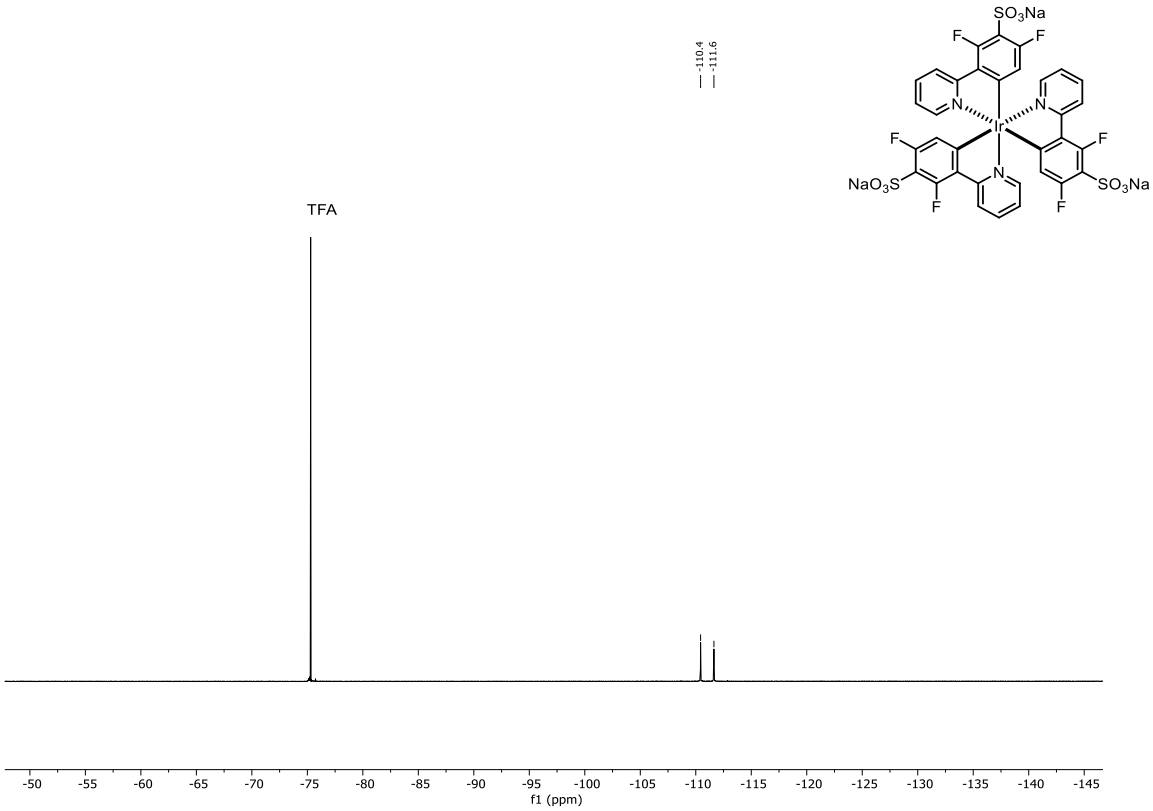

Figure S17. ^{19}F {^{1}H} NMR spectrum of **IrdFsppy** in D_2O.

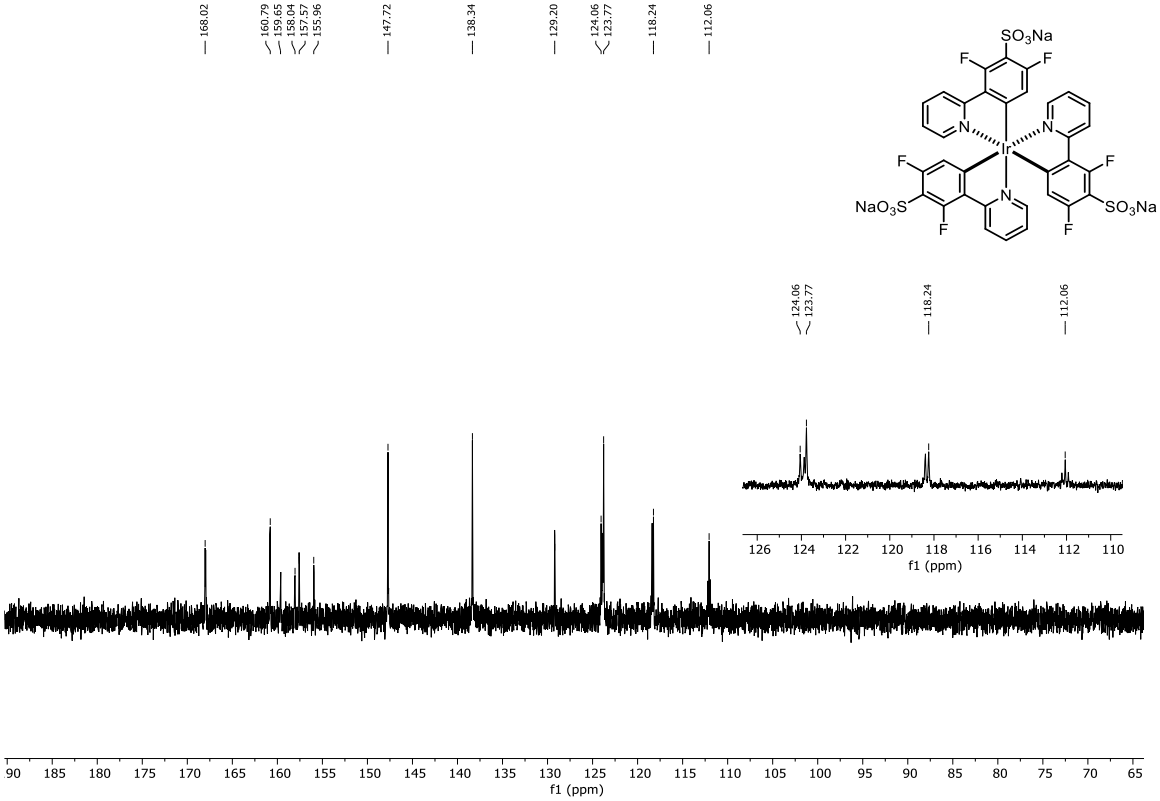

Figure S18. ^{13}C {^{1}H} NMR spectrum of **IrdFsppy** in D_2O.

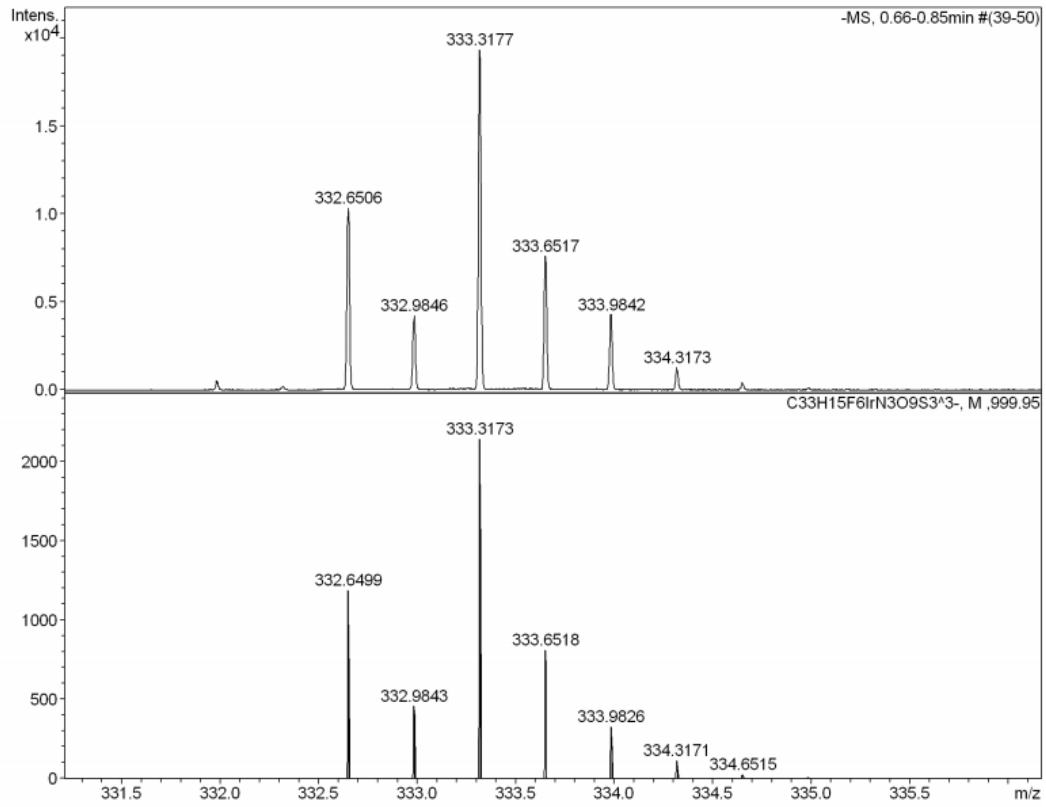

Figure S19. High-resolution ESI mass spectrum of **IrdFsppy** (top) in comparison to the calculated spectrum (bottom).

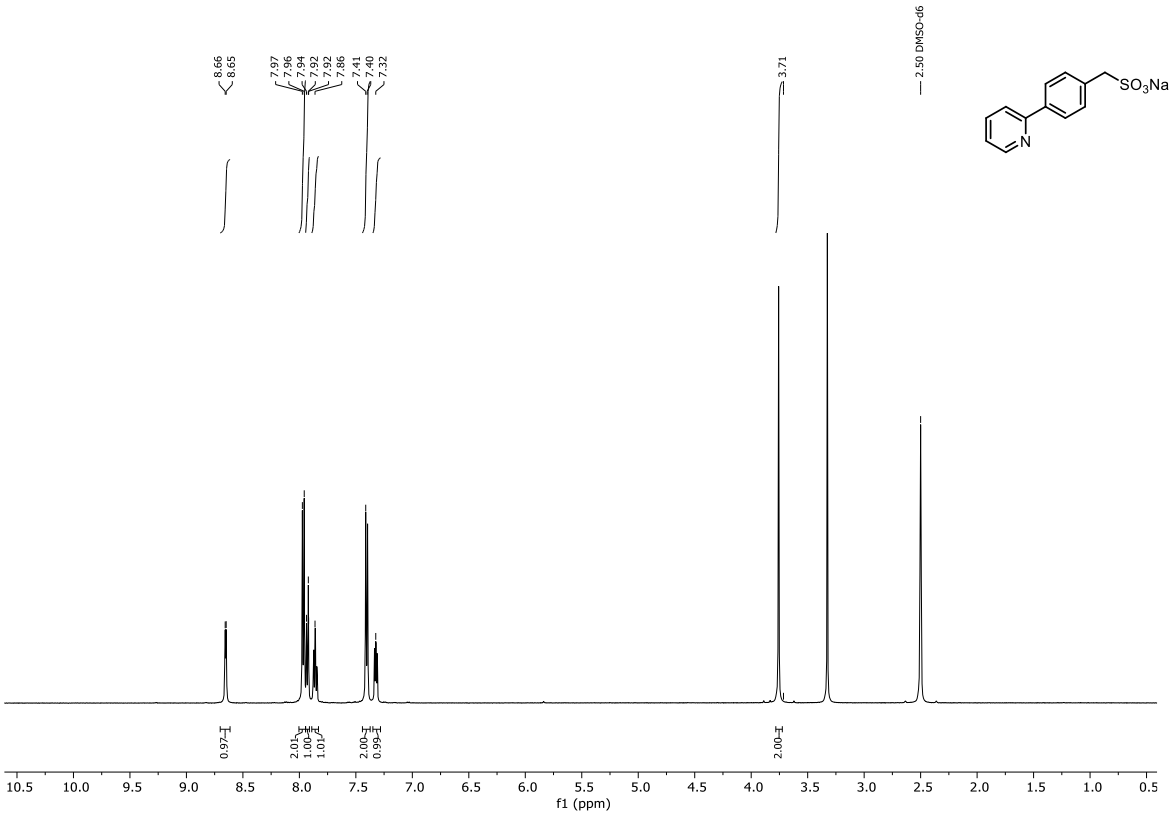

Figure S20. ^{1}H NMR spectrum of sodium (4-(pyridine-2-yl)phenyl)methanesulfonate (**sCH$_2$ppyH**) in DMSO-*d$_6$*.

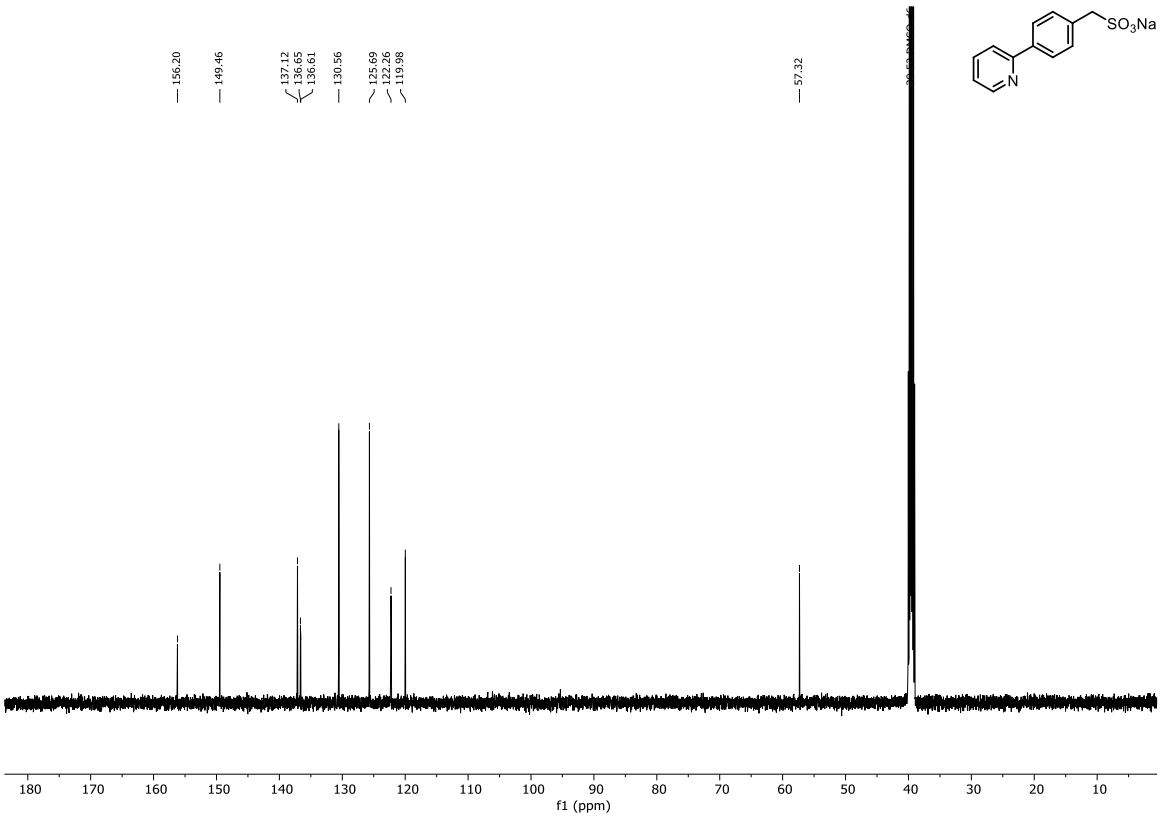

Figure S21. ^{13}C {^{1}H} NMR spectrum of sodium (4-(pyridine-2-yl)phenyl)methanesulfonate (**sCH$_2$ppyH**) in DMSO-*d$_6$*.

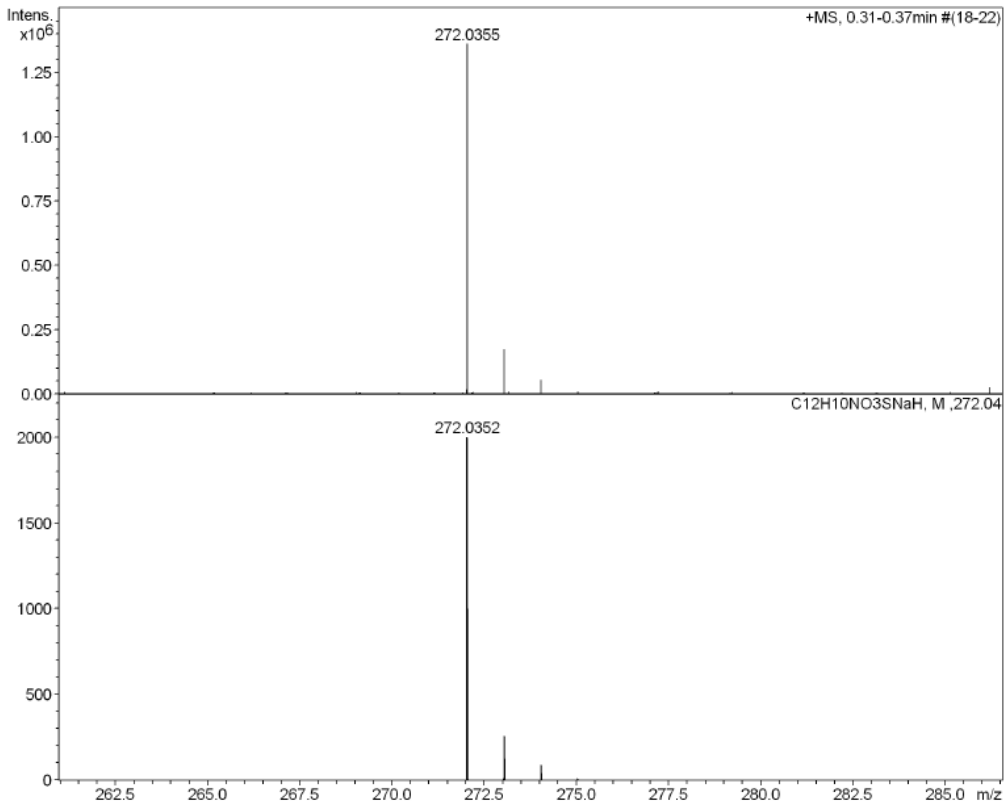

Figure S22. High-resolution ESI mass spectrum of sodium (4-(pyridine-2-yl)phenyl)methanesulfonate (**sCH$_2$ppyH**, top) in comparison to the calculated spectrum (bottom).

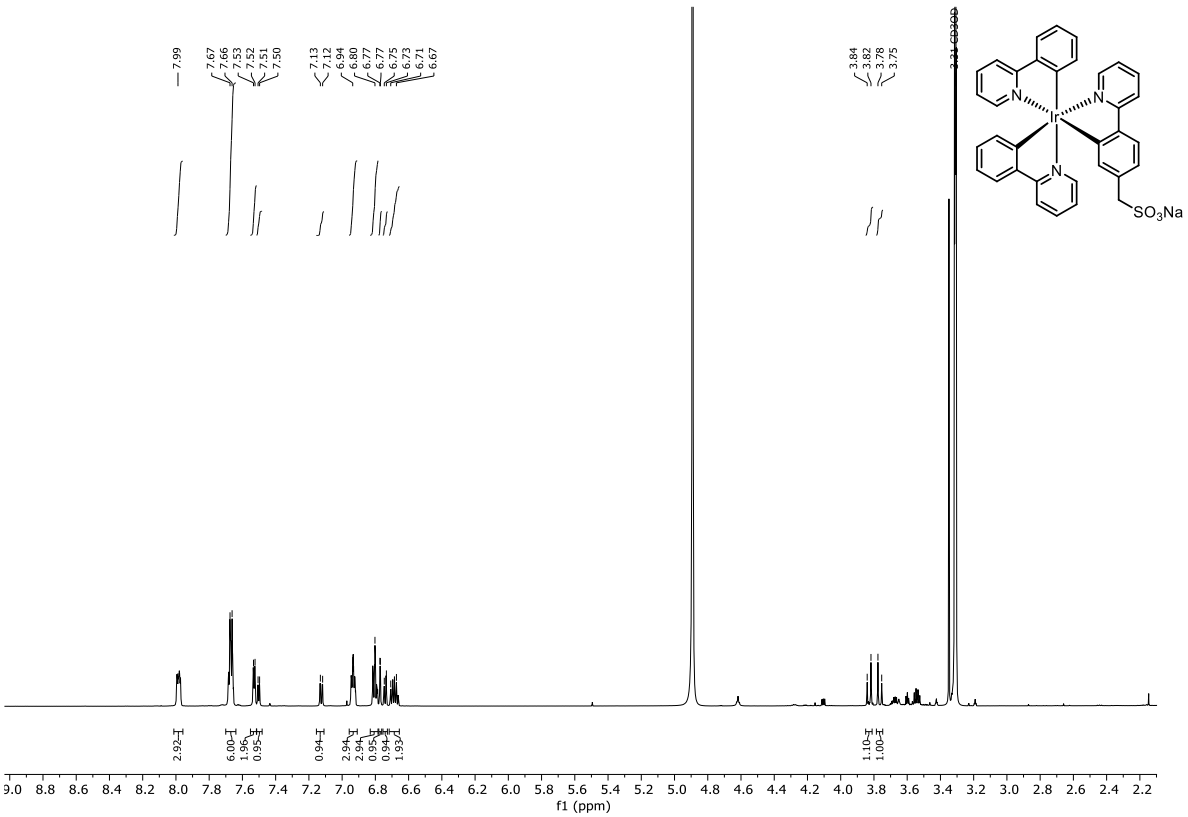

Figure S23. ^{1}H NMR spectrum of **Ir(sCH$_2$ppy)ppy$_2$** in CD_3OD.

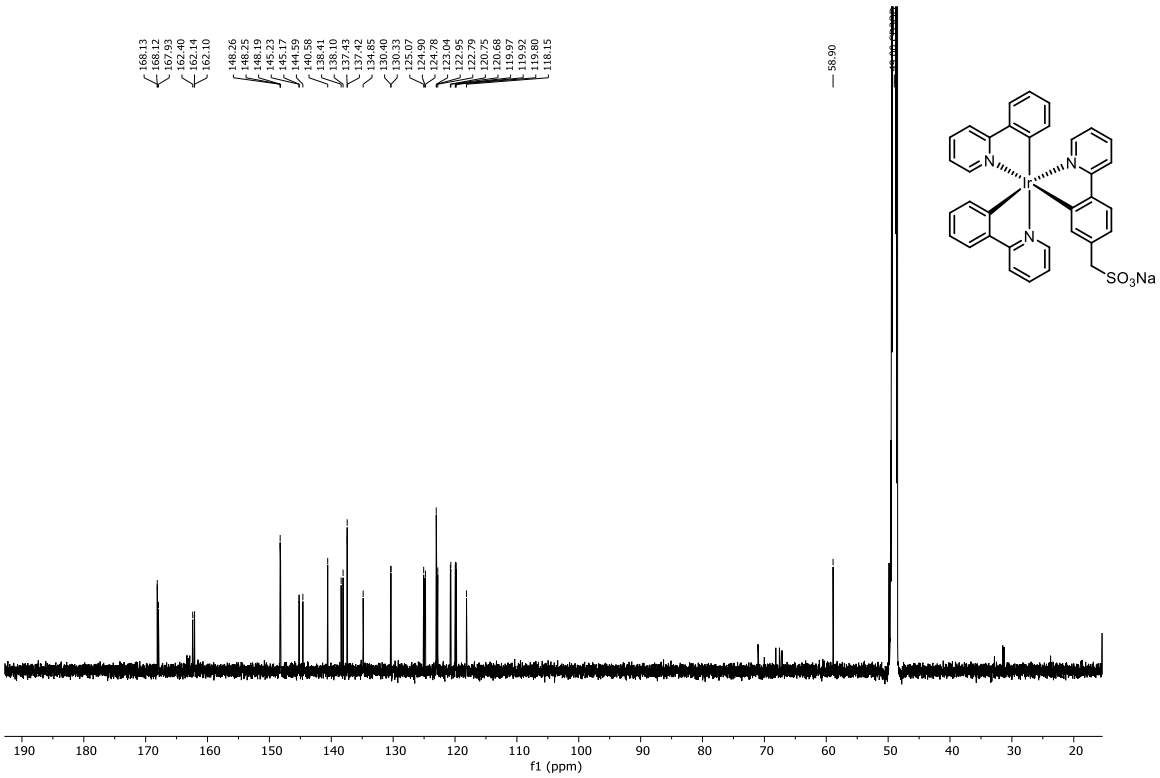

Figure S24. ^{13}C {^{1}H} NMR spectrum of **Ir(sCH$_2$ppy)ppy$_2$** in CD_3OD.

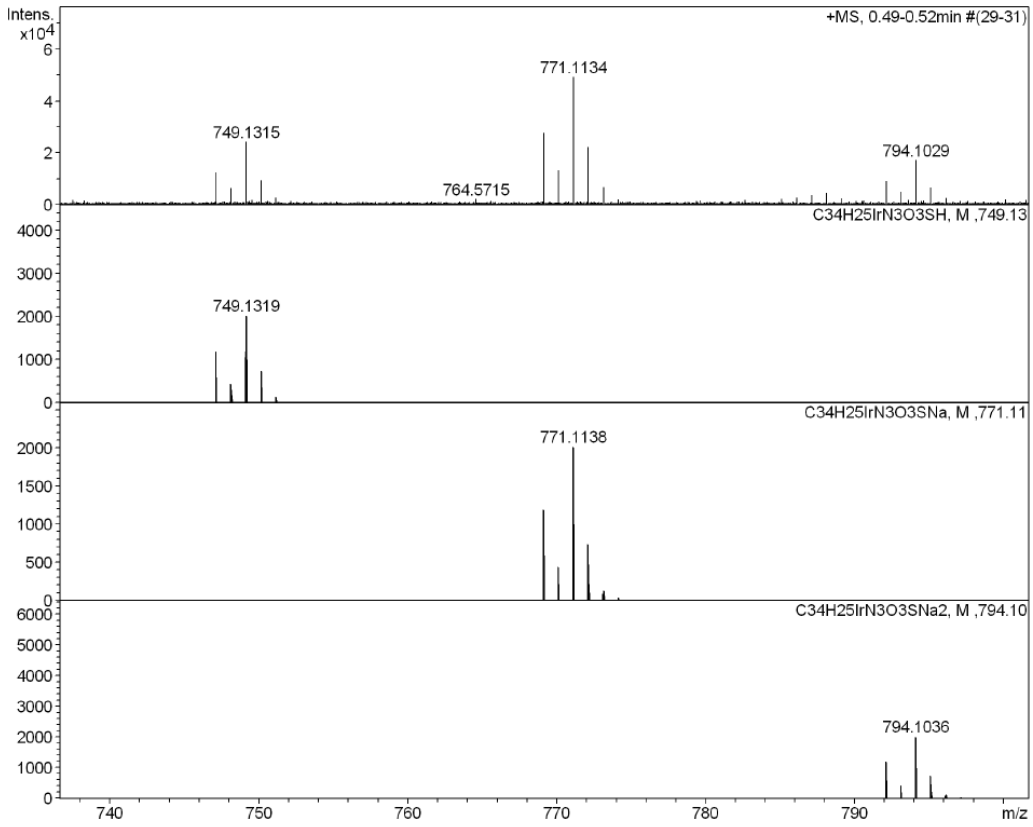

Figure S25. High-resolution ESI mass spectrum of **Ir(sCH$_2$ppy)ppy$_2$** (first panel) in comparison to the calculated spectra of the different species.

7 Bibliography

[1] C. K. Prier, D. A. Rankic, D. W. C. MacMillan, *Chem. Rev.* **2013**, *113*, 5322–5363.
[2] J. W. Tucker, C. R. J. Stephenson, *J. Org. Chem.* **2012**, *77*, 1617–1622.
[3] L. Marzo, S. K. Pagire, O. Reiser, B. König, *Angew. Chemie - Int. Ed.* **2018**, *57*, 10034–10072.
[4] K. L. Skubi, T. R. Blum, T. P. Yoon, *Chem. Rev.* **2016**, *116*, 10035–10074.
[5] C. K. Prier, D. W. C. MacMillan, in *Visible Light Photocatal. Org. Chem.*, WILEY-VCH Verlag GmbH & Co. KgaA, Weinheim, **2018**, pp. 299–329.
[6] J. Twilton, C. C. Le, P. Zhang, M. H. Shaw, R. W. Evans, D. W. C. MacMillan, *Nat. Rev. Chem.* **2017**, *1*, 52.
[7] C. L. Pitman, A. J. M. Miller, *ACS Catal.* **2014**, *4*, 2727–2733.
[8] D. Sandrini, M. Maestri, R. Ziessel, *Inorganica Chim. Acta* **1989**, *163*, 177–180.
[9] S. M. Barrett, C. L. Pitman, A. G. Walden, A. J. M. Miller, *J. Am. Chem. Soc.* **2014**, *136*, 14718–14721.
[10] C. L. Pitman, K. R. Brereton, A. J. M. Miller, *J. Am. Chem. Soc.* **2016**, *138*, 2252–2260.
[11] T. Suenobu, D. M. Guldi, S. Ogo, S. Fukuzumi, *Angew. Chemie - Int. Ed.* **2003**, *42*, 5492–5495.
[12] M. B. Chambers, D. A. Kurtz, C. L. Pitman, M. K. Brennaman, A. J. M. Miller, *J. Am. Chem. Soc.* **2016**, *138*, 13509–13512.
[13] P. Szuromi, B. Jasny, D. Clery, J. Austin, B. Hanson, *Science* **2007**, *315*, 781.
[14] I. E. Agency, *Key world energy Stat.* **2019**.
[15] Z. J. N. Steinmann, A. M. Schipper, M. Hauck, S. Giljum, G. Wernet, M. A. J. Huijbregts, *Environ. Sci. Technol.* **2017**, *51*, 6360–6366.
[16] V. Balzani, A. Credi, M. Venturi, *ChemSusChem* **2008**, *1*, 26–58.
[17] M. Höök, X. Tang, *Energy Policy* **2013**, *52*, 797–809.
[18] N. S. Lewis, D. G. Nocera, *Proc. Natl. Acad. Sci. U. S. A.* **2006**, *103*, 15729–15735.
[19] T. P. Yoon, M. A. Ischay, J. Du, *Nat. Chem.* **2010**, *2*, 527–532.
[20] G. L. Araújo, A. Martí, *Sol. Energy Mater. Sol. Cells* **1994**, *33*, 213–240.
[21] R. A. Barrow, R. E. Moore, L.-H. Li, M. A. Tius, *Tetrahedron* **2000**, *56*, 3339–3351.
[22] J. Barber, *Chem. Soc. Rev.* **2009**, *38*, 185–196.
[23] S. H. Lee, J. H. Kim, C. B. Park, *Chem. - A Eur. J.* **2013**, *19*, 4392–4406.
[24] J. A. Maciá-Agulló, A. Corma, H. Garcia, *Chem. - A Eur. J.* **2015**, *21*, 10940–10959.
[25] C. J. Seel, T. Gulder, *ChemBioChem* **2019**, *20*, 1871–1897.
[26] M. G. Walter, E. L. Warren, J. R. McKone, S. W. Boettcher, Q. Mi, E. A. Santori, N. S. Lewis, *Chem. Rev.* **2010**, *110*, 6446–6473.
[27] A. Kudo, Y. Miseki, *Chem. Soc. Rev.* **2009**, *38*, 253–278.
[28] A. J. Morris, G. J. Meyer, E. Fujita, *Acc. Chem. Res.* **2009**, *42*, 1983–1994.
[29] K. M. Waldie, A. L. Ostericher, M. H. Reineke, A. F. Sasayama, C. P. Kubiak, *ACS Catal.* **2018**, *8*, 1313–1324.
[30] D. Ravelli, D. Dondi, M. Fagnoni, A. Albini, *Chem. Soc. Rev.* **2009**, *38*, 1999–2011.
[31] E. B. Corcoran, M. T. Pirnot, S. Lin, S. D. Dreher, D. A. Dirocco, I. W. Davies, S. L. Buchwald, D. W. C. MacMillan, *Science* **2016**, *353*, 279–283.
[32] W. J. Yoo, T. Tsukamoto, S. Kobayashi, *Org. Lett.* **2015**, *17*, 3640–3642.
[33] R. G. Pearson, *Chem. Rev.* **1985**, *85*, 41–49.
[34] E. S. Wiedner, M. B. Chambers, C. L. Pitman, R. M. Bullock, A. J. M. Miller, A. M.

Appel, *Chem. Rev.* **2016**, *116*, 8655–8692.
[35] R. N. Perutz, B. Procacci, *Chem. Rev.* **2016**, *116*, 8506–8544.
[36] C. L. Pitman, A. J. M. Miller, *ACS Catal.* **2014**, *4*, 2727–2733.
[37] M. H. Shaw, J. Twilton, D. W. C. MacMillan, *J. Org. Chem.* **2016**, *81*, 6898–6926.
[38] N. A. Romero, D. A. Nicewicz, *Chem. Rev.* **2016**, *116*, 10075–10166.
[39] E. C. Gentry, R. R. Knowles, *Acc. Chem. Res.* **2016**, *49*, 1546–1556.
[40] S. Zhu, M. Rueping, *Chem. Commun.* **2012**, *48*, 11960–11962.
[41] L. Capaldo, D. Ravelli, *European J. Org. Chem.* **2017**, *2017*, 2056–2071.
[42] S. Protti, M. Fagnoni, D. Ravelli, *ChemCatChem* **2015**, *7*, 1516–1523.
[43] D. Ravelli, M. Fagnoni, T. Fukuyama, T. Nishikawa, I. Ryu, *ACS Catal.* **2018**, *8*, 701–713.
[44] S. D. Halperin, H. Fan, S. Chang, R. E. Martin, R. Britton, *Angew. Chemie - Int. Ed.* **2014**, *53*, 4690–4693.
[45] H. Li, M. T. Zhang, *J. Photochem. Photobiol. A Chem.* **2018**, *355*, 109–113.
[46] A. Lipp, G. Lahm, T. Opatz, *J. Org. Chem.* **2016**, *81*, 4890–4897.
[47] S. Kamijo, G. Takao, K. Kamijo, M. Hirota, K. Tao, T. Murafuji, *Angew. Chemie - Int. Ed.* **2016**, *55*, 9695–9699.
[48] H. C. Lo, C. Leiva, O. Buriez, J. B. Kerr, M. M. Olmstead, R. H. Fish, *Inorg. Chem.* **2001**, *40*, 6705–6716.
[49] R. Ruppert, S. Herrmann, E. Steckhan, *J. Chem. Soc. Chem. Commun.* **1988**, *1*, 1150.
[50] J. Ryu, D. H. Nam, S. H. Lee, C. B. Park, *Chem. - A Eur. J.* **2014**, *20*, 12020–12025.
[51] S. H. Lee, D. H. Nam, J. H. Kim, J.-O. Baeg, C. B. Park, *ChemBioChem* **2009**, *10*, 1621–1624.
[52] K. T. Oppelt, E. Wöß, M. Stiftinger, W. Schöfberger, W. Buchberger, G. Knör, *Inorg. Chem.* **2013**, *52*, 11910–11922.
[53] V. Balzani, G. Bergamini, S. Campagna, F. Puntoriero, *Photochemistry and Photophysics of Coordination Compounds: Overview and General Concepts*, Springer-Verlag Berlin Heidelberg, **2007**.
[54] R. P. Wayne, *Basic Concepts of Photochemical Transformations*, Springer-Verlag Berlin Heidelberg, **2005**.
[55] P. Klán, J. Wirz, *Photochemistry of Organic Compounds: From Concepts to Practice*, John Wiley & Sons, Ltd, **2009**.
[56] J. C. Deaton, F. N. Castellano, in *Iridium(III) Optoelectron. Photonics Appl.*, John Wiley & Sons, Inc., Chichester, West Sussex, **2017**, pp. 1–69.
[57] C. Rosso, G. Filippini, P. G. Cozzi, A. Gualandi, M. Prato, *ChemPhotoChem* **2019**, *3*, 193–197.
[58] J. Haimerl, I. Ghosh, B. König, J. Vogelsang, J. M. Lupton, *Chem. Sci.* **2019**, *10*, 681–687.
[59] F. Strieth-Kalthoff, M. J. James, M. Teders, L. Pitzer, F. Glorius, *Chem. Soc. Rev.* **2018**, *47*, 7190–7202.
[60] L. Capaldo, D. Ravelli, *European J. Org. Chem.* **2017**, 2056–2071.
[61] D. M. Arias-Rotondo, J. K. McCusker, *Chem. Soc. Rev.* **2016**, *45*, 5803–5820.
[62] P. Herr, F. Glaser, L. A. Büldt, C. B. Larsen, O. S. Wenger, *J. Am. Chem. Soc.* **2019**, *141*, 14394–14402.
[63] J. J. Devery, J. D. Nguyen, C. Dai, C. R. J. Stephenson, *ACS Catal.* **2016**, *6*, 5962–5967.
[64] J. H. Shon, S. Sittel, T. S. Teets, *ACS Catal.* **2019**, *9*, 8646–8658.
[65] C. Kerzig, X. Guo, O. S. Wenger, *J. Am. Chem. Soc.* **2019**, *141*, 2122–2127.

[66] F. Glaser, C. Kerzig, O. S. Wenger, *Angew. Chemie Int. Ed.* **2020**, *59*, 10266–10284.
[67] I. Ghosh, T. Ghosh, J. I. Bardagi, B. König, *Science* **2014**, *346*, 725–728.
[68] M. Häring, R. Pérez-Ruiz, A. J. Von Wangelin, D. D. Díaz, *Chem. Commun.* **2015**, *51*, 16848–16851.
[69] N. G. W. Cowper, C. P. Chernowsky, O. P. Williams, Z. K. Wickens, *J. Am. Chem. Soc.* **2020**, *142*, 2093–2099.
[70] H. Kim, H. Kim, T. H. Lambert, S. Lin, *J. Am. Chem. Soc.* **2020**, 2087–2092.
[71] J. P. Barham, B. König, *Angew. Chemie Int. Ed.* **2019**, *59*, 2–18.
[72] K. T. Tarantino, P. Liu, R. R. Knowles, *J. Am. Chem. Soc.* **2013**, *135*, 10022–10025.
[73] N. Hoffmann, *European J. Org. Chem.* **2017**, *2017*, 1982–1992.
[74] T. P. Yoon, *Acc. Chem. Res.* **2016**, *49*, 2307–2315.
[75] R. Brimioulle, T. Bach, *Science* **2013**, *342*, 840–843.
[76] K. F. Biegasiewicz, S. J. Cooper, M. A. Emmanuel, D. C. Miller, T. K. Hyster, *Nat. Chem.* **2018**, *10*, 770–775.
[77] B. A. Sandoval, S. I. Kurtoic, M. M. Chung, K. F. Biegasiewicz, T. K. Hyster, *Angew. Chemie - Int. Ed.* **2019**, *58*, 8714–8718.
[78] T. K. Hyster, *Synlett* **2020**, *31*, 248–254.
[79] Z. Lu, T. P. Yoon, *Angew. Chemie - Int. Ed.* **2012**, *51*, 10329–10332.
[80] J. B. Metternich, R. Gilmour, *J. Am. Chem. Soc.* **2015**, *137*, 11254–11257.
[81] E. R. Welin, C. Le, D. M. Arias-Rotondo, J. K. McCusker, D. W. C. MacMillan, *Science* **2017**, *355*, 380–385.
[82] M. H. Shaw, V. W. Shurtleff, J. A. Terrett, J. D. Cuthbertson, D. W. C. MacMillan, *Science* **2016**, *352*, 1304–1308.
[83] J. Twilton, M. Christensen, D. A. DiRocco, R. T. Ruck, I. W. Davies, D. W. C. MacMillan, *Angew. Chemie - Int. Ed.* **2018**, *57*, 5369–5373.
[84] X. Guo, O. S. Wenger, *Angew. Chemie - Int. Ed.* **2018**, *57*, 2469–2473.
[85] D. M. Schultz, F. Lévesque, D. A. DiRocco, M. Reibarkh, Y. Ji, L. A. Joyce, J. F. Dropinski, H. Sheng, B. D. Sherry, I. W. Davies, *Angew. Chemie - Int. Ed.* **2017**, *56*, 15274–15278.
[86] J. J. Warren, T. A. Tronic, J. M. Mayer, *Chem. Rev.* **2010**, *110*, 6961–7001.
[87] J. W. Darcy, B. Koronkiewicz, G. A. Parada, J. M. Mayer, *Acc. Chem. Res.* **2018**, *51*, 2391–2399.
[88] O. S. Wenger, *Chem. - A Eur. J.* **2011**, *17*, 11692–11702.
[89] S. C. Jensen, S. B. Homan, E. A. Weiss, *J. Am. Chem. Soc.* **2016**, *138*, 1591–1600.
[90] J. J. Concepcion, M. K. Brennaman, J. R. Deyton, N. V. Lebedeva, M. D. E. Forbes, J. M. Papanikolas, T. J. Meyer, *J. Am. Chem. Soc.* **2007**, *129*, 6968–6969.
[91] J. C. Lennox, D. A. Kurtz, T. Huang, J. L. Dempsey, *ACS Energy Lett.* **2017**, *2*, 1246–1256.
[92] T. M. Monos, C. R. J. Stephenson, in *Iridium(III) Optoelectron. Photonics Appl.*, John Wiley & Sons, Inc., Chichester, West Sussex, **2017**, pp. 541–581.
[93] J. D. Nguyen, E. M. D'Amato, J. M. R. Narayanam, C. R. J. Stephenson, *Nat. Chem.* **2012**, *4*, 854–859.
[94] A. Singh, A. Arora, J. D. Weaver, *Org. Lett.* **2013**, *15*, 5390–5393.
[95] S. Lamansky, P. Djurovich, D. Murphy, F. Abdel-Razzaq, H. E. Lee, C. Adachi, P. E. Burrows, S. R. Forrest, M. E. Thompson, *J. Am. Chem. Soc.* **2001**, *123*, 4304–4312.
[96] Z. Liu, M. Guan, Z. Bian, D. Nie, Z. Gong, Z. Li, C. Huang, *Adv. Funct. Mater.* **2006**, *16*, 1441–1448.

[97] J. I. Goldsmith, W. R. Hudson, M. S. Lowry, T. H. Anderson, S. Bernhard, *J. Am. Chem. Soc.* **2005**, *127*, 7502–7510.
[98] B. F. Disalle, S. Bernhard, *J. Am. Chem. Soc.* **2011**, *133*, 11819–11821.
[99] V. Guerchais, J. L. Fillaut, *Coord. Chem. Rev.* **2011**, *255*, 2448–2457.
[100] V. Fernández-Moreira, F. L. Thorp-Greenwood, M. P. Coogan, *Chem. Commun.* **2010**, *46*, 186–202.
[101] T. Huang, Q. Yu, S. Liu, W. Huang, Q. Zhao, *Dalt. Trans.* **2018**, *47*, 7628–7633.
[102] H. Huang, S. Banerjee, P. J. Sadler, *ChemBioChem* **2018**, *19*, 1574–1589.
[103] A. Juris, V. Balzani, F. Barigelletti, S. Campagna, P. Belser, A. Von Zelewsky, *Coord. Chem. Rev.* **1988**, *84*, 85–277.
[104] D. Paul Rillema, G. Allen, T. J. Meyer, D. Conrad, *Inorg. Chem.* **1983**, *22*, 1617–1622.
[105] L. A. Büldt, X. Guo, A. Prescimone, O. S. Wenger, *Angew. Chemie - Int. Ed.* **2016**, *55*, 11247–11250.
[106] L. A. Büldt, X. Guo, R. Vogel, A. Prescimone, O. S. Wenger, *J. Am. Chem. Soc.* **2017**, *139*, 985–992.
[107] H. Kvapilová, W. Sattler, A. Sattler, I. V. Sazanovich, I. P. Clark, M. Towrie, H. B. Gray, S. Záliš, A. Vlček, *Inorg. Chem.* **2015**, *54*, 8518–8528.
[108] W. Sattler, L. M. Henling, J. R. Winkler, H. B. Gray, *J. Am. Chem. Soc.* **2015**, *137*, 1198–1205.
[109] W. Sattler, M. E. Ener, J. D. Blakemore, A. A. Rachford, P. J. Labeaume, J. W. Thackeray, J. F. Cameron, J. R. Winkler, H. B. Gray, *J. Am. Chem. Soc.* **2013**, *135*, 10614–10617.
[110] P. Chábera, K. S. Kjaer, O. Prakash, A. Honarfar, Y. Liu, L. A. Fredin, T. C. B. Harlang, S. Lidin, J. Uhlig, V. Sundström, R. Lomoth, P. Persson, K. Wärnmark, *J. Phys. Chem. Lett.* **2018**, *9*, 459–463.
[111] J. D. Braun, I. B. Lozada, C. Kolodziej, C. Burda, K. M. E. Newman, J. van Lierop, R. L. Davis, D. E. Herbert, *Nat. Chem.* **2019**, *11*, 1144–1150.
[112] A. B. Tamayo, B. D. Alleyne, P. I. Djurovich, S. Lamansky, I. Tsyba, N. N. Ho, R. Bau, M. E. Thompson, *J. Am. Chem. Soc.* **2003**, *125*, 7377–7387.
[113] K. Nakamaru, *Bull. Chem. Soc. Jpn.* **1982**, *55*, 1639–1640.
[114] L. Flamigini, A. Barbieri, C. Sabatini, B. Ventura, F. Barigelletti, *Top. Curr. Chem.* **2007**, *281*, 143–204.
[115] K. Teegardin, J. I. Day, J. Chan, J. Weaver, *Org. Process Res. Dev.* **2016**, *20*, 1156–1163.
[116] J. H. Shon, T. S. Teets, *Comments Inorg. Chem.* **2020**, *40*, 53–85.
[117] Y. Pellegrin, F. Odobel, *Comptes Rendus Chim.* **2017**, *20*, 283–295.
[118] M. G. Colombo, T. C. Brunold, T. Riedener, H. U. Güdel, M. Förtsch, H. B. Bürgi, *Inorg. Chem.* **1994**, *33*, 545–550.
[119] P. J. Hay, *J. Phys. Chem. A* **2002**, *106*, 1634–1641.
[120] A. Singh, K. Teegardin, M. Kelly, K. S. Prasad, S. Krishnan, J. D. Weaver, *J. Organomet. Chem.* **2015**, *776*, 51–59.
[121] X. Guo, Y. Okamoto, M. R. Schreier, T. R. Ward, O. S. Wenger, *Chem. Sci.* **2018**, *9*, 5052–5056.
[122] B. Pfund, D. M. Steffen, M. R. Schreier, M.-S. Bertrams, C. Ye, K. Börjesson, O. S. Wenger, C. Kerzig, *J. Am. Chem. Soc* **2020**, *142*, 10468–10476.
[123] G. Zhao, C. Yang, L. Guo, H. Sun, R. Lin, W. Xia, *J. Org. Chem.* **2012**, *77*, 6302–6306.
[124] Z. Lu, M. Shen, T. P. Yoon, *J. Am. Chem. Soc.* **2011**, *133*, 1162–1164.

[125] L. J. Rono, H. G. Yayla, D. Y. Wang, M. F. Armstrong, R. R. Knowles, *J. Am. Chem. Soc.* **2013**, *135*, 17735–17738.
[126] L. Ruiz Espelt, E. M. Wiensch, T. P. Yoon, *J. Org. Chem.* **2013**, *78*, 4107–4114.
[127] J. Du, L. R. Espelt, I. A. Guzei, T. P. Yoon, *Chem. Sci.* **2011**, *2*, 2115–2119.
[128] M. Neumann, K. Zeitler, *Chem. - A Eur. J.* **2013**, *19*, 6950–6955.
[129] R. Maidan, Z. Goren, J. Y. Becker, I. Willner, *J. Am. Chem. Soc* **1984**, *106*, 6217–6222.
[130] E. L. Tyson, Z. L. Niemeyer, T. P. Yoon, *J. Org. Chem.* **2014**, *79*, 1427–1436.
[131] D. A. Nicewicz, D. W. C. MacMillan, *Science* **2008**, *322*, 77–80.
[132] J. L. Jeffrey, F. R. Petronijević, D. W. C. MacMillan, *J. Am. Chem. Soc.* **2015**, *137*, 8404–8407.
[133] F. R. Petronijević, M. Nappi, D. W. C. MacMillan, *J. Am. Chem. Soc.* **2013**, *135*, 18323–18326.
[134] D. Kalyani, K. B. McMurtrey, S. R. Neufeldt, M. S. Sanford, *J. Am. Chem. Soc.* **2011**, *133*, 18566–18569.
[135] S. H. Lee, D. S. Choi, S. K. Kuk, C. B. Park, *Angew. Chemie - Int. Ed.* **2018**, *57*, 7958–7985.
[136] J. Chen, Z. Guan, Y. H. He, *Asian J. Org. Chem.* **2019**, *8*, 1775–1790.
[137] V. Uppada, S. Bhaduri, S. B. Noronha, *Curr. Sci.* **2014**, *106*, 946–957.
[138] H. Wu, C. Tian, X. Song, C. Liu, D. Yang, Z. Jiang, *Green Chem.* **2013**, *15*, 1773–1789.
[139] J. G. West, D. Huang, E. J. Sorensen, *Nat. Commun.* **2015**, *6*, 10093–10100.
[140] P. J. Sarver, V. Bacauanu, D. M. Schultz, D. A. Dirocco, Y. Lam, E. C. Sherer, D. W. C. MacMillan, *Nat. Chem.* **2020**, *12*, 459–467.
[141] T. J. Whittemore, C. Xue, J. Huang, J. C. Gallucci, C. Turro, *Nat. Chem.* **2020**, *12*, 180–185.
[142] J. C. Peters, G. C. Fu, *Science* **2016**, *351*, 681–685.
[143] J. M. Ahn, T. S. Ratani, K. I. Hannoun, G. C. Fu, J. C. Peters, *J. Am. Chem. Soc.* **2017**, *139*, 12716–12723.
[144] H. Q. Do, S. Bachman, A. C. Bissember, J. C. Peters, G. C. Fu, *J. Am. Chem. Soc.* **2014**, *136*, 2162–2167.
[145] A. C. Bissember, R. J. Lundgren, S. E. Creutz, J. C. Peters, G. C. Fu, *Angew. Chemie* **2013**, *125*, 5233–5237.
[146] C. L. Pitman, A. J. M. Miller, *ACS Catal.* **2014**, *4*, 2727–2733.
[147] K. R. Brereton, A. G. Bonn, A. J. M. Miller, *ACS Energy Lett.* **2018**, *3*, 1128–1136.
[148] C. Müller, A. Bauer, T. Bach, *Angew. Chemie - Int. Ed.* **2009**, *48*, 6640–6642.
[149] C. Jiang, W. Chen, W. H. Zheng, H. Lu, *Org. Biomol. Chem.* **2019**, *17*, 8673–8689.
[150] A. Bauer, F. Westkämper, S. Grimme, T. Bach, *Nature* **2005**, *436*, 1139–1140.
[151] A. Caron, É. Morin, S. K. Collins, *ACS Catal.* **2019**, *9*, 9458–9464.
[152] W. Ding, L. Q. Lu, Q. Q. Zhou, Y. Wei, J. R. Chen, W. J. Xiao, *J. Am. Chem. Soc.* **2017**, *139*, 63–66.
[153] S. Sato, T. Morikawa, T. Kajino, O. Ishitani, *Angew. Chemie - Int. Ed.* **2013**, *52*, 988–992.
[154] A. J. Huckaba, H. Shirley, R. W. Lamb, S. Guertin, S. Autry, H. Cheema, K. Talukdar, T. Jones, J. W. Jurss, A. Dass, N. I. Hammer, R. H. Schmehl, C. E. Webster, J. H. Delcamp, *ACS Catal.* **2018**, *8*, 4838–4847.
[155] S. A. Green, S. W. M. Crossley, J. L. M. Matos, S. Vásquez-Céspedes, S. L. Shevick, R. A. Shenvi, *Acc. Chem. Res.* **2018**, *51*, 2628–2640.
[156] S. W. M. Crossley, C. Obradors, R. M. Martinez, R. A. Shenvi, *Chem. Rev.* **2016**, *116*,

8912–9000.
[157] D. M. Smith, M. E. Pulling, J. R. Norton, *J. Am. Chem. Soc.* **2007**, *129*, 770–771.
[158] G. Hilt, *ChemCatChem* **2014**, *6*, 2484–2485.
[159] J. A. Labinger, J. E. Bercaw, *Nature* **2002**, *417*, 507–514.
[160] D. Wang, D. Astruc, *Chem. Rev.* **2015**, *115*, 6621–6686.
[161] S. E. Clapham, A. Hadzovic, R. H. Morris, *Coord. Chem. Rev.* **2004**, *248*, 2201–2237.
[162] V. Artero, M. Fontecave, *Coord. Chem. Rev.* **2005**, *249*, 1518–1535.
[163] J. R. McKone, S. C. Marinescu, B. S. Brunschwig, J. R. Winkler, H. B. Gray, *Chem. Sci.* **2014**, *5*, 865–878.
[164] R. M. Bullock, A. M. Appel, M. L. Helm, *Chem. Commun.* **2014**, *50*, 3125–3143.
[165] Y. Matsubara, E. Fujita, M. D. Doherty, J. T. Muckerman, C. Creutz, *J. Am. Chem. Soc.* **2012**, *134*, 15743–15757.
[166] H. Fong, J. C. Peters, *Inorg. Chem.* **2015**, *54*, 5124–5135.
[167] F. Bertini, N. Gorgas, B. Stöger, M. Peruzzini, L. F. Veiros, K. Kirchner, L. Gonsalvi, *ACS Catal.* **2016**, *6*, 2889–2893.
[168] R. H. Morris, *Chem. Rev.* **2016**, *116*, 8588–8654.
[169] D. C. Eisenberg, J. R. Norton, *Isr. J. Chemsitry* **1991**, *31*, 55–66.
[170] Y. Hu, J. R. Norton, *J. Am. Chem. Soc.* **2014**, *136*, 5938–5948.
[171] J. Choi, L. Tang, J. R. Norton, *J. Am. Chem. Soc.* **2007**, *129*, 234–240.
[172] S. W. M. Crossley, F. Barabé, R. A. Shenvi, *J. Am. Chem. Soc.* **2014**, *136*, 16788–16791.
[173] G. Li, J. L. Kuo, A. Han, J. M. Abuyuan, L. C. Young, J. R. Norton, J. H. Palmer, *J. Am. Chem. Soc.* **2016**, *138*, 7698–7704.
[174] J. Hartung, M. E. Pulling, D. M. Smith, D. X. Yang, J. R. Norton, *Tetrahedron* **2008**, *64*, 11822–11830.
[175] J. Choi, M. E. Pulling, D. M. Smith, J. R. Norton, *J. Am. Chem. Soc.* **2008**, *130*, 4250–4252.
[176] V. D. Parker, M. Tilset, *J. Am. Chem. Soc.* **1989**, *111*, 6711–6717.
[177] M. D. Tzirakis, I. N. Lykakis, M. Orfanopoulos, *Chem. Soc. Rev.* **2009**, *38*, 2609–2621.
[178] G. Li, J. L. Kuo, A. Han, J. M. Abuyuan, L. C. Young, J. R. Norton, J. H. Palmer, *J. Am. Chem. Soc.* **2016**, *138*, 7698–7704.
[179] J. C. Lo, Y. Yabe, P. S. Baran, *J. Am. Chem. Soc.* **2014**, *136*, 1304–1307.
[180] J. Choi, L. Tang, J. R. Norton, **2007**, 234–240.
[181] R. E. Adams, T. A. Grusenmeyer, A. L. Griffith, R. H. Schmehl, *Coord. Chem. Rev.* **2018**, *362*, 44–53.
[182] L. Schmermund, V. Jurkaš, F. F. Özgen, G. D. Barone, H. C. Büchsenschütz, C. K. Winkler, S. Schmidt, R. Kourist, W. Kroutil, *ACS Catal.* **2019**, *9*, 4115–4144.
[183] T. Quinto, V. Köhler, T. R. Ward, *Top. Catal.* **2014**, *57*, 321–331.
[184] H. Wu, C. Tian, X. Song, C. Liu, D. Yang, Z. Jiang, *Green Chem.* **2013**, *15*, 1773–1789.
[185] J. J. Soldevila-Barreda, A. Habtemariam, I. Romero-Canelón, P. J. Sadler, *J. Inorg. Biochem.* **2015**, *153*, 322–333.
[186] J. J. Soldevila-Barreda, P. C. A. Bruijnincx, A. Habtemariam, G. J. Clarkson, R. J. Deeth, P. J. Sadler, *Organometallics* **2012**, *31*, 5958–5967.
[187] K. Seelbach, B. Riebel, W. Hummel, M. R. Kula, V. I. Tishkov, A. M. Egorov, C. Wandrey, U. Kragl, *Tetrahedron Lett.* **1996**, *37*, 1377–1380.
[188] H. T. Ding, D. F. Liu, Z. L. Li, Y. Q. Du, X. H. Xu, Y. H. Zhao, *J. Appl. Microbiol.* **2011**, *111*, 1075–1085.

[189] V. Köhler, Y. M. Wilson, M. Dürrenberger, D. Ghislieri, E. Churakova, T. Quinto, L. Knörr, D. Häussinger, F. Hollmann, N. J. Turner, T. R. Ward, *Nat. Chem.* **2013**, *5*, 93–99.
[190] Y. Okamoto, V. Köhler, C. E. Paul, F. Hollmann, T. R. Ward, *ACS Catal.* **2016**, *6*, 3553–3557.
[191] J. Canivet, G. Süss-Fink, P. Štěpnička, *Eur. J. Inorg. Chem.* **2007**, 4736–4742.
[192] H. K. Song, S. H. Lee, K. Won, J. H. Park, J. K. Kim, H. Lee, S. J. Moon, D. K. Kim, C. B. Park, *Angew. Chemie - Int. Ed.* **2008**, *47*, 1749–1752.
[193] K. Koga, Y. Matsubara, T. Kosaka, K. Koike, T. Morimoto, O. Ishitani, *Organometallics* **2015**, *34*, 5530–5539.
[194] W. Dong, J. Tang, L. Zhao, F. Chen, L. Deng, M. Xian, *Green Chem.* **2020**, *22*, 2279–2287.
[195] S. M. Barrett, C. L. Pitman, A. G. Walden, A. J. M. Miller, *J. Am. Chem. Soc* **2014**, *136*, 14718–14721.
[196] A. Mc Skimming, S. B. Colbran, *Chem. Soc. Rev.* **2013**, *42*, 5439–5488.
[197] U. Kölle, M. Grätzel, *Angew. Chemie Int. Ed. English* **1987**, *26*, 567–570.
[198] E. Steckhan, S. Herrmann, R. Ruppert, E. Dietz, M. Frede, E. Spika, *Organometallics* **1991**, *10*, 1568–1577.
[199] H. C. Lo, O. Buriez, J. B. Kerr, R. H. Fish, *Angew. Chemie Int. Ed.* **1999**, *38*, 1429–32.
[200] H. C. Lo, C. Leiva, O. Buriez, J. B. Kerr, M. M. Olmstead, R. H. Fish, *Inorg. Chem.* **2001**, *40*, 6705–6716.
[201] C. L. Pitman, O. N. L. Finster, A. J. M. Miller, *Chem. Commun.* **2016**, *52*, 9105–9108.
[202] L. M. A. Quintana, S. I. Johnson, S. L. Corona, W. Villatoro, W. A. Goddard III, M. K. Takase, D. G. Vandervelde, J. R. Winkler, H. B. Gray, J. D. Blakemore, *Proc. Natl. Acad. Sci. U. S. A.* **2016**, *113*, 6409–6414.
[203] F. Hildebrand, C. Kohlmann, A. Franz, S. Lütz, *Adv. Synth. Catal.* **2008**, *350*, 909–918.
[204] J. J. Soldevila-Barreda, I. Romero-Canelón, A. Habtemariam, P. J. Sadler, *Nat. Commun.* **2015**, *6*, 6582.
[205] Y. K. Yan, M. Melchart, A. Habtemariam, A. F. A. Peacock, P. J. Sadler, *J. Biol. Inorg. Chem.* **2006**, *11*, 483–488.
[206] C. B. Park, S. H. Lee, E. Subramanian, B. B. Kale, S. M. Lee, J. O. Baeg, *Chem. Commun.* **2008**, 5423–5425.
[207] D. H. Nam, S. H. Lee, C. B. Park, *Small* **2010**, *6*, 922–926.
[208] S. H. Lee, D. H. Nam, C. B. Park, *Adv. Synth. Catal.* **2009**, *351*, 2589–2594.
[209] D. H. Nam, C. B. Park, *ChemBioChem* **2012**, *13*, 1278–1282.
[210] E. Steckhan, R. Wienkamp, *Angew. Chem. Int. Ed. Engl.* **1983**, *22*, 497.
[211] R. K. Yadav, J. O. Baeg, G. H. Oh, N. J. Park, K. J. Kong, J. Kim, D. W. Hwang, S. K. Biswas, *J. Am. Chem. Soc.* **2012**, *134*, 11455–11461.
[212] S. Choudhury, J.-O. Baeg, N.-J. Park, R. K. Yadav, *Angew. Chemie* **2012**, *124*, 11792–11796.
[213] J. H. Kim, S. H. Lee, J. S. Lee, M. Lee, C. B. Park, *Chem. Commun.* **2011**, *47*, 10227–10229.
[214] A. K. Mengele, G. M. Seibold, B. J. Eikmanns, S. Rau, *ChemCatChem* **2017**, *9*, 4369–4376.
[215] J. S. Lee, S. H. Lee, J. H. Kim, C. B. Park, *Lab Chip* **2011**, *11*, 2309–2311.
[216] J. H. Kim, M. Lee, J. S. Lee, C. B. Park, *Angew. Chemie* **2012**, *124*, 532–535.
[217] T. Ghosh, T. Slanina, B. König, *Chem. Sci.* **2015**, *6*, 2027–2034.

[218] L. Zedler, A. K. Mengele, K. M. Ziems, Y. Zhang, M. Wächtler, S. Gräfe, T. Pascher, S. Rau, S. Kupfer, B. Dietzek, *Angew. Chemie - Int. Ed.* **2019**, *58*, 13140–13148.
[219] C. Kerzig, O. S. Wenger, *Chem. Sci.* **2018**, *9*, 6670–6678.
[220] K. A. El Roz, F. N. Castellano, *Chem. Commun.* **2017**, *53*, 11705–11708.
[221] M. Giedyk, R. Narobe, S. Weiß, D. Touraud, W. Kunz, B. König, *Nat. Catal.* **2020**, *3*, 40–47.
[222] Z. C. Litman, Y. Wang, H. Zhao, J. F. Hartwig, *Nature* **2018**, *560*, 355–359.
[223] E. Steckhan, S. Herrmann, R. Ruppert, E. Dietz, M. Frede, E. Spika, *Organometallics* **1991**, *10*, 1568–1577.
[224] D. Recognition, H. C. Lo, R. H. Fish, *Communications* **2002**, 478–481.
[225] K. Saito, N. Matsusue, H. Kanno, Y. Hamada, H. Takahashi, T. Matsumura, *Jpn. J. Appl. Phys.* **2004**, *43*, 2733–2734.
[226] A. Shmailov, L. Alimbarova, I. Vatsouro, V. Tafeenko, E. Shokova, V. Kovalev, *Tetrahedron* **2012**, *68*, 4765–4772.
[227] L. Vandromme, H. U. Reißig, S. Gröper, J. P. Rabe, *European J. Org. Chem.* **2008**, 2049–2055.
[228] X. Zeng, A. S. Batsanov, M. R. Bryce, *J. Org. Chem.* **2006**, *71*, 9589–9594.
[229] J. Brooks, Y. Babayan, S. Lamansky, P. I. Djurovich, I. Tsyba, R. Bau, M. E. Thompson, *Inorg. Chem.* **2002**, *41*, 3055–3066.
[230] D. Mauzerall, F. H. Westheimer, *J. Am. Chem. Soc.* **1955**, *77*, 2261–2264.
[231] C. E. Paul, S. Gargiulo, D. J. Opperman, I. Lavandera, V. Gotor-Fernández, V. Gotor, A. Taglieber, I. W. C. E. Arends, F. Hollmann, *Org. Lett.* **2013**, *15*, 180–183.
[232] P. L. Hentall, N. Flowers, T. D. H. Bugg, *Chem. Commun.* **2001**, *1*, 2098–2099.
[233] F. Hollmann, I. W. C. E. Arends, K. Buehler, *ChemCatChem* **2010**, *2*, 762–782.
[234] J. D. Petersen, P. C. Ford, *J. Phys. Chem.* **1974**, *78*, 1144–1149.
[235] M. Montalti, A. Credi, L. Prodi, M. T. Gandolfi, *Handbook of Photochemistry*, Taylor And Francis, Boca Raton, **2006**.
[236] J. C. Deaton, C. M. Taliaferro, C. L. Pitman, R. Czerwieniec, E. Jakubikova, A. J. M. Miller, F. N. Castellano, *Inorg. Chem.* **2018**, *57*, 15445–15461.
[237] F. M. Hörmann, C. Kerzig, T. S. Chung, A. Bauer, O. S. Wenger, T. Bach, *Angew. Chemie - Int. Ed.* **2020**, 2–12.
[238] H. Senboku, H. Komatsu, Y. Fujimura, M. Tokuda, *Synlett* **2001**, 418–420.
[239] G. R. Fulmer, A. J. M. Miller, N. H. Sherden, H. E. Gottlieb, A. Nudelman, B. M. Stoltz, J. E. Bercaw, K. I. Goldberg, *Organometallics* **2010**, *29*, 2176–2179.
[240] F. Li, C. Sun, N. Wang, *J. Org. Chem.* **2014**, *79*, 8031–8039.
[241] T. P. Brewster, A. J. M. Miller, D. M. Heinekey, K. I. Goldberg, *J. Am. Chem. Soc.* **2013**, *135*, 16022–16025.
[242] M.-T. Youinou, R. Ziessel, *J. Organomet. Chem.* **1989**, *363*, 197–208.
[243] S. M. Smith, G. L. Hoang, R. Pal, M. O. B. Khaled, L. S. W. Pelter, X. C. Zeng, J. M. Takacs, *Chem. Commun.* **2012**, *48*, 12180–12182.
[244] A. Garzan, A. Jaganathan, N. Salehi Marzijarani, R. Yousefi, D. C. Whitehead, J. E. Jackson, B. Borhan, *Chem. - A Eur. J.* **2013**, *19*, 9015–9021.
[245] F. Giacomina, A. Alexakis, *European J. Org. Chem.* **2013**, 6710–6721.
[246] X. Sun, K. Frimpong, K. L. Tan, *J. Am. Chem. Soc.* **2010**, *132*, 11841–11843.
[247] A. Blanc, F. D. Toste, *Angew. Chemie - Int. Ed.* **2006**, *45*, 2096–2099.
[248] J. J. Molloy, J. B. Metternich, C. G. Daniliuc, A. J. B. Watson, R. Gilmour, *Angew. Chemie - Int. Ed.* **2018**, *57*, 3168–3172.

[249] S. McIntyre, E. Hörmann, F. Menges, S. P. Smidt, A. Pfaltz, *Adv. Synth. Catal.* **2005**, *347*, 282–288.
[250] T. Kippo, T. Fukuyama, I. Ryu, *Org. Lett.* **2011**, *13*, 3864–3867.
[251] P. V. Ramachandran, D. R. Nicponski, *Chem. Commun.* **2014**, *50*, 15216–15219.
[252] E. Sagot, D. S. Pickering, X. Pu, M. Umberti, T. B. Stensbøl, B. Nielsen, M. Chapelet, J. Bolte, T. Gefflaut, L. Bunch, *J. Med. Chem.* **2008**, *51*, 4093–4103.
[253] G. Li, D. Leow, L. Wan, J. Q. Yu, *Angew. Chemie - Int. Ed.* **2013**, *52*, 1245–1247.
[254] C. Tao, L. Sun, B. Wang, Z. Liu, Y. Zhai, X. Zhang, D. Shi, W. Liu, *Tetrahedron Lett.* **2017**, *58*, 305–308.
[255] C. Stueckler, C. K. Winkler, M. Bonnekessel, K. Faber, *Adv. Synth. Catal.* **2010**, *352*, 2663–2666.
[256] C. T. Yang, Z. Q. Zhang, J. Liang, J. H. Liu, X. Y. Lu, H. H. Chen, L. Liu, *J. Am. Chem. Soc.* **2012**, *134*, 11124–11127.
[257] D. F. Taber, C. M. Paquette, P. G. Reddy, *Tetrahedron Lett.* **2009**, *50*, 2462–2463.
[258] M. Ficker, S. W. Svenningsen, T. Larribeau, J. B. Christensen, *Tetrahedron Lett.* **2018**, *59*, 1125–1129.
[259] Y. Arai, R. Tomita, G. Ando, T. Koike, M. Akita, *Chem. - A Eur. J.* **2016**, *22*, 1262–1265.
[260] W. Hüggenberg, A. Seper, I. M. Oppel, G. Dyker, *European J. Org. Chem.* **2010**, 6786–6797.
[261] R. Bejot, S. Anjaiah, J. R. Falck, C. Mioskowski, *European J. Org. Chem.* **2007**, 101–107.
[262] J. C. Anderson, R. H. Munday, *J. Org. Chem.* **2004**, *69*, 8971–8974.
[263] C. Sabot, K. A. Kumar, C. Antheaume, C. Mioskowski, *J. Org. Chem.* **2007**, *72*, 5001–5004.
[264] G. E. M. Crisenza, N. G. McCreanor, J. F. Bower, *J. Am. Chem. Soc.* **2014**, *136*, 10258–10261.
[265] A. C. Hernandez-Perez, S. K. Collins, *Angew. Chemie - Int. Ed.* **2013**, *52*, 12696–12700.
[266] C. Quinton, V. Alain-Rizzo, C. Dumas-Verdes, F. Miomandre, G. Clavier, P. Audebert, *RSC Adv.* **2014**, *4*, 34332–34342.
[267] J. A. M. Simões, J. L. Beauchamp, *Chem. Rev.* **1990**, *90*, 629–688.
[268] D. D. M. Wayner, V. D. Parker, *Acc. Chem. Res.* **1993**, *26*, 287–294.
[269] D. J. Goebbert, P. G. Wenthold, *Int. J. Mass Spectrom.* **2006**, *257*, 1–11.
[270] L. Yu-Ran, *Comprehensive Handbook of Chemical Bond Energies*, Taylor & Francis Group, Boca Raton, **2007**.
[271] J. Masnovi, E. G. Samsel, R. M. Bullock, *J. Chem. Soc. Chem. Commun.* **1989**, 1044–1045.
[272] R. Hollis, L. Hughes, V. W. Bowry, K. U. Ingold, *J. Org. Chem.* **1992**, *57*, 4284–4287.
[273] C. P. Rosenau, B. J. Jelier, A. D. Gossert, A. Togni, *Angew. Chemie - Int. Ed.* **2018**, *57*, 9528–9533.
[274] H. Woo, S. Cho, Y. Han, W. S. Chae, D. R. Ahn, Y. You, W. Nam, *J. Am. Chem. Soc.* **2013**, *135*, 4771–4787.
[275] Y. You, S. Y. Park, *J. Am. Chem. Soc.* **2005**, *127*, 12438–12439.
[276] J. R. Carlise, X. Y. Wang, M. Weck, *Macromolecules* **2005**, *38*, 9000–9008.
[277] K. J. Suhr, L. D. Bastatas, Y. Shen, L. A. Mitchell, G. A. Frazier, D. W. Taylor, J. D. Slinker, B. J. Holliday, *Dalt. Trans.* **2016**, *45*, 17807–17823.

[278] M. S. Abdel-Maksoud, M. R. Kim, M. I. El-Gamal, M. M. Gamal El-Din, J. Tae, H. S. Choi, K. T. Lee, K. H. Yoo, C. H. Oh, *Eur. J. Med. Chem.* **2015**, *95*, 453–463.
[279] M. M. C. H. Van Schie, C. E. Paul, I. W. C. E. Arends, F. Hollmann, *Chem. Commun.* **2019**, *55*, 1790–1792.

Curriculum Vitae

Personal Details

Name	Mirjam Schreier
Date of Birth	27.06.1990
Birthplace	Solothurn SO, Switzerland

Education

2016-2020	PhD in the group of Prof. Dr. Oliver S. Wenger University of Basel, Switzerland
2013-2015	Master Studies in Chemistry University of Basel, Switzerland Master Thesis in the group of Prof. Dr. Andreas Pfaltz entitled "*Synthesis and Screening of Chiral N-Heterocyclic Carbene Catalysts for the Asymmetric Cross-Benzoin Reaction*"
2009-2013	Bachelor Studies in Chemistry University of Basel, Switzerland
2004-2008	Kantonsschule Solothurn, SO

Publications

Mirjam R. Schreier, Xingwei Guo, Oliver S. Wenger
Photoinduced Hydrogen Atom Transfer from an Iridium Complex to Unactivated Olefins
Chem. Sci. **2020**, *11*, 8582-8594.

Björn Pfund, Debora M. Steffen, Mirjam R. Schreier, Maria-Sophie Bertrams, Chen Ye, Karl Börjesson, Oliver S. Wenger, Christoph Kerzig
UV Light Generation and Challenging Photoreactions Enabled by Upconversion in Water
J. Am. Chem. Soc. **2020**, *142*, 10468-10476.

> This manuscript was previously published as a preprint on the preprint server ChemRxiv: DOI: 10.26434/CHEMRXIV.11914992.V1

Xingwei Guo, Yasunori Okamoto, Mirjam R. Schreier, Thomas. R. Ward, Oliver S. Wenger, Reductive Amination and Enantioselective Amine Synthesis by Photoredox Catalysis
Eur. J. Org. Chem., **2020**, 1288-1293.

Xingwei Guo, Yasunori Okamoto, Mirjam R. Schreier, Thomas. R. Ward, Oliver S. Wenger, Enantioselective synthesis of amines by combining photoredox and enzymatic catalysis in a cyclic reaction network
Chem. Sci., **2018**, *9*, 5052-5056.

Poster Contributions to Conferences

09/2019	SCS Fall Meeting *Photoinduced Hydrogen Atom Transfer Reactions Catalyzed by Iridium Hydrides* Zürich, Switzerland
07/2019	23rd International Symposium on the Photochemistry and Photophysics of Coordination Compounds (ISPPCC) *Iridium Hydrides as Hydrogen Atom Transfer Catalysts Activated by Visible-Light* Hong Kong
06/2019	SCS Photochemistry Symposium *Photochemical Regeneration of NADH with Water-Soluble Photosensitizers* Fribourg, Switzerland
05/2019	Annual NCCR Fellow Retreat *Photochemical Regeneration of NADH with Water-Soluble Photosensitizers* Grindelwald, Switzerland
03/2019	Koordinationschemie-Treffen *Iridiumhydride katalysieren die Übertragung von Wasserstoff-atomen unter Einfluss von sichtbarem Licht* München, Germany
09/2018	SCS Fall Meeting *Photoinduced Multielectron Accumulation in Hexakispyridylbenzenes* Lausanne, Switzerland
08/2018	43rd International Conference on Coordination Chemistry (ICCC) *Iridium Hydrides as Hydrogen Atom Transfer Catalysts Activated by Visible-Light* Sendai, Japan
05/2018	Annual NCCR Fellow Retreat *Efficient Photochemical NADH-Regeneration in Aqueous Systems* Magglingen, Switzerland

08/2017	International Conference on Molecular Systems Engineering (ICMSE) *Photochemical Regeneration of 1,4-NAD(P)H* Basel, Switzerland
05/2017	Annual NCCR Fellow Retreat *Merging Photocatalysis and Biocatalysis: Photochemical Regeneration of 1,4-NADH* Grindelwald, Switzerland
09/2016	SCS Fall Meeting *Rhodium-Complexes for the Photochemical NAD(P)H Regeneration* Zurich, Switzerland
04/2016	Annual NCCR Fellow Retreat *Towards NADH generation: light-induced charge accumulation and photoreduction of NAD^+* Magglingen, Switzerland

Other Contributions to Science

05/2016 – 02/2017	Active board member of the PhD Chemistry Community (PCC) at the University of Basel, organization of research seminars, symposia and networking events at the Department of Chemistry

Lorenzo Delarue Bizzini, Sabine Malzkuhn, Cedric Stress, Diana Tahchieva, Mirjam Schreier, Serena Rigo, Andrea Pannwitz, Linda Bannwart,
Basel Chemistry Symposium 2016 in Memory of Professor Jules Piccard (Conference Report)
Chimia, **2017**, *71*, 246-247.